



Terms and Conditions of Use of Digitised Theses from Trinity College Library Dublin

Copyright statement

All material supplied by Trinity College Library is protected by copyright (under the Copyright and Related Rights Act, 2000 as amended) and other relevant Intellectual Property Rights. By accessing and using a Digitised Thesis from Trinity College Library you acknowledge that all Intellectual Property Rights in any Works supplied are the sole and exclusive property of the copyright and/or other IPR holder. Specific copyright holders may not be explicitly identified. Use of materials from other sources within a thesis should not be construed as a claim over them.

A non-exclusive, non-transferable licence is hereby granted to those using or reproducing, in whole or in part, the material for valid purposes, providing the copyright owners are acknowledged using the normal conventions. Where specific permission to use material is required, this is identified and such permission must be sought from the copyright holder or agency cited.

Liability statement

By using a Digitised Thesis, I accept that Trinity College Dublin bears no legal responsibility for the accuracy, legality or comprehensiveness of materials contained within the thesis, and that Trinity College Dublin accepts no liability for indirect, consequential, or incidental, damages or losses arising from use of the thesis for whatever reason. Information located in a thesis may be subject to specific use constraints, details of which may not be explicitly described. It is the responsibility of potential and actual users to be aware of such constraints and to abide by them. By making use of material from a digitised thesis, you accept these copyright and disclaimer provisions. Where it is brought to the attention of Trinity College Library that there may be a breach of copyright or other restraint, it is the policy to withdraw or take down access to a thesis while the issue is being resolved.

Access Agreement

By using a Digitised Thesis from Trinity College Library you are bound by the following Terms & Conditions. Please read them carefully.

I have read and I understand the following statement: All material supplied via a Digitised Thesis from Trinity College Library is protected by copyright and other intellectual property rights, and duplication or sale of all or part of any of a thesis is not permitted, except that material may be duplicated by you for your research use or for educational purposes in electronic or print form providing the copyright owners are acknowledged using the normal conventions. You must obtain permission for any other use. Electronic or print copies may not be offered, whether for sale or otherwise to anyone. This copy has been supplied on the understanding that it is copyright material and that no quotation from the thesis may be published without proper acknowledgement.

NOISE SOURCE IDENTIFICATION FOR DUCTED FANS

GARETH J. BENNETT

Department of Mechanical & Manufacturing Engineering

Parsons Building

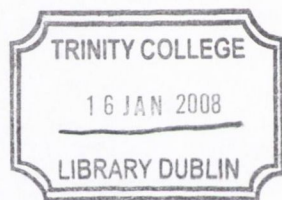
Trinity College

Dublin 2

Ireland

April 2006

A thesis submitted to the University of Dublin in partial
fulfillment of the requirements for the degree of Ph.D.



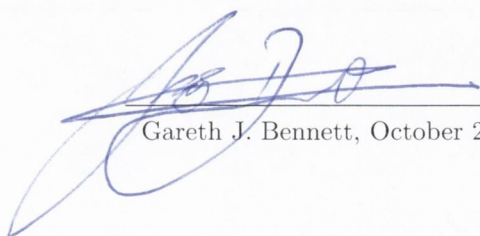
THESIS

8319

Declaration

I declare that I am the author of this thesis and that all work described herein is my own, unless otherwise referenced. Furthermore, this work has not been submitted in whole or part, to any other university or college for any degree or qualification.

I authorise the library of Trinity College, Dublin to lend this thesis.



Gareth J. Bennett, October 2006

Abstract

Understanding combustion noise source mechanisms, designing efficient acoustic liners and optimising active control algorithms for noise reduction requires the identification of the frequency and modal content of the combustion noise contribution. Coherence-based noise source identification techniques have been developed which can be used to identify the contribution of combustion noise to near and far-field acoustic measurements of aero-engines. A number of existing identification techniques from the literature, as well as some new techniques, are implemented and evaluated under controlled experimental conditions. A series of tests are conducted to examine the efficacy of each of the procedures for specific applications. An experimental rig was designed and built to gain a fundamental physical understanding of the convection of combustion noise through the turbine of an aero-engine. The identification techniques are applied to this rig, with the objective of separating the pressure field into its constituent parts.

The underlying assumption with these identification techniques is that the propagation\convection path, from combustion can to measurement point, is a linear one. It is shown that where the combustion noise propagates in a non-linear fashion the identified contribution will be inaccurate. The experimental rig, consisting of a vane-axial fan mounted in a duct, allows potential non-linear interaction mechanisms between a convected sound source and the fan to be investigated. Tests carried out on the experimental rig allow a non-linear interaction tone, between the rotor BPF and a convected tone, to be generated. An experimental technique was developed which enabled an acoustic modal decomposition to be performed in the duct. From the modal decomposition, it is suggested that the modal energy at the BPF and the convected tone combine to produce a sum tone, which due to its modal composition will only propagate once above its cut-on frequency. It is suggested that this is analogous with rotor-rotor interaction theories but further analysis to understand the exact process of this modal interaction is required.

Acknowledgments

I would like to express my heartfelt gratitude to Professor John Fitzpatrick for his help and guidance over the last four years, and for encouraging me to return to Trinity College to work on the SILENCE(R) project. I sincerely wish that our collaboration in projects professional, as well social, continue into the future.

The administrative and technical staff are a support without which no thesis could be completed. Joan Gillen, Tom Haveron, Gabrielle, JJ and Sean have been instrumental in the completion of this work. I would like to mention, in particular, Alan Reid, the Chief Experimental Officer, for his help in designing the experimental rig.

This Ph.D. was partly supported by the SILENCE(R) project under EU contract no. G4RD-CT-2001-00500. Whilst working on this contract I have come into contact with engineers from all over Europe and have had an opportunity to visit their work places and hometowns. I have been impressed with their friendliness, engineering achievements, the beauty of their countries, but most of all, with their food! In particular, I would like to acknowledge Alastair Moore from Rolls Royce Plc. and Alain Dravet from SNECMA Moteurs.

My workmates in the lab. have made my workplace both pleasurable and inspirational. My post-graduate and post-doctorate colleagues from the Sound and Vibration Laboratory: Orla, Damien, Ludo, Franck, Björn, Petr, David, Stephen, John, Eoin and Meaghan are exemplary engineers, possessing a thirst for knowledge and an enthusiasm to contribute, that has led to an environment of learning true to the ideal of any University.

To my sister Edel, and my mother, Amy, I would like to express my deepest gratitude. For their support in all matters through the years, and endless love, I could never thank them enough. Happiness, health and long life to us all. My new and extended family, Dr. Seán Devitt and his wife Ann, Séamus, Daniela, Marie and Jim, have all helped and supported me in this work. I count myself truly fortunate to have been welcomed into their lives and hearts. As for my two darling little nieces Sofia and Rebecca, they put things in perspective. I'll give them each a copy of my thesis when they turn eighteen!

Ann, my cosmic mate, my best friend, my true love and inspiration. You bring joy to my life and provide me with the strength and will to live it. My partner now, an angle that came down to save me. This work, and my life I dedicate to you.

To Ann

Contents

Nomenclature	viii
1 Introduction	1
1.1 Background	1
1.2 Objectives of Thesis	2
1.3 Thesis Outline	4
2 Pressure Field In A Cylindrical Duct	5
2.1 Duct Acoustic Modes	5
2.2 Propagation	9
2.3 Radiation	13
2.4 Plane Wave Duct Acoustics	15
2.4.1 Plane Wave Decomposition	16
2.4.2 Reflection Coefficient	17
2.4.3 Acoustic Impedance	19
2.4.4 Transmission Loss	20
2.5 Core Noise Generation Mechanisms	21
2.5.1 Rotor Only	21
2.5.2 Rotor-Stator Interaction	23
2.5.3 Combustion	24
2.5.4 Inflow Distortion-Rotor Interaction	26
2.6 Contribution of Thesis	26
3 Experimental Rig	29
3.1 Introduction	29
3.2 Anechoic Termination	29
3.2.1 Horn Theory	30
3.3 Vaneaxial Fan	38
3.4 Instrumentation and Analysis	39

3.4.1	Signal Processing	40
4	Preliminary Experimental Results	41
4.1	Introduction and Objectives	41
4.2	Microphone Calibration	42
4.3	Closed Ended Duct	43
4.3.1	Theory	43
4.3.2	Results	46
4.4	Open Ended Duct	48
4.4.1	Theory	48
4.4.2	Results	50
4.5	Fan Installed (Not Rotating)	52
4.6	Fan Installed (Rotating)	54
5	Source Identification	71
5.1	Introduction	71
5.2	Identification Techniques	71
5.2.1	Coherent Output Spectrum	72
5.2.2	Signal Enhancement	73
5.2.3	Conditional Spectral Analysis	74
5.2.4	System of Non-Linear Equations	74
5.2.5	The Two Test Procedure	75
5.3	Experimental Setup	75
5.4	Experimental Results	76
5.5	Evaluation of Techniques	77
5.6	Linear Noise Source Separation	78
5.6.1	Conditional Spectral Analysis Applied to Experimental Rig	78
5.6.2	Conditioned Frequency Response Functions Across The Fan	84
6	Non-Linear Analysis	97
6.1	Introduction	97
6.2	Non-Linear Simulations	99
6.3	Time Domain Averaging	105
6.4	Investigation above plane wave region	106
6.4.1	Tyler and Sofrin Analysis	108
7	Acoustic Modal Decomposition In a Duct	113
7.1	Introduction	113
7.2	Mathematical Formulation	115

7.3	Experimental Results	121
7.3.1	Test Set-ups	121
7.3.2	Decomposition Results	123
7.4	Discussion	127
8	Conclusions	137
8.1	Future Work	138
A	Fan Specifications	145
B	Signal Processing	147
B.1	Ergodic Random Data	147
B.2	Mean Value	148
B.3	Variance	148
B.4	Mean Square Value	148
B.5	Fourier Transform	149
B.6	Power Spectrum and Power Spectral Density	150
B.7	The PSD from Digital Data Analysis	151
B.8	Matlab and the PSD	152
B.9	The dB Spectrum	152
B.10	Matlab Code to Calculate the PSD	153
B.11	The Cross Spectral Density Function	154
B.12	The Frequency Response Function	154
B.13	The Ordinary Coherence Function	155
B.14	Phase Angle and Convection Speed	156
C	Microphone Calibration	157
D	FEA Analysis of Duct	159

Nomenclature

r, θ, x	Polar co-ordinates of duct
$p(r, \theta, x, t)$	Acoustic pressure in duct
$\vec{V}(x, y, z)$	Mean flow velocity vector: $iu(x, y, z) + jv(x, y, z) + kw(x, y, z)$
u	Constant mean flow velocity in x direction
\vec{u}	Particle velocity vector
k	Wavenumber $\frac{\omega}{c}$, also integer index
k_x	Axial wavenumber
k_r	Radial wavenumber
m	Azimuthal or circumferential mode index.
n	Radial mode index.
$J_m(\cdot)$	Bessel function of the first kind of order m
$J'_m(\cdot)$	Derivative of Bessel function of the first kind of order m
$\Psi_{m,n}(r, \theta)$	Eigenfunction of $(m, n)^{th}$ mode
$A_{m,n}$	Amplitude of $(m, n)^{th}$ mode
$\beta_{m,n}$	Cut-off ratio for $(m, n)^{th}$ mode
$C_{m,n}$	Normalisation constant of $(m, n)^{th}$ mode
$a_{m,n}^+(x)$	Amplitude of incident $(m, n)^{th}$ radial mode
$a_{m,n}^-(x)$	Amplitude of reflected $(m, n)^{th}$ radial mode
$k_{r,m,n}$	Transverse eigenvalue of the $(m, n)^{th}$ mode
a	Radius of duct
Δ	Added length correction
α	Length end correction
S	Cross-sectional area
COP	Coherent output power

M	Mach Number
$\vec{\nabla}(\cdot)$	Gradient operator: $i \frac{\partial(\cdot)}{\partial x} + j \frac{\partial(\cdot)}{\partial y} + k \frac{\partial(\cdot)}{\partial z}$
OGV	Outlet Guide Vane
IGV	Inlet Guide Vane
FEA	Finite Element Analysis
$(\cdot)_i$	Incident
$(\cdot)_r$	Reflected
$(\cdot)_u$	Upstream
$(\cdot)_d$	Downstream
$(\cdot)_{ui}$	Upstream Incident
$(\cdot)_{di}$	Downstream Incident
$(\cdot)_t$	Transmitted
$(\cdot)^+$	Incident
$(\cdot)^-$	Reflected
R	Reflection Coefficient
R_0	Reflection Coefficient at $x = 0$
ρ_0	Density of air at atmospheric conditions
c	Speed of sound
Z_a	Acoustic impedance
z_c	Characteristic acoustic impedance
ω	Circular frequency
TL	Transmission Loss
W	Sound Power
A	Cross-sectional area of duct
\hat{G}_{xx}	Averaged single-sided power spectral density of signal $x(t)$
Δf	Frequency resolution bandwidth
PSD	Power Spectral Density
h	Harmonic index and horn shape factor
B	Rotor blade number
V	Stator Vane number
Ω	Rotational speed [radians/s]
RPM	Rotational Speed [Revolutions Per Minute]
RPS	Rotational Speed [Revolutions Per Second]
U	Spatially dependent volume flowrate.

Chapter 1

Introduction

1.1 Background

Growth in air traffic and the desire to locate airports closer to built up areas has resulted in aircraft pollution, by way of emissions and noise, becoming an increasing environmental problem. The European Research Commission has responded to this pollution issue, through the Advisory Council for Aeronautics Research in Europe (ACARE), by including the “Challenge to the Environment” as one of the five objectives in its Strategic Research Agenda (SRA). The environmental goals of the SRA’s 20 year agenda, “Vision 2020”, are very challenging:

- Reduce the perceived noise by half
- Reduce the emitted CO_2 by 50 %
- Reduce the emitted NO_x by 80 %

In the Fifth Framework Programme, two large-scale projects in the field of the environment: EEFAE and SILENCE(R) have been funded. Whilst the EEFAE project, “Efficient and Environmentally Friendly Aircraft Engine”, is principally concerned with emissions reduction, SILENCE(R), (Significantly Lower Community Exposure to Aircraft Noise) is concerned mostly with environmental noise. It is within the SILENCE(R) project that aspects of this research are based.

SILENCE(R) is the largest aircraft noise research project ever supported by the European Commission and was launched in April 2001. Under the direction of Snecma Moteurs, 51 companies from 16 countries are involved in the 6-year research project with a budget of 112M€. The main objective of SILENCE(R) is to perform large-scale validation of over 20 noise technologies that were initiated through European and national projects in 1998. These aircraft, engine, nacelle and landing gear technologies, combined with new noise abatement procedures, will allow new aircraft to be developed with a noise reduction of 6 dB per aircraft operation.

The aero-engines of civil aircraft are the dominant noise sources for most flight conditions although airframe noise is a significant contributor at landing. The two largest sources of aero-engine noise, the fan and the jet, have been significantly reduced as a consequence of years of research. With their reduction, a threshold is being reached, which will form the new noise floor and limit the benefits to be gained by reducing these dominant components, unless the noise sources which set this threshold are in turn reduced. Of these, combustion, or core noise, is currently a focus of research activity. At relatively low jet velocities, such as would occur at engine idle, during taxiing, and at approach and cruise conditions, core noise is considered a significant contributor to the overall sound level. The trend of core noise attaining increasing attention will continue with the incorporation of low NO_x combustors and increasingly higher by-pass ratios into modern engine designs. A better understanding of combustion noise generation, propagation and radiation will aid in the design of noise suppression devices to alleviate community noise problems.

1.2 Objectives of Thesis

Understanding combustion noise source mechanisms, designing efficient acoustic liners and optimising active control algorithms for noise reduction requires the identification of the frequency and modal content of the combustion noise contribution. An acoustic measurement of a system of interest will most often be the summation of a number of separate acoustic sources along with some extraneous noise. Figure 1.1 illustrates the principle noise sources in an aero-engine. For the case where it is not possible to remove individual sources without effecting the behaviour of the others, the challenge is to decompose the measurement signal into its constituent parts. For acoustic sources that are considered to be stationary random processes with zero mean and where systems are constant-parameter linear systems, figure 1.2, a multiple-input/single-output model, can be used to represent the system. The extraneous noise term, $n(t)$, accommodates all deviations from the model, such as acoustic sources greater than M which are unaccounted for, non-stationary effects, acquisition, instrument and mathematical noise along with unsteady pressure fluctuations local to the sensor, such as flow or hydrodynamic noise. As the acoustic noise sources in an aero-engine overlap in the frequency domain, with varying amplitudes, as shown in figure 1.3, it can be difficult to quantify the individual contributions. One of the principal objectives of this thesis is to develop algorithms to accurately identify the combustion noise contribution to a far-field acoustic measurement.

Coherence-based identification techniques can be used to identify the contribution of combustion noise to near and far field acoustic measurements of aero-engines. These techniques condition from external measurements additional core noise sources, as well as other noise sources generated exterior to the engine. The underlying assumption with these identification techniques is that the propagation\convection path, from combustion can to measurement point, is a linear one. Results from the European contract *Resound*, showed a drop in coherence between combustion noise measure-

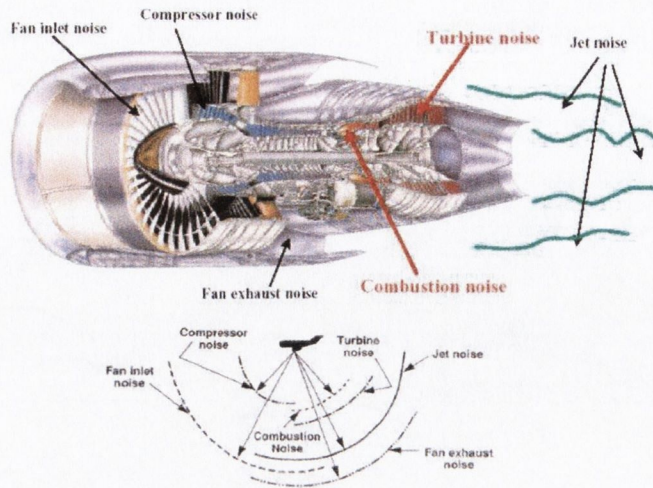


FIGURE 1.1: Principal aero-engine acoustic noise sources. Length of vector representative of average power level of individual source with its angle indicating the directivity of maximum lobe.

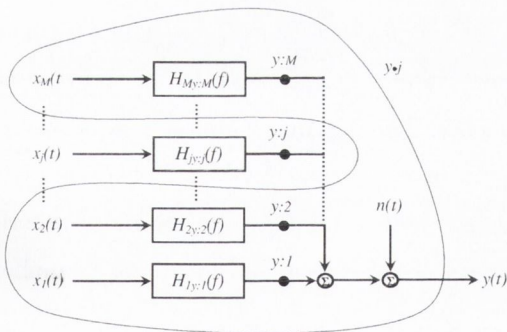


FIGURE 1.2: Multiple Source Acoustic Measurement

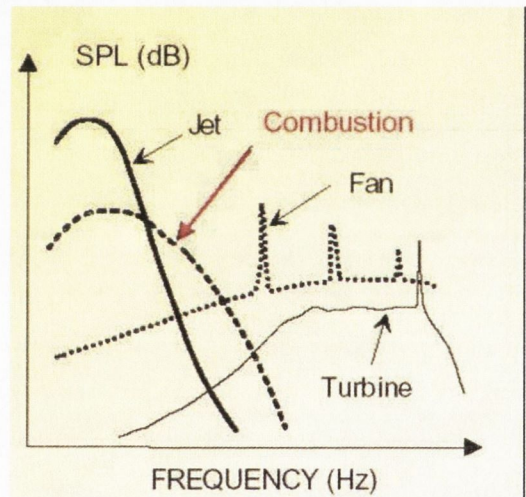


FIGURE 1.3: Qualitative spectra indicating frequency content of individual aero-engine noise sources.

ments made at the combustor can with pressure transducers, and microphone array measurements focused on the exit plane of an aero-engine, when the rpm of the engine was increased, Siller *et al* [58]. For the situation where the combustion noise has propagated through the system in a non-linear fashion, as illustrated schematically in figure 1.4, the identified contribution will be inaccurate. A second principal objective of this thesis examines the scenario where a fluctuating pressure is modified, in a *non-linear* sense, as it is convected through a rotating vane-axial fan, and how this affects the identification techniques.

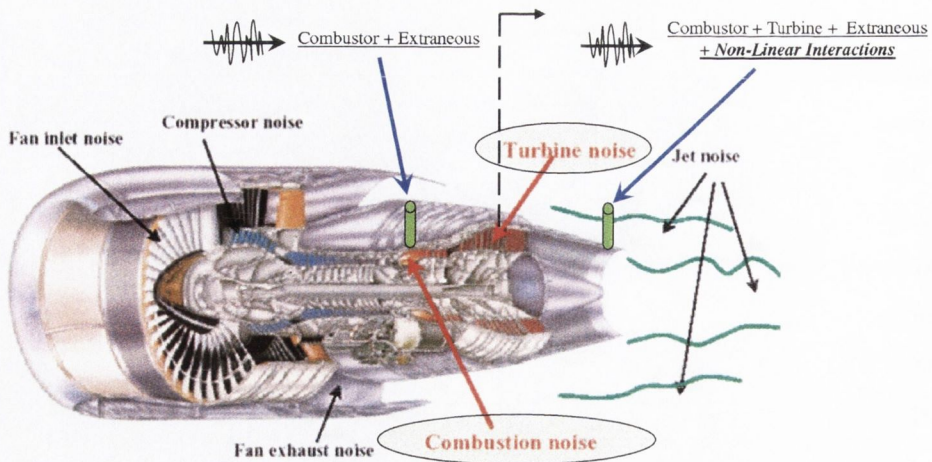


FIGURE 1.4: Schematic of aero-engine depicting modification of combustor noise due to convection through turbine.

1.3 Thesis Outline

Chapter 2 summarises the theory of acoustic mode propagation in a duct and some core noise source generation mechanisms. **Chapter 3** details the design of an experimental rig built to facilitate the realisation of the thesis objectives. The preliminary experiments of **chapter 4** serve to validate the test equipment and processing techniques as well as to characterise this principal test rig under different test conditions. **Chapter 5** modifies and evaluates existing acoustic source identification techniques with experimental data from a separate test rig designed for the purpose. These techniques are then applied to experimental data from the principal rig in order to separate fan and flow noise from a fluctuating pressure signal convected through the fan. The non-linear interaction, between the fluctuating pressure signal and the fan, is examined in **chapter 6**. The modal content of the nBPF's and the interaction tones are determined with an acoustic modal decomposition technique described in **chapter 7**. The final chapter summarises the findings of this thesis and identifies a number of possible future directions for this research.

Chapter 2

Pressure Field In A Cylindrical Duct

The usual approach in the analysis of duct acoustics is to approximate the duct by an infinite cylinder and to solve the differential equations by separation of variables. This leads to an eigenvalue problem, the solution of which give the duct propagation modes. Each mode represents a different way in which sound may travel down the duct. A complete description of the sound field in the duct consists of knowing the complex amplitude of each mode.

2.1 Duct Acoustic Modes

For acoustic propagation in an infinite hard walled cylindrical duct with superimposed constant mean flow velocity \vec{V} , the pressure, $p = p(r, \theta, x, t)$, in cylindrical coordinates as defined by figure 2.1, is found as a solution of the homogeneous convective wave equation,

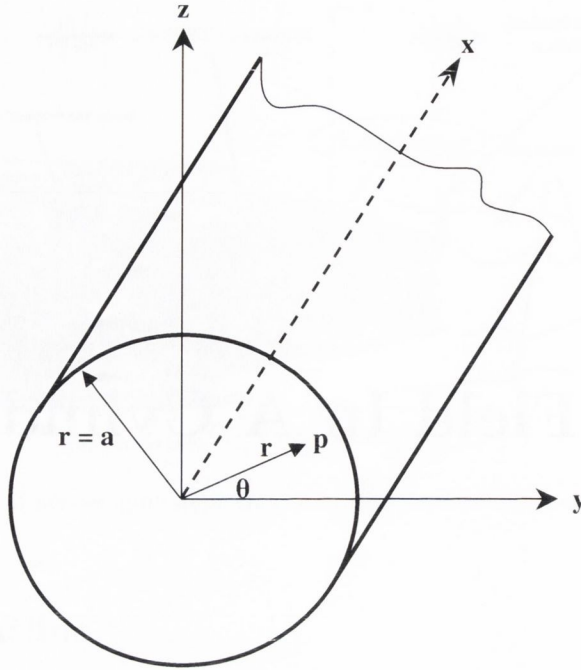
$$\frac{1}{c^2} \frac{D^2 p}{Dt^2} - \frac{\partial^2 p}{\partial x^2} - \frac{1}{r} \frac{\partial}{\partial r} \left(r \frac{\partial p}{\partial r} \right) - \frac{1}{r^2} \frac{\partial^2 p}{\partial \theta^2} = 0 \quad (2.1)$$

where the substantive derivative is defined to be

$$\frac{D}{Dt} = \frac{\partial}{\partial t} + \vec{V} \frac{\partial}{\partial x}$$

This solution is found as a combination of the characteristic functions of equation (2.1) each of which satisfy specific boundary conditions. The solution to (2.1) with mean flow can be shown to be equal to that of the no-flow condition with a modification made to the axial wavenumber. To simplify the derivation, the no-flow case will be presented here with the mean flow form of the axial wavenumber introduced in equations (2.21) and (2.22).

The boundary conditions considered are

FIGURE 2.1: Polar coordinate system for a cylindrical duct, (r, θ, x)

- the radial component of the pressure gradient vanishes at the boundary walls: $\frac{\partial p}{\partial r} = 0$ at $r = a$;
- at both ends of an arc $2\pi r$ long, located anywhere in the azimuthal direction, the pressure and pressure gradient must be the same;
- at a reference plane, $x = 0$, normal to the cylinder axis, the pressure is specified as an arbitrary function of r , satisfying the first two conditions and a periodic function of time;

The characteristic functions are obtained as solutions to the ordinary differential equations into which the wave equation separates on substitution of the form $p = R(r)\Theta(\theta)X(x)T(t)$. Assuming the time dependent term to be harmonic, the spatially dependent equations can be shown to be equal to,

$$\frac{d^2 X}{dx^2} = -k_x^2 X \quad (2.2)$$

$$\frac{d^2 \Theta}{d\theta^2} = -m^2 \Theta \quad (2.3)$$

$$r^2 \frac{d^2 R}{dr^2} + r \frac{dR}{dr} + ((k^2 - k_x^2)r^2 - m^2) R = 0 \quad (2.4)$$

where equation (2.4) is a Bessel equation for $R(r)$. The characteristic functions, in complex form, applying the boundary conditions are

$$X = e^{(-jk_x x)} \tag{2.5}$$

$$\Theta = e^{(jm\theta)} \tag{2.6}$$

$$R = J_m(k_r r) \tag{2.7}$$

$$T = e^{(j\omega t)} \tag{2.8}$$

with

$$k^2 = k_r^2 + k_x^2 \tag{2.9}$$

As the radial velocity at the wall ($r = a$) must be equal to zero, k_r takes only such values as to satisfy the equation

$$J'_m(k_r a) = 0 \tag{2.10}$$

where $J_m(\cdot)$ is a Bessel function of the first kind of order m , $J'_m(\cdot)$ is its derivative, and is related to the Bessel function by

$$J'_m(\cdot) = -J_m(\cdot) \qquad m = 0 \tag{2.11}$$

$$J'_m(\cdot) = \frac{J_{m-1}(\cdot) - J_{m+1}(\cdot)}{2} \qquad m = 1, 2, \dots \tag{2.12}$$

Figure 2.2 shows plots of the Bessel function and of its derivative for a number of m orders. According to equation (2.10), k_r can be calculated from the roots (or zero crossings) of this derivative. For a given Bessel function derivative of order m , an infinite number of roots exist and from this it will be shown that for each circumferential mode of order m there are an infinite number of associated radial modes.

Denoting the value of k_r corresponding to the n^{th} root of this equation as $k_{(r,m,n)}$, the general solution to equation (2.1), with or without mean flow, can be expressed as a linear combination of eigenfunctions,

$$p(r, \theta, x, t) = \mathbf{Re} \left[\sum_{m=0}^{+\infty} \sum_{n=1}^{+\infty} A_{m,n}(x) \Psi_{m,n}(r, \theta) e^{-j\omega t} \right] \tag{2.13}$$

where the eigenfunctions, $\Psi_{m,n}(r, \theta)$, of amplitude $A_{m,n}(x)$ will depend uniquely on the cross-sectional shape of the duct. For the case of a hard walled cylindrical duct, the eigenfunction is

$$\Psi_{m,n}(r, \theta) = J_m(k_{r,m,n} r) e^{jm\theta} \tag{2.14}$$

An examination of equation (2.13) can be used to discuss the physics of the sound field in the duct. The eigenfunction is a mode shape which may be generated at a frequency ω in the (r, θ) plane

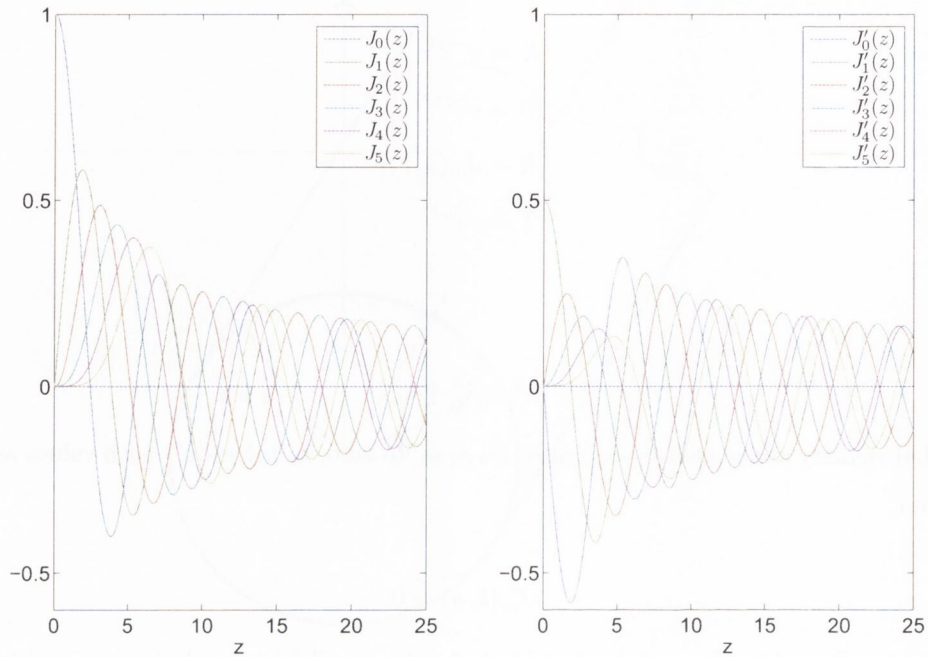


FIGURE 2.2: The first five orders of the Bessel function of the first kind and its derivative.

perpendicular to the x -axis, and which may propagate as a travelling wave upstream or downstream in the duct in accordance with the x dependent amplitude. The eigenvalues of this equation provide frequencies above which generated modes propagate unattenuated but below which excited modes exponentially decay. Several modes may coexist in the duct at a frequency of excitation, so long as this frequency is above their individual cut-off frequencies. The pressure in the duct is assumed to fluctuate harmonically as can be seen from the exponential time term, $e^{(-j\omega t)}$. $k_{r,m,n}$ is the transverse eigenvalue of the $(m,n)^{th}$ mode and is also called the transverse, combined radial-circumferential or simply the radial wavenumber.

In order to remain consistent with the notation for rectangular ducts, where m and n represent the number of nodes in the transverse plane, the n index for a circular duct is used not in fact to indicate the n^{th} root of equation (2.10) but rather the number of azimuthal (or circumferential) pressure nodes in the transverse plane. This results in the plane wave mode being denoted as $(m,n) = (0,0)$ as discussed in Munjal [48] and Eriksson [19]. Table 2.1 presents some of the zero crossings for the first six circumferential mode orders. The eigenvalue or radial wavenumber, $k_{r,m,n}$, for a circular cross-section is dependent on the radius of the duct, where these values have been calculated using the `fzero` function in Matlab's Optimization toolbox.

Given the values in table 2.1, the function $J_m(k_{r,m,n}r)$ is plotted to illustrate some radial mode shapes. A value of $a=0.025\text{m}$ is used, as this is the radius of the rig to be used in the experiments as discussed in chapter 3. Figure 2.3 shows the first 4 radial mode shapes for the first four m orders of

m, n	0	1	2	3	4	5
0	0	3.83	7.02	10.17	13.32	16.47
1	1.84	5.33	8.54	11.71	14.86	18.02
2	3.05	6.71	9.97	13.17	16.35	19.51
3	4.20	8.02	11.35	14.59	17.79	20.97
4	5.32	9.28	12.68	15.96	19.20	22.40
5	6.42	10.52	13.99	17.31	20.58	23.80

TABLE 2.1: $k_{(r,m,n)}a$

the Bessel function.

Full two-dimensional mode shapes, including the azimuthal variation, are plotted for some examples in figures 2.4, 2.5, 2.6 and 2.7. According to equation (2.14), it can be seen that the normal modes are sinusoids in the circumferential direction and Bessel functions in the radial direction where m specifies the circumferential mode number and n indicates the associated radial mode number. The $(0, 0)$ mode indicates the plane wave mode, $(1, 0)$ the first circumferential (or azimuthal) mode and $(0, 1)$ the first radial mode. Physically, the circumferential mode number indicates the periodicity of the circumferential acoustic mode pattern. For example, a mode of $m = 4$ is periodic over $\frac{1}{4}$ of the duct. Alternatively, it may be observed that a mode of $m = 4$ has four nodal lines passing through the centre of the circular section. Although the radial modes are not periodic along the radius of the duct, the radial mode number indicates the number of circumferential node lines to be found in the acoustic pattern.

Equation (2.13) may now be re-written upon substitution of equation (2.14) as

$$p(r, \theta, x, t) = \mathbf{Re} \left[\sum_{m=0}^{+\infty} \sum_{n=0}^{+\infty} A_{m,n}(x) J_m(k_{r,m,n}r) e^{jm\theta} e^{-j\omega t} \right] \quad (2.15)$$

or as

$$\hat{p}(r, \theta, x, \omega) = \sum_{m=0}^{+\infty} \sum_{n=0}^{+\infty} \hat{A}_{m,n}(x, \omega) J_m(k_{r,m,n}r) e^{jm\theta} \quad (2.16)$$

in the frequency domain, where $\hat{p}(r, \theta, x, \omega)$, the complex pressure is a solution of the Helmholtz equation, and where $\hat{A}_{m,n}(x, \omega)$ is a complex modal magnitude. It should be noted here that the sum over n is from zero to infinity.

2.2 Propagation

Another common way of expressing equation (2.16), as used by Enghardt *et al* [18] and Tapken *et al* [62]), and one where the functional form of $\hat{A}_{m,n}(x, \omega)$ is expressed explicitly, is where the complex circumferential mode distribution is isolated, being a function of θ only, by writing

$$\hat{p}(r, \theta, x, \omega) = \sum_{m=0}^{+\infty} \hat{A}_m(x, r, \omega) e^{jm\theta} \tag{2.17}$$

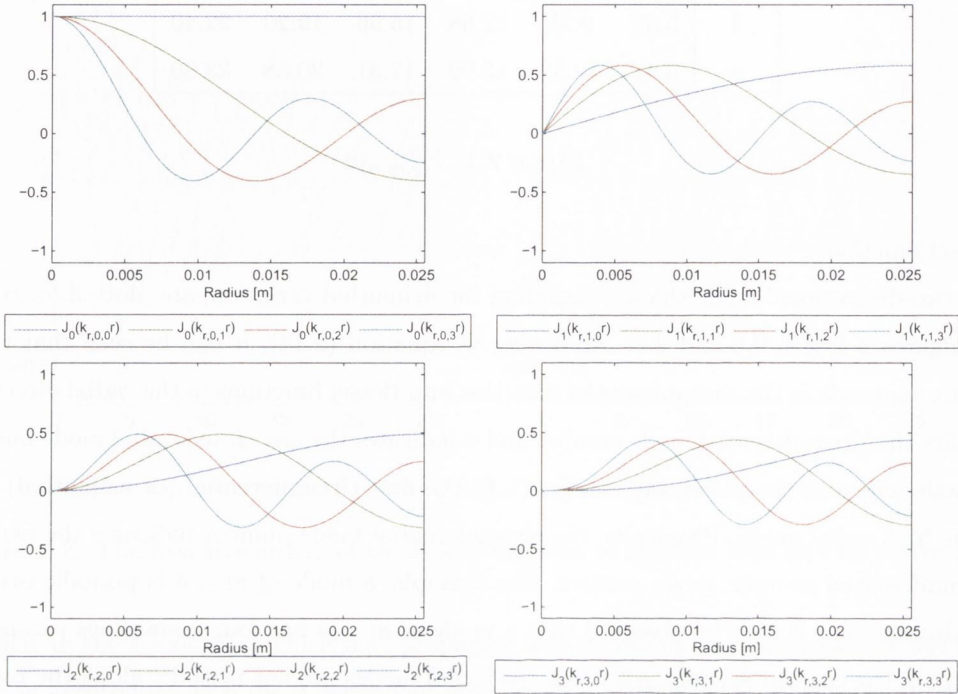


FIGURE 2.3: The first four radial mode shapes for Bessel functions of order 0 → 3. $J_m(k_{r,m,n}r)$ is plotted for $a = 0.025m$. The centerline of the duct is at $r = 0$.

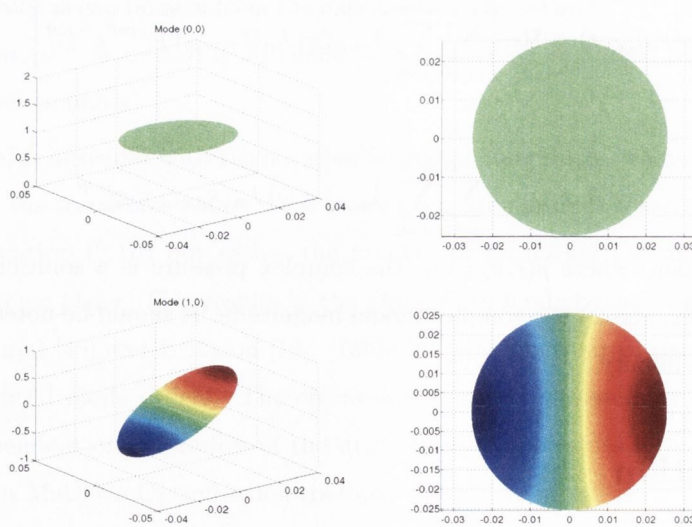


FIGURE 2.4: Acoustic Mode Shapes; (0, 0) and (1, 0)

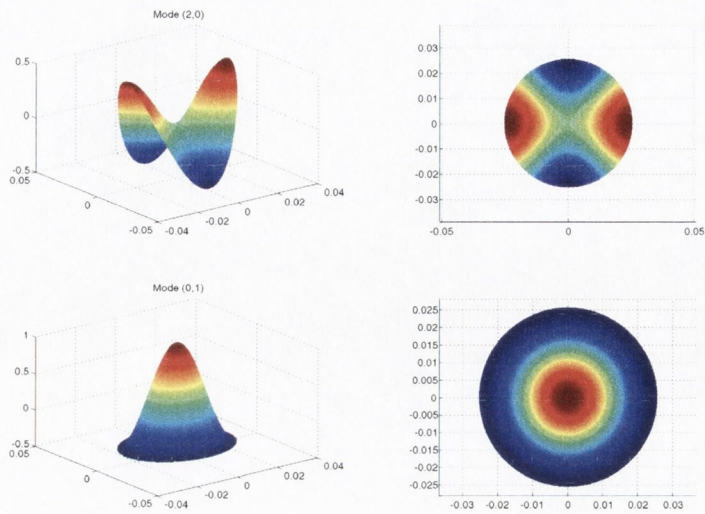


FIGURE 2.5: Acoustic Mode Shapes; (2, 0) and (0, 1)

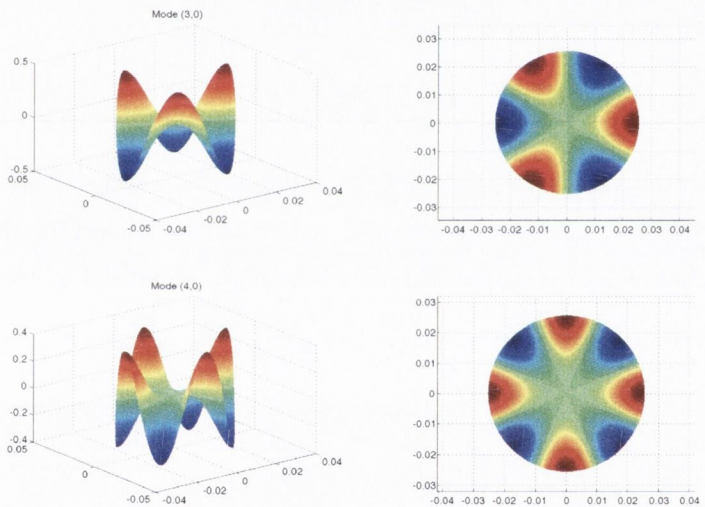


FIGURE 2.6: Acoustic Mode Shapes; (3, 0) and (4, 0)

where the amplitude of the circumferential mode of order m separates out into a series of radial modes as

$$\hat{A}_m(x, r, \omega) = \sum_{n=0}^{+\infty} \left[\hat{a}_{m,n}^+(\omega) e^{-jk_{x,m,n}^+ x} + \hat{a}_{m,n}^-(\omega) e^{+jk_{x,m,n}^- x} \right] J_m(k_{r,m,n} r) \quad (2.18)$$

Equation (2.16) can thus also be written as

$$\hat{p}(r, \theta, x, \omega) = \sum_{m=0}^{+\infty} \sum_{n=0}^{+\infty} \left[\hat{a}_{m,n}^+(\omega) e^{-jk_{x,m,n}^+ x} + \hat{a}_{m,n}^-(\omega) e^{+jk_{x,m,n}^- x} \right] J_m(k_{r,m,n} r) e^{jm\theta} \quad (2.19)$$

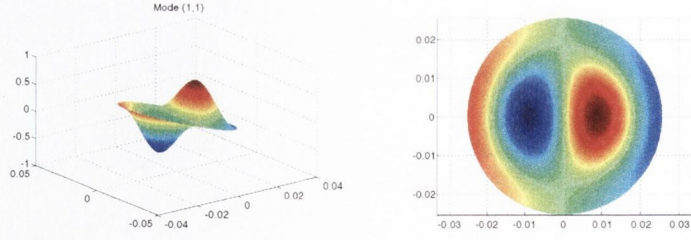


FIGURE 2.7: Acoustic Mode Shapes; (1, 1)

where

$$\hat{A}_{m,n}(x, \omega) = \left[\hat{a}_{m,n}^+(\omega) e^{-jk_{x,m,n}^+ x} + \hat{a}_{m,n}^-(\omega) e^{+jk_{x,m,n}^- x} \right] \quad (2.20)$$

Equation (2.18) includes incident and reflected travelling acoustic waves with $\hat{a}_{m,n}^+(\omega)$ being the magnitude of the forward propagating mode and $\hat{a}_{m,n}^-(\omega)$ the magnitude of the rearward propagating mode. The axial propagation characteristic of the (m, n) mode is defined by the axial wavenumber, $k_{x,m,n}$ computed from

$$k_{x,m,n}^+ = \frac{k}{\beta^2} \left[\sqrt{1 - \left(\frac{\beta k_{r,m,n}}{k} \right)^2} - M \right] \quad (2.21)$$

$$k_{x,m,n}^- = \frac{k}{\beta^2} \left[\sqrt{1 - \left(\frac{\beta k_{r,m,n}}{k} \right)^2} + M \right] \quad (2.22)$$

where $\beta = \sqrt{1 - M^2}$ and M is the Mach number of the mean flow inside the duct.

Focusing on one of the exponential terms containing the axial wavenumber for the incident wave, e.g. $e^{-jk_{x,m,n}^+ x}$, it can be deduced that, if the wavenumber is real, then the term will be oscillatory and will propagate. If the term is imaginary, then the wave will exponentially decay. By defining a cut-off ratio for a particular (m, n) mode as

$$\beta_{m,n} = \frac{k}{\beta k_{r,m,n}} \quad (2.23)$$

it is evident that $\beta_{m,n} < 1$ results in a decaying mode whereas $\beta_{m,n} > 1$ will result in a propagating mode. The transitional point between these two conditions, where $\beta_{m,n} = 1$, is used to define the

cut-off frequency for a particular (m, n) mode. $\frac{k}{\beta k_{r,m,n}} = 1$ can be re-written as

$$\omega_{m,n}^{cut-off} = c k_{r,m,n} \sqrt{1 - M^2} \quad (2.24)$$

In summary, if a mode is excited at a frequency which is any frequency above its cut-off frequency then the mode is said to be cut-on, and will thus propagate down a duct. For frequencies below, the mode is cut off and will exponentially decay, the rate of decay increasing as the cut-off ratio decreases.

For zero mean flow, the axial wavenumber is more simply related to the free stream wavenumber, $k = \frac{\omega}{c}$, and the transverse wavenumber by

$$k_{x,m,n} = \sqrt{k^2 - k_{r,m,n}^2} \quad (2.25)$$

Equation (2.24) demonstrates how the cut-off frequency is lowered with increasing flow speed as Morfey [46] observed experimentally.

Although the transverse wavenumber is fixed for a particular mode due to the boundary conditions, as the frequency ω may vary, so then may the axial wavenumber. The axial propagation velocity (or phase velocity) for a particular mode is given by

$$c_{x,m,n} = \frac{\omega}{k_{x,m,n}} \quad (2.26)$$

and its wavelength is simply

$$\lambda_{x,m,n} = \left| \frac{2\pi}{k_{x,m,n}} \right| \quad (2.27)$$

However, just above cut-on, the wavelength is appreciably greater than would be the case in free-field and the phase velocity in the x -direction is correspondingly high, as required to satisfy the relation $f = \frac{c}{\lambda} = \frac{c_{x,m,n}}{\lambda_{x,m,n}} = const$. As the frequency increases above cut-off, $\lambda_{x,m,n}$ and $c_{x,m,n}$ rapidly approach their free-space values. This behaviour may be seen in figure (2.8), where the expressions may be derived from (2.25) as

$$\lambda_{x,m,n} = \left(\frac{1}{c} \sqrt{f^2 - f_{r,m,n}^2} \right)^{-1} = \left(\frac{1}{\lambda^2} - \frac{1}{\lambda_{r,m,n}^2} \right)^{-\frac{1}{2}} \quad (2.28)$$

$$c_{x,m,n} = f \lambda_{x,m,n} \quad (2.29)$$

with, for this example, $k_{r,m,n} = \frac{2\pi(4000)}{c}$, where 4000Hz is approximately the plane wave cut-off frequency for the duct diameter to be used in the experiments described in this thesis in chapter 3.

2.3 Radiation

If a mode has been generated/excited at a frequency above its cut-on frequency, it will propagate along a duct. For a duct of practical interest, i.e. not infinitely long, the waves will travel to the end

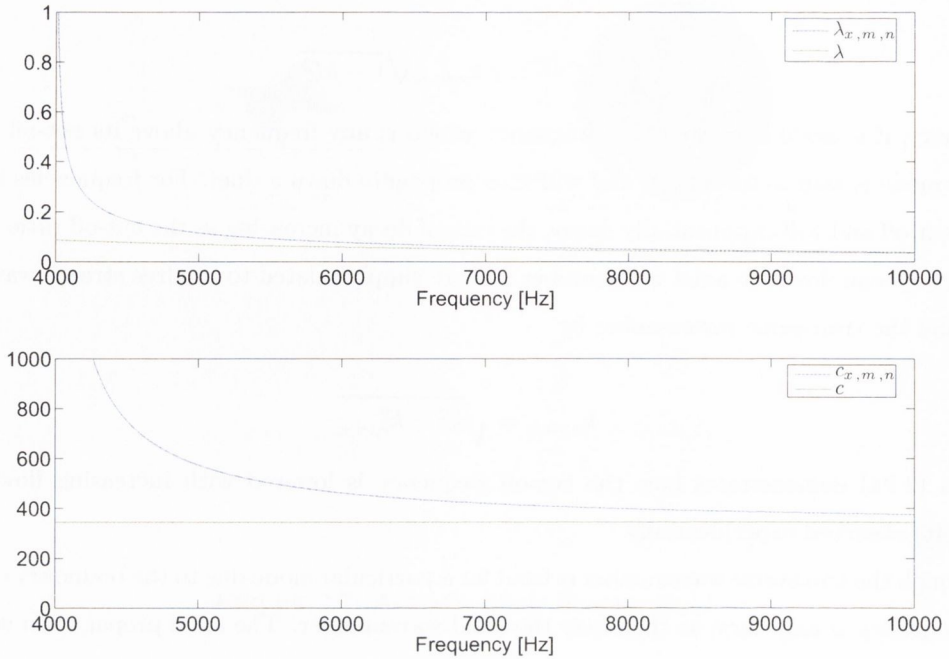


FIGURE 2.8: Variation of axial wavelength and phase velocity with frequency compared with that in free-field. $f_{cut-on} = 4kHz$ for this example.

of the duct. If the duct is open, the duct face will be subject to a fluctuating pressure field which may radiate to the far field. Some of the earliest work carried out on sound radiation from cylindrical ducts was by Levine and Schwinger [43] using the Wiener-Hopf technique. The subject of later work by Homicz and Lordi [28], Lansing [42], and Rice [51] *et al* was the determination of the directions of peak radiation for duct acoustic modes. For a particular mode (m, n) , the angle for the peak radiated lobe can be expressed as

$$\cos(\theta_{peak}^{m,n}) = \sqrt{1 - M^2} \sqrt{\frac{1 - \frac{1}{\beta_{m,n}^2}}{1 - M^2(1 - \frac{1}{\beta_{m,n}^2})}} \quad (2.30)$$

where equation (2.23) defines the cut-off ratio $\beta_{m,n}$.

From equation (2.30), two main observations may be made. The first is that, as the Mach number increases, the angle that the main lobe makes with the duct axis decreases. The second is that for a particular flow velocity, the modes that are well above their cut-off frequency radiate towards the axis of the duct, whereas, as the frequency decreases towards the cut-off frequency, the modes radiate at wider far field angles. Each mode will produce a radiation pattern, the sound pressure level directivity being a summation of the individual patterns.

2.4 Plane Wave Duct Acoustics

A duct scenario of great practical importance is one where the frequencies considered lie below the first higher order mode cut-off frequency which, using equation (2.24), is given by

$$f_{cut-off} = \frac{1.84c}{2\pi a} \quad (2.31)$$

where a is the radius of the duct, $M = 0$ and the value 1.84 comes from table 2.1.

For the plane wave mode, or $(m, n) = (0, 0)$, equation (2.19) reduces to

$$\hat{p} = \hat{p}_i e^{-jk_i x} + \hat{p}_r e^{jk_r x} \quad (2.32)$$

as both $J_m(k_{r,m,n}r)$ and $e^{jm\theta}$ reduce to unity and the summations over m and n disappear. The complex amplitudes of the forward and backward travelling plane waves are defined here to be \hat{p}_i and \hat{p}_r . Equation (2.32) is a plane wave solution to the Helmholtz equation. Equation (2.32) could have been derived directly from analysis of the one dimensional wave equation

$$\frac{\partial^2 p}{\partial t^2} - c^2 \frac{\partial^2 p}{\partial x^2} = 0 \quad (2.33)$$

where it can be shown that any function of the form

$$p(x, t) = g(ct \pm x) \quad (2.34)$$

is a solution. These can be shown to be waves travelling steadily along with speed c parallel to the x axis, maintaining a constant profile, and, since there is no dependence on y or z , the wavefronts are all planes parallel to the yz plane. These wave fronts are known as plane waves. For the x -axis taken to be positive to the right, the plus sign in equation (2.34) must correspond to waves travelling towards the left and the negative sign to waves travelling towards the right. Figure 2.9 (a), taken from Hall [24], shows a rightward travelling sinusoidal wave.

Since equation (2.33) is a linear differential equation, any sum of two solutions is also a solution. Thus in general the duct could support waves $g(ct + x)$ and $g(ct - x)$ at the same time. An important physical reason for such a situation could be the presence of waves reflected from the end of a duct. For a duct of finite length L , describing the pressure distribution for the whole duct in terms of travelling waves remains possible but becomes unwieldy because of repeated reflections between the two ends. It is therefore more convenient to study *standing waves*. The example of two sinusoidal waves with equal amplitudes moving in opposite directions

$$p(x, t) = A \sin k(ct + x) - A \sin k(ct - x)$$

can be used to illustrate the case. This expression has two important properties illustrated in figure 2.9 (b), neither of which would be true for one travelling wave term alone. In the first instance, there

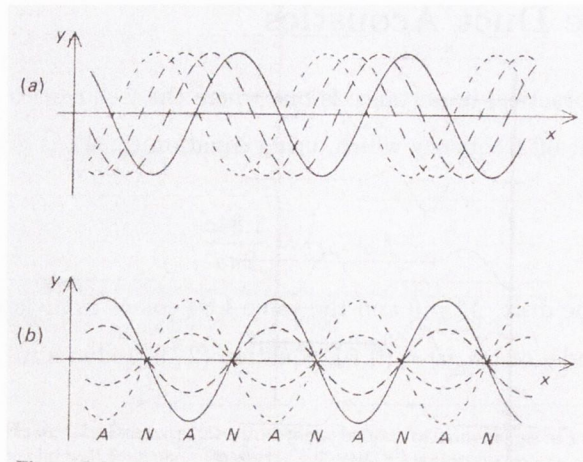


FIGURE 2.9: Sinusoidal travelling wave (a) contrasted with standing wave (b).

are some values of x where p remains zero at all times; such points are called *nodes* of the standing wave. Secondly, there are some values of t for which p is zero simultaneously at all locations.

Consider now the duct in figure 2.10 where acoustic waves emanating from the speaker travel to the right in the direction of the positive x -axis. These waves are known as *incident waves* and in complex notation are given by $\hat{p}_i e^{j\omega t - jk_i x}$. The left running waves reflected from an obstruction are denoted by $\hat{p}_r e^{j\omega t + jk_r x}$. The different wave numbers result from the Doppler shift caused by the mean flow velocity u , if there is one. With $u > 0$ in the positive x direction,

$$\begin{aligned} k_i &= \frac{\omega}{c + u} = \frac{k}{1 + M} \\ k_r &= \frac{\omega}{c - u} = \frac{k}{1 - M} \end{aligned} \quad (2.35)$$

which are equivalent to equations (2.21) and (2.22) for plane waves.

\vec{u} , the particle velocity, comes from the momentum equation (Euler equation);

$$\rho_0 \frac{\partial \vec{u}}{\partial t} = -\vec{\nabla} p \quad (2.36)$$

and is given by

$$\vec{u} = -\frac{1}{j\omega\rho_0} \frac{\partial \hat{p}}{\partial x} = \frac{1}{\rho_0 c} (\hat{p}_i e^{-jk_i x} - \hat{p}_r e^{jk_r x}) \quad (2.37)$$

2.4.1 Plane Wave Decomposition

As demonstrated above, the pressure in a duct may consist of an incident plus a reflected wave (depending on the end condition). Whilst it is the summation of these two that a single microphone located in the duct would measure, with information from a second microphone, located at a different axial location, the pressure field may be decomposed into the incident and reflected components. As

the waves are planar, the microphones can be located anywhere on a plane of location x . Therefore, it is preferable to mount the microphones flush with the inside surface of such a duct to reduce scattering from the microphones themselves. With regard to figure 2.10, the complex pressures measured by microphones 1 and 2 are

$$\hat{p}_1 = \hat{p}_i e^{-jk_i x_1} + \hat{p}_r e^{jk_r x_1} \quad \text{and} \quad \hat{p}_2 = \hat{p}_i e^{-jk_i x_2} + \hat{p}_r e^{jk_r x_2} \tag{2.38}$$

Algebraic manipulation of these equations gives the complex amplitudes of the incident and reflected travelling waves

$$\hat{p}_i = \frac{\hat{p}_1 e^{-jk_r x_1} - \hat{p}_2 e^{-jk_r x_2}}{e^{-j(k_i+k_r)x_1} - e^{-j(k_i+k_r)x_2}} \tag{2.39}$$

and

$$\hat{p}_r = \frac{\hat{p}_1 e^{jk_i x_1} - \hat{p}_2 e^{jk_i x_2}}{e^{j(k_i+k_r)x_1} - e^{j(k_i+k_r)x_2}} \tag{2.40}$$

It is important to note that the position of the reference plane will determine the signs of x_1 and x_2 .

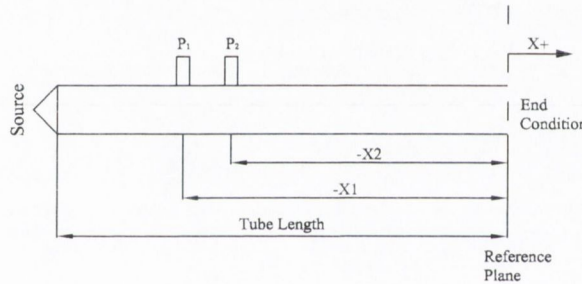


FIGURE 2.10: Schematic of Test Rig

2.4.2 Reflection Coefficient

Acoustic behaviour at a termination is often described in terms of the reflection coefficient R , defined as the ratio of the reflected wave pressure to that of the incident wave

$$R = |R|e^{j\theta}$$

where $|R|$ and θ are, respectively, the magnitude and phase of the reflection coefficient. Now, with reference to equation (2.32), if we divide the second term on the *rhs* by $\hat{p}_i e^{-jk_i x}$ we get

$$R = \frac{\hat{p}_r}{\hat{p}_i} e^{j(k_i+k_r)x} \tag{2.41}$$

According to equation (2.41), we see that for this case of plane wave propagation and neglecting losses at the duct wall, the magnitude of the reflection coefficient is equal at all planes along the duct. A phase of $(k_i + k_r)x$ is the result of the reference plane being chosen at a point x from $x = 0$.

For $x = 0$, the reflection coefficient R is therefore simply

$$R_0 = \frac{\hat{p}_r}{\hat{p}_i} \quad (2.42)$$

Clearly the reflection coefficient may be calculated directly from equation 2.41 using equations 2.39 and 2.40 with some averaging to improve the signal to noise ratio. However, there exist numerous publications describing a variety of techniques for the robust calculation of the reflection coefficient. One of the more comprehensive papers on two microphone random excitation methods is that of Chung and Blaser [12], which has been standardised in the Standard, BS EN ISO 10534-2:2001 [2]. However the following formulation, which can be shown to be equivalent to that of Chung and Blaser [12], is quite an elegant one, which employs the frequency response function between the two microphones, an average of which can usually be determined reliably. Using equation (2.32), a frequency response function between the two microphones at $+x_1$ and $+x_2$ can be defined as,

$$H_{12}(\omega) = \frac{\hat{p}_2(\omega)}{\hat{p}_1(\omega)} = \frac{\hat{p}_i e^{-jk_i x_2} + \hat{p}_r e^{jk_r x_2}}{\hat{p}_i e^{-jk_i x_1} + \hat{p}_r e^{jk_r x_1}} \quad (2.43)$$

By dividing above and below by \hat{p}_i and dropping the ω notation, the frequency response function may be expressed in terms of the reflection coefficient,

$$H_{12} = \frac{e^{-jk_i x_2} + R_0 e^{jk_r x_2}}{e^{-jk_i x_1} + R_0 e^{jk_r x_1}} \quad (2.44)$$

which can be re-arranged to present the reflection coefficient in terms of the frequency response function, *i.e.*

$$R_0 = \frac{e^{-jk_i x_2} - H_{12} e^{-jk_i x_1}}{H_{12} e^{jk_r x_1} - e^{jk_r x_2}} \quad (2.45)$$

Drop Out Frequency

Seybert and Ross [55] and Chung and Blaser [13] have both examined how the reflection coefficient cannot be determined at discrete frequency points for which the microphone spacing is an integer multiple of the half wavelength of sound, *i.e.* located at nodes, or whenever

$$\begin{aligned} s &= n\left(\frac{\lambda}{2}\right), \quad n = 1, 2, 3, \dots \\ \text{or} & \\ s &= n\left(\frac{c}{2f}\right), \quad n = 1, 2, 3, \dots \end{aligned} \quad (2.46)$$

As these frequency points can be predicted, the discontinuities can be ignored. Alternatively, to avoid these points up to a frequency f_{crit} , the microphone spacing, s , can be chosen such that

$$s \leq \frac{c}{2f_{crit}} \quad \text{or} \quad f_{crit} \leq \frac{c}{2s} \quad (2.47)$$

where f_{crit} could be chosen to equal f_{cutoff} , equation (2.31), for example.

Another approach is to supplement the lost information with that gained from a second test using different microphone spacings. These two tests might be amalgamated into one by performing a least squares solution using more than two microphones, such as used, for example, by Seung-Ho Jang and Jeong-Guon Ih [31], Chu [10] and Fujimori and Miura [22]. A schematic of the approach is shown in figure 2.11.

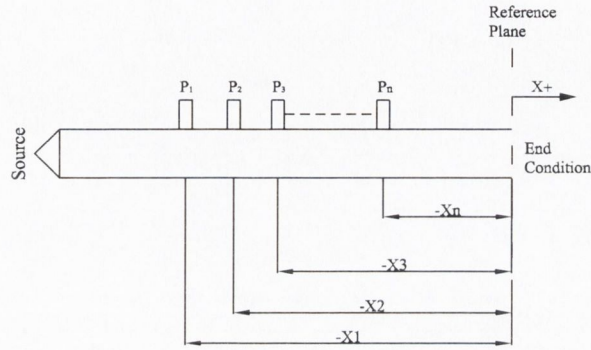


FIGURE 2.11: Schematic for least squares technique

2.4.3 Acoustic Impedance

The acoustic impedance $Z_a(f)$ is given by

$$Z_a = \frac{p}{u} \tag{2.48}$$

the dependency on frequency understood. As impedance has units of pressure per unit velocity, impedance can be interpreted as how much pressure is required to cause a medium to move at 1 meter per second. Using equations (2.32), (2.37) and (2.48) with $x = 0$ the impedance can be expressed as a function of the reflection coefficient by

$$Z_a = \rho_0 c \frac{1 + R}{1 - R} \tag{2.49}$$

In the case of an infinitely long duct of uniform cross section, waves would travel away from the input and never return from the other end. From equations (2.41) and (2.49) while letting $p_r = 0$, this would result in an impedance of

$$z_c = \rho_0 c \tag{2.50}$$

for a travelling wave which can be seen to be real and to not depend on frequency. The term, z_c , is known as the characteristic impedance, which is a property of the medium alone. In addition, by dividing equation (2.49) by the characteristic impedance, z_c , a normalised impedance can be expressed

$$Z_n = \frac{1 + R}{1 - R} \quad (2.51)$$

with

$$Z_n = \frac{Z_a}{\rho_0 c}$$

The reflection coefficient is related to this normalised impedance by

$$R = \frac{Z_n - 1}{Z_n + 1} \quad (2.52)$$

2.4.4 Transmission Loss

Transmission Loss (TL) is the acoustical power level difference between the incident and transmitted waves through an element of interest assuming an anechoic termination, i.e.

$$TL = 10 \log_{10} \frac{W_i}{W_t} \quad (2.53)$$

where W_i is the incident sound power and W_t is the transmitted sound power. The sound power for each wave can be expressed in terms of the incident and transmitted rms pressure amplitudes by

$$W_i = \frac{\hat{p}_i^2}{\rho c} A_u \quad (2.54)$$

and

$$W_t = \frac{\hat{p}_t^2}{\rho c} A_d \quad (2.55)$$

where the rms pressure amplitude, as a function of frequency, can be expressed as

$$\begin{aligned} \hat{p}_i &= \sqrt{\hat{G}_{ii} * \Delta f} \\ \hat{p}_t &= \sqrt{\hat{G}_{tt} * \Delta f} \end{aligned} \quad (2.56)$$

where \hat{G}_{ii} and \hat{G}_{tt} are the upstream incident and downstream transmitted single-sided averaged power spectral densities respectively. Δf is the frequency resolution bandwidth. A_u and A_d are the upstream and downstream cross-sectional areas. For an anechoic termination, \hat{G}_{tt} is equal to the PSD of any microphone reading downstream which is equal to the downstream incident PSD, $\hat{G}_{di,di}$. It is important to note, however, that the termination must be anechoic for the TL to be calculated in this way. A common mistake is to apply decomposition downstream in the absence of an anechoic termination and to assume \hat{G}_{tt} is equal to $\hat{G}_{di,di}$ for this condition. This is incorrect as $\hat{G}_{di,di}$, when there is no anechoic termination, is the sum of \hat{G}_{tt} plus the successive downstream reflections from the element of the downstream reflected wave ($\hat{G}_{dr,dr}$).

2.5 Core Noise Generation Mechanisms

The sound field radiated from a ducted vane-axial fan, such as the low pressure turbine of an aero-engine or gas turbine, consists of a number of tones on a broad band noise floor. Ignoring effects which occur to the radiated field outside the engine, such as the “Haystacking” or spectral broadening of the tones due to scattering in the turbulent shear layer, the radiated sound field is made up of a superposition of noise sources generated from within the duct. The noise generating mechanisms are numerous. Broad-band noise can be generated from turbulence, turbulent boundary layers interacting with rotor blades as discussed in Joseph and Parry [34], convected broad band core noise originating from the combustor, vortex shedding and transient aerodynamic loading variations due to turbulence and blade vibration. The tonal content can be made up of convected duct tones upstream of the turbine, thermo-acoustic instabilities in the combustor, the spinning potential field of the rotors alone (measurable only in close proximity to the rotors when the rotor tip speed is subsonic), “buzz-saw” or combination tone noise when rotor tip speeds are supersonic, rotor-stator/rotor-OGV interaction noise and sum and difference tones due to interactions between different rotor stages. In addition to these, noise, whether narrow band, broad band or tonal in nature, may be generated by the interaction between a rotor and a flow distortion.

2.5.1 Rotor Only

A fundamental noise generating element in a turbine or fan is the rotor. Considering initially plug flow with no flow distortions, the noise due to steady aerodynamic blade loading is the source of greatest importance. Consider a fan with B blades each equally spaced $\frac{2\pi}{B}$ apart. Figure (2.12), taken from Tyler and Sofrin [63], is a developed view showing typical pressure contours around a rotor blade assembly at an arbitrary radius, the details of which will vary depending on blade pitch angle, camber, etc.

As this steady pressure field or potential field is due to the rotor, it must spin with the rotor angular velocity of $\Omega = 2\pi N$, where $N = \frac{rpm}{60}$, with respect to a fixed coordinate system. The pressure, therefore depends on a specific combination of angle and time coordinates, *viz.* $(\theta - \Omega t)$. This form $p(\theta, t) = p(\theta - \Omega t)$ is a travelling wave and is similar to the travelling wave solution to the 1-D wave equation, $(\frac{x}{c} - t)$. The pressure measured at a fixed radius and axial position will therefore be periodic with angular period of $\frac{2\pi}{B}$ radians. Unless the pressure fluctuation from one period to the next is a pure sinusoid, a Fourier decomposition of this periodic signal would reveal a fundamental frequency equal to $B\Omega$ along with harmonics $hB\Omega$ of varying relative magnitudes, where h is the harmonic index. The Fourier series may be written as

$$p(\theta, t) = \sum_{h=0}^{\infty} a_h \cos[hB(\theta - \Omega t) + \phi_h] \quad (2.57)$$

where a_h and ϕ_h are amplitude and phase parameters required to synthesize the particular pressure

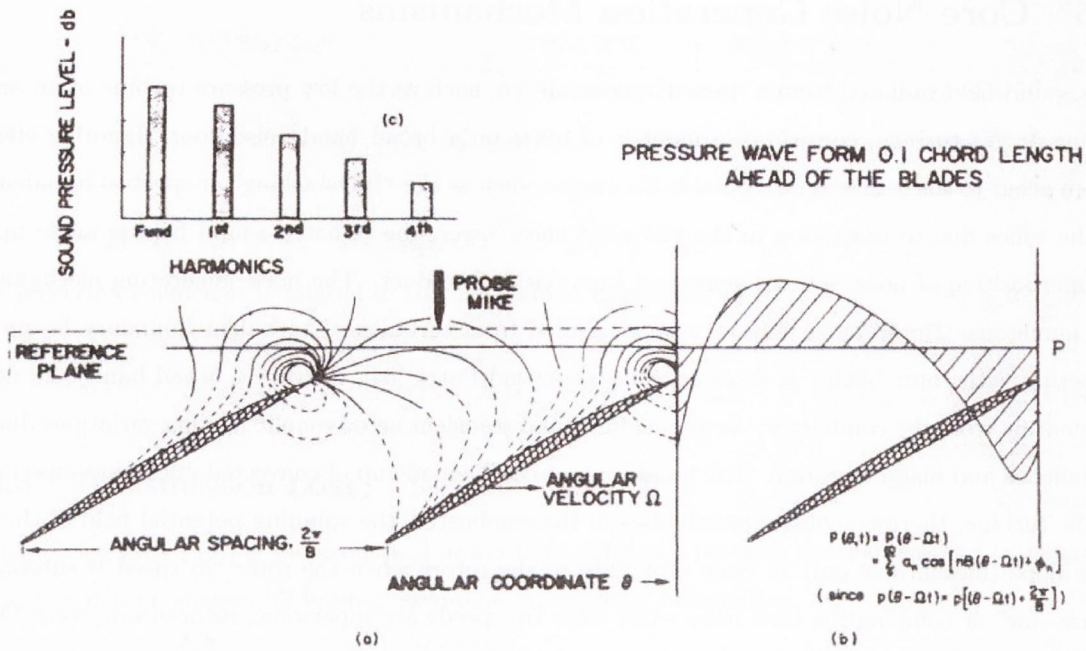


FIGURE 2.12: Pressure field around a rotor-blade assembly.

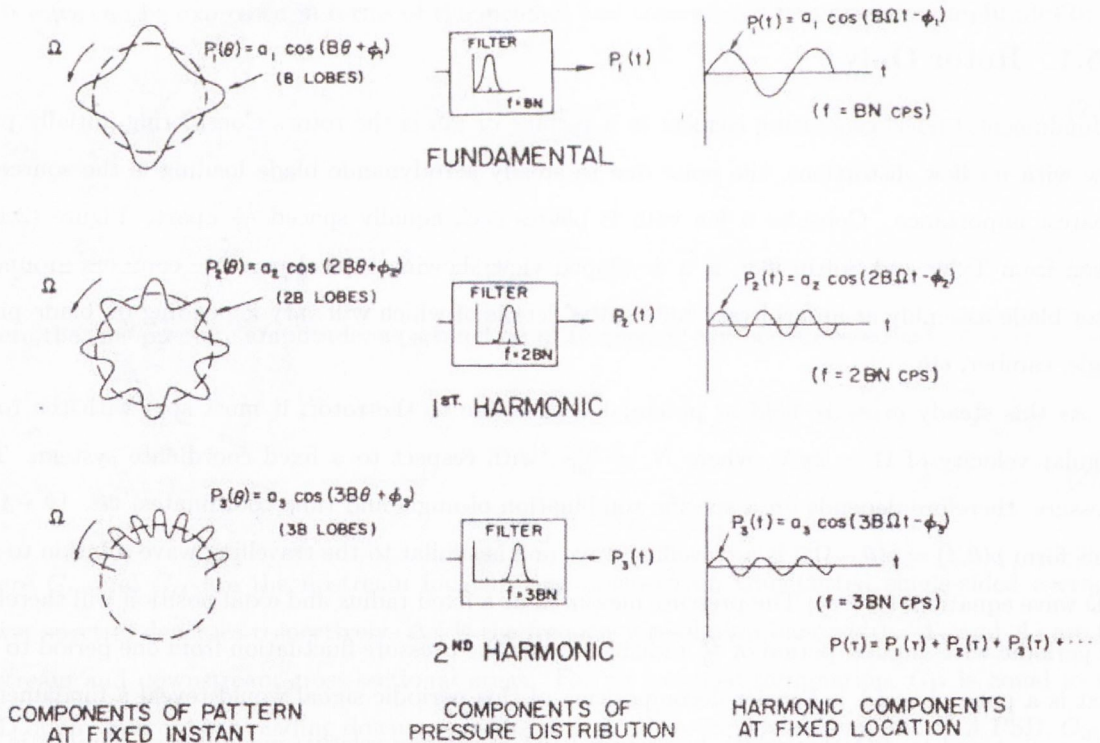


FIGURE 2.13: Spatial and temporal pressure variation for a four bladed rotor.

wave.

By setting t or θ equal to zero, spatial or temporal representations of the pressure field may

be examined. Figure (2.13), also taken from Tyler and Sofrin [63], shows a plot of the pressure distribution as a function of angular position at a fixed distance forward of the blades for a four bladed rotor. Referring to the spatial representations, it can be seen that the pressure field is a superposition of “lobed” patterns each rotating at shaft speed: the fundamental pattern having the same number of lobes as blades, generating a fundamental blade pass frequency of $B\Omega$ radians/s; the harmonics also rotating at shaft speed generating harmonic multiples of this frequency equal to $hB\Omega$ radians/s. Both Tyler and Sofrin [63] and Moore [45] have performed experiments to validate this theory. If we center attention on a single frequency, so that the pressure of the h^{th} harmonic is the h^{th} term only, and allow m to equal the number of lobes at one of these discrete frequencies, the following form of (2.57) may be written,

$$p(\theta, t) = a_m \cos[m(\theta - \Omega t) + \phi_h] \quad (2.58)$$

In this form, the pressure distribution at the plane of the rotor can be naturally interpreted as an m -lobe pattern rotating at angular velocity Ω radians per second and generating at every point a fluctuating pressure with frequency $f = \frac{m\Omega}{2\pi} = mN$ Hz.

The circumferential wavelength of this generated mode on the surface of the duct is $\lambda_s = \frac{2\pi a}{m}$. By introducing the circumferential velocity at which the pattern sweeps the cylindrical wall, $c_s = a\Omega$, equation (2.24) may be rewritten in terms of the circumferential Mach number, M_s , and the mode number, through the relation $c_s = M_s c$, as

$$k_x = \frac{m}{a} \sqrt{M_s^2 - 1} \quad (2.59)$$

given that $f = \frac{c}{\lambda} = \frac{c_s}{\lambda_s}$ and thus $\lambda_s = M_s \lambda$. Equation (2.59) is an important version of the propagation condition which states that, in order for the pressure field of a spinning lobed pattern to propagate in the duct, the circumferential Mach number, M_s , at which it sweeps the cylinder wall, must be equal to or greater than unity. As modes generated at the fundamental frequency and each of the harmonics spin at the rotor tip speed, Ωr , this implies that the “rotor-alone” noise contributes to the radiated sound field only under the conditions of super-sonic tips speeds. Moore [45] performed a number of experiments on sub-sonic rotors, measured these excited modes close to the rotor and compared their decay rates to the theory of Tyler and Sofrin [63].

2.5.2 Rotor-Stator Interaction

The noise generated by the rotor of a turbine or compressor in close proximity to either a stator, IGV or OGV was first comprehensively reported by Tyler and Sofrin [63]. Unlike the rotating potential field generated by a rotor in isolation, the generating mechanisms attributable to the all-encompassing term “rotor-stator interaction” arise from *unsteady* loading over the blades. Some of these are:

1. cutting of wakes of upstream stators by rotor blades;

2. impingement of rotating blade wakes on downstream stators;
3. interruption of the rotating periodic pressure field of the rotor by the proximity of reflecting objects, apart from wake effects.

Whereas the rotor field structure generated by the rotor-alone model consists of a single hB lobe pattern per $hB\Omega$ frequency, each rotating at the rotor speed Ω , the rotor-stator interaction effect results in an infinite number of modes being generated at each of the $hB\Omega$ frequencies. The number of lobes being different per mode yet generating a frequency of $hB\Omega$, implies that the modes must be rotating at differing speeds. The most important outcome of this is that, if a particular interaction pattern has fewer lobes than the number of blades, then it must rotate at a speed greater than Ω to generate the same frequency and thus it becomes possible for the interaction to produce propagating modes for a subsonic tip speed.

After a certain amount of manipulation, the pressure in the plane of the rotor can be shown to be equal to

$$p_{m,h} = V a_{m,h} \cos \left[m \left(\theta - \frac{hB}{m} \Omega t \right) + \phi_{m,h} \right] \quad (2.60)$$

where m is restricted to

$$m = hB + kV, \quad k = \dots - 1, 0, +1, \dots \quad (2.61)$$

where h is the harmonic index, B the number of blades, and V the number of upstream or downstream vanes/stators. Thus the number of blades and stators determines the circumferential modes excited in the duct. For negative values of m , the modes spin counter to the direction of rotation of the rotor. This form of pressure differs from that given in equation (2.58) and reveals their differences. Now for a particular harmonic, h , of blade-passage frequency, the interaction field is the superposition of an infinite number of rotating patterns. The number of lobes in each pattern is given by the successive values of m , generated as an index, k , ranges over all positive and negative integers in the expression in equation (2.61). Each m lobe pattern turns at a different speed, $\frac{hB\Omega}{m}$ radians per second, as is required to generate h times blade-passage frequency.

2.5.3 Combustion

The two largest sources of aero-engine noise, the fan and the jet, have been significantly reduced over many years of intensive research. With their reduction, a threshold is being reached, which will form the new noise floor and limit the benefits to be gained by reducing these dominant components, unless the noise sources which set this threshold are in turn reduced. Of these, combustion, or core noise, is an area of current research activity. At relatively low jet velocities, such as would occur at engine idle, during taxiing, and at approach and cruise conditions, core noise is considered a significant

contributor to the overall sound level. The trend of core noise attracting increasing attention will continue with the incorporation of low NO_x combustors and the increase in by-pass ratio in modern engine design.

Opinion is divided as to whether core noise may or may not also include compressor noise as well as components of turbine and flow noise not associated with the combustion process. Combustion noise is still a poorly understood process and falls into two categories: direct combustion noise, which is produced by the chemical combustion process itself and thermo-acoustic instability; and indirect combustion noise, or *entropy* noise, which occurs when fluid with a non-uniform entropy distribution is accelerated or decelerated. These “hot spots” radiate sound due to a fluctuating mass flux. One of the more recent works on indirect combustion is that by Schemel *et al* [54] which experimentally and numerically investigates noise emission in the presence of swirl flow.

The combustion noise energy is confined to the low to mid-frequency ranges (300Hz -1200Hz for the CFM56 SNECMA engine), with a far field directivity peak at approximately 120° from the inlet axis. A well-known method to predict combustion noise is SAE ARP876 [1]. This method, which assumes combustion noise to have a spectrum with a fixed frequency shape and a peak frequency of 400Hz, is sometimes used qualitatively, once its frequency peak has been shifted to match measured data.

The contribution of core noise to farfield sound level measurements of turbofan engines is poorly understood. This is due to its broadband low frequency content being often masked by jet noise. A number of experimental techniques to identify combustion noise have been developed over the years. Karchmer [37], [38] and [35] used the ordinary coherence function between internal and farfield microphones and derived the core noise at farfield locations by calculating the coherent output power. Karchmer [36] also used the conditioned coherence function to locate the core noise source region. Extraneous noise contamination at internal pressure measurement locations can result in the derived core noise at the farfield location being significantly lower than the true value. Shivashankara, [56] and [57], used Chung’s flow noise rejection technique [11] to separate internal core noise components from farfield measurements. Hsu and Ahuja [29] extended Chung’s technique to develop a partial coherence-based technique that uses five microphones to extract ejector internal mixing noise from farfield signatures which were assumed to contain the ejector mixing noise, the externally generated mixing noise, and also another correlated mixing noise presumably from the ejector inlet. Wherever there is more than one source, all of these approaches necessitate the location of at least one sensor near one of the sources, e.g. the core noise source, which is also required not to measure any other correlated source. When there is only one source, it has been shown that if Chung’s technique is used, then no direct measure of the source is necessary. Minami [44] develops a technique where only farfield measurements are needed to separate any number of correlated sources from extraneous noise, which, due to its distributed nature, could be jet noise for example. A number of these techniques are applied to experimental data in chapter 5.

2.5.4 Inflow Distortion-Rotor Interaction

Section 2.5.2 discusses the generation of tones at blade passing frequencies and harmonics for the case where a rotor interacts with a stationary periodic disturbance, such as that caused by a mean flow passing through a stator. Cumpsty [14] derives a kinematic analysis of the interaction of the spinning modes created by such a rotor-stator pair with a second rotor. This analysis is presented to explain the appearance of tones, in the radiated noise spectrum of a turbo-machine, at sum and difference frequencies of the harmonics of the blade passing frequencies of multiple rotor stages.

The pressure field resulting from the interaction of a spinning mode from a rotor-stator pair of B_1 blades and V_1 vanes with a single rotor of B_2 blades, is shown to be

$$p(\theta, t) = \sum_{m=-\infty}^{\infty} B_2 a_m e^{i[m\theta - (h_1 B_1 \Omega_1 \pm h_2 B_2 \Omega_2)t + \phi_m]}, \quad h_2 = \dots - 1, 0, +1, \dots \quad (2.62)$$

where m is restricted to

$$m = \pm h_2 B_2 + m_1 = \pm h_2 B_2 + h_1 B_1 + k V_1, \quad k = \dots - 1, 0, +1, \dots \quad (2.63)$$

and Ω_1 and Ω_2 are the rotational speeds of the two rotor shafts respectively. The sum and difference frequencies are shown here to be $h_1 B_1 \Omega_1 \pm h_2 B_2 \Omega_2$.

Holste and Neise [27] also extended Tyler and Sofrin's [63] theory for the interaction case of two rotors, and a further advancement for the case of two rotors and multiple stators is reported in Enghardt [17]. The results are similar to those of Cumpsty's and are transcribed here as

$$\omega = h_1 B_1 \Omega_1 - h_2 B_2 \Omega_2, \quad h = 1, 2, 3, \dots \quad (2.64)$$

with

$$m = h_1 B_1 - h_2 B_2 - k_1 V_1 - k_2 V_2 - \dots, \quad k = \dots - 1, 0, +1, \dots \quad (2.65)$$

A full non-linear solution of the Euler equations employing a non-linear time marching approach has examined, in a simple way, self interaction and combination interaction of two frequencies in a rotor-stator environment, as reported in Nallasamy [49].

2.6 Contribution of Thesis

It has been discussed that coherence based identification techniques can be used to identify the contribution of combustion noise to near and far field acoustic measurements of aero-engines. These techniques condition from external measurements additional core noise sources such as turbine noise, as well as other noise sources generated exterior to the engine. The underlying assumption with these identification techniques is that the propagation\convection path, from combustion can to measurement point, is a linear one. For the situation where the combustion noise is acted upon in

a non-linear fashion, as illustrated schematically in figure 2.14, the identified contribution will be inaccurate. This thesis examines the scenario where a fluctuating pressure is modified, in a *non-linear* sense, as it is convected through a rotating vane-axial fan. This work looks at and develops a number of linear and non-linear noise source identification techniques which can be used to identify the contribution of combustion noise to near and far-field acoustic measurements of aero-engines. To do this, an experimental rig was designed and built to gain a fundamental physical understanding of the convection of noise through a vane-axial fan to examine the potential interactions.

Section 2.5.4 has highlighted a potential mechanism where energy at two different frequencies may interact to induce energy at a third. In the work of that section, the upstream energy source is a rotor-stator pair whose excited spinning modes impinge upon a second rotor. The case where broad band or narrow band noise, such as may originate from a combustor, interacts with a rotor-stator pair, producing noise at sum and difference frequencies is explored in this thesis, the effect being similar to a non-linear quadratic operation.

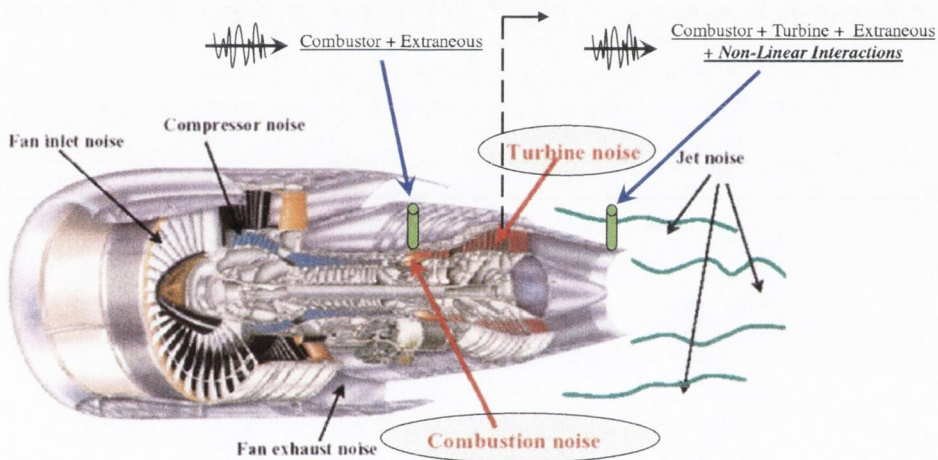


FIGURE 2.14: Schematic of aero-engine depicting modification of combustion noise due to convection through turbine.

The first part of the thesis is devoted to the study of the pressure field in a cylindrical duct. The second part is devoted to the study of the stress field in a cylindrical duct. The third part is devoted to the study of the deformation field in a cylindrical duct. The fourth part is devoted to the study of the failure field in a cylindrical duct. The fifth part is devoted to the study of the fracture field in a cylindrical duct. The sixth part is devoted to the study of the fatigue field in a cylindrical duct. The seventh part is devoted to the study of the creep field in a cylindrical duct. The eighth part is devoted to the study of the buckling field in a cylindrical duct. The ninth part is devoted to the study of the vibration field in a cylindrical duct. The tenth part is devoted to the study of the acoustics field in a cylindrical duct. The eleventh part is devoted to the study of the radiation field in a cylindrical duct. The twelfth part is devoted to the study of the scattering field in a cylindrical duct. The thirteenth part is devoted to the study of the diffraction field in a cylindrical duct. The fourteenth part is devoted to the study of the reflection field in a cylindrical duct. The fifteenth part is devoted to the study of the transmission field in a cylindrical duct. The sixteenth part is devoted to the study of the absorption field in a cylindrical duct. The seventeenth part is devoted to the study of the emission field in a cylindrical duct. The eighteenth part is devoted to the study of the excitation field in a cylindrical duct. The nineteenth part is devoted to the study of the propagation field in a cylindrical duct. The twentieth part is devoted to the study of the interaction field in a cylindrical duct. The twenty-first part is devoted to the study of the coupling field in a cylindrical duct. The twenty-second part is devoted to the study of the conversion field in a cylindrical duct. The twenty-third part is devoted to the study of the transformation field in a cylindrical duct. The twenty-fourth part is devoted to the study of the modulation field in a cylindrical duct. The twenty-fifth part is devoted to the study of the mixing field in a cylindrical duct. The twenty-sixth part is devoted to the study of the blending field in a cylindrical duct. The twenty-seventh part is devoted to the study of the dispersion field in a cylindrical duct. The twenty-eighth part is devoted to the study of the diffusion field in a cylindrical duct. The twenty-ninth part is devoted to the study of the permeation field in a cylindrical duct. The thirtieth part is devoted to the study of the sorption field in a cylindrical duct. The thirty-first part is devoted to the study of the absorption field in a cylindrical duct. The thirty-second part is devoted to the study of the emission field in a cylindrical duct. The thirty-third part is devoted to the study of the excitation field in a cylindrical duct. The thirty-fourth part is devoted to the study of the propagation field in a cylindrical duct. The thirty-fifth part is devoted to the study of the interaction field in a cylindrical duct. The thirty-sixth part is devoted to the study of the coupling field in a cylindrical duct. The thirty-seventh part is devoted to the study of the conversion field in a cylindrical duct. The thirty-eighth part is devoted to the study of the transformation field in a cylindrical duct. The thirty-ninth part is devoted to the study of the modulation field in a cylindrical duct. The fortieth part is devoted to the study of the mixing field in a cylindrical duct. The forty-first part is devoted to the study of the blending field in a cylindrical duct. The forty-second part is devoted to the study of the dispersion field in a cylindrical duct. The forty-third part is devoted to the study of the diffusion field in a cylindrical duct. The forty-fourth part is devoted to the study of the permeation field in a cylindrical duct. The forty-fifth part is devoted to the study of the sorption field in a cylindrical duct. The forty-sixth part is devoted to the study of the absorption field in a cylindrical duct. The forty-seventh part is devoted to the study of the emission field in a cylindrical duct. The forty-eighth part is devoted to the study of the excitation field in a cylindrical duct. The forty-ninth part is devoted to the study of the propagation field in a cylindrical duct. The fiftieth part is devoted to the study of the interaction field in a cylindrical duct.



The diagram illustrates the geometry of the cylindrical duct and the internal structures that influence the pressure field. The duct is shown in a perspective view, with various internal components labeled. The diagram is used to describe the physical setup of the experiment or simulation. The internal structures are arranged in a way that creates a specific flow path or pressure distribution within the duct. The diagram is a key element of the thesis, providing a visual representation of the cylindrical duct and its internal configuration.

Contribution of Thesis

The contribution of this thesis is to provide a comprehensive study of the pressure field in a cylindrical duct. The study is based on a combination of theoretical analysis and experimental data. The results of the study are presented in a series of plots and graphs, which show the pressure distribution within the duct under various conditions. The study also includes a detailed discussion of the physical mechanisms that govern the pressure field in a cylindrical duct. The results of the study are compared with existing literature, and the differences are explained. The study provides a valuable contribution to the understanding of the pressure field in a cylindrical duct, and it is hoped that it will be useful to other researchers in the field.

Chapter 3

Experimental Rig

3.1 Introduction

Figure 3.1 shows schematically how a Turbofan engine might be instrumented with high specification dynamic pressure transducers at the combustion cans in order to measure the source noise. Also shown are transducers aft of the turbine in the hot stream jet flow. Microphones would normally be the transducer of choice in the far field. A rig was built with a view to representing some of the main features of this set-up and is shown schematically in figure 3.2.

A speaker represents the source noise which is directed down a brass tube of 3mm wall thickness with an internal diameter of 0.051m. This end of the tube is open and allows air to be sucked down the pipe by a vaneaxial fan situated at a minimum of 1.2m from the entrance, according to the test set-up. This vaneaxial fan which has a single 8 blade rotor stage downstream of a single 5 vane stator stage represents a simplified turbine of the turbofan engine. The tube ends with an open anechoic termination designed to reduce flow expansion/separation noise as well as reflections. A number of microphones can be located upstream and downstream of the fan, at various axial and circumferential positions, such that they are mounted flush with the inside of the pipe. Additional microphones can be located in the near-field. Also illustrated, is how the electrical signal to the speaker can be recorded with a view to using this signal to condition the measured pressures.

3.2 Anechoic Termination

In order to simplify the acoustic field and thus the test conditions as much as possible, an anechoic termination was designed to be fitted to the downstream end of the tube. Although reflected travelling waves cannot be avoided upstream of the fan due to reflections from the fan itself, an anechoic termination was fitted at the end of the duct to create a unidirectional downstream pressure field. The benefits of such a set-up are multifold. Firstly, peaks in the spectra resulting from standing

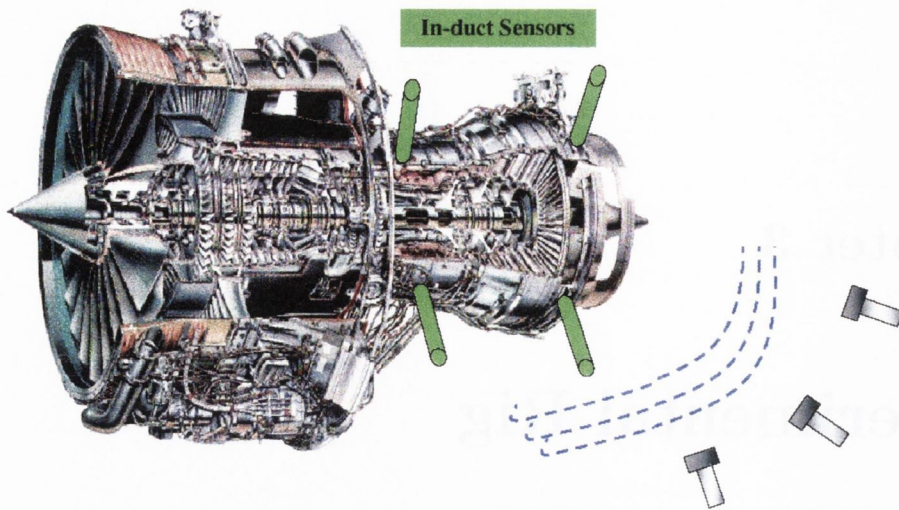


FIGURE 3.1: Instrumented engine with farfield microphones.

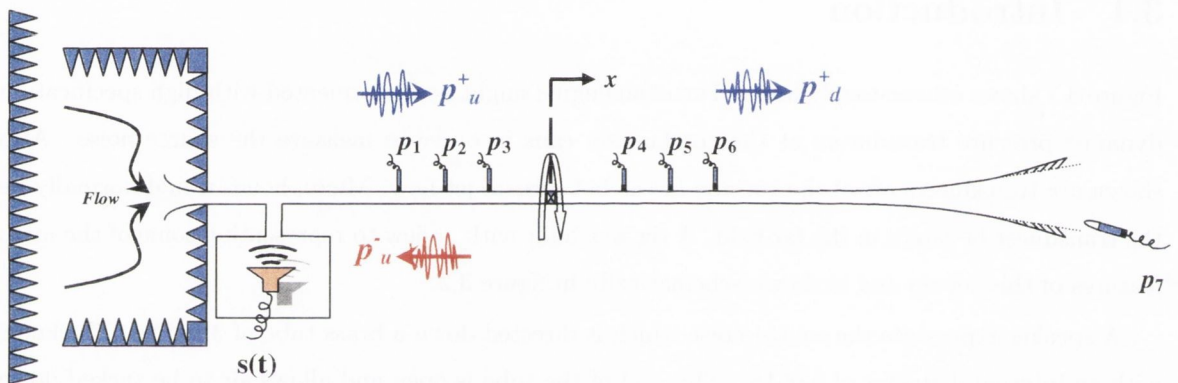


FIGURE 3.2: Schematic of Experimental Rig

wave resonances, which would confuse the diagnostic, could be avoided. Secondly, the location of the microphones would not have to be chosen in order to accommodate these standing waves and associated nodes. Thirdly the dynamic range would be reduced, again due to resonant peak elimination resulting in better signal to noise ratios. And, fourthly, and most importantly, the incident signal measured downstream from the fan, could be assumed to be the sum only, of the upstream incident wave, plus the contribution from the fan plus any interaction between the two.

A number of possible anechoic terminations are presented in the European standard ISO 10534 [3], some of which have been incorporated into experimental rigs, for example in the work of Bolleter *et al* [9] and Elmady and Bodén [16].

3.2.1 Horn Theory

Horn theory is commonplace in loudspeaker design where the objective is to improve the efficiency of cone dynamic speakers. The cause of the low efficiency is the poor mechanical impedance match

between the relatively dense solid materials of the driver and the low radiation impedance presented by the fluid around it. By placing the speaker in a duct of infinite length, an impedance of ρc is presented to the cone which is both larger and purely resistive and thus a better match. Due to the obvious impracticality of an infinite length duct, and that also, for sound transmission the objective is to radiate sound into the environment, a truncated duct is used. While providing an improved high impedance, a duct whose open end is smaller than the wavelength of the frequency sent out is a very inefficient radiator of sound, causing, as seen in section 4.4, either resonances at some frequencies or inefficient transmission at others. Horn loaded speakers are those which combine a duct with a judiciously flared shape which allows the sound to radiate into the farfield while minimising reflections. Although we are unconcerned here with maximising the impedance match between the sound source and the surrounding air for the sake of efficiency, we are interested in eliminating reflections due to the impedance mismatch and it is with this in mind that horn theory is attractive.

The objective is to design the horn such that the cross sectional area, which depends on the distance x along the axis, changes so slowly that the particle velocity remains parallel to the surface of the horn and thus does not reflect from it. If the power $P = pU$, where U is the spacially dependant volume flow rate, is considered to remain constant while the impedance $\frac{p}{U} = \frac{z_c}{A}$ becomes smaller as A increases, then p and U must change and the horn can be considered to act as an impedance-matching device which can accept a high- p , low- U wave and gradually transform it into a low- p , high- U wave suitable for radiation into the low impedance environment.

The acoustic requirement of the anechoic termination to be designed was that it should be efficient above 1kHz. That is to say there should be little reflection above this frequency. In order to design the horn, three analytical solutions were considered as options, *viz.*, conical, exponential and catenoidal. The behaviour of each of these shapes begins with Webster's approximate wave equation;

$$\frac{\partial^2 p}{\partial t^2} = c^2 \frac{1}{S} \frac{\partial}{\partial x} \left(S \frac{\partial p}{\partial x} \right) \quad (3.1)$$

which models the propagation of pressure waves in a horn assuming that no transverse modes exist. Under this assumption any point within the horn falls on some isophase surface which spans the cross section of the horn and over which pressure is constant.

Although the surfaces of constant phase within each of these chosen horn shapes are not necessarily plane, they are, if well designed, *one-parameter* waves, and lend themselves well to Webster's equation.

Analytical solution - infinite length

The Conical Horn - infinite length Unlike the exponential and catenoidal horn, an exact solution can be found for the conical shape which is the solution to the one dimensional spherical wave equation.

The areas of the phase surfaces for the cone are

$$S = S_0 \left[1 + \frac{x}{x_0} \right]^2 \quad \text{for} \quad S_0 = \pi r_0^2 \quad \text{and} \quad x_0 = \frac{r_0}{\tan(\theta)} \quad (3.2)$$

and where x_0 is the distance back from the throat to where the apex of the cone would be. The specific acoustic impedance at the throat of the horn is given by Morse [47] to be

$$z = \rho c \left[\frac{1}{1 + \left(\frac{\lambda}{2\pi x_0}\right)^2} - j \frac{\left(\frac{\lambda}{2\pi x_0}\right)}{1 + \left(\frac{\lambda}{2\pi x_0}\right)^2} \right] \quad (3.3)$$

where the cone is sufficiently long that reflections are considered to be negligible.

The power radiated from a cone at low frequencies is relatively small and its effect (as for all horn shapes) is negligible at high frequencies where the waves are radiated out in narrow beams and the confining effect of the walls of the horn is not significant. Thus at a particular length, with increasing frequency, the behaviour in a cone being the same as for a one-dimensional spherical wave, the waves become approximately plane and thus the impedance tends asymptotically towards ρc . The low frequency effect of the cone is improved by reducing the internal angle tending towards an infinite pipe and again an impedance of ρc .

The Exponential Horn - infinite length For the exponential horn, the cross sectional areas are of the form

$$S = S_0 e^{\left(\frac{2x}{h}\right)} \quad (3.4)$$

Here, h is a shape factor and is the distance in which the diameter of the horn cross-section increases by a factor $e = 2.718$. Again, the amplitude of the pressure waves decrease with distance from the throat but for this case the waves propagate at a speed greater than the speed of sound in the free-field. In addition, the velocity differs for different frequencies, which makes the exponential horn a dispersing medium for sound waves. The velocity increases with decreasing frequency to a cut-off frequency where the velocity becomes infinite. At this frequency, the entire volume of the horn moves in phase. Below this frequency the horn is an inefficient radiator of sound as there is no true wave motion. This cut-off frequency ω_{cut} decreases with increasing h and as a large mouth diameter is required to prevent reflections, it is seen that a long slowly flaring shape is optimum. The specific acoustic impedance for an exponential horn is derived by Morse [47] to be

$$z = \rho c \left[\sqrt{1 - \frac{\omega_0^2}{\omega^2}} - j \frac{\omega_0}{\omega} \right] \quad \text{for} \quad \left[\omega > \omega_0 = \frac{c}{h} \right] \quad (3.5)$$

The Catenoidal Horn - infinite length The third horn shape considered was Catenary, whose cross sectional areas are of the form in equation (3.6),

$$S = S_0 \cosh^2\left(\frac{x}{h}\right) \quad (3.6)$$

For large values of x , the difference between it and an exponential shape is indistinguishable. However, the slope is zero at the throat which results in no discontinuity at an interface with a

tube and thus these potential reflections are eliminated. Similar to the exponential shape, the wave velocity in the horn is greater than that in open space and there is a cut-off frequency below which the horn is inefficient. Unlike both the Conical and Exponential horns however, as seen in equation (3.7), the impedance is purely resistive and although also tending toward ρc with increasing frequency, is always greater. Thus, although the cut-on frequency of the catenoidal horn is slightly higher than that of the exponential, its impedance just above cut-on is significantly higher resulting in an improved impedance match and an associated improvement in low-frequency sound transmission.

$$z = \rho c \left[\frac{1}{\sqrt{1 - \frac{\omega_0^2}{\omega^2}}} \right] \quad \text{for} \quad \left[\omega > \omega_0 = \frac{c}{h} \right] \quad (3.7)$$

Analytical Evaluation - infinite length In order to simply evaluate the three considered termination shapes for efficiency, the reflection coefficient is plotted using the input impedances given in equations (3.3), (3.5) and (3.7). By using equation (2.52) and defining now the reference plane, $x = 0$, to be at the end of the duct, or, equivalently, the throat of the horn, the reflection coefficient can be expressed in terms of the impedance.

It can be shown that the amplitude of the reflected wave is small when compared to that of the incident wave and the horn may be treated as infinitely long whenever the radius a of the mouth is such that $ka > 3$, Kinsler *et al* [41]. If the horn is to be non-reflecting above 1kHz then the radius of the mouth is to be at least 0.16m. Figure 3.3(a) shows the geometries for the three horn shapes where the throat diameter is equal to that of the duct. For the exponential and catenoidal horns the shape factor was chosen to result in a mouth radius equal to 0.1612m. For the cone, an internal angle of 6 degrees is chosen. These cone parameters were chosen to investigate its suitability as a termination to serve both acoustically and as a suitable flow expansion to decrease separation noise. 6 degrees was considered a sufficiently small gradient to avoid separation.

Figure 3.3(b) plots the reflection coefficients for each of these terminations. As was discussed above, both the exponential and catenoidal horns have cut-off frequencies below which they are inefficient. These can be determined to be 85 and 117 Hz respectively. The catenoidal, while having a cut-off frequency which is higher than that of the exponential, is more efficient at frequencies just above it and is the best performing of the three horns. The conical horn while performing better at very low frequencies, i.e. below the cut-offs of the other two, transmits sound relatively poorly at low frequencies for the internal angle chosen.

Analytical Solution - finite length

Although, equations (3.3), (3.5) and (3.7), give a good insight into the general comparative performance of these horn shapes, they each depend on the underlying assumption that the mouth diameter is infinitely large with the result that a perfect impedance match with the environment is made and thus no reflections result. Gervais *et al* [23] has developed a more realistic solution for an exponential

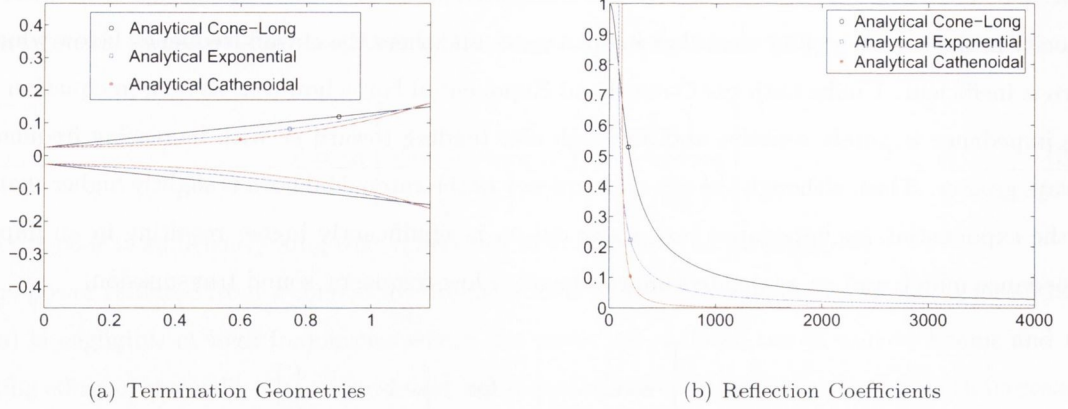


FIGURE 3.3: Comparison between three shapes of horn. The infinite length theory of Morse [47] is assumed

and catenoidal termination of finite length. The derivation results in the reflection coefficient of each of these horns at their throat and is quite involved. First of all, it is necessary to determine the impedance of the expansion at the mouth which allows the calculation of the pressure derivative at a given point. It is then necessary to express the reflection coefficient at the mouth by identifying the impedances. This allows the impedance at the throat to be defined, and from that, the reflection coefficient at this plane.

The Exponential Horn - finite length A summary of the results where Q_{exp} is the reflection coefficient at the mouth and Z_{exp} the resulting impedance at the throat is given here.

$$h = \frac{2L}{\ln(\frac{S_L}{S_0})} \quad (3.8)$$

$$Q_{exp} = [\cos(2kL) - j \sin(2kL)] \frac{-(\frac{L}{h})^2 - j\frac{L}{h} \sqrt{(kL)^2 - (\frac{L}{h})^2}}{(kL)^2 + kL \sqrt{(kL)^2 - (\frac{L}{h})^2}} \quad (3.9)$$

$$Z_{exp} = \frac{1}{S} \frac{kL(1 + Q_{exp})}{-j\frac{L}{h}(1 + Q_{exp}) + kL(1 - Q_{exp})} \quad (3.10)$$

The Catenoidal Horn - finite length Again just a summary of the result is presented here.

$$h = \frac{L}{\cosh^{-1}(\sqrt{\frac{S_L}{S_0}})} \quad (3.11)$$

$$k' = k \sqrt{1 - \frac{1}{(kh)^2}} \quad (3.12)$$

$$Q_{cat} = \frac{-(\frac{L}{h})^2 (1 + \tanh^2 \frac{L}{h}) - 2j\frac{L}{h} \sqrt{(kL)^2 - (\frac{L}{h})^2} \tanh(\frac{L}{h})}{2(kL)^2 + 2kL \sqrt{(kL)^2 - (\frac{L}{h})^2} - (\frac{L}{h})^2 (1 - \tanh^2(\frac{L}{h}))} e^{(-2jk'L)} \quad (3.13)$$

$$Z_{cat} = \frac{1}{S} \frac{kL}{\sqrt{(kL)^2 - \left(\frac{L}{h}\right)^2}} \left[\frac{1 + Q_{cat}}{1 - Q_{cat}} \right] \quad (3.14)$$

Analytical Evaluation - finite length For both horns, the reflection coefficient at the throat can be calculated using equation (2.52) with equations (3.10) and (3.14). Figure 3.4 compares the results for these solutions for the two horns with the same geometry as given in figure 3.3(a). These results are much more realistic and agree well with the results found in Kinsler *et al* [41], which states that if $ka > 3$ and the horn opens into an infinite baffle, then a 10% reflection is predicted. The cut-off frequencies appear again in this solution and are similar to those given by equations (3.5) and (3.7). The fact that the terminations are now finite, results in two distinct differences. Firstly, the reflection coefficients are generally higher for all frequencies than those given by the infinite horn theory. Secondly, periodic variations are found in the reflection coefficient which decrease with increasing frequency. These are particularly marked for the exponential horn. This indicates that the horn behaves as an acoustic duct of constant diameter, in which standing waves may develop for certain frequencies, (acoustic resonance). However, as the frequency increases, then the impedance match improves with the environment and the magnitude of the standing wave and the reflection coefficient decrease. A similar phenomenon can be seen with the catenoidal horn but to a lesser extent.

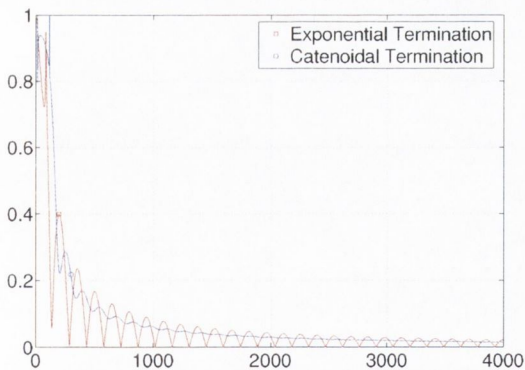


FIGURE 3.4: Analytical solution for reflection coefficient using the theory of Gervais *et al* [23]

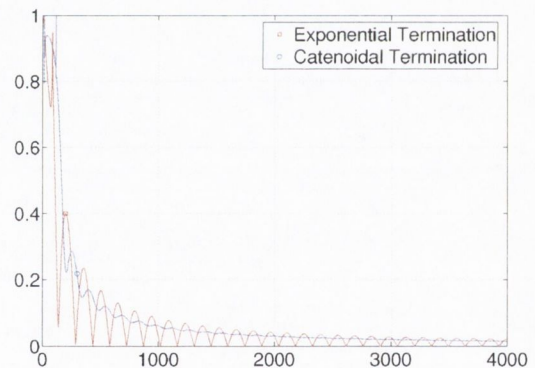


FIGURE 3.5: Reflection coefficient comparison for a catenoidal termination. The finite difference code of [53] assumes a radiation condition at the exit plane. The analytical theory is that of Gervais *et al* [23].

Finite Difference Solution - Catenoidal

Based on the findings above, the catenoidal horn proves to be the most suitable termination having the best characteristics. Before a termination was manufactured, a finite difference model was developed in order to verify the results of equation (3.14). This wave expansion method of Ruiz and Rice [53]

was applied in three dimensions for the catenoidal horn given in figure 3.3(a). The complex pressure was calculated at two points on the inner surface of the modeled duct and the reflection coefficient calculated using the transfer function technique given in equation (2.45). The reflection coefficient was calculated as a function of frequency for a simple harmonic input at the upstream inlet of the duct in figure 3.6(a). A number of radiation conditions were tried both at the exit plane of the horn and also on a sphere in the nearfield of the horn mouth. The mesh for these conditions is shown in figure 3.6(b). Figure 3.5 shows the calculated reflection coefficient for the exit plane radiation condition compared with that from equation (3.14). The general result is qualitatively quite good. Of particular interest is the way the first circumferential mode, which should cut-on at just below 4kHz for this diameter duct, is evident by the deviation of the reflection coefficient at this frequency, highlighting how plane wave theory no longer holds above this frequency. Neither the theory of Morse [47], nor Gervais *et al* [23] allow for higher order modes. The poor performance of the horn at low frequencies is also noticeable. However, no distinct lower cut-off frequency is calculated. Periodic fluctuations are seen in the reflection coefficient. This fact and the fact that the overall value of R is overestimated is slightly unexpected, as with a radiation condition fixed at the exit plane, a lower value for R would be expected with no reflections to cause the standing waves. Despite these slight differences, the response of the horn is deemed acceptably good to fix the dimensions of the horn and to design a termination for the rig.

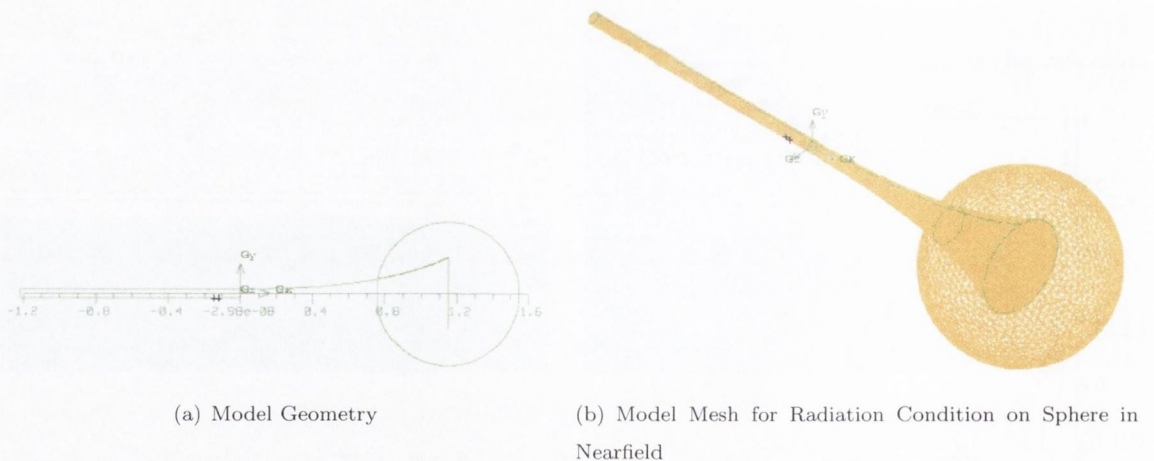


FIGURE 3.6: Finite Difference Model and example of Mesh

Experimental Termination - Catenoidal

As the required termination was quite large (1.18m long by 0.1612m mouth radius) and the shape difficult to manufacture by traditional means, it was decided to use a rapid prototyping machine, which would lend itself well to producing a complex 3 dimensional form. As the maximum volume the machine could work on at a time is 8 inches square by 12 inches high, the horn had to be broken up into parts and the expansion made piecemeal. Pro-engineer was used to help design the parts and

the flanges necessary for assembly. The interfaces of the parts were designed with a lip on one part to locate with a recess on its mating part which would allow the two parts to locate correctly ensuring a flush surface on the inside at the joints. Pro-engineer allowed the parts to be saved as *.stl* files which could be read by the rapid-prototyping machine. Figures 3.7 and 3.8 show two different views of the horn as solid-modelled with Pro-engineer.

As already mentioned, as the horn is to be used with flow and as the rate of flare of the horn is such that flow separation would be certain to occur, additional design had to be built into the expansion so that flow noise in the horn would not become a significant noise source. A fine, stainless steel, woven wire cloth (mesh) was formed into a truncated cone of 6 degree internal angle and folded in between two specific flanges, located axially where a 6 degree angle intersected tangentially the inside surface of the horn. The mesh, being approximately acoustically transparent would not reflect sound, yet would contain the flow, preventing separation. The cavity between the mesh and the inside surface of the horn was filled with sound absorbing material (Rockwool). This separation prevention feature is shown schematically in figure 3.2, and in-situ in the experimental rig in figures 3.9, 3.10 and 3.11.

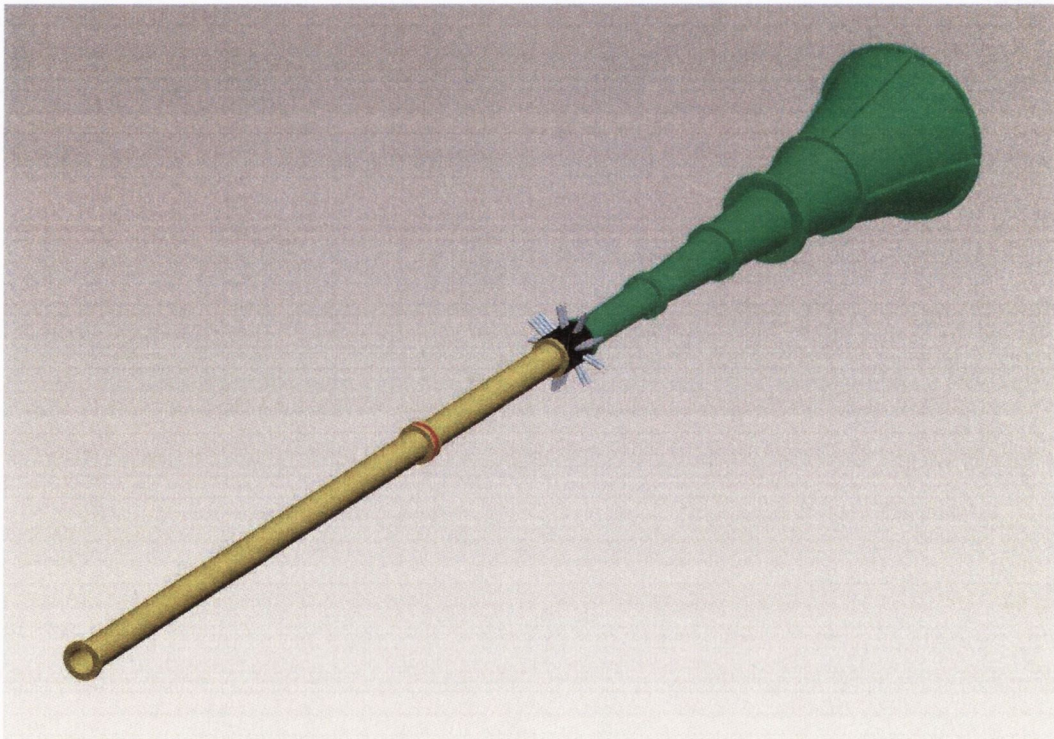


FIGURE 3.7: Solid model assembly of the anechoic termination shown in green. Some sample lengths of ducting are shown in brass, with a typical location for the fan indicated at the plane indicated with the colour red.



FIGURE 3.8: A view of the model looking upstream.

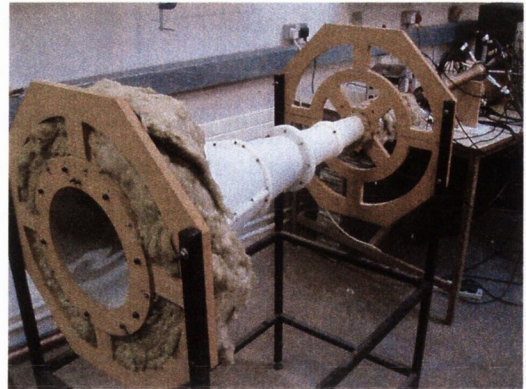


FIGURE 3.9: The assembled anechoic termination.

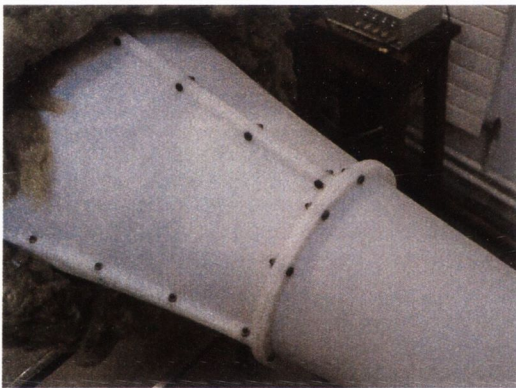


FIGURE 3.10: A view of the termination detailing assembly flanges.

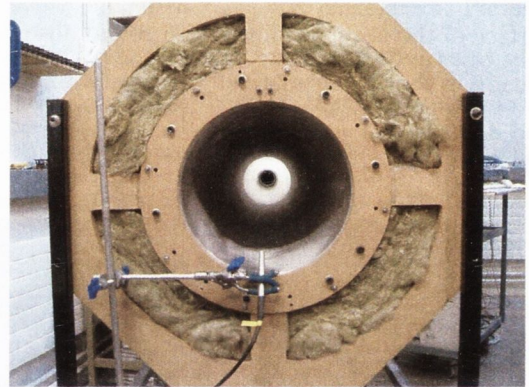


FIGURE 3.11: Looking upstream into the termination the wire mesh, included at an internal angle of 12° to reduce expansion noise, is visible.

3.3 Vaneaxial Fan

In order to represent the turbine, and to provide rotation to the flow, a vaneaxial fan was inserted into the rig. This fan had a single 8 blade rotor stage downstream of a single 5 vane stator stage. The fan was just less than 2 inches in diameter and fit snugly into the pipe. The fan had a high rotational speed of 16500rpm at the nominal design voltage of the fan of 26VDC. With 8 blades this would result in a BPF of 2200Hz. By applying a higher voltage higher BPF's could be attained. Acoustic tones could be heard at these high rpms. Max velocities of approx 12m/s were measured with a pitot-static tube inserted into the tube. An image of the fan is provided in figure 3.12 and a specification sheet of the fan is given in appendix A.



FIGURE 3.12: Vane-axial fan used in the experimental rig. A specification sheet is to be found in appendix A.

3.4 Instrumentation and Analysis

A Hewlett Packard Dynamic Signal Analyser 35660A or a B&K Noise Generator (Type 1405) were used to provide a sound signal for the speaker. The HP Signal Analyser was used to supply either band passed random noise or a single frequency tone. The B&K Noise Generator which produced white noise up to 20kHz was usually used in conjunction with a Barr and Stroud filter which could be configured as high pass, low pass or band pass. These signals were amplified with a Ling Dynamic Systems power amplifier, LDS PA500, before being fed to the 600W JBL 2206 H speaker. To improve the efficiency of the speaker, it was mounted into an enclosure with outlet diameter equal to that of the pipe.

As a large number of microphones were needed for some of the test configurations, at least three microphone types were used. The most numerous were 30 custom built electret microphones (KE 4 Sennheiser electret) and amplifiers. The outside diameter of these microphones was 8mm. Eight $\frac{1}{4}$ inch (nominal) GRAS microphones were also used. Four of these were of type 40BH which are high pressure microphones and were used in conjunction with a GRAS power module (12AN) which supplied both a DC voltage to the microphone preamps and also a 200VDC polarisation voltage. The second four GRAS microphones were of type 40PR which are array microphones and were used in conjunction with a PCB 4 channel ICP sensor signal conditioner. The GRAS microphones were 7mm in outside diameter.

A 32 channel data acquisition system was used to acquire the data. This consisted of 2 X 16 bit simultaneously sampling Kinetic Systems V200 cards mounted into a National Instruments chassis. A PC running LabView, was used via a National Instruments PCI card to acquire the data from the

National Instruments MXI controller card in the chassis. All data, once acquired into time domain files by LabView, were subsequently processed using Matlab.

3.4.1 Signal Processing

Many real life physical phenomena can not be represented with a mathematical expression that will determine their instantaneous values at any time t . The noise of a jet engine is an example of this. Nondeterministic data of this type are referred to as *random time functions*. However, in spite of the irregular character of the random function, many random phenomena exhibit some degree of statistical regularity, and certain averaging procedures can be applied to establish gross characteristics useful in engineering design.

In the frequency domain, the principal functions used are; the auto-power spectral density function $\hat{G}_{xx}(\omega)$, the cross-power spectral density function $\hat{G}_{xy}(\omega)$, the frequency response function $H_{xy}(\omega)$, the coherence function $\gamma_{xy}^2(\omega)$ and the phase $\phi_{xy}(\omega)$. Appendix B, gives an overview of the signal processing techniques used to process the data acquired using the A/D converter.

Chapter 4

Preliminary Experimental Results

4.1 Introduction and Objectives

In order to verify the correct operation of the experimental equipment, and of the implementation of the analysis techniques such as those discussed in sections (2.4.1), (2.4.2) and (2.4.3), an initial set of tests were performed. The results of these tests are presented in sections 4.3 and 4.4. In these initial tests, a number of simple benchmark cases were examined whose known theoretical solutions could be used for comparison.

The following configurations have been chosen to examine the acoustic properties of specific end conditions, *viz.* a closed-ended and an open-ended duct. For the cases where the plane $x = 0$ does not coincide with the end of the duct, the *input impedance* of a length of pipe L , terminated by the end condition, is being examined.

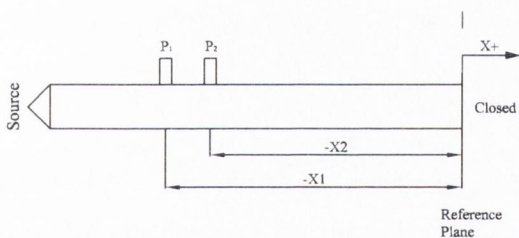


FIGURE 4.1: Closed duct

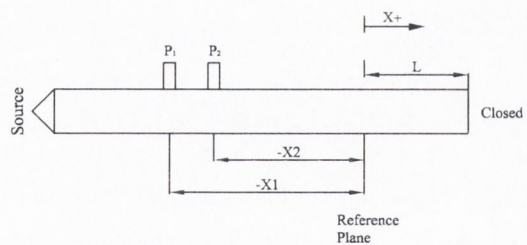
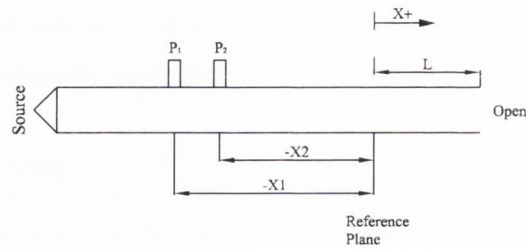


FIGURE 4.2: Closed duct of length L

A second set of preliminary tests were performed to allow the characterisation of the experimental rig described in chapter 3, and to evaluate its properties such as the reflection coefficient of the anechoic termination and the noise spectrum of the fan etc. A series of tests were performed on the rig for two different test set-ups;

1. Broad band noise, high pass filtered at 500Hz, low pass filtered at 3000Hz. The fan not rotating
2. Broad band noise, high pass filtered at 500Hz, low pass filtered at 3000Hz. The fan rotating at

FIGURE 4.3: Open duct of length L

17250 rpm

for seven microphone locations as shown in figure 3.2. The source signal feeding the loudspeaker was also acquired. The results of these tests are presented in sections 4.5 and 4.6. For these latter tests, one microphone located upstream, one downstream and one in the exit plane region (microphone 7) is sufficient to provide a pressure measurement at the three locations of interest. A second microphone upstream and downstream will allow the coherence, frequency response function, reflection coefficient and impedance to be calculated. Also, and most importantly, the second microphone at each of these locations will allow the pressure field to be decomposed into an incident and reflected wave for frequencies below the plane wave cut-off. This will allow the propagation and convection of pressure through the fan and into the nearfield to be analysed.

The diameter of the duct to be used in all of these tests is 0.05115m resulting in a plane wave cut-off frequency of

$$f_{cutoff} = \frac{1.84c}{2\pi a} = 3894Hz \quad \text{for} \quad c = 340m/s \quad (4.1)$$

using equation (2.31).

4.2 Microphone Calibration

Although most microphones are calibrated and issued with calibration certificates, which state sensitivity and frequency response when supplied, it is unlikely that any two microphones will respond in exactly the same way to the same excitation. This could be due to any number of reasons from the gain of the microphone to the cabling used or indeed to the characteristics of any one of the components used in the chain of acquisition. It is therefore important to measure the frequency response function (or simply transfer function) between the two microphones so that gain and phase mismatch may be accounted for. When a number of microphones are to be used, a good approach is to calibrate all microphones with respect to a single high quality microphone.

In a cylindrical duct, advantage may be taken of the fact that only plane waves propagate below a certain cut-off frequency. By locating two microphones in the same plane along the duct, see figure 4.4, they can be exposed to the same pressure wave distribution for frequencies below the cut-off

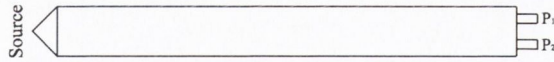


FIGURE 4.4: Schematic for Calibration Technique

frequency. This can be realised by boring two holes the diameter of the microphones in an end-cap fitted to the end of a duct and flush mounting the microphones with the inside of the cap surface. Broad band noise of $0\text{Hz} - f_{cut-off}\text{Hz}$ should be transmitted from a speaker located at the other end of the duct.

The frequency response function, $H_{12,cal}$ ¹, can be recorded for this set-up and an example is shown in figure 4.5. Although these microphones match each other quite well, there are differences between them, see figure 4.6, especially at low frequencies. By dividing the frequency response functions measured for other test set-ups, e.g. with microphone 1 at $-x1$ and microphone 2 at $-x2$, in figures 4.1, 4.2 and 4.3 for example, by $H_{12,cal}$, these differences can be accounted for;

$$H_{12} = \frac{H_{12,error}}{H_{12,cal}} \quad (4.2)$$

As a duct of 0.05115m was used for calibration for these tests, figure 4.5 clearly shows the plane wave cut-off frequency of just below 4kHz. Above this frequency, due to the existence of higher acoustic modes, the two microphones no longer necessarily measure the same pressure and thus the frequency response function between them is not necessarily unity nor would there be a zero phase difference expected.

4.3 Closed Ended Duct

4.3.1 Theory

Standing Waves Frequencies

Figure 4.7 shows how standing waves might fit in a cylindrical duct of a single closed end. As an anti-node is required at the closed end, the wavelengths are limited to

$$(2n - 1)\left(\frac{\lambda_n}{4}\right) = L_c \text{ or } f_n = (2n - 1)\frac{c}{4L_c} \quad (4.3)$$

Closed End at $x=0$

With reference to figure 4.1, the particle velocity u reduces to zero at $x = 0$ for the closed end condition. Therefore equation (2.37) can be expressed as

$$p_i - p_r = 0 \quad \text{for } u = 0 \text{ and } x = 0$$

¹The frequency dependent notation will be omitted henceforth for simplicity of representation.

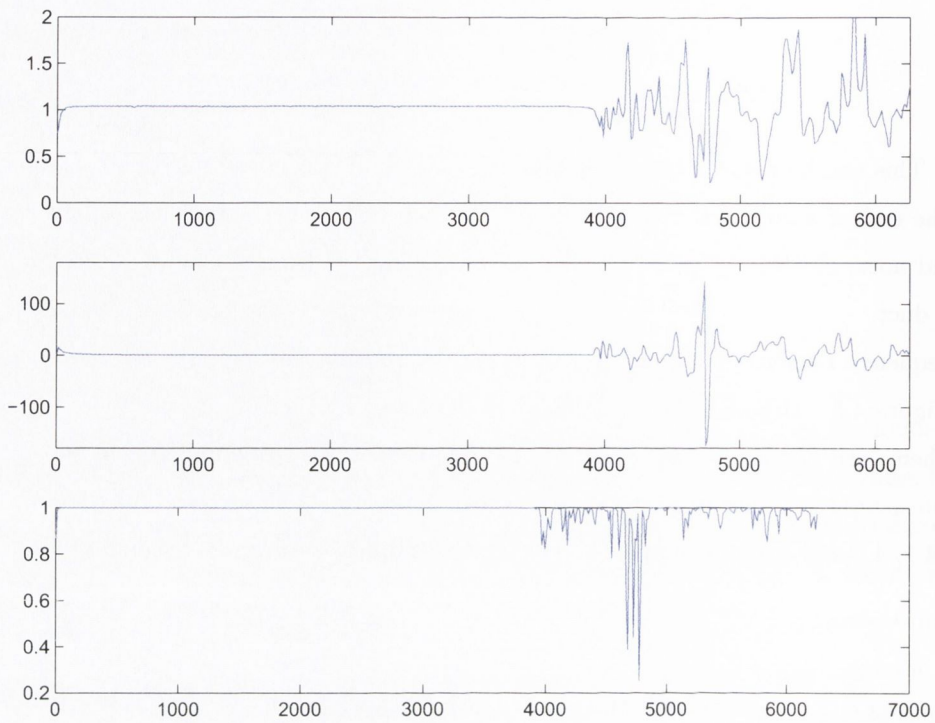


FIGURE 4.5: Magnitude and Phase of TF with Coherence between microphone 1 & microphone 2

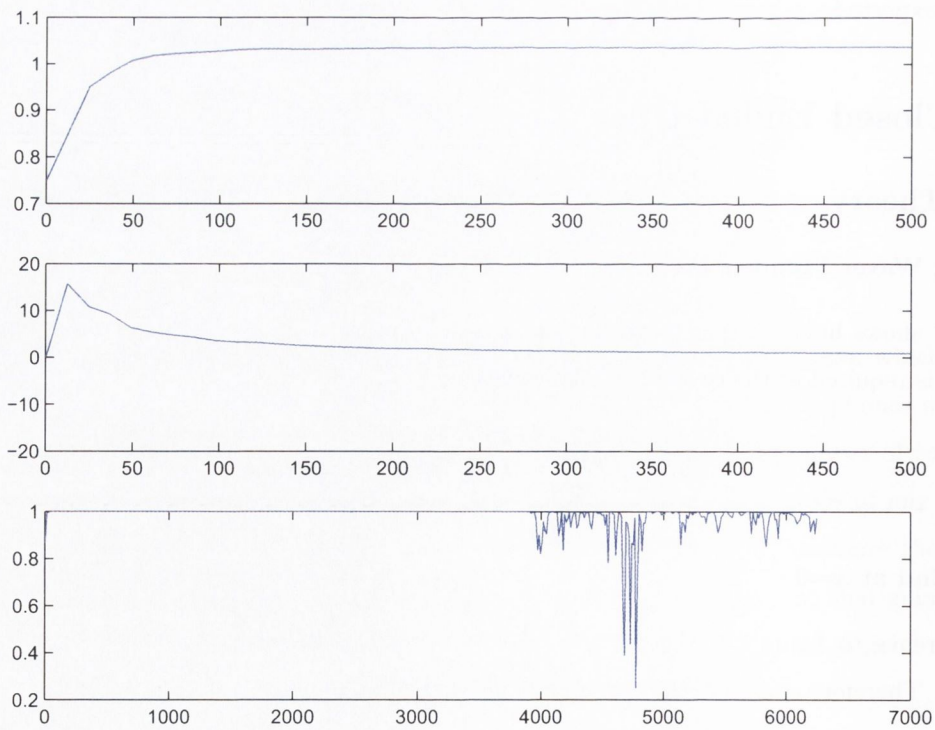


FIGURE 4.6: Magnitude and Phase of TF with Coherence. Close up of low frequencies.

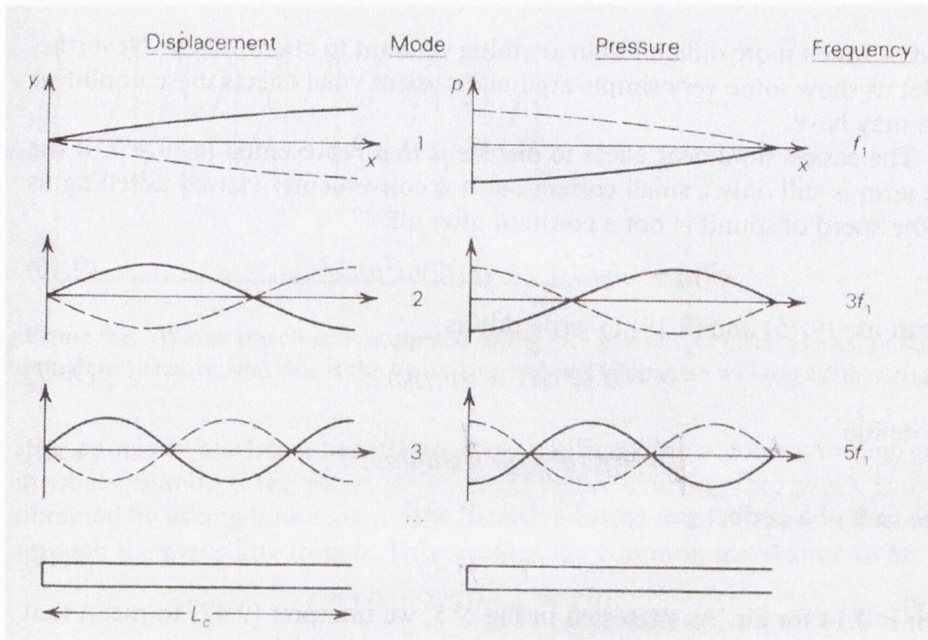


FIGURE 4.7: Examples of standing waves in a cylindrical duct of length L_c closed at one end

and equations (2.42) and (2.49) give

$$R = 1 \text{ and } Z_a \rightarrow \infty \quad \text{for } u = 0 \text{ and } x = 0 \tag{4.4}$$

Closed End at $x=L$

If instead, the pipe is terminated with a solid boundary at $x=L$, then figure 4.2 is more pertinent. We can re-structure the impedance equation (2.48) as

$$Z_a(x) = \frac{p(x)}{u(x)} = \rho_0 c \frac{p_i e^{-jkx} + p_r e^{jkx}}{p_i e^{-jkx} - p_r e^{jkx}} \tag{4.5}$$

By making use of equation (4.5) and eliminating p_i and p_r , values of the acoustic impedance at $x = 0$

$$Z_a(0) = \rho_0 c \frac{p_i + p_r}{p_i - p_r} \tag{4.6}$$

can be related to that at $x = L$

$$Z_a(L) = \rho_0 c \frac{p_i e^{-jkL} + p_r e^{jkL}}{p_i e^{-jkL} - p_r e^{jkL}} \tag{4.7}$$

to give

$$Z_a(0) = \frac{Z_a(L) \cos(kL) + j\rho_0 c \sin(kL)}{\frac{jZ_a(L)}{\rho_0 c} \sin(kL) + \cos(kL)} \tag{4.8}$$

and

$$Z_a(L) = \frac{Z_a(0)\cos(kL) - j\rho_0 c \sin(kL)}{-j\frac{Z_a(0)}{\rho_0 c} \sin(kL) + \cos(kL)} \quad (4.9)$$

Now, from equation (4.8) with $Z_a(L) \rightarrow \infty$, the input impedance of the duct of length L with a rigid termination is

$$Z_a(0)_{closed\ end} = -j\rho_0 c \cot(kL) \quad (4.10)$$

In accordance with equation (2.41), for no mean flow, a phase of $-2kL$ in the reflection coefficient results from the closed end being located at L ,

$$R = |R|e^{-j2kL} \quad (4.11)$$

4.3.2 Results

Closed End at $x=0$

The first configuration to be looked at is that of the simple closed duct of figure 4.1. Figure 4.8 shows the autospectra of the two microphones where the resonant frequencies of equation (4.3) can be clearly seen. This figure also shows the frequency response of the speaker to be high in the frequency range of interest. For this closed-ended duct set-up, $x_1 = -0.1505m$ and $x_2 = -0.0755m$. In the open-ended duct tests in a later section x_2 is moved closer to x_1 with $x_2 = -0.1255m$. By changing x_2 , and thus the spacing s between the microphones, the drop-out frequency of equation (2.47) can be investigated. As the sampling rate of acquisition was fixed at $12.5kHz$, all of the figures below will show information above the cut-off frequency in order to demonstrate the effects of the superposition of the higher mode(s).

Using equation (2.44) with $R = 1$ for a closed end, see equation (4.4), and the Euler expression for a complex no. i.e., $e^{jkx} = \cos(kx) + j\sin(kx)$, the theoretical frequency response function between the two microphones for the closed duct case can be shown to equal,

$$H_{12,theo,c} = \frac{\cos(kx_2)}{\cos(kx_1)} \quad (4.12)$$

Figure 4.9 displays the magnitude and phase of this expression, in blue, plotted versus the experimental frequency response function, in red, as calculated with Matlab. For the magnitude there is excellent agreement between the two up to the cut-off frequency. The phase too agrees well up to the cut-off frequency. It should be noted here that the theoretical phase can only be 0 or 180 degrees as a result of the sign being plus or minus. Also shown is the experimental coherence between the two signals which is excellent (≈ 1) up to the cut-off frequency. The usual fall-off in coherence is seen at nodes, where there is poor signal to noise ratio, and at the anti-nodes where the low damping leads to high signal levels and non-linearities.

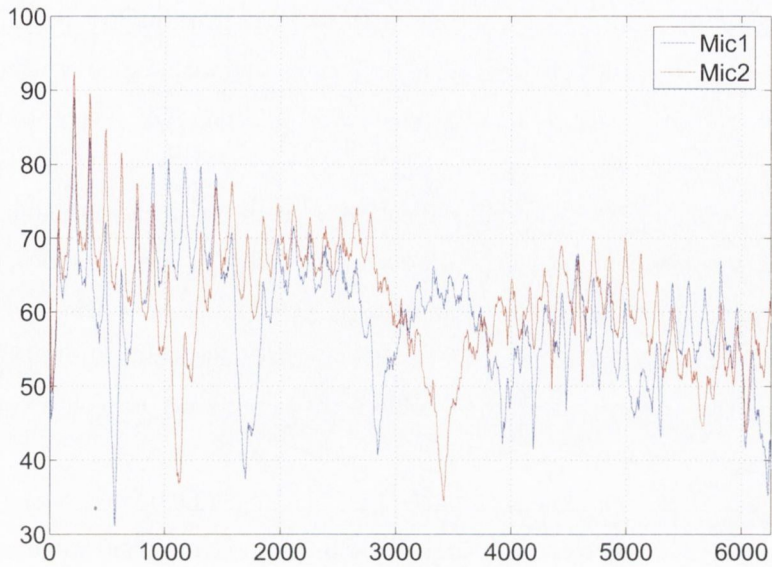


FIGURE 4.8: Autospectra of microphones 1 & 2. Closed duct.

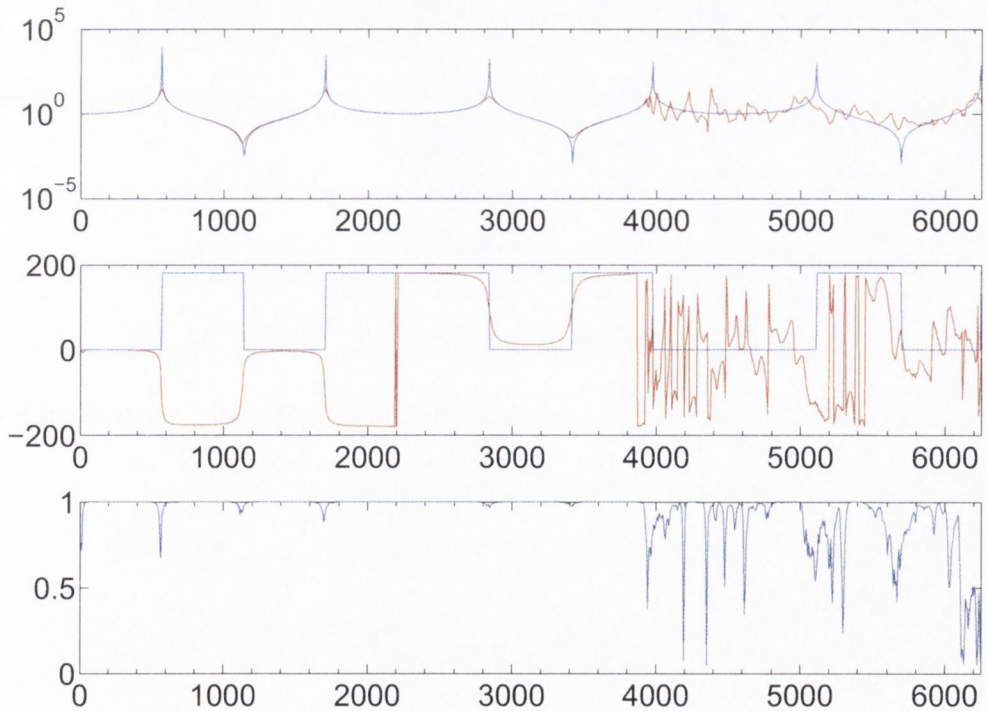


FIGURE 4.9: Frequency response function and coherence for closed duct. Theoretical - blue, experimental - red.

Closed End at $x=L$

Equation (4.10) gives an expression for the input impedance of a duct of length L with a rigid termination. This theoretical solution (divided by ρc) is compared with the experimentally determined result using equation (2.51) in figure 4.10(b), where $L = 0.110m$. The errors seen in the resistive and reactive parts of the impedance are discussed in Seybert and Ross [55] and are attributed to the indeterminate character of the impedance function at frequencies where the phase angle is small for systems with high reflection coefficient. Under such conditions any numerical or measurement errors are magnified in the calculation of the impedance. Overall the agreement is very good with the greatest deviation from theory occurring in the resistive part (which should be zero for all frequencies) where the phase changes abruptly. Also, to be noted is the error at the drop-out frequency of $2267Hz$ for $s = 0.075m$.

From this expression for the impedance and using equation (2.52), the theoretical value of the reflection coefficient may be plotted against the experimentally determined value as shown in figure 4.10(a). As discussed in section 2.4.2, the magnitude of the reflection coefficient is equal at all planes along the duct and this is demonstrated here by comparing the magnitude of R in equation (4.4) to that of figure 4.10(a), i.e. both are equal to unity irrespective of axial location.

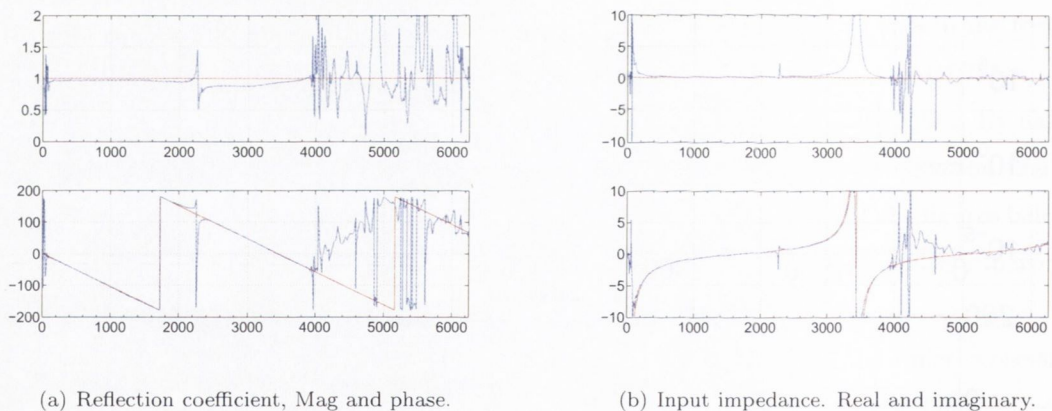


FIGURE 4.10: Theoretical Vs experimental results for closed duct of length L . A drop-out is seen at $f = 2267Hz$ due to the microphone spacing. Theoretical - red, experimental - blue.

4.4 Open Ended Duct

4.4.1 Theory

Standing Wave Frequencies

Similar to a closed-ended duct, an open-ended duct, as alluded to already, presents problems by way of unwanted resonances occurring at its own normal modes which are a function of its length. Equation (4.13) gives the normal mode frequencies.

$$n \left(\frac{\lambda_n}{2} \right) = L_0 \quad \text{or} \quad f_n = \frac{nc}{2L_0} \quad (4.13)$$

where L_0 is the total effective length of the open duct.

Open End

On first inspection one might assume the end condition for an open duct to be $p(0) = 0$ at $x = 0$. However, the situation of zero impedance at the open end is never quite what really happens, as in fact $p \neq 0$ at the open end, but rather at some small distance outside, Δ . This is understood by recognising that the air in the space surrounding the opening presents an additional load which must also be moved.

This additional impedance imposed by the atmosphere on the acoustic radiation from the end of the duct is termed the *radiation impedance* and will always have a resistive as well as a reactive part.

Levine and Schwinger [43] developed a rigorous and explicit solution for the problem of sound radiation from an unflanged circular pipe which solves for radiation resistance also. A summary of the results is given here in terms of the reflection coefficient;

$$R = -|R|e^{j2k\Delta} \quad (4.14)$$

where

$$|R| = e^{-\frac{(ka)^2}{2}} \left(1 + \frac{1}{6}(ka)^4 \left[\log \frac{1}{\gamma ka} + \frac{19}{12} \right] \right) \quad ka < 1 \quad (4.15)$$

$$|R| = (\pi ka)^{\frac{1}{2}} e^{-ka} \left(1 + \frac{3}{32} \frac{1}{(ka)^2} \right) \quad ka > 1$$

and $\gamma = 1.781$. Plots of $|R|$ and the frequency dependent end correction, α , are given versus ka in the paper and are shown here in figure 4.11.

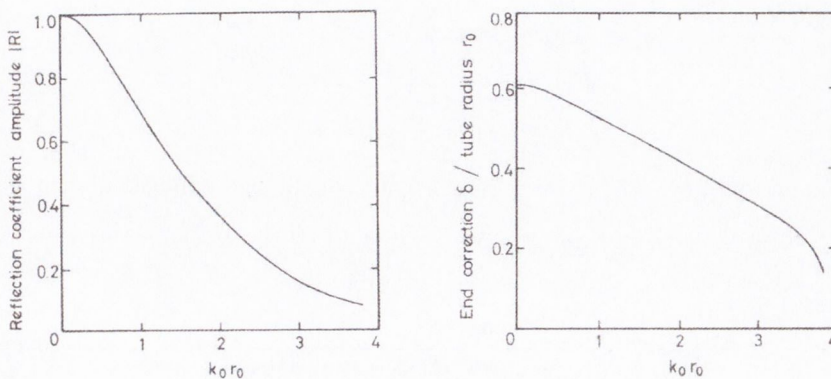


FIGURE 4.11: $|R|$ and $\frac{\Delta}{a}$ Vs ka . (Levine and Schwinger [43])

Also noted is that in the long wave (or low frequency) limit, $ka \ll 1$, the reflection coefficient assumes the form

$$R = -e^{j2k\Delta} \quad (4.16)$$

where

$$\frac{\Delta}{a} = \alpha = 0.6133 \quad (4.17)$$

The form for the end correction as given in Levine and Schwinger [43] proves tedious to evaluate. Munjal however [48], presents a development of the work of Levine and Schwinger [43] by Davies *et al* [15] to include some empirical formulae to describe the frequency dependent end correction α and modulus $|R|$.

A close empirical fit to the values of end correction and reflection coefficient modulus, as shown in figure 4.11, is given by the following expressions:

$$\frac{\Delta}{r} = 0.6133 - 0.1168(kr)^2, \quad kr < 0.5 \quad (4.18)$$

$$\frac{\Delta}{r} = 0.6393 - 0.1104kr, \quad 0.5 < kr < 2$$

$$|R| = 1 + 0.01336kr - 0.59079(kr)^2 + 0.33576(kr)^3 - 0.06432(kr)^4, \quad 0 < kr < 1.5 \quad (4.19)$$

4.4.2 Results

In order to avoid drop-out frequencies in the frequency range of interest, positions of $x_1 = -0.1505m$ and $x_2 = -0.1255m$ were chosen such that the first drop-out ($6725Hz$) occurs above the plane wave cut-off frequency.

Open End at $x=L$.

An extended length solution for an open ended duct incorporates the additional inertance provided by the atmosphere by way of a length correction

$$l_e = l + \alpha a, \quad (\alpha a = \Delta)$$

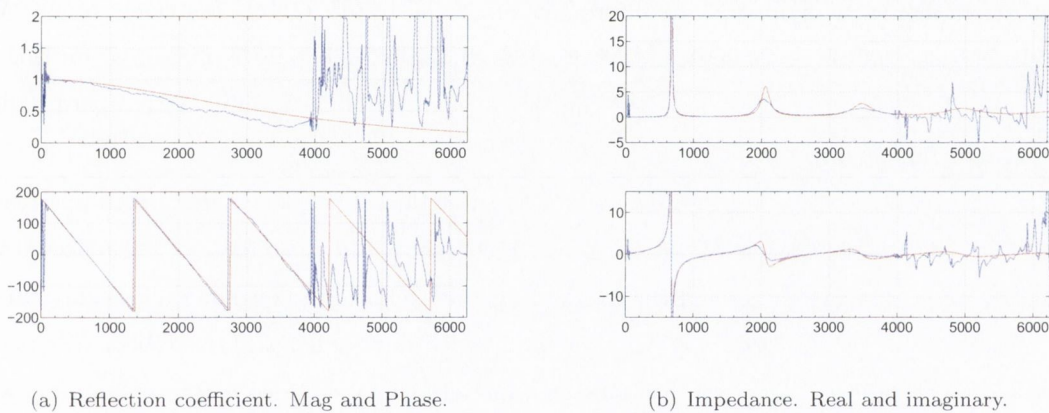
where α is termed an *end correction*, which is a function of the end condition, such as the size of a flange if present, and a is the radius of the duct. The end correction for cases where $ka \ll 1$ have been calculated, see King [40] or Rayleigh [50] for example, as

$$\begin{aligned} \alpha &= 0.61 && \text{(semi-infinite pipe, no flange)} \\ \alpha &= 0.82 && \text{(semi-infinite pipe, infinite flange)} \\ \alpha &= 0.79 && \text{(hole in infinite flange)} \end{aligned} \quad (4.20)$$

However, these solutions do not take the radiation resistance into account. As discussed, Levine and Schwinger, [43], have provided the full solution for a semi-infinite pipe with no flange. The empirical fit given by Davies *et al* [15] will be used here to calculate the phase of the reflection coefficient, see equations (4.14) and (4.18). The magnitude will be calculated using the expressions given by Levine and Schwinger [43], equation (4.15).

Using this resistance incorporating approach, the full solution is given below for the *input* impedance of an open duct of length L , the schematic of which is shown in figure 4.3. Equations (4.15) and (4.18) are implemented with the Δ augmented by the amount L in the phase.

We see now in figure 4.12(a), how the theoretical $|R|$ decreases with frequency. In the higher frequency region, the experimentally measured reflection coefficient tends to be lower in magnitude than the theoretical value. This behaviour has been noted by a number of authors including Chung and Blaser [13] and Seybert and Ross [55]. The positive value for the theoretical resistive impedance shown in figure 4.12(b), demonstrates that sound is being dissipated.



(a) Reflection coefficient. Mag and Phase.

(b) Impedance. Real and imaginary.

FIGURE 4.12: Open duct of length L . Theory Vs Experimental. Theoretical - red, experimental - blue.

There is a slight off-set between the theoretical and experimental results which may be attributed to the finite flange of $0.012m$ on the experimental rig as opposed to the zero flange assumed in the theory. It has also been observed that the results vary dramatically with the temperature dependent sound speed according to equation (B.39). A sound speed of $344m/s$ was used in the above analysis assuming a temperature of just over $293K$. An accurate recording of the temperature in the duct should be taken for a more complete comparison.

From figure 4.12(b) we see that unlike the closed duct case of figure 4.10(b), due to the finite radiation resistance, the real part of the impedance is never zero, indeed it tends toward unity. As it is the normalised impedance which is being plotted unity translates as $\rho_0 c$ or the characteristic impedance z_c . This shows that in accordance with the falling off of reflection coefficient with frequency the duct is no longer able to form resonances and behaves, at high frequency, as if it were to be of infinite length or have an anechoic termination.

Referring to the reactance in figure 4.12(b), we see a repeated pattern where the reactance increases from negative to positive. This behaviour can be explained using equation (4.21). Like a mechanical oscillator where the spring force provides the dominant opposing force at low frequency to be followed by the inertial force at higher frequencies, with a Helmholtz resonator type system the compliance term dominates and is negative at low frequencies in equation (4.21) to be replaced by the positive inertance term at higher frequencies. The cycle repeats itself at resonances of the system of air of length L . The resonances are where the local resistance maxima are to be found.

$$Z_a = R_a + j(\omega M_a - \frac{1}{\omega C_a}) \quad (4.21)$$

4.5 Fan Installed (Not Rotating)

Sampling at 12.5kHz allows a frequency range of 0-6250Hz to be analysed. Figure 4.13 shows the SPL's of microphones 1,2,5,6,7 and the filtered source signal in dB for this frequency range. With excitation between 500Hz and 3000Hz little pressure at the microphones is measured outside this range. Figure 4.14 shows the same data between the range of 500-3000Hz only. With regard to figure 4.14, several phenomena can be observed.

Due to the presence of the fan, standing waves as a function of frequency are formed upstream of the fan. The reflection coefficient shown in figure 4.15(b), shows the magnitude of the reflected wave from the fan to be approximately half the incident for the excitation frequency range. The standing wave frequencies that might form in a closed or open-ended duct of length L have been discussed in sections 4.3 and 4.4. The fan end condition being a mix of open and closed will form standing waves in a similar fashion. These standing wave frequencies are seen as peaks in the SPLs of microphones 1 and 2 in figure 4.14.

In addition to the smaller peaks it can be seen that the SPL's rise and dip on a larger scale also. For microphone 1 we see dips at around 1kHz, 1.8kHz and 2.4kHz for example. An explanation for this can be given with the aid of figure 2.9. For a standing wave of a particular frequency, the microphone may be located near a node or antinode of the wave. If near an anti-node the SPL will be large whereas if near a node the SPL will be low. Theoretically if the microphone were to be located at the node it would not detect that frequency at all. However, due to the finite area of the diaphragm some energy would probably be measured. As the two microphones are located at different locations in the duct, the two SPLs differ from each other as a result of the fact that the microphones measure different amounts of energy for different standing wave frequencies.

With regard to figure 4.16(b), the magnitude of the reflection coefficient downstream can be seen to be less than 0.1 over the excitation frequency range. Thus, effectively no standing wave can be formed in the downstream section of the duct. However, the SPL's of microphones 5 and 6 are seen to be of the same form as those of microphones 1 and 2 and are approximately equal to each other.

It can therefore be deduced that the pressure measured in the downstream section is the propagated upstream incident pressure wave after any transmission loss through the fan has been taken into account. The difference between the upstream and downstream incident pressure waves is clearly accounted for in figure 4.21 by the transmission loss and it is seen in figure 4.19(b) and 4.20 how the SPL's of microphones 5 and 6 are equal to the downstream incident pressure wave. The transmission loss is calculated with the aid of equation (2.53).

The experimental reflection coefficient calculated downstream of the fan, compares very well with the theory of Gervais *et al* [23], as can be seen in figure 4.17. This demonstrates the successful account of reflections incorporated into the theory as opposed to the more simplified theory of section 3.2.1.

The SPL of microphone 7 in figure 4.14 is seen to be different in form to those of microphones 5 and 6. This is because the pressure field being emitted from the duct has been modified due to radiation. The raw signal from microphone 7, which is less sensitive than microphones 1, 2, 5 and 6, was magnified by a gain of 50dB at its amplifier in order to improve its signal to noise ratio. This explains why it has a higher SPL.

Above each of the spectra in figures 4.13 and 4.14 is the rms value as calculated from the square root of the area under the PSD between $0 - 6250Hz$. It was verified that this equaled the rms of the signal calculated in the time domain, which for zero mean would equal the standard deviation of the signal. The dB representation of this rms value is also shown at the top of the figures.

Figures 4.15(a) and 4.16(a) show the frequency response functions between microphones 1 and 2 and also 5 and 6. It was with these frequency response functions that the reflection coefficients were calculated in accordance with equation (2.45). The standing wave nature of the pressure field upstream is evident from the magnification and attenuation seen in the magnitude of the frequency response function. Downstream it can be seen clearly how the pressure wave is unidirectional with a constant magnitude and a increasing frequency dependent phase lag measured .

The impedance downstream, figure 4.18(b), is seen to be real and constant with a value of unity. As it is the normalised impedance that is plotted, using equation (2.51), the impedance is thus measured to be equal to the characteristic impedance for air in a duct of infinite length, ρc , as expressed in equation (2.50), which would be expected for an anechoic termination.

Figures 4.19 and 4.20 show how the incident and reflected spectra upstream and downstream of the fan compare and the spectra of the microphone signals that were used to calculate them, using equations (2.39) and (2.40). The subscripts u and d denote upstream and downstream respectively whereas the subscripts i and r indicate the incident and reflected components. With regard to the downstream signals first, the reflected signal is significantly lower than the incident; approximately $20dB$ lower over the frequency range of interest. However, it is not zero and the fact that it is of the same form as the incident wave shows that it is reflection, as opposed to sound originating from outside the termination, that contributes most to the wave travelling in the reflected direction. Being so low however, its influence is minimal and from figure 4.20 the incident pressure is seen to be

effectively equal to the pressure measured at both microphones 5 and 6.

Figure 4.22 shows two frequency response functions across the fan. For the frequency response function involving the source signal, figure 4.22(b), given that the source signal is flat for the excitation frequency range, the magnitude of the frequency response function is simply the amplitude of the pressure divided by a constant. The phase lag angle, from equation (B.38) can be seen to be of constant slope and to be greater between the source and G_{di} than between G_{ui} and G_{di} as the propagation time, from equation (B.40), would be greater due to the greater distance from the source. For the magnitude in figure 4.22(a), it is seen how there is a loss of energy across the fan for the full frequency range which is at its greatest at approximately $1.8kHz$. This is presumably due to viscous losses through the fan. The very same information is seen in figure 4.21.

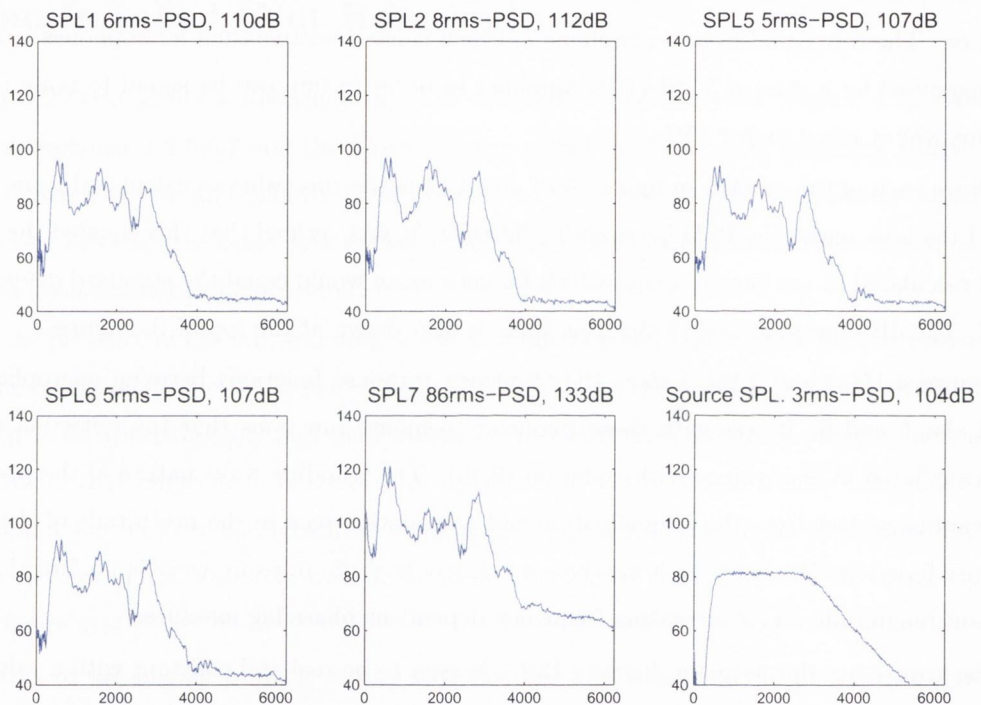


FIGURE 4.13: SPL of microphones 1,2,5,6, and 7 and source signal.

4.6 Fan Installed (Rotating)

For the second rig characterisation test, as described in 4.1, in addition to the same filtered broadband signal, the fan was turned on. The vane-axial fan has 8 rotor blades and 5 stator blades and produces a significant blade pass frequency at $8XRPS$. In addition to this frequency, acoustic energy can be measured at integer multiples of the BPF as discussed in section 2.5.2. As the tip velocity of the fan is subsonic, this tonal energy, measured at this distance from the fan, must be the result of rotor-stator

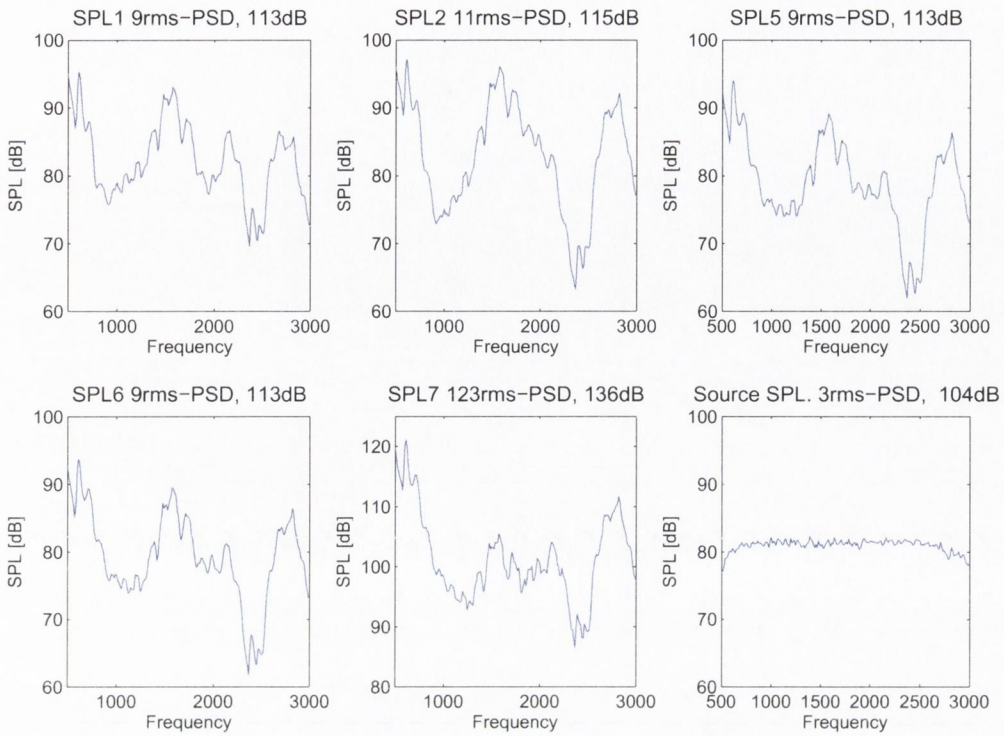
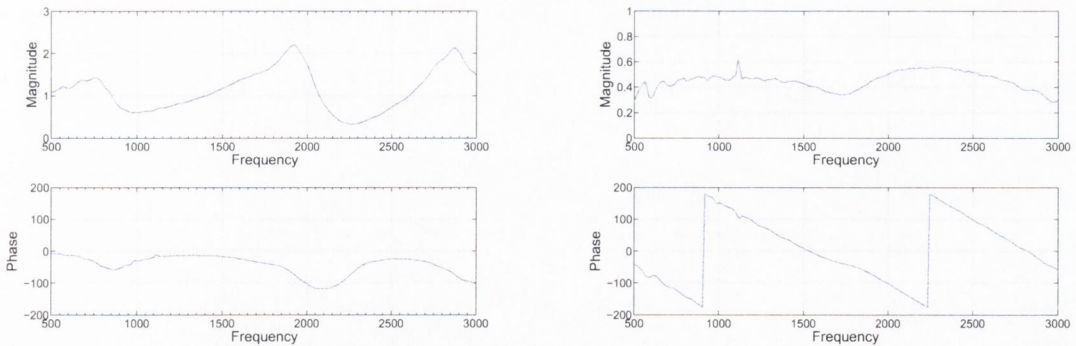
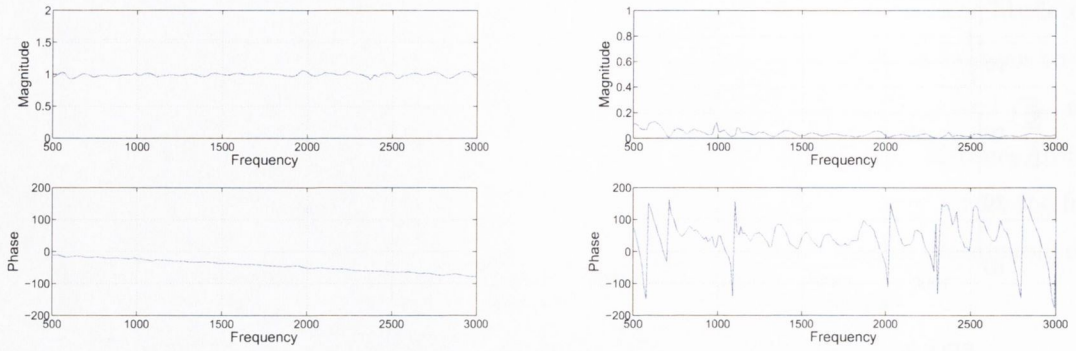


FIGURE 4.14: SPL of microphones 1,2,5,6, and 7 and source signal between 500Hz and 3000Hz



(a) Frequency response function between mics1 and 2 (b) Reflection coefficient using microphones 1 and 2. Reference plane at microphone 2.

FIGURE 4.15: Transfer Function and Reflection coefficient for microphones 1 and 2



(a) Frequency response function between microphones 5 and 6 (b) Reflection coefficient using microphones 5 and 6. Reference plane at microphone 6.

FIGURE 4.16: Transfer Function and Reflection coefficient for microphones 5 and 6

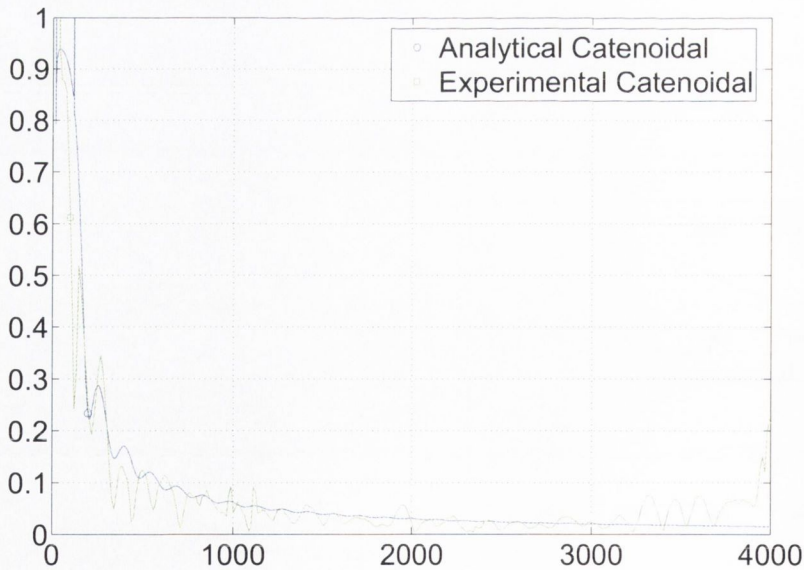
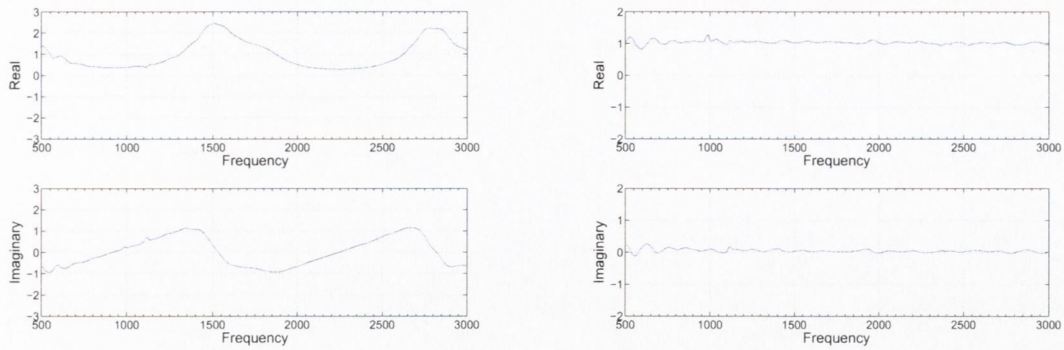
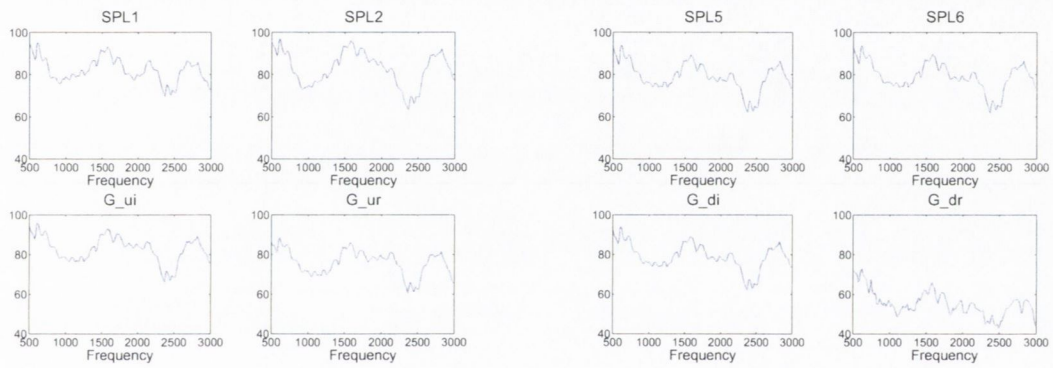


FIGURE 4.17: Experimental reflection coefficient versus the analytical solution of Gervais *et al* [23].



(a) Impedance using microphones 1 and 2. Reference plane at microphone 2. (b) Impedance using microphones 5 and 6. Reference plane at microphone 6

FIGURE 4.18: Impedance upstream and downstream of the fan. Fan not rotating.



(a) Incident and reflected SPLs upstream of fan with SPLs of microphones 1 and 2 (b) Incident and reflected SPLs downstream of fan with SPLs of microphones 5 and 6

FIGURE 4.19: Decomposed signals

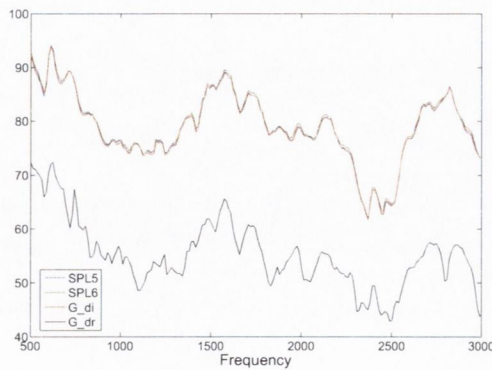
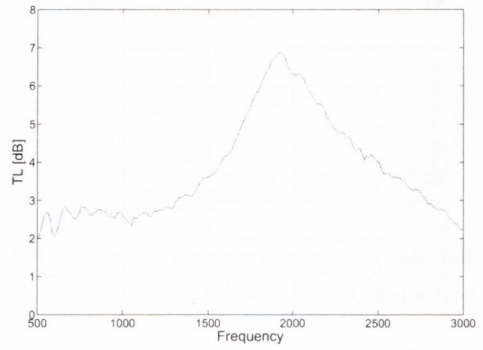
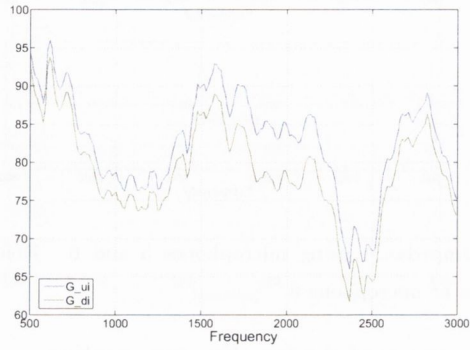


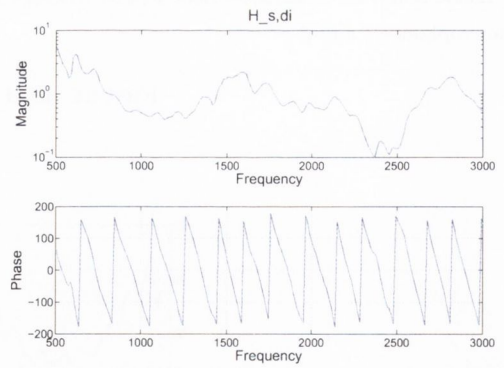
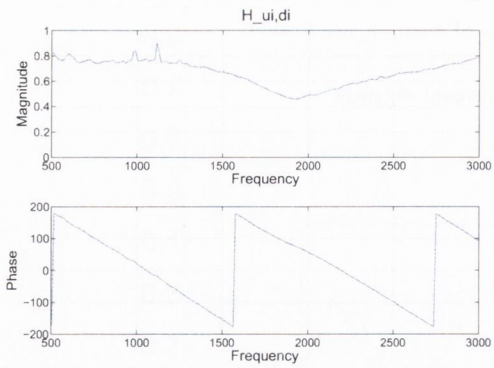
FIGURE 4.20: Incident and reflected SPLs downstream of fan with SPLs of microphones 5 and 6



(a) Comparison of incident signal upstream with incident signal downstream

(b) Transmission Loss across the fan using upstream incident and downstream incident

FIGURE 4.21: Incident losses across the fan



(a) Frequency response function between the incident wave upstream and the incident wave downstream

(b) Frequency response function between the source signal and the incident wave downstream

FIGURE 4.22: Magnitude and phase of frequency response functions

interaction. For the maximum attainable RPM of the fan, 17625rpm, a BPF of approx 2350Hz was measured.

The plots from the previous subsection are now presented again for this new test configuration to highlight to effect of the fan.

In figure 4.23 we see two principle differences to the no fan case. Firstly, there is now pressure measured above and below the excitation frequency range of 500-3000Hz. This is most likely due to the broad band flow noise. The sources here are turbulence at the intake of the pipe, turbulence in the pipe, turbulent flow noise over the microphone surfaces in the pipe which are not perfectly flush and turbulence caused by separation in the expansion. Excitation across the first cut-on frequency of $\approx 4kHz$ highlights a sharp rise as an additional acoustic mode is excited. This rise is typically found at each cut-on frequency. The second principle difference is the presence of a peak at the BPF and at its first harmonic at 4.7kHz. In figure 4.24 we see that the flow noise has raised the floor of the spectra, e.g., the lower values of approx 62dB for microphone 6 at 2.4kHz are now over 10dB higher. In figure 4.25(a) we see that, due to the additional acoustic sources, the pressure field in the duct has changed and that the frequency response function between microphones 5 and 6 differs from the no-fan case. This difference is particularly marked at the frequencies where the SPLs have changed the most from the no-fan case (refer to figure 4.24).

For the reflection coefficient downstream, we see that for some frequency ranges, there is greater reflection measured than for the no-fan case. This might either mean that the end condition is now more reflecting or that additional noise is being generated downstream of the reference plane. We see from figure 4.25(b), that while the expansion is doing a reasonable job at reducing expansion noise, the reflection coefficient is greater than 0.1 below 1500Hz and thus at first inspection could not be called anechoic below this frequency. These conclusions however, would be incorrect for frequencies where one microphone signal contained noise which was uncorrelated with the other microphone signal. When this noise exists, and is significantly large, it does not contribute to the relationship between the two pressure measurements in a linear, causal way, but simply serves to mask the frequency response function. It is this very fact that it is difficult to draw clear conclusions from this type of plot contaminated with flow noise that motivates signal enhancement techniques to be employed. These will be used in a later section to extract the signal coherent with the speaker to help determine how the end condition of a rotating fan differs from that of a non-rotating fan. It is flow noise difficulties such as these that no doubt prevented Johnston and Schmidt [32] from being conclusive in the study of acoustic reflection from an obstruction in a pipe with flow.

Another source of error in most of these plots is the assumption of plane wave propagation. This is a reasonable assumption for the no flow condition below the 1st cut-on frequency of 4kHz. However, for $M > 0$ this assumption becomes less valid. Johnston and Schmidt [32] state that the measuring locations should be situated far enough from any obstruction (in our case the fan) so that the near field effects can be neglected, i.e. a wavelength of the lowest frequency to be studied. For microphone

2, which is located only 0.1255m from the fan, this would mean that only frequencies above $2775Hz$ could be assumed to be plane. However, it would be hoped that the stator would help to reduce the higher order spinning modes and that other higher order modes would not be excited or would not propagate as far as the microphone locations. The higher order modes in the duct will be examined in more detail in chapter 6. As the admittance and impedance functions are calculated directly from the reflection coefficient, the possibility of uncorrelated noise contamination means that is difficult to draw conclusions from these plots without signal enhancement.

Coherence, as discussed in appendix B.13, is a good indicator to detect if an uncorrelated input is being measured at the input and/or output. In figure 4.26 we see a significant drop in the coherence function when the fan is turned on. By referring to figure 4.24, we see how the coherence drops most for the frequencies where the SPLs measured with the fan differ the greatest from the no-fan case. This seems to imply that the additional noise generated when the fan is turned on is flow noise and being distributed in nature is uncorrelated from one location to the next. Therefore the flow noise measured by one microphone would be uncorrelated with the flow noise measured at the next, resulting in the drop in coherence. The exception to this in figure 4.26 is for the BPF. Although this is an additional noise source it is far greater than any other source at that frequency, it propagates up the pipe and being measured by all microphones results in a high coherence at this frequency.

The coherences measured between the source and the microphones, as seen in figure 4.27, are seen to drop for frequencies where the microphone SPL measurement in figure 4.24 differs most from the no-fan case. This is in contrast to figure 4.26 where it is the combined differences between the two microphones which cause the drop. The exception here again is the BPF where there is an extremely low coherence this time due to the fact that there is no measurement of this in the source signal and thus is completely uncorrelated with it.

Figure 4.28 shows coherences using the decomposed signals. Each stage of the progression is shown, *viz.*, from source to upstream incident, from upstream incident to downstream incident and downstream incident to the near-field. Also shown is the coherence between the upstream incident signal and the near-field. Taking the first coherence, $C_{s,ui}$, we see a drop, as expected, at the BPF due to the presence of the signal in the duct which is not measured in the source signal. Apart from that drop there is only a small drop in coherence at around $1kHz$ and this is due to the fact that the incident signal changes little when the fan is turned on except in this frequency range, refer to figure 4.32 for verification of this. The second plot, $C_{ui,di}$, sees more extensive loss in coherence. This is due primarily to the uncorrelated noise appearing in the downstream incident measurement as can be seen in figure 4.32. At the BPF this time however, the coherence is high as both measurements are taken in the duct. Only a loss in coherence is seen in the lower frequency ranges in the third plot of figure 4.28. This would seem to imply that there is more than simply linear radiation of the downstream incident signal into the near field but that there is also an uncorrelated noise being generated between the downstream incident reference plane and the position of microphone 5, most likely expansion noise.

By reference to figure 4.25(b) it is seen that the downstream reflection coefficient is greater than zero for the same frequency range below $1.5kHz$. This latter plot, with an observation of G_{dr} of figure 4.30(b), supports this theory. Again there is high coherence at the BPF. The fourth plot in this figure is similar to $C_{ui,di}$ as would be expected although not as expected the coherence is actually higher below $1kHz$.

Another set of coherences in figure 4.29 are presented to highlight similarities between the *source* signal and the *ui* signal when looking at coherences with either the *di* signal or the near field microphone 7 signal. Apart from at the BPF they are very similar. This is significant as it demonstrates that the upstream incident signal can be used for signal conditioning when a record of the source is unattainable. The coherence drops generally in the frequency ranges where the broad band extraneous noise masks the *di* or microphone 7 signal the most. When using the *ui* signal as opposed to the *source* signal, the main difference (apart from the BPF) is that the coherence is slightly higher at the standing wave frequencies due to their presence in both the *ui* and *di* signals which serves to amplify their contribution. Conversely, the coherence is lower at the frequencies that are not standing wave frequencies.

The coherences with respect to the near field microphone are lower for the full frequency range whether the fan is turned on or not. This is certainly due to the fact that this microphone, which is not insulated from background lab noise, being located outside the duct, is measuring more than just the radiated sound from the duct. Ideally the rig would be located in a silent anechoic chamber insulated from external noise. As is shown in figure 3.2, an attempt was made to isolate microphone 7 from any path to the speaker other than the one down the duct by building a sound absorbing box around the duct inlet.

Figures 4.30 and 4.31 show the signals at the four microphone positions along with the upstream and downstream incident and reflected signals and how they relate to one another. The most striking observation is how much greater the *dr* spectrum is now, particularly at the lower frequencies. As has been mentioned already, this is seen in the reflection coefficient too when the magnitude of the reflected signal attains a similar order of magnitude to the incident magnitude. An interesting result of this is how the *dr* signal is actually greater than either the microphone 5 or microphone 6 SPLs for frequencies below approx. $1250Hz$. An explanation as to how this is possible has already been given in section 4.5.

Figure 4.32 shows the decomposed signals with and without the influence of the fan. It is interesting to note how the *ui* signal is little effected except at the lower SPL levels and the weak presence of the BPF. This result may be partly due to efforts made to create a partially anechoic termination at the upstream end, see figure 3.2. Thus, since it seems that little additional noise is created upstream and combined with the fact that the the microphones are located some distance from the upstream termination, $\approx 1m$, little of the additional noise created downstream of this reference plane seems to be reflected back down the pipe from the upstream end. Another conclusion to be drawn from

this plot is how it seems that there is little noise created locally from flow around the microphones protruding into the duct. Broad band noise and harmonic fan noise is measured closer to the fan, however, as seen in the ur and di signals. The dr signal shows the expansion noise as previously discussed.

Figure 4.33 shows how additional noise created between the upstream and downstream reference planes results in a negative transmission loss proving a useful tool in noise source detection. The frequency response function between the ui signal and the di signal is shown in figure 4.34(a). A deviation from the no-fan case can result due to at least two circumstances. The first is if the single-input/single-output model is violated either through extraneous noise measured at one of the microphones which is uncorrelated with the measurements at the other microphones or through a non-linearity. The second arises if the frequency response function changes as a result of the rotating fan or the flow, for example. In order to identify this latter phenomenon, if present, signal enhancement techniques will be employed to remove the extraneous noise or additional inputs.

The frequency response function, plotted in 4.34(a), was calculated using the first of the two formulations given in equation (B.34). This is the optimum form for the case where more extraneous noise is present in the output than input, which seems likely when considering the differences between di in figure 4.32 with the fan compared to it when the fan is not turned on. We see the greatest difference in the frequency response function at the BPF which is an additional input created between the two measurement planes. The other differences are seen in the frequency ranges where the signals are low in the ui and di signals, and would be thus most susceptible to noise pollution by the extraneous noise. The frequency response function across the fan and other formulations of it, will be discussed further in section 5.6.2.

Figure 4.34(b) shows the frequency response function with the di signal using the *source* signal instead of the ui signal. This TF differs little from the no-fan case due to effective signal enhancement that takes place due to the employment of the cross spectra using the source signal. As the source signal measurement is unchanged when the fan is turned on, the cross spectra effectively removes the uncorrelated part from the di signal.

Figure 4.35 shows the unwrapped phases from figure 4.34(b) to highlight the effect of turning on the fan and thus introducing a convection velocity in addition to the sound speed propagation velocity. By calculating the slope of figure 4.36(a) a distance d can be calculated using equation (B.43) with the assumption of $c = 344m/s$. (c could be calculated more accurately with a thermometer and a barometer). The distance, d , needs to be calculated first as it is difficult to determine exactly where the speaker begins. Using equation (B.42) the convection velocity is calculated to be approx. $8.5m/s$. A measurement was taken with a pitot tube on the centreline of the duct and gave $12m/s$. The discrepancy here is due to the the microphones being located flush to the duct.

Two additional comments can be made about figure 4.35. The first is that neither curve is straight nor do they pass through zero although the curves tend in that direction. The second is that as the

form of the fan-on phase curve is similar to the fan-off curve one might deduce that the higher modes are having little significance and that the acoustic waves are planar.

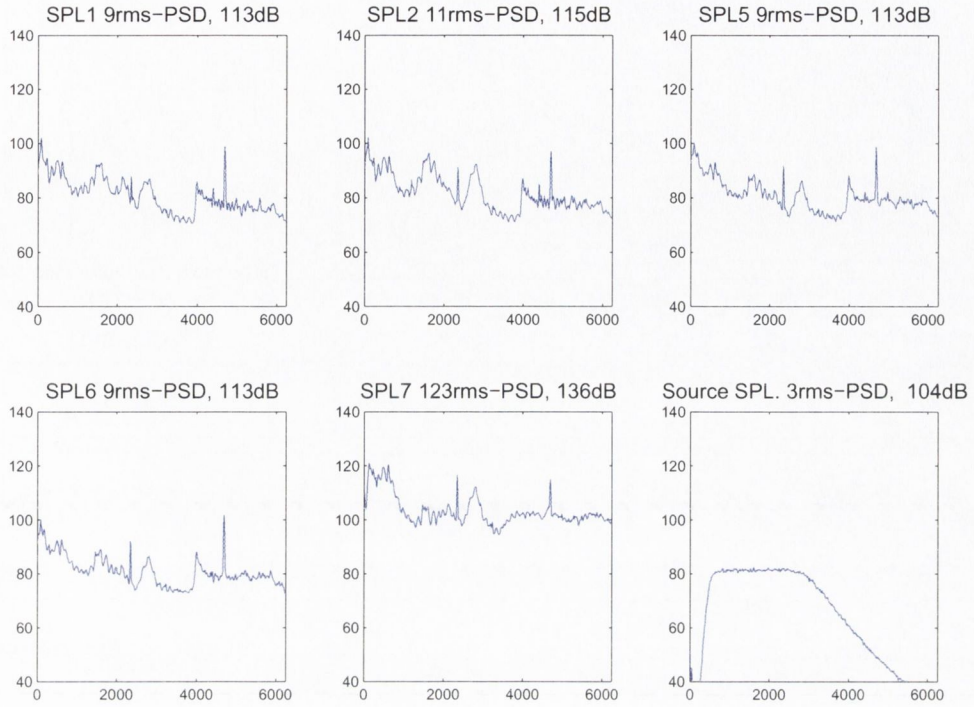


FIGURE 4.23: SPL of microphones 1,2,5,6, and 7 and source signal. With fan, BPF=2350Hz.

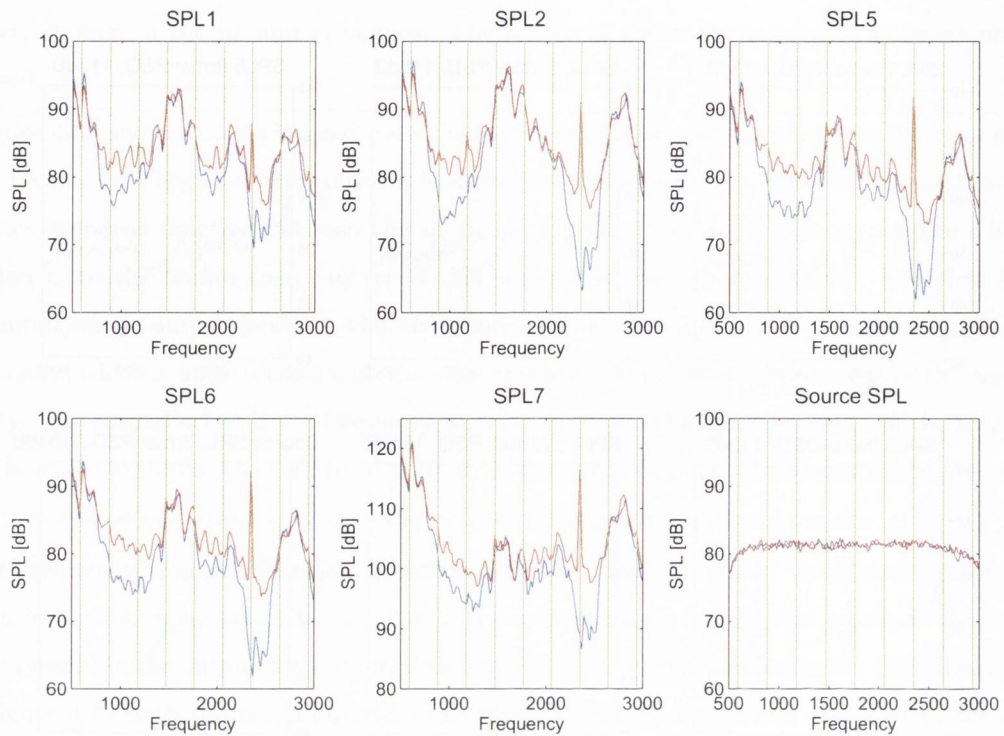
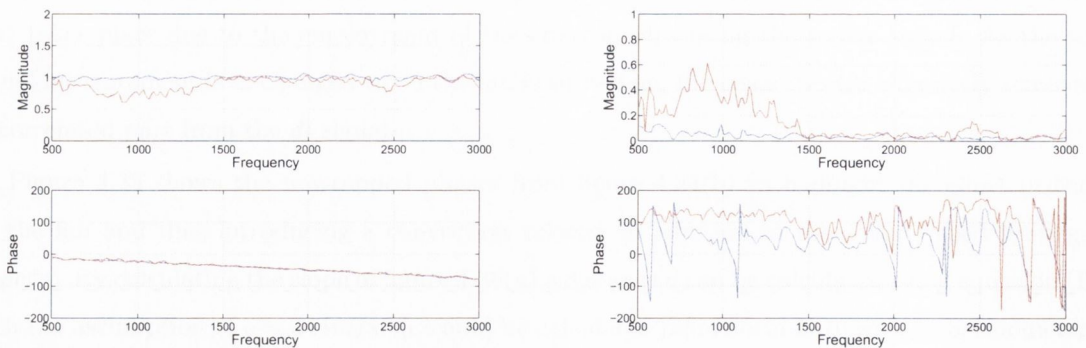


FIGURE 4.24: SPL of microphones 1,2,5,6, and 7 and source signal. Close up between 500Hz and 3000Hz. Without (blue) and with (red) fan, BPF=2350Hz.



(a) Frequency response function between microphones 5 and 6 (b) Reflection coefficient using microphones 5 and 6. Reference plane at microphone 6.

FIGURE 4.25: Frequency Response Function and Reflection Coefficient for microphones 5 and 6. Without (blue) and with (red) fan, BPF=2350Hz.

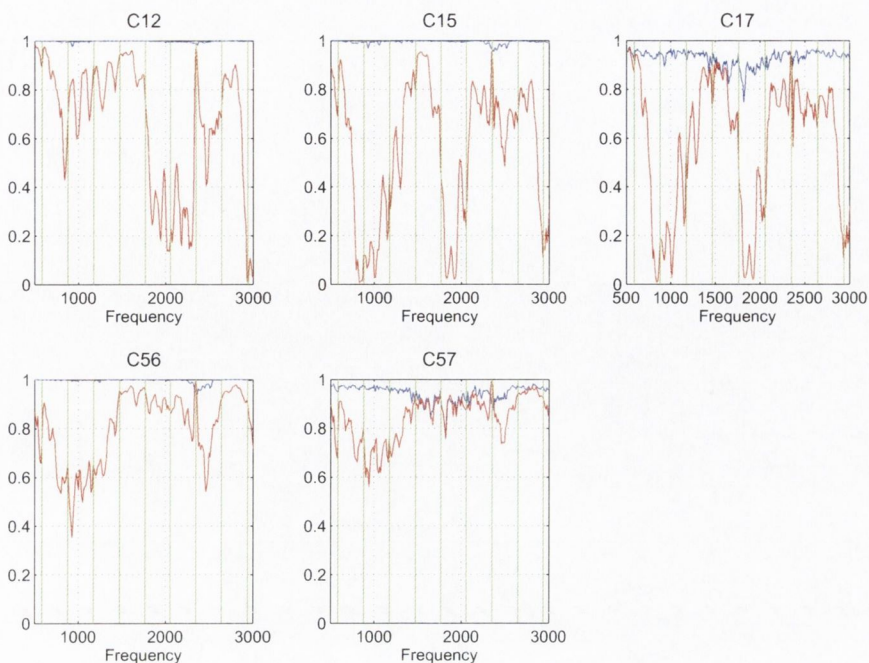


FIGURE 4.26: Coherence between some of the microphones. Without (blue) and with (red) fan, BPF=2350Hz.

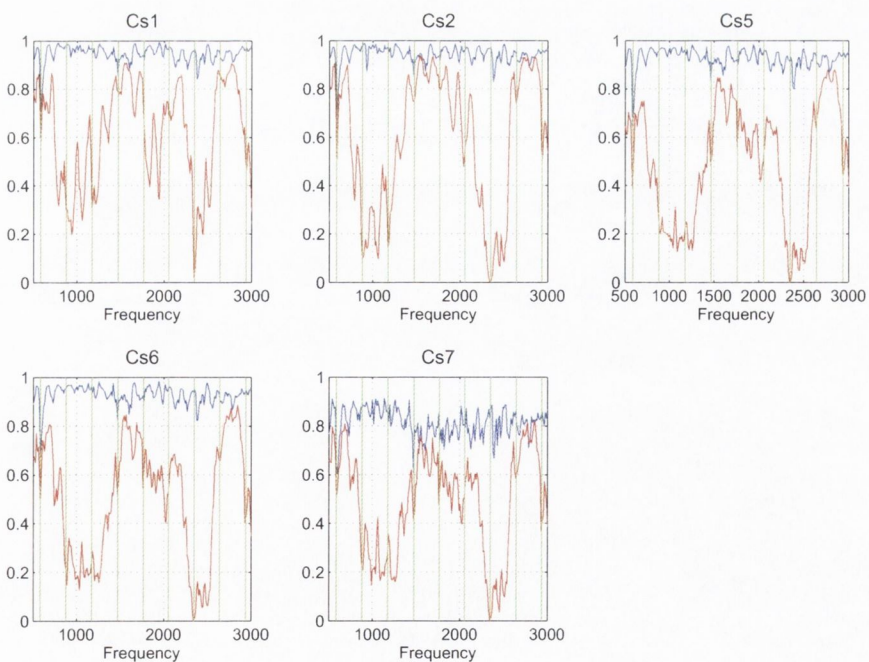


FIGURE 4.27: Coherence between the source and some of the microphones. Without (blue) and with (red) fan, BPF=2350Hz.

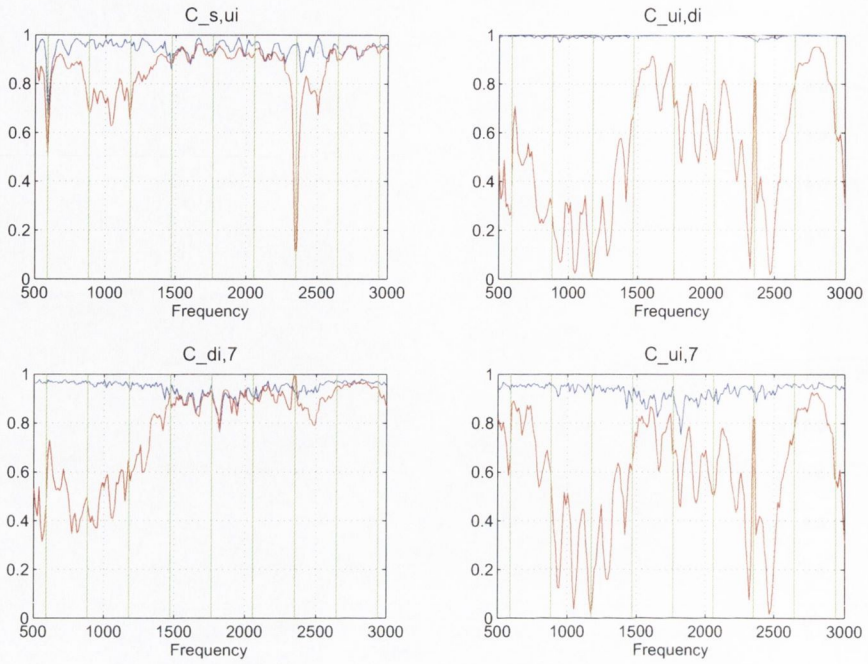


FIGURE 4.28: Coherence between some of the decomposed signals. Without (blue) and with (red) fan, BPF=2350Hz.

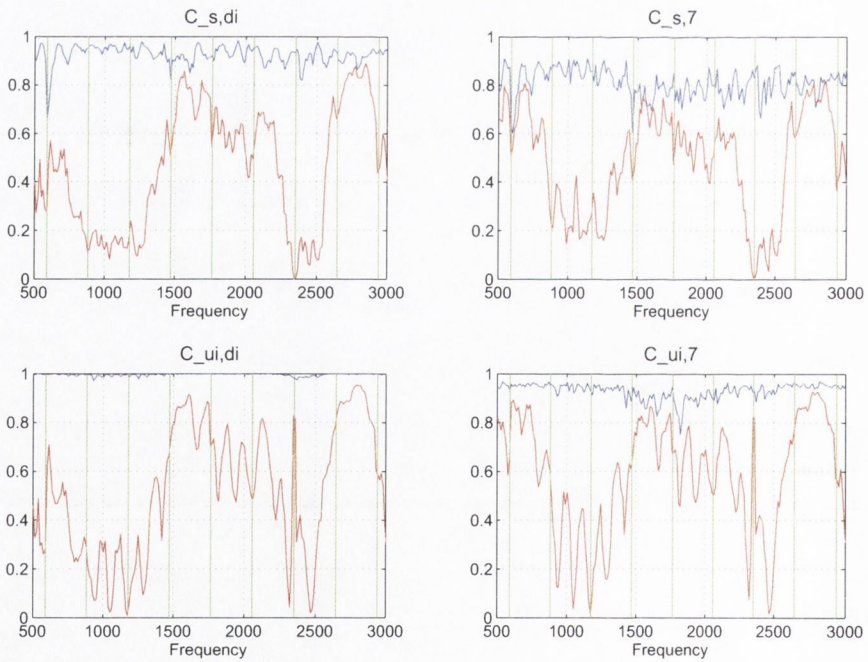
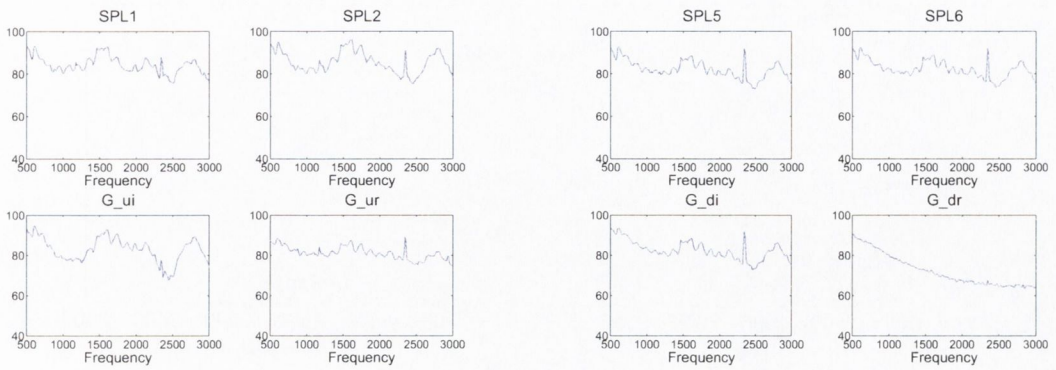


FIGURE 4.29: Comparison between source and upstream incident coherence with downstream incident and near-field coherence. Without (blue) and with (red) fan, BPF=2350Hz.



(a) Incident and reflected SPLs upstream of fan with SPLs of microphones 1 and 2
 (b) Incident and reflected SPLs downstream of fan with SPLs of microphones 5 and 6

FIGURE 4.30: Decomposed signals. With fan, BPF=2350Hz.

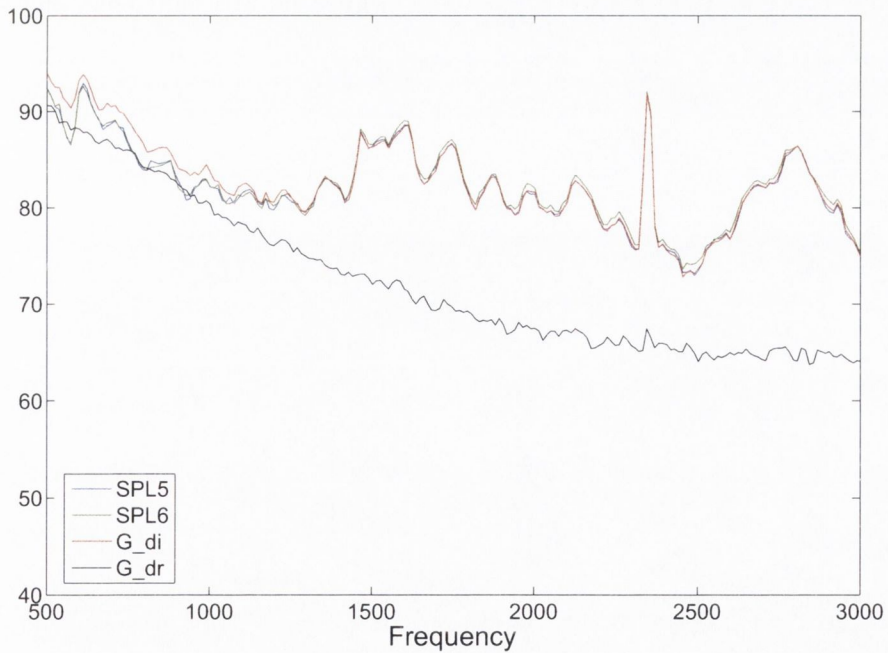


FIGURE 4.31: Incident and reflected SPLs downstream of fan with SPLs of microphones 5 and 6. With fan, BPF=2350Hz.

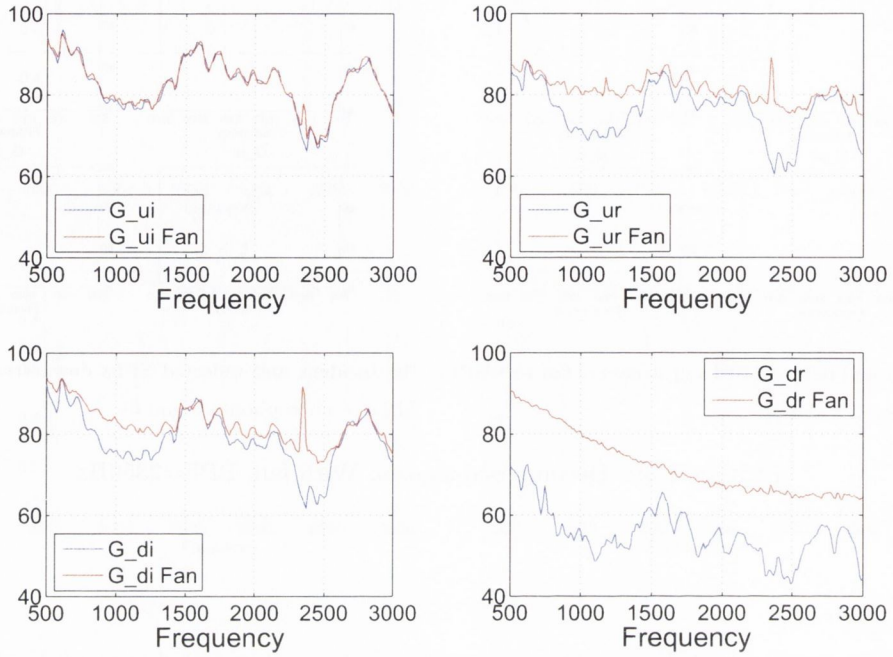
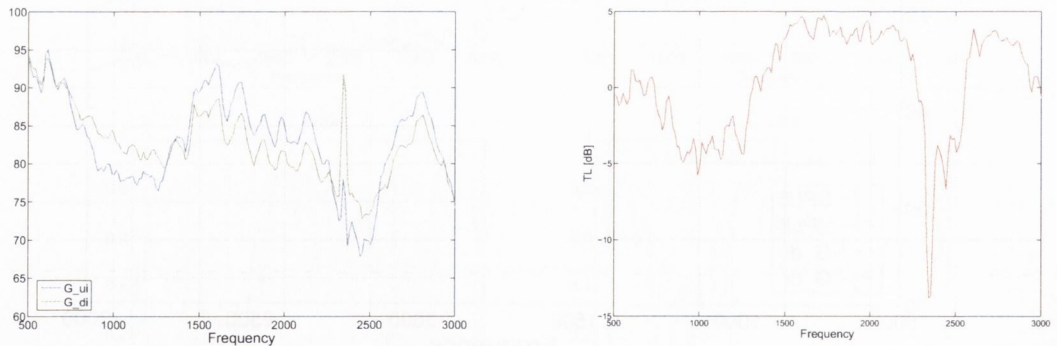
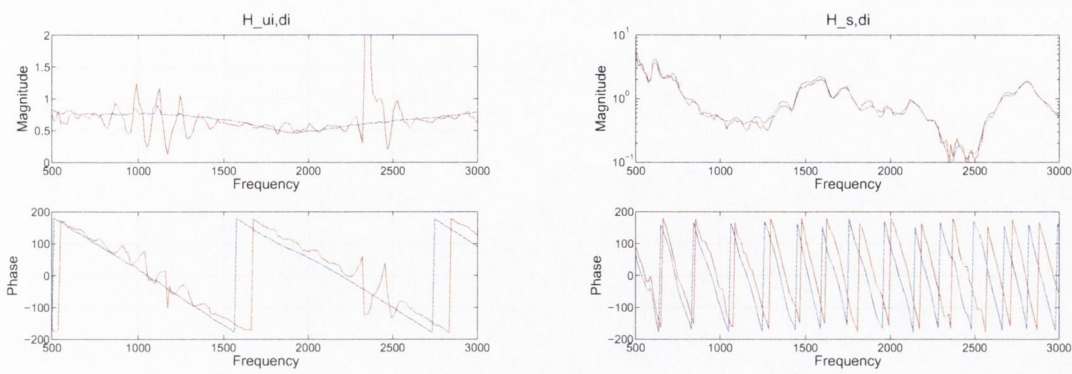


FIGURE 4.32: Decomposed signals upstream and downstream. Without (blue) and with (red) fan, BPF=2350Hz.



(a) Comparison of incident signal upstream with incident signal downstream. Without and with fan, BPF=2350Hz. (b) Transmission Loss across the fan using upstream incident and downstream incident. With fan, BPF=2350Hz.

FIGURE 4.33: Incident losses across the fan. With fan, BPF=2350Hz.



(a) Frequency response function between the incident wave upstream and the incident wave downstream (b) Frequency response function between the source signal and the incident wave downstream

FIGURE 4.34: Magnitude and phase of frequency response functions. Without (blue) and with (red) fan, BPF=2350Hz.

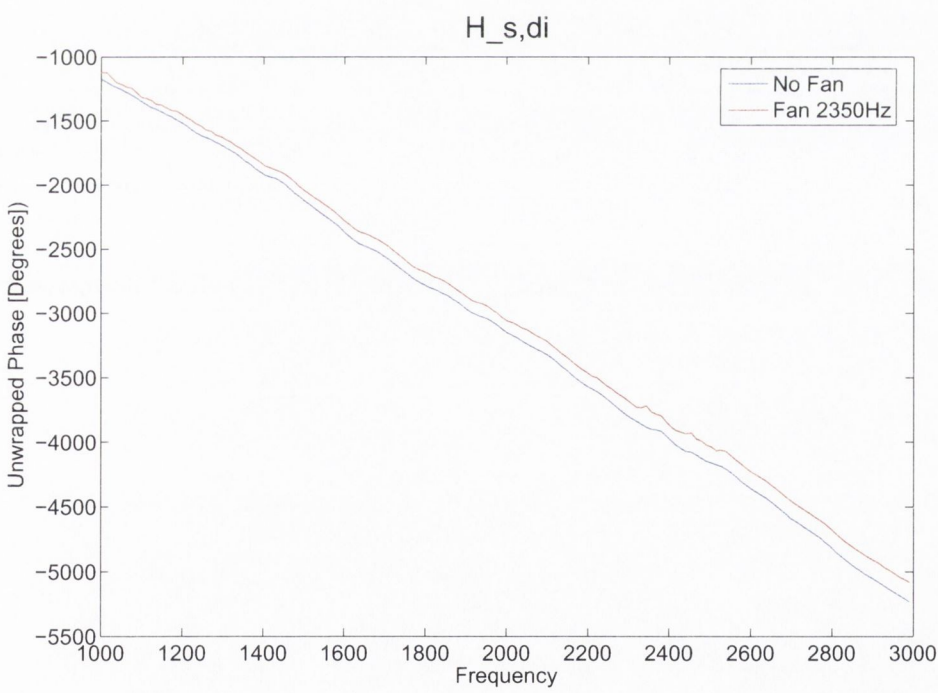
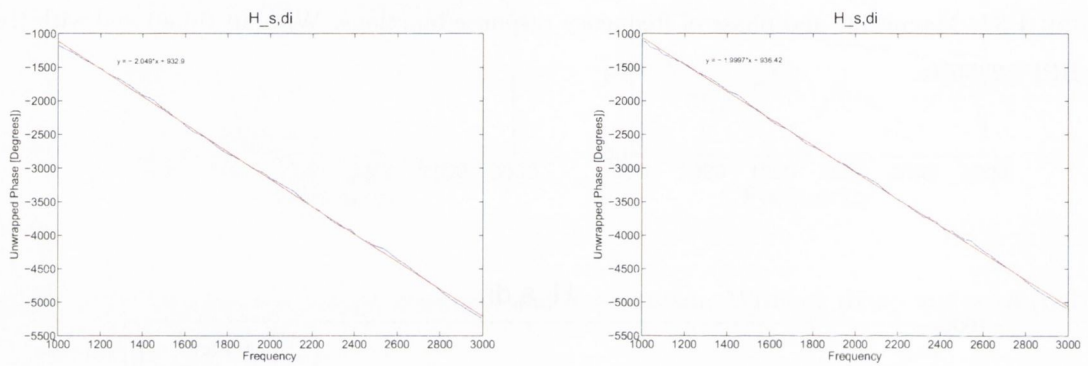


FIGURE 4.35: Effect of convection velocity on phase between the source and the downstream incident signal. Without and with fan, BPF=2350Hz. Convection velocity calculated to be 8.48m/s.



(a) Phase between the source and the downstream incident signal with no fan. Slope=2.049.

(b) Phase between the source and the downstream incident signal. Slope=1.9997. With fan turned on, BPF=2350Hz.

FIGURE 4.36: Effect of convection velocity on phase between the source and the downstream incident signal.

Chapter 5

Source Identification

5.1 Introduction

An acoustic measurement of a system of interest will most often be the summation of a number of separate acoustic sources along with some extraneous noise. For the case where it is not possible to turn individual sources off without effecting the behaviour of the others, the challenge

is to decompose the measurement signal into its constituent parts. For acoustic sources that are considered to be stationary random processes with zero mean and where systems are constant-parameter linear systems, figure 5.1, a multiple-input/single-output model, can be used to represent the system. The extraneous noise term, $n(t)$, accommodates all deviations from the model, such as acoustic sources greater than M which are unaccounted for, non-linear operations, non-stationary effects, acquisition, instru-

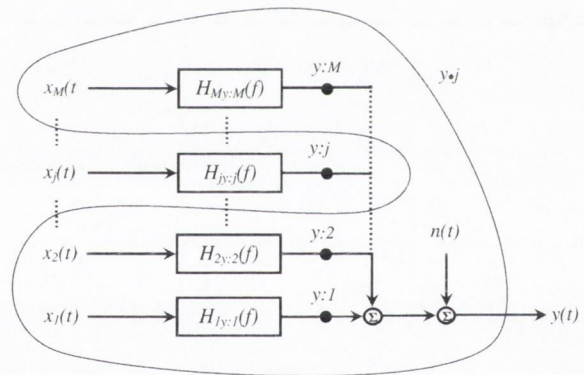


FIGURE 5.1: Multiple Source Acoustic Measurement

ment and mathematical noise along with unsteady pressure fluctuations local to the sensor, such as flow or hydrodynamic noise.

5.2 Identification Techniques

In real situations extraneous noise may be measured at the input and/or output of the system. Figure 5.2 shows the general model where $u(t)$ passes through the system to produce the true output $v(t)$. $m(t)$ and $n(t)$ represent the extraneous noise measured within $x(t)$ and $y(t)$. The *coherence function*,

which is the principle tool used in these techniques, is defined in section B.13.

Four techniques of source identification are examined in this section and the performance of each evaluated with experimental data. The procedures are all frequency domain methods and depend to some extent on the coherence function. The Coherent Output Spectrum (COS) technique, reported by Halvorsen and Bendat [25], requires a measure of at least one input and one output irrespective of the number of inputs. The Signal Enhancement(SE) technique, developed by Chung [11], requires three output measurements for the identification of a single unmeasured source. The Conditional Spectral Analysis (CSA) technique, proposed by Hsu and Ahuja [29], is a combination of these, where one of two inputs is monitored with three output measurements. The final technique considered is applicable to a system which contains any number of inputs. For this, no input measure is required and the number of output measurements is a function of the number of inputs, as reported by Minami and Ahuja [44]. A series of tests have been conducted to examine the efficacy of each of the procedures for specific applications.

5.2.1 Coherent Output Spectrum

A particular case of interest is where there is no input noise and the output noise is uncorrelated with both the input and output measurements, *viz.* $x(t) = u(t)$, $y(t) = v(t) + n(t)$ and $G_{xn} = G_{vn} = 0$. Given these conditions, the following expressions can be expressed:

$$G_{vv} = \frac{|G_{xv}|^2}{G_{xx}} = \frac{|G_{xy}|^2}{G_{xx}} = G_{yy}\gamma_{xy}^2 \quad (5.1)$$

$$G_{nn} = G_{yy} - \frac{|G_{xy}|^2}{G_{xx}} = G_{yy}(1 - \gamma_{xy}^2) \quad (5.2)$$

The product $G_{yy}\gamma_{xy}^2$, as discussed by Halvorsen and Bendat [25], is called the *coherent output spectrum* and $G_{yy}(1 - \gamma_{xy}^2)$ is termed the *noise output spectrum*. This is a highly significant result as we see that the unmeasurable component of y which is attributable to the input x can be determined from the measured records. We can see, as presented graphically in figure 5.1, that the coherent output spectrum decomposes the output into one part correlated with the input, and a second uncorrelated with the input, *viz.*, $y(t) = y : j(t) + y \cdot j(t)$.

The principle limitation of the COS technique is that a measure of one source of interest alone, *i.e.* a source which is uncorrelated with other inputs to the output measurement, may be difficult to obtain and that it in turn may also contain extraneous noise. When this is the case, the calculated coherent output spectrum $G_{v'v'}$ may be significantly less than the actual G_{vv} as illustrated in equation (5.3).

$$G_{v'v'} = \gamma_{x'y}^2 G_{yy} = G_{vv} \frac{G_{xx}}{G_{xx} + G_{mm}} \leq G_{vv} \quad (5.3)$$

The techniques of Karchmer in [38] and [36] each use the *COS* technique to measure the core noise contribution of a gas turbine or aircraft engine to a farfield measurement. This ability to measure the core noise continues to receive attention because, although the core noise is typically a less significant engine acoustic source, it sets an acoustic threshold below which the engine noise may not pass despite the large reduction in jet and fan noise in recent years. In addition, the current trend towards high-bypass engines and low Nox combustors will result in the core noise becoming a more significant source which will need to be measured and suppressed.

5.2.2 Signal Enhancement

As shown in equation (5.3), an input measurement which contains noise will result in an erroneously low coherent output spectrum. If the coherence between the input and output is high, one may be confident in the calculated COS. However, if the coherence is low, then it is difficult to establish whether this is due to noise in the output measurement only or whether there is noise present in the input also. Chung [11] developed a technique which can accommodate for the situation as seen in the model in figure 5.2 if at least three output measurements are available. If three measurements each contain the same correlated source, a new model may be depicted, as in figure 5.3.

With regard to figure 5.3, Chung [11] and Bendat and Piersol [7] demonstrate that the contribution of the input to each of the outputs can be calculated using only the three output measurements. For G_{y_2} , for example, the following can be derived:

$$G_{y_2:x} = \frac{|\gamma_{y_1 y_2}| |\gamma_{y_2 y_3}|}{|\gamma_{y_1 y_3}|} G_{y_2 y_2} = \frac{|G_{y_1 y_2}| |G_{y_2 y_3}|}{|G_{y_1 y_3}|} \tag{5.4}$$

The noise is calculated through subtraction from the total measurement. A typical application of this technique is to remove self-induced flow noise from a microphone measurement. Stoker *et al* [60] applied this technique for separating wind-tunnel background and wind noise from measurements made in the interior of an automobile test in a wind-tunnel.

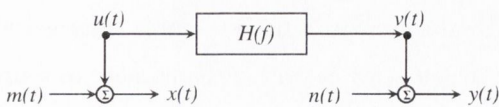


FIGURE 5.2: Input/Output Relationship with Noise

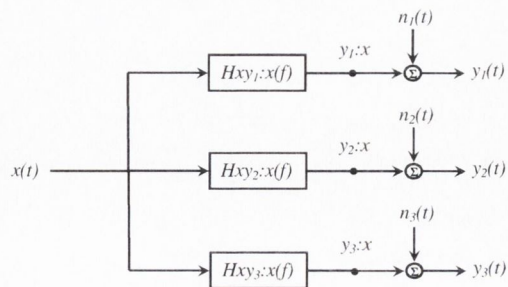


FIGURE 5.3: Signal Enhancement Model

5.2.3 Conditional Spectral Analysis

One of the limitations of the SE technique is that for measurement locations within the same pressure field, the technique may be applied only when there is a single correlated source between the records. Minami and Ahuja [44] discuss the errors resulting from using the Signal Enhancement technique when two sources, as opposed to only one source, are buried within extraneous noise. For the situation where there are only two correlated sources, and a measure of one of them is attainable, the COS and the SE techniques may be used in conjunction with each other and with conditional spectral analysis to successfully identify both sources and the extraneous noise. This approach is presented by Hsu and Ahuja [29].

The problem case is illustrated in figure 5.4(a). The first stage consists of separating out the part correlated with the measurable source, using the COS technique, and thus identifies its contribution. The second stage uses a partial coherence form of the SE technique on the residual to remove the extraneous noise, see figure 5.4(b). A measure of at least one of only two sources and three output measurements are required for this technique.

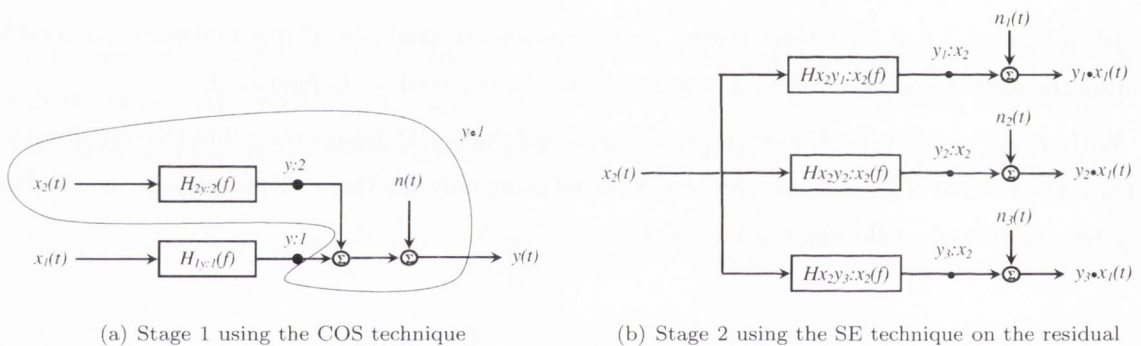


FIGURE 5.4: Conditional Spectral Analysis Technique

5.2.4 System of Non-Linear Equations

The techniques discussed above set out how up to two distinct sources can be identified from within a measurement containing them and uncorrelated noise. However, a measure of at least one of the sources, which itself may or may not contain further uncorrelated noise, is necessary when more than one source is present. Minami and Ahuja [44] report a technique where an unlimited number of uncorrelated noise sources can be identified from within extraneous noise when no source is measurable: only output measurements are required, the number of which is a function of the number of sources. The method consists of defining relationships between the various contributions at each microphone and then solving numerically the subsequent system of non-linear equations for the unknowns of interest. *Matlab's fsolve* function, from its *Optimisation Toolbox*, was used to solve the system of non-linear equations. The function was evoked as a function of frequency.

5.2.5 The Two Test Procedure

The limitation of the SE technique is that only one correlated source between the measurements may be present. For the Non-Linear technique, in principle, any number of sources can be present. However, an initial decision has to be made as to the number in order to formulate the necessary system of equations needed for the identification. A simple procedure, as reported by Bennett and Fitzpatrick [8], is presented here which can be used to verify the number of sources assumed. The procedure, which will be called “The Two Test Procedure”, entails performing an identification with three microphones, $M1$, $M2$ and $M3$ and then performing a second identification where two of the microphones are re-used in conjunction with a fourth microphone located elsewhere, i.e. $M1$, $M2$ and $M4$. For frequency ranges where the identifications lead to similar results for one of the common microphones, it can be deduced that there is only one significant source. If the results differ however, then there must be other significant sources present in that range.

5.3 Experimental Setup

In order to investigate the performance of these four existing techniques and this new procedure, experiments were carried out using real acoustic data acquired from microphones in an acoustic field where the noise sources were small speakers.

The objective of the techniques was to identify the spectra of the individual sources measured at each microphone location in the presence of extraneous noise and/or other source fields. In order to have a “solution” against which the performance could be evaluated, a measurement at the microphones of each source in turn, with the other sources turned off, was recorded.

A schematic of the geometric layout of the experiment is shown in figure 5.5. Four micro-

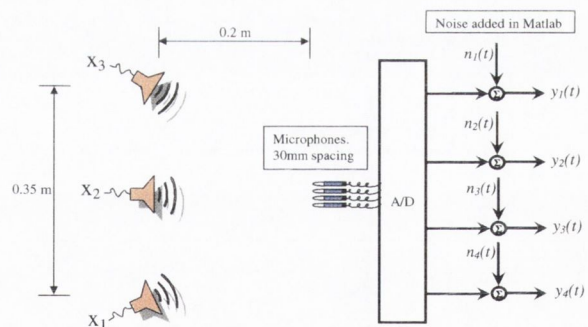


FIGURE 5.5: Schematic of the Test Set-up

phones were used in conjunction with three speakers. The microphones and speakers were all located close together, with the microphones mounted directly on the ground, hence reducing reflections from it, in order to ensure coherences close to unity between the microphones for the individual sources.

The extraneous noise terms were incorporated by adding different random noise to each of the measured signals after acquisition. The addition of the noise at the software stage helped ensure that it was uncorrelated between the signals. The coherences between the various noise signals generated were verified to be close to zero.

In order to evaluate the performance of the techniques over a wide frequency range the speakers were excited with broadband noise. Three separate noise generators, band passed [250Hz-8kHz],

ensured three completely uncorrelated source signals. In each of the tests, an acquisition of the voltage feeding the speakers was taken. These readings, x_1 , x_2 and x_3 represent a pure measurement of the acoustic source.

Data acquisition parameters: For each of the channels, a sample rate of 12.5kHz was used to acquire 20 seconds worth of data. For averaging, a block length of 1024 points (bandwidth of 12.2Hz) was used with a 50% overlap and a hanning window.

5.4 Experimental Results

Figure 5.6 shows a sample single source model for speaker x_1 only, whereas figure 5.7 depicts a model where two speakers both contribute to the pressure field. These set-ups will be referred to as Test Case 1 and Test Case 2. Some sample auto-spectra (PSD's) are given for microphone 2 in figure 5.8. In each of the three plots an additional speaker is turned on. After each acquisition, random noise (shown in green) was added to the signal measured by the microphone. Thus, the black plot is the “total” signal y_2 used in the techniques. The pre-recorded individual speaker measurements are superimposed onto the plots to illustrate their contribution to the total signal. It is these spectra that the techniques, operating on only the measured spectra plus noise, attempt to identify.

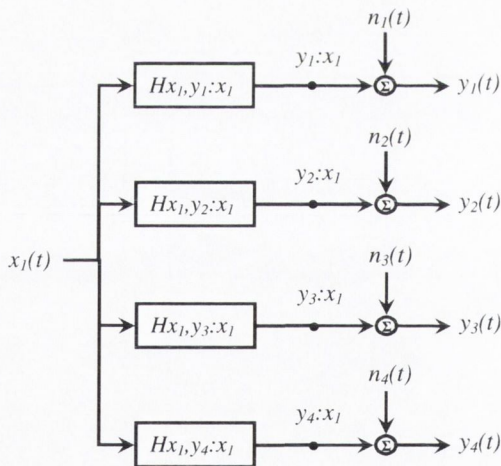


FIGURE 5.6: Test Case 1

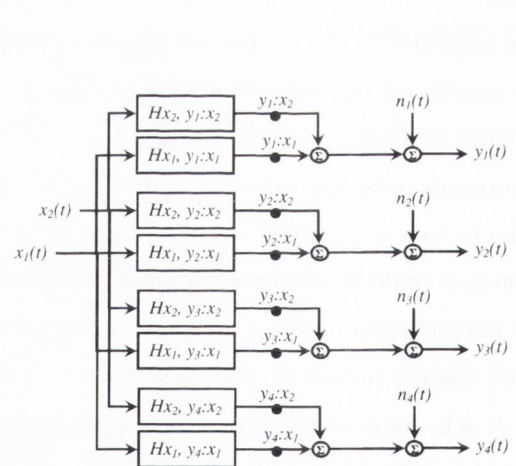


FIGURE 5.7: Test Case 2

Results are presented next, in figure 5.9, which demonstrate the performance of the COS technique for Test Cases 1 and 2. The total signal, Gy_2 , is used in conjunction with the x_1 signal and equations 5.1 and 5.2 to separate the part correlated with x_1 from the part uncorrelated with it. The overlined quantities in the plots are the identified contributions.

Figure 5.11(a) presents results for y_2 for both the SE and Non-Linear techniques for Test Case 1 using microphones $M1$, $M2$ and $M3$ initially and then $M1$, $M2$ and $M4$ in order to illustrate the “Two Test Procedure”. Figure 5.11(b) shows the same analysis for Test Case 2.

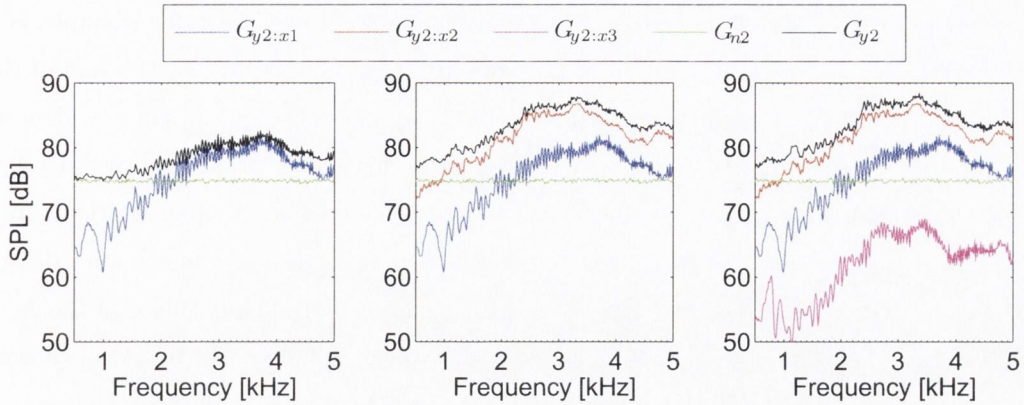


FIGURE 5.8: SPL's at Microphone 2 for 1, 2 and 3 Sources.

Hsu and Ahuja [29] present a very useful variation of the CSA technique where a formulation allows for noise in the source measurement. The block diagram for this model is given in figure 5.12(a). The assumption here is that the source measurements may contain noise but that it must be uncorrelated with all other measurement noise and inputs. Two such measurements are required. Results for the CSA technique and its variation are presented in figure 5.10.

5.5 Evaluation of Techniques

The ability of the COS technique to successfully identify a source buried within extraneous noise and/or other sources has been demonstrated in figure 5.9. A direct measure of the source is required. As discussed above, when a pure measurement of the object source is not possible the COS technique will give inaccurate results. Instead the SE or Non-linear techniques can be used for a single source situation. Both techniques perform well, accurately identifying the source and noise contributions to the measurement when no measure of the source is available, see figure 5.11(a). The limitation of the SE technique is that there can only be one correlated source between the microphone measurements. The same limitation applies to the Non-Linear technique formulated for a single source model.

In order to verify the number of sources assumed, the “Two test Procedure” can be used. In figure 5.11(b) the SE and Non-linear techniques are applied to Test Case 2. Here it can be seen that the results up to approximately 1.5kHz using either $M3$ or $M4$ as the third microphone give similar results. Above this frequency limit the results differ. The conclusion here is that for all four microphone readings, below 1.5kHz there is only one significant source. This conclusion is borne out in figure 5.8. For Test Case 2, one of the correlated sources is approx 10dB below both the noise and the second correlated source level in this frequency range. Referring again to figure 5.11(b) we see that below 1.5kHz the noise is correctly identified. Interestingly, it is the sum of the two sources, albeit one is 10dB larger than the other, that is also identified in this range as opposed to merely the larger of the two. Above this frequency limit, the results are inconclusive.

The benefit of the CSA technique over the COS technique for Test Case 2, for example, is that it can identify the second source in addition to the noise term, as opposed to just the sum of the two. The first plot in figure 5.10 shows each contribution to the y_2 measurement individually identified. In the second plot, the same contributions are identified, yet in this case a variation of the technique was employed which allowed for extraneous noise in the source measurement. In order to try and replicate this situation, two different windowed linear-phase finite impulse response filters were designed in *Matlab* and applied to the measured source signal x_1 . The magnitude and phase of the frequency response functions between x_1 and the filtered signals are given in figure 5.12(b). Also, shown is the frequency response function between the two filtered signals. This is a good physical approximation to the reality as a phase lag between the signals due to their differing locations and magnitude variations would be expected. To these signals, different random noise was added resulting in y_4 and y_5 , as per figure 5.12(a).

Although the results are not presented here, the ‘‘Two Test Procedure’’ was performed on CSA technique also. The results show that when a third source, x_3 , was turned on, the procedure could be used successfully to verify the number of sources present.

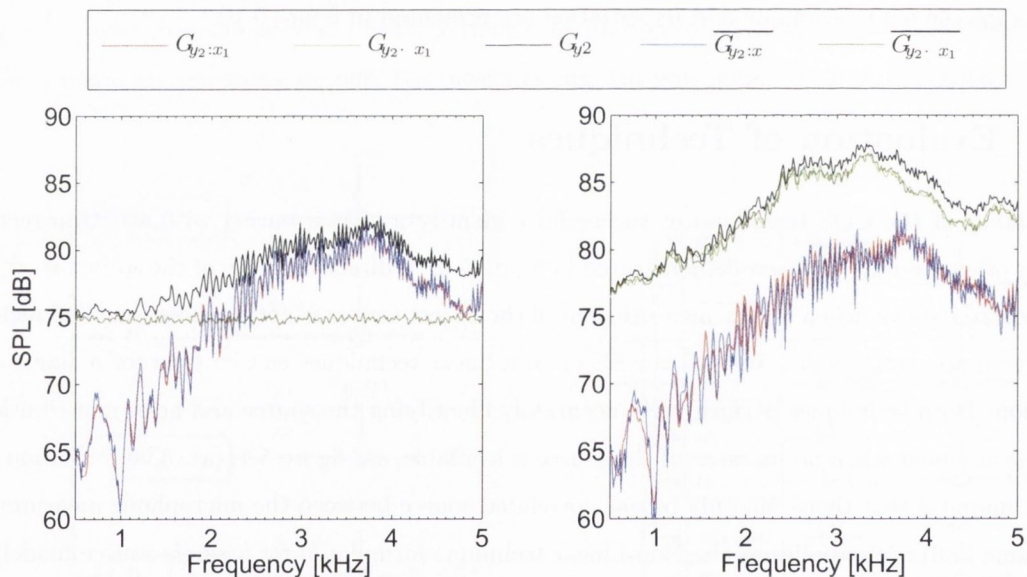


FIGURE 5.9: Results for the COS technique for Test Cases 1 and 2.

5.6 Linear Noise Source Separation

5.6.1 Conditional Spectral Analysis Applied to Experimental Rig

Given the results of section 5.4, the technique described in section 5.2.3 was chosen to be applied downstream of the fan using pressure measurements from three microphones : microphones 4, 5 and 6 (refer to figure 3.2). The objective here was to decompose the measured pressure spectra

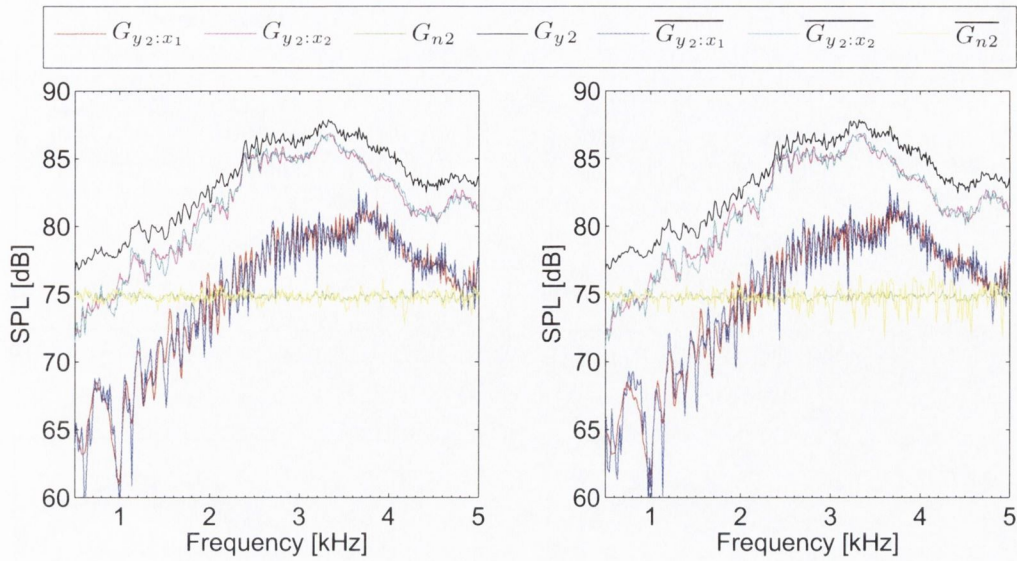


FIGURE 5.10: Results for the CSA Technique and its variation for Test Case 2.

into constituent components, thus leading to their identification. The models assumed are shown in figures 5.13 and 5.14 for the no-fan and fan turned on configurations as previously described in 4.6. As is shown in both models, all microphones are expected to measure a source from the speaker, some uncorrelated noise and an allowance is made for a second correlated source signal, which should be the fan noise contribution for the second test configuration. The method discussed by Hsu and Ahuja [29] is developed here with application to the models of 5.13 and 5.14 in a slightly more intuitive way.

Bendat and Piersol [7] analyse various multiple-input/multiple-output systems and develop relationships between conditioned spectra. Pertinent to this problem are results where it is calculated that if two signals, i and j , are composed of at least two components each, where r is one of them, then the cross-spectrum between i and j with the linear effects of r removed can be expressed as

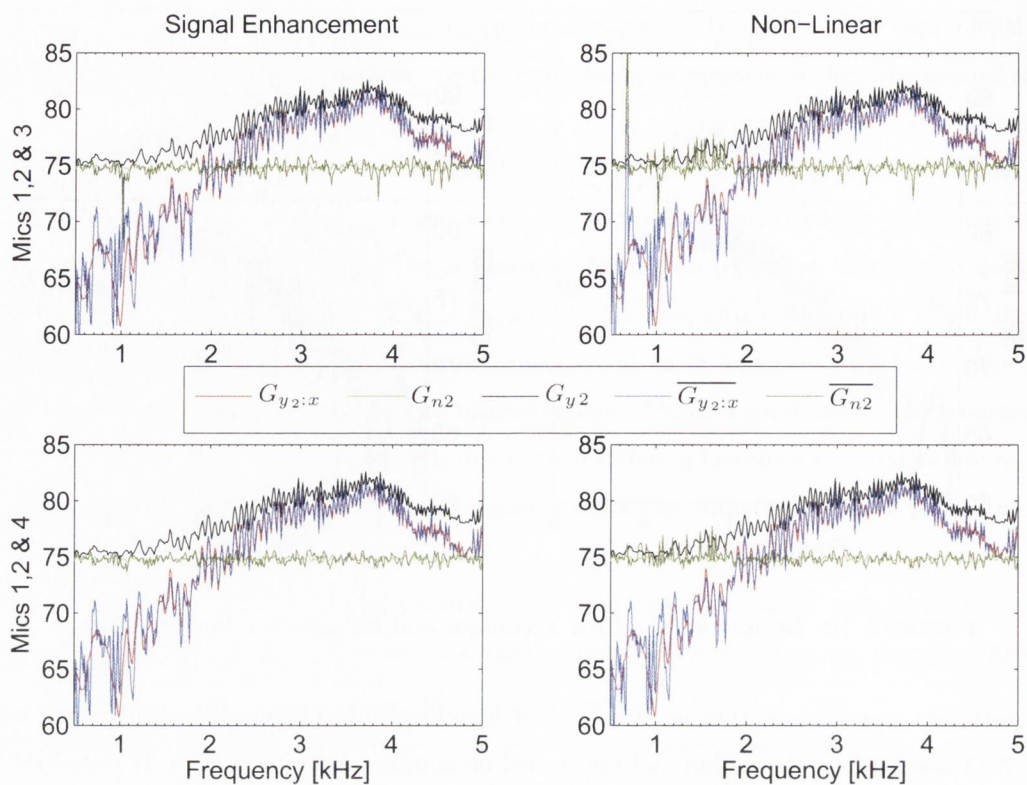
$$G_{ij:r} = G_{ij} - \frac{G_{ir}G_{rj}}{G_{rr}} \quad (5.5)$$

It can be seen from this equation that the part correlated with r must then be

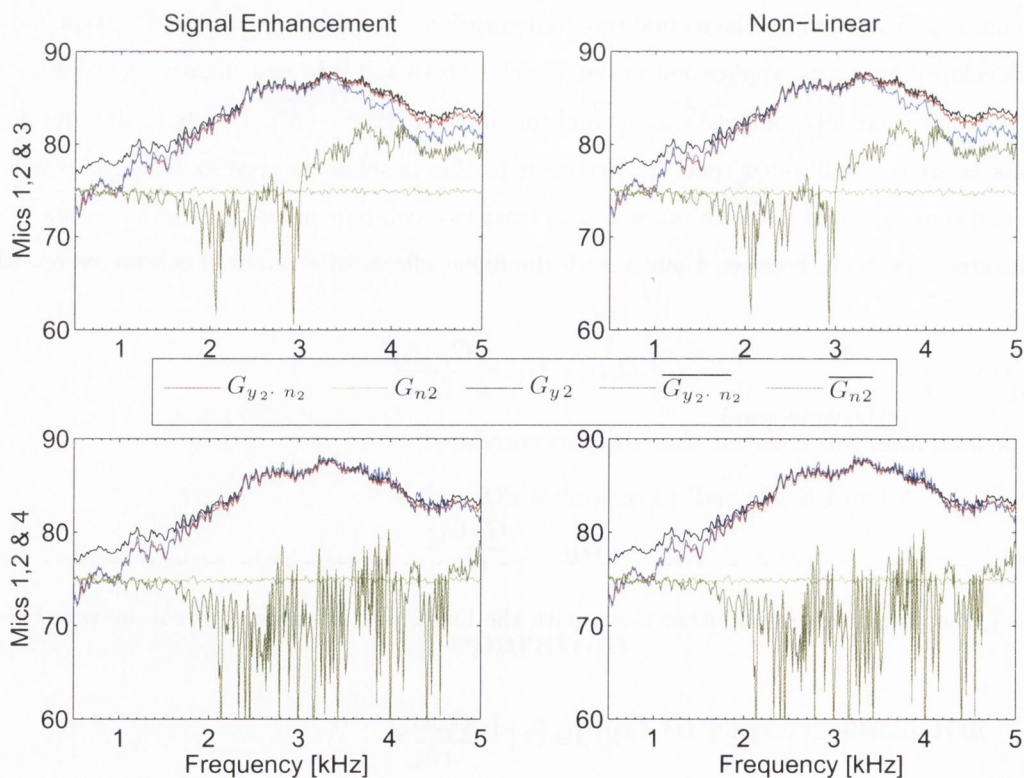
$$G_{ij:r} = \frac{G_{ir}G_{rj}}{G_{rr}} \quad (5.6)$$

For $i = j$, the autospectrum of either i or j with the linear part of r removed can be written as

$$\begin{aligned} G_{ii:r} &= G_{ii} - \frac{G_{ir}G_{ri}}{G_{rr}} \\ &= G_{ii} - \frac{G_{ri}^*G_{ri}}{G_{rr}} \\ &= G_{ii} - \frac{|G_{ri}|^2}{G_{rr}} \end{aligned} \quad (5.7)$$

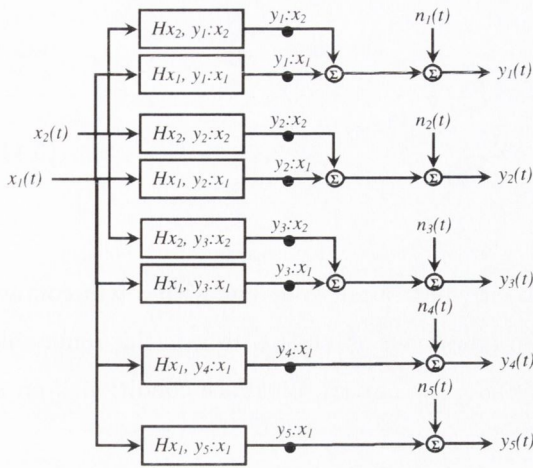


(a) Results for the SE and Non-Linear Techniques for Test Case 1. In the second row microphones 1, 2 and 4 are used.

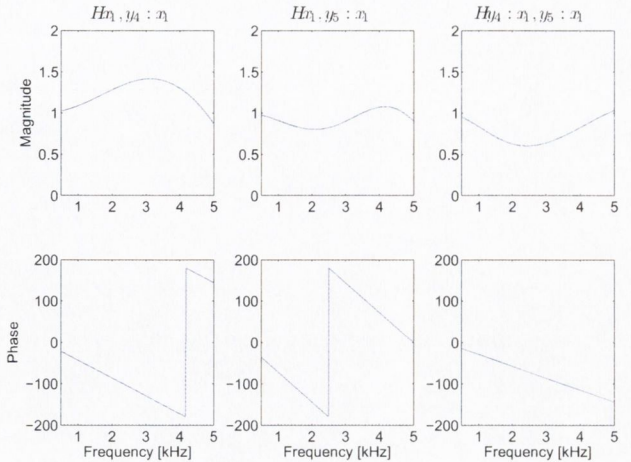


(b) Results for the SE and Non-Linear Techniques for Test Case 2. In the second row microphones 1, 2 and 4 are used.

FIGURE 5.11: Comparing the SE and Non-Linear Techniques for Test Cases 1 and 2. The “Two Test Procedure” is used to verify the number of sources.



(a) CSA model with variation to accommodate noise in source signals.



(b) Frequency response functions as a result of using FIR1 filters

FIGURE 5.12: CSA Technique

Upon closer inspection of the correlated part we see that this is the previously derived coherent output spectrum written in a different form;

$$\begin{aligned}
 G_{ii:r} &= \frac{|G_{ri}|^2}{G_{rr}} \\
 &= \frac{|G_{ri}|^2}{G_{rr}G_{ii}} G_{ii} \\
 &= \gamma_{ri}^2 G_{ii}
 \end{aligned}
 \tag{5.8}$$

and thus the uncorrelated part could also be written as

$$G_{ii:r} = (1 - \gamma_{ri}^2)G_{ii}
 \tag{5.9}$$

The *partial coherence function* between i and j with the linear effects of r removed, as derived in Bendat and Piersol [7], may now be defined as the ordinary coherence function between the conditioned spectra;

$$\gamma_{ij:r}^2 = \frac{|G_{ij:r}|^2}{G_{ii:r}G_{jj:r}}
 \tag{5.10}$$

Thus referring to figures 5.13 or 5.14, the part of the y spectra coherent with the source, can be calculated using the coherent output spectrum technique of section 5.2.1, expressed here in conditioned spectra form

$$\begin{aligned}
G_{v_1 v_1} &= G_{y_1 y_1 : s} = \frac{|G_{s y_1}|^2}{G_{ss}} \\
G_{v_2 v_2} &= G_{y_2 y_2 : s} = \frac{|G_{s y_2}|^2}{G_{ss}} \\
G_{v_3 v_3} &= G_{y_3 y_3 : s} = \frac{|G_{s y_3}|^2}{G_{ss}}
\end{aligned} \tag{5.11}$$

From observation it can be seen that the part of the y spectra not coherent with s will contain contributions from only x_2 (or the Fan) and the extraneous noise terms, the n^s . It is on this remaining part that the SE technique of section 5.2.2 is applied, using the partial coherence conditioned on s , to successfully recover the k spectra.

$$\begin{aligned}
G_{k_1 k_1} &= \frac{|\gamma_{y_1 y_2 : s}| |\gamma_{y_1 y_3 : s}|}{|\gamma_{y_2 y_3 : s}|} G_{y_1 y_1 : s} \\
G_{k_2 k_2} &= \frac{|\gamma_{y_1 y_2 : s}| |\gamma_{y_2 y_3 : s}|}{|\gamma_{y_1 y_3 : s}|} G_{y_2 y_2 : s} \\
G_{k_3 k_3} &= \frac{|\gamma_{y_1 y_3 : s}| |\gamma_{y_2 y_3 : s}|}{|\gamma_{y_1 y_2 : s}|} G_{y_3 y_3 : s}
\end{aligned} \tag{5.12}$$

The noise spectra can be calculated by removing the k spectra from the part of the y spectra not coherent with s .

$$\begin{aligned}
G_{n_1 n_1} &= G_{y_1 y_1 : s} - G_{k_1 k_1} = \left(1 - \frac{|\gamma_{y_1 y_2 : s}| |\gamma_{y_1 y_3 : s}|}{|\gamma_{y_2 y_3 : s}|} \right) G_{y_1 y_1 : s} \\
G_{n_2 n_2} &= \left(1 - \frac{|\gamma_{y_1 y_2 : s}| |\gamma_{y_2 y_3 : s}|}{|\gamma_{y_1 y_3 : s}|} \right) G_{y_2 y_2 : s} \\
G_{n_3 n_3} &= \left(1 - \frac{|\gamma_{y_1 y_3 : s}| |\gamma_{y_2 y_3 : s}|}{|\gamma_{y_1 y_2 : s}|} \right) G_{y_3 y_3 : s}
\end{aligned} \tag{5.13}$$

again refer to equation B.37 for the definition of the modulus of the coherence function.

For configuration 1, viz. broad band noise, high pass filtered at 500Hz, low pass filtered at 3000Hz, the fan not rotating - the results of the identification are shown in figure 5.15 for each of the three microphone signals, in accordance with the model from figure 5.13 and using equations 5.11, 5.12 and 5.13. In each of the three plots we see the total pressure measured (the y 's), the component correlated with the speaker (the v 's), the component uncorrelated with the other two microphone signals (the n 's) and then a third component which is correlated between the microphones but uncorrelated with the speaker. We may make a number of comments. Firstly regarding the noise term; as expected the energy here is low with a broad band floor superimposed with harmonics related to electrical signals picked up by the cables and signal processing numerical noise. The microphone used in position 4 is an electret based microphone whereas microphones 5 and 6 are condenser microphones which should explain why the noise level from these latter microphones are similar to each other. The latter microphones seem to have a higher noise floor than the electret one - the product literature states

$\approx 40\text{dBA}$. Also as might be expected, the v signals, or the signals correlated with the speaker, are effectively of the same magnitude as the total sum-the y 's. The allowance for a second correlated signal shows a significant, although smaller, spectrum of the same form as the v spectrum for each of the microphones. This is due to the fact that not only the speaker is exciting the tube but also broad band background noise and vibration from the lab. A background noise test where an acquisition is made with no speaker or fan excitation verifies this. Ideally this whole rig would be placed in an anechoic room sound insulated from external noise sources.

For the second test configuration - broad band noise, high pass filtered at 500Hz, low pass filtered at 3000Hz, the fan rotating at 17250 rpm - the same identification was performed. These results are shown in figure 5.16. Again, commencing with the noise identification, it can be seen the the level has increased significantly but the frequency components are independent of the BPF and the standing wave frequencies as would be expected for uncorrelated noise. The spectra contain most energy at the lower frequencies displaying a striking similarity to a turbulent spectrum and it is deduced that the uncorrelated noise between the microphones is dominated by flow noise which is distributed in nature in the pipe. The level of noise identified for the first microphone is 10-20dB higher at the first microphone position. It is unclear if this is due to the different make of microphone being more sensitive to flow noise or whether it is due to the closer proximity to the fan.

Figure 5.17 is a useful figure which shows the difference between the identified terms for the two test configurations for microphone 5 only. As can be seen, the total measurement at microphone 5 (or the y signal) is greater when the fan is turned on. The components are the uncorrelated noise term as discussed already, the original speaker signal which is correctly identified and the other correlated input termed the "fan noise".

Figure 5.18 shows just the fan noise for microphone 5 and superimposed are multiples of the RPM of the fan. Again a number of comments may be made. It can be seen that many of the RPM multiples are visible in the spectrum. From the theory of section 2.5.2, energy at these frequencies would not be expected and must be due either to vibration energy from unbalance and/or acoustic energy from a lack of similarity between the vanes. Energy at BPF and 2XBPF is seen and is predicted however. Also, up to the cut-off frequency the standing wave frequencies are again present being excited by broad-band noise created as a result of the fan. As stated in Joseph and Parry [34], the generation of broadband noise in turbofan engines results from the interaction of turbulence and solid surfaces, the dominant mechanisms being between the rotor and ingested turbulence, between the turbulent eddies and the rotor trailing edge, between the turbulent wake shed from the rotor onto the stator and through interaction between the rotor tip and the turbulent boundary layer at the casing wall. Unlike the drops in magnitude as a result of the microphones being located near nodes of certain frequencies, as discussed in section 4.5, the magnitudes here decrease fairly linearly with frequency. This is because the standing wave frequencies are convected with the flow and thus pass by the microphone positions. At the cut-on frequency of the second mode, $\approx 4kHz$, we see a large

rise in energy with the microphones measuring a combination of the two modes.

Figure 5.19 shows the same information as that in figure 5.17 but with the whole frequency axis of zero to the Nyquist Frequency plotted. As the speaker signal is filtered at 500Hz and 3000Hz there is less identified energy measured outside this range. For the fan noise however, not being filtered, we see that this is identified beyond $3kHz$ as would be expected.

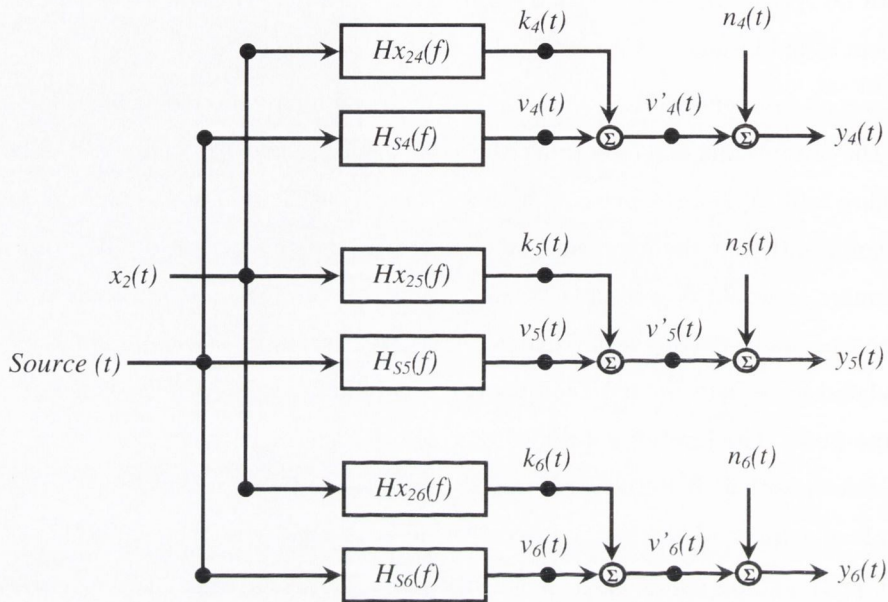


FIGURE 5.13: Model assumed for microphones 4,5, and 6 downstream of fan when fan not turned on. Source input, correlated input and uncorrelated noise.

5.6.2 Conditioned Frequency Response Functions Across The Fan

The most basic representation of an aero-turbine, or a fan in a duct, is given in figure 5.20. As was briefly discussed in section 3.1, the speaker noise could represent aero-engine core noise, or combustion noise, for example, which is convected through a rotating fan. Due to impedance mismatch at both open ends of the duct, pressure waves are reflected, resulting in incident and reflected waves forming standing waves and their associated resonances. Figure 5.21 shows a block diagram for two pressure measurements, one upstream and one downstream of the fan. By implementing an anechoic end condition downstream of the fan, the relationship between the upstream incident wave and the downstream incident wave can be examined, see figure 5.22. Although some fan noise will be present in the upstream incident signal, by reducing reflections from the upstream end, most of what is convected through the fan should be made up of speaker noise with some flow noise only. This block diagram describing the incident waves' relationship is given in figure 5.23. The limited amount of upstream fan noise is demonstrated by examining figure 4.32.

The standard form of the frequency response function or frequency response function is given in

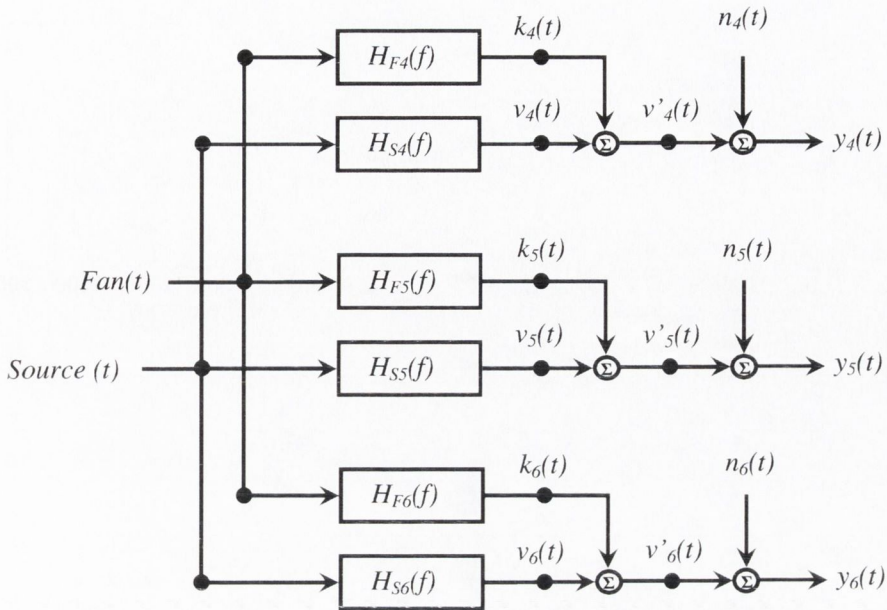


FIGURE 5.14: Model assumed for microphones 4,5, and 6 downstream of fan. With fan turned on, BPF=2350Hz. Source input, Fan noise input and uncorrelated noise.

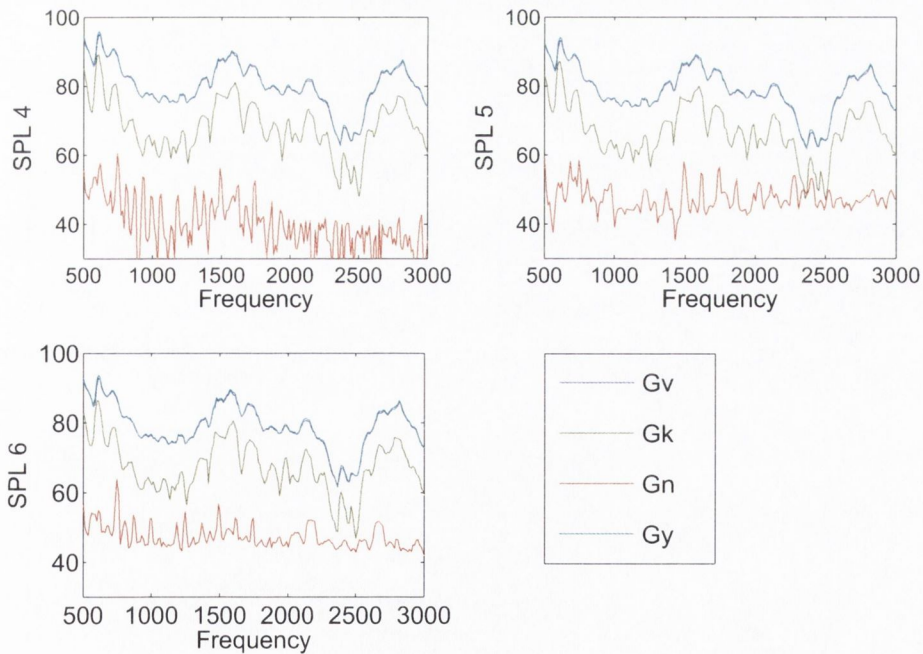


FIGURE 5.15: The results of the identification for configuration 1, viz. broad band noise, high pass filtered at 500Hz, low pass filtered at 3000Hz, the fan not rotating - for each of the three microphone signals, in accordance with the model from figure 5.13.

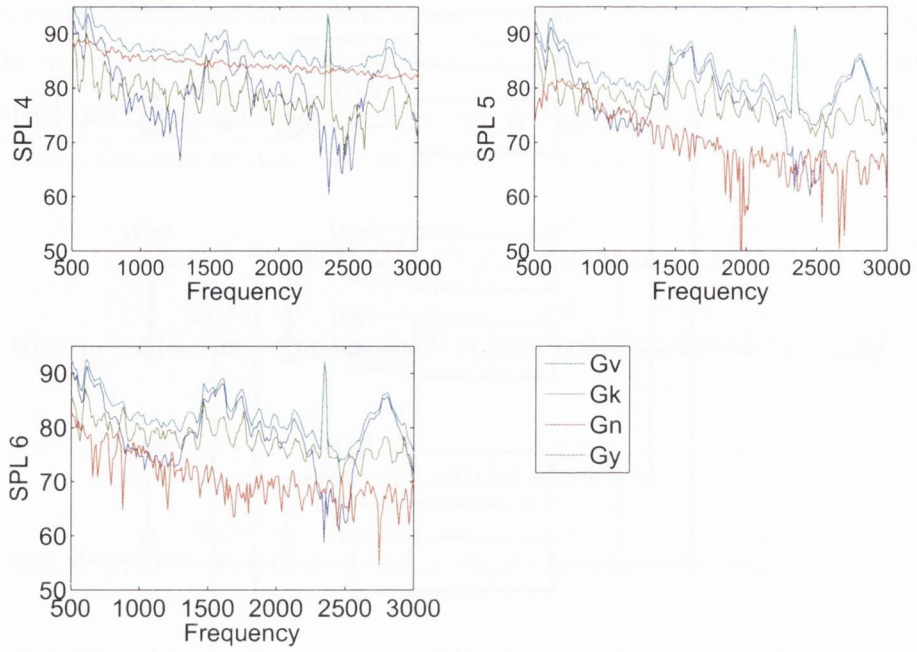


FIGURE 5.16: The results of the identification for configuration 2, viz. broad band noise, high pass filtered at 500Hz, low pass filtered at 3000Hz, the fan rotating - for each of the three microphone signals, in accordance with the model from figure 5.14.

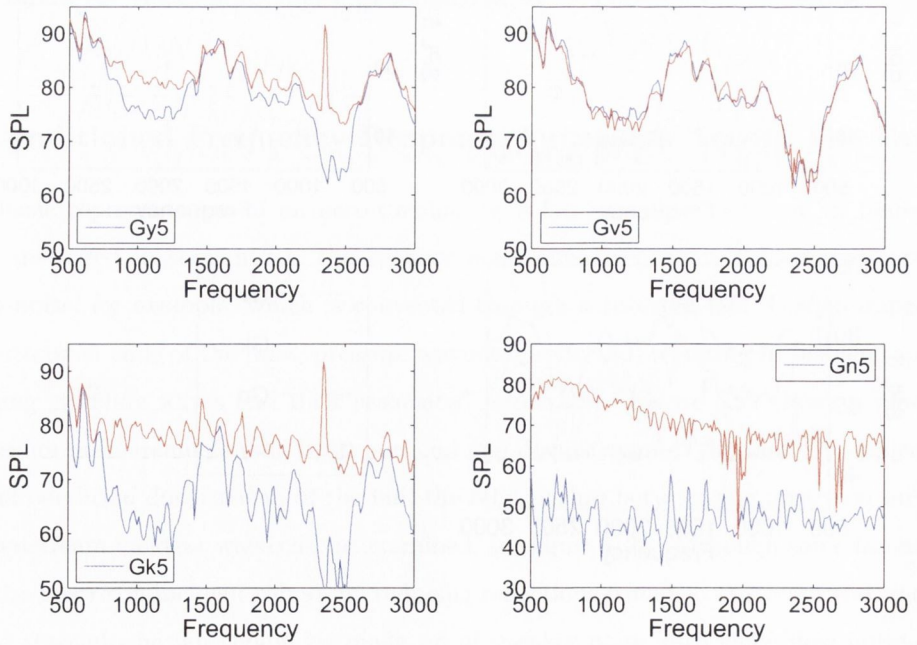


FIGURE 5.17: For microphone 5 only, the results of the identification with and without the fan turned on.

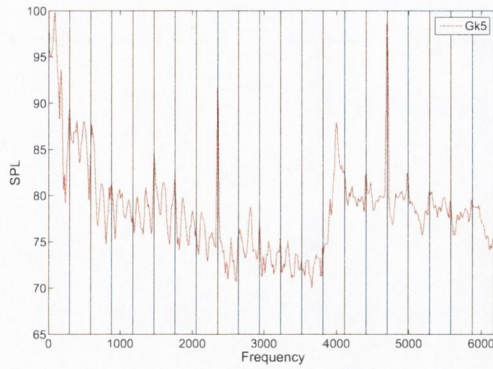


FIGURE 5.18: The identified fan noise at microphone 5, with the fan turned on, with multiples of the RPM superimposed.

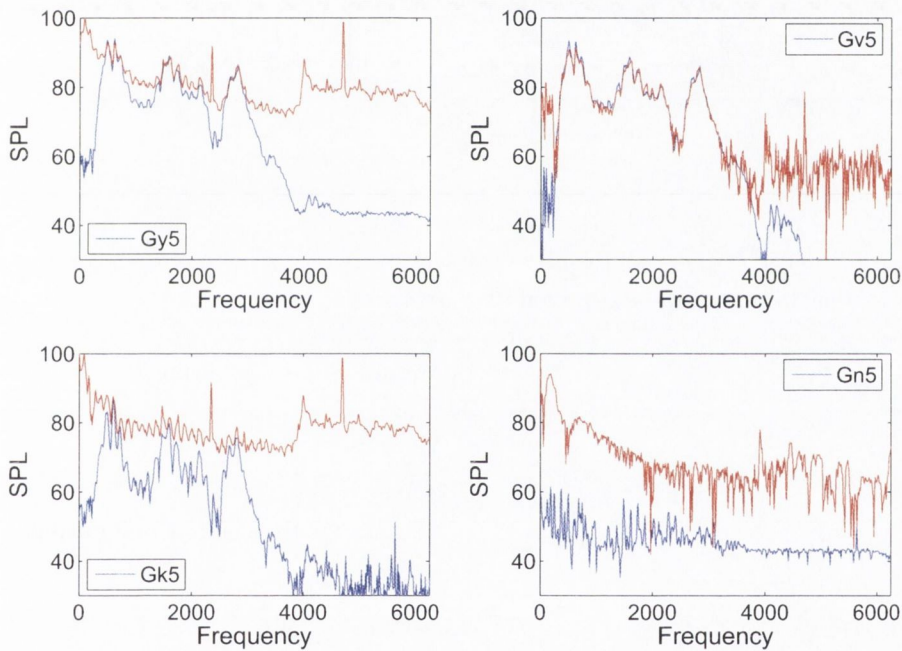


FIGURE 5.19: The same as figure 5.17 but the frequency axis has been extended from 0Hz to the Nyquist Frequency.

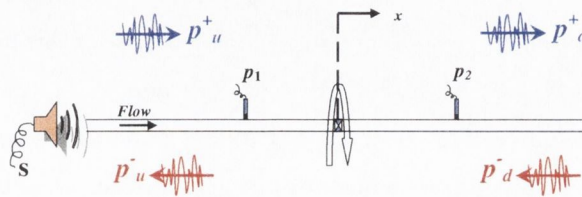


FIGURE 5.20:

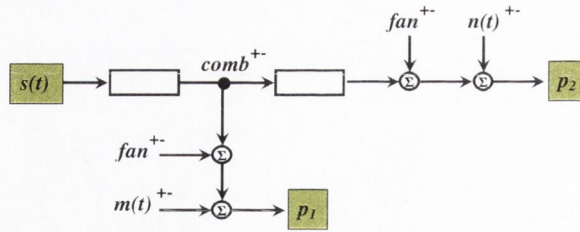


FIGURE 5.21:

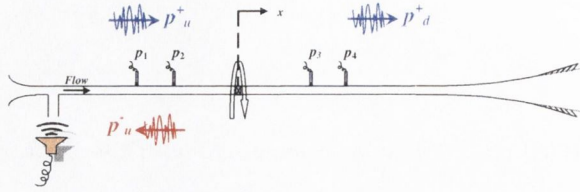


FIGURE 5.22:

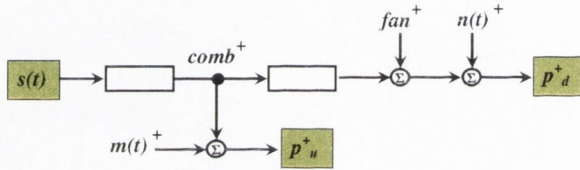


FIGURE 5.23:

section B.12. Other formulations which could be used are;

$$H_{ij(a)} = \frac{G_{ij}(f)}{G_{ii}(f)} \quad \dots \quad \text{Minimise noise at output} \quad (5.14)$$

$$H_{ij(b)} = \frac{G_{jj}(f)}{G_{ji}(f)} \quad \dots \quad \text{Minimise noise at input} \quad (5.15)$$

$$H_{ij(c)} = \sqrt{\frac{G_{ij}(f) G_{jj}(f)}{G_{ii}(f) G_{ji}(f)}} \quad \dots \quad \text{Minimise noise at input and output} \quad (5.16)$$

$$|H_{ij(d)}| = \sqrt{\frac{G_{jj}(f)}{G_{ii}(f)}} \quad \dots \quad \text{Magnitude only} \quad (5.17)$$

Due to the fact that the cross spectrum will only contain energy correlated between two signals, equations (5.14) and (5.15) effectively condition out noise in a limited way. However, as both input and output contain extraneous noise, both of these techniques will fail to represent fully the model of figure 5.2. A third form of the frequency response function is introduced in equation (5.16) and attempts to reduce noise at both the input and output signals. Use of this frequency response function can be found in standard ISO 10534 [2] and Åbom [6] for example.

With a measure of the source of interest, e.g. the voltage powering the speaker in the experimental rig, or a pressure measurement at the combustor in an aero-engine, a number of additional frequency response functions may be derived which will result in a more thorough conditioning of the signals, resulting in H_{vij} in the block diagram of the system in figure 5.24. The first of these can be viewed as

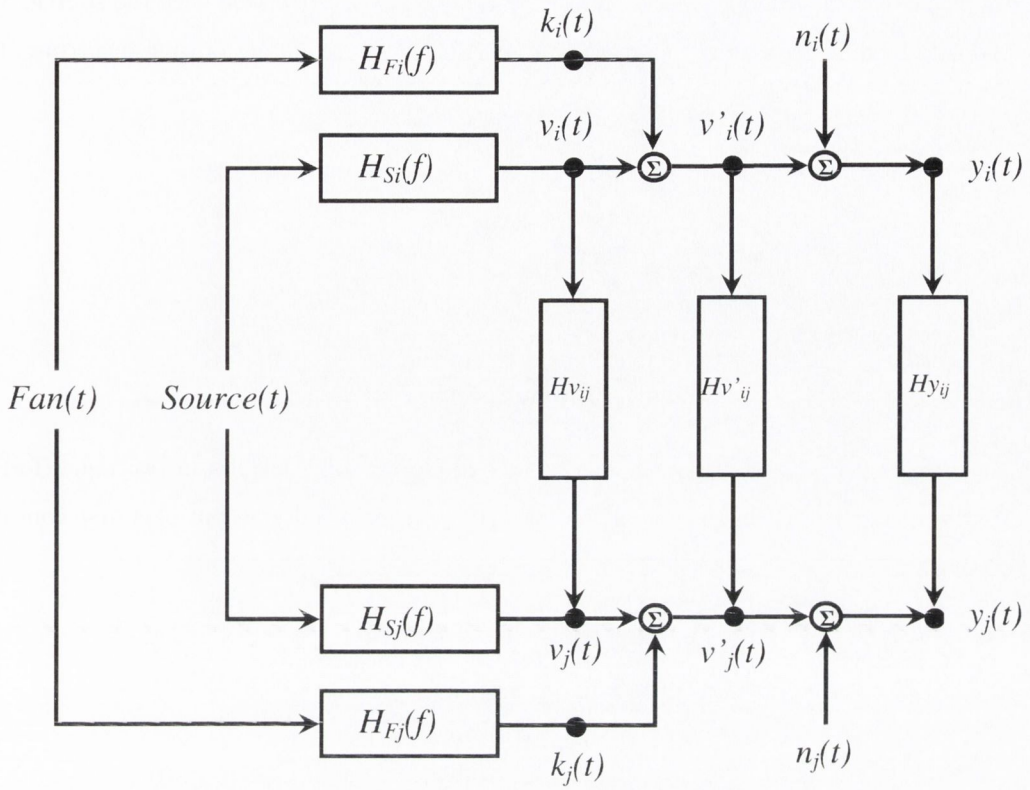


FIGURE 5.24:

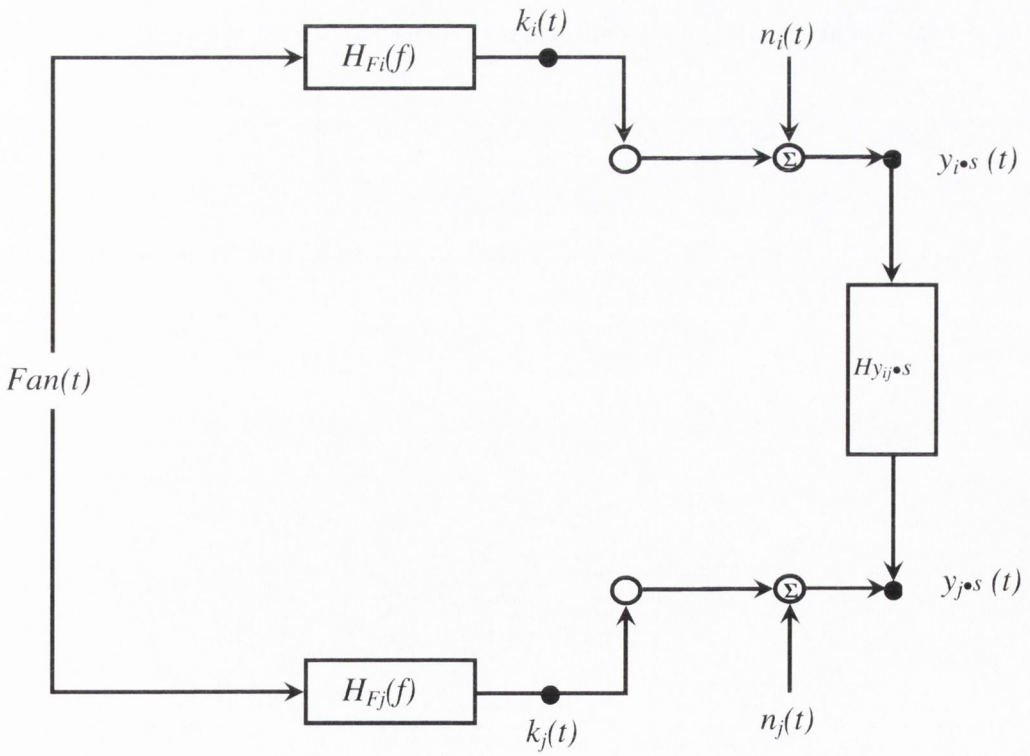


FIGURE 5.25:

the part of y_j correlated with the source divided by the part of y_i correlated with the source. Which is the same as the coherent output spectrum at y_j divided by the coherent output spectrum at y_i ;

$$|H_{vij}|^2 = \frac{G_{jj:s}}{G_{ii:s}} = \frac{|G_{sj}|^2}{|G_{si}|^2} \frac{G_{ss}}{G_{ss}} \quad (5.18)$$

$$= \frac{\text{Coherent Output Spectrum at } j}{\text{Coherent Output Spectrum at } i} = \frac{\gamma_{sj}^2 G_{jj}}{\gamma_{si}^2 G_{ii}} \quad (5.19)$$

where the y notation has been dropped for the sake of clarity. This results in two equal forms for the modulus which gives the magnitude of the frequency response function but of course contains no phase information;

$$|H_{vij(a)}| = \frac{|G_{sj}|}{|G_{si}|} \quad (5.20)$$

$$|H_{vij(b)}| = \sqrt{\frac{\gamma_{sj}^2 G_{jj}}{\gamma_{si}^2 G_{ii}}} \quad (5.21)$$

Conditioned frequency response functions that contain phase information can also be derived. Wagstaff and Henrio [64] use the non-modulus form of above to give;

$$H_{vij} = \frac{G_{sj}}{G_{si}} \quad (5.22)$$

This expression is equivalent to a frequency response function which can be derived from equations (5.8) and (5.8).

$$H_{vij} = \frac{G_{ij:s}}{G_{ii:s}} \quad (5.23)$$

$$= \frac{G_{is} G_{sj}}{G_{ss}} \quad (5.24)$$

$$= \frac{|G_{si}|^2}{G_{ss}} \frac{G_{is} G_{sj}}{|G_{si}|^2} \quad (5.25)$$

These expressions for the conditioned frequency response functions between pressure measurements at i and j can be summarized as follows;

$$H_{ij} : s_{(a)} = \frac{G_{ij:s}}{G_{ii:s}} = \frac{G_{is}G_{sj}}{|G_{si}|^2} = \frac{G_{sj}}{G_{si}} \quad (5.26)$$

$$H_{ij} : s_{(b)} = \frac{G_{jj:s}}{G_{ji:s}} = \frac{|G_{sj}|^2}{G_{js}G_{si}} = \frac{G_{sj}}{G_{si}} \quad (5.27)$$

$$H_{ij} : s_{(c)} = \sqrt{\frac{G_{ij:s} G_{jj:s}}{G_{ii:s} G_{ji:s}}} = \frac{G_{sj}}{G_{si}} \quad (5.28)$$

$$|H_{ij} : s_{(d)}| = \sqrt{\frac{G_{jj:s}}{G_{ii:s}}} = \left| \frac{G_{sj}}{G_{si}} \right| \quad (5.29)$$

where again the $:$ convention for the correlated part is used. Similarly, the frequency response functions across the fan between the residual may be expressed using the following variations;

$$H_{ij} \cdot s_{(a)} = \frac{G_{ij \cdot s}}{G_{ii \cdot s}} = \frac{G_{ij} - G_{ij:s}}{G_{ii} - G_{ii:s}} \quad (5.30)$$

$$H_{ij} \cdot s_{(b)} = \frac{G_{jj \cdot s}}{G_{ji \cdot s}} = \frac{G_{jj} - G_{jj:s}}{G_{ji} - G_{ji:s}} \quad (5.31)$$

$$H_{ij} \cdot s_{(c)} = \sqrt{\frac{G_{ij \cdot s} G_{jj \cdot s}}{G_{ii \cdot s} G_{ji \cdot s}}} \quad (5.32)$$

$$|H_{ij} \cdot s_{(d)}| = \sqrt{\frac{G_{jj \cdot s}}{G_{ii \cdot s}}} = \sqrt{\frac{(1 - \gamma_{sj}^2)G_{jj}}{(1 - \gamma_{si}^2)G_{ii}}} \quad (5.33)$$

where this time \cdot , denotes the uncorrelated part.

Using the basic frequency response function expressions given by equations (5.14), (5.15) and (5.16), figure 5.26 shows the three formulations to be equivalently good for the set-up where the fan is not turned on, i.e., no fan or flow noise. This figure, whilst seeming trivial, is useful however, as it highlights the bounding of the phase between $+\pi/2$ and $-\pi/2$ due to the square root operation in Matlab. Figure 5.27, with the fan turned on this time, highlights the differences between the three TF formulations. Comparing equations (5.14) and (5.15) first, we see how there is demonstrated to be less flow noise in the upstream measurement, as the formulation, equation (5.14), which assumes more noise in the downstream measurement gives the better result. Given that flow noise and fan noise would be expected to be measured at both upstream and downstream locations, we see equation (5.16) gives the best result, reducing the effect of flow noise in the frequency ranges where the signal to noise ratio is low, ref. figure 4.24. Evidence of the BPF is seen in all three plots.

Figure 5.28, shows the benefit to be gained when a measure of the source signal is incorporated into the formulation. As is demonstrated in equations (5.26), (5.27) and (5.28), the three formulations are equal and give a frequency response function across the fan very close to the test result when the fan is not turned on. This demonstrates a successful conditioning out of additional inputs.

The next set of tests were carried out to determine the optimum frequency response function formulation across the fan using the incident pressure signals, \mathbf{u}_i and \mathbf{d}_i . Reference to figure 5.29 shows that there is far more flow noise present in the downstream incident signal than that of the

upstream. This is partly thanks to the anechoic termination and its flow noise reduction functionality, and partly to do with the vanes, which straighten the flow, being located upstream of the rotor. The difference in flow noise level is such that equation (5.28), which is a compromise formulation, still results in a more erroneous result. The formulation of equation (5.27) gives the satisfactory result of low flow noise and a positive large value at the BPF, demonstrating its creation between the two measurement planes.

Once again the frequency response function correlated with the source signal, gave excellent results, as seen in figure 5.30, and figure 5.30 shows the plots when the block diagram of the residual of figure 5.25 are examined.

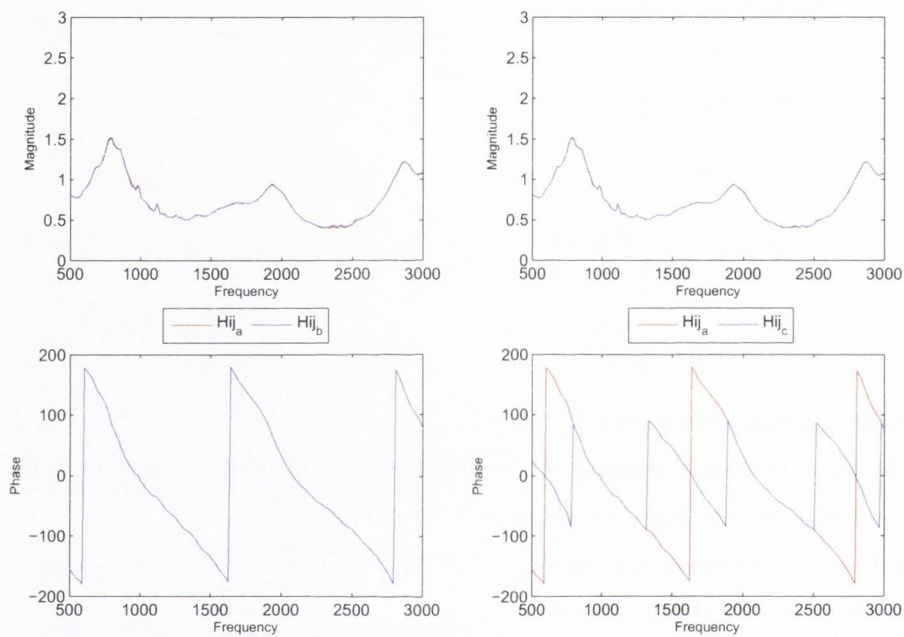


FIGURE 5.26: Basic frequency response functions between microphones 1 and 5. The fan not rotating.

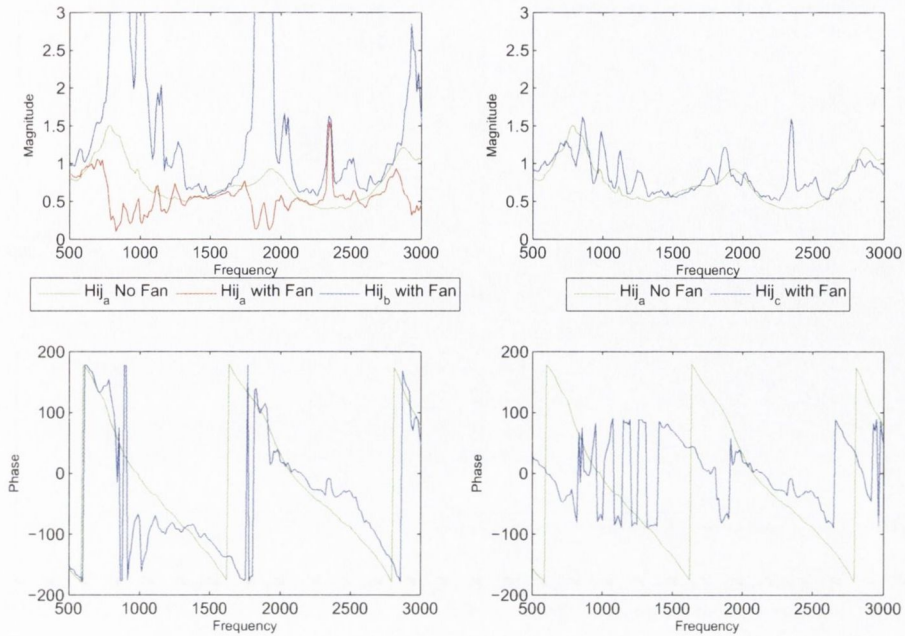


FIGURE 5.27: Basic frequency response functions between microphones 1 and 5. The fan rotating Vs the no fan case.

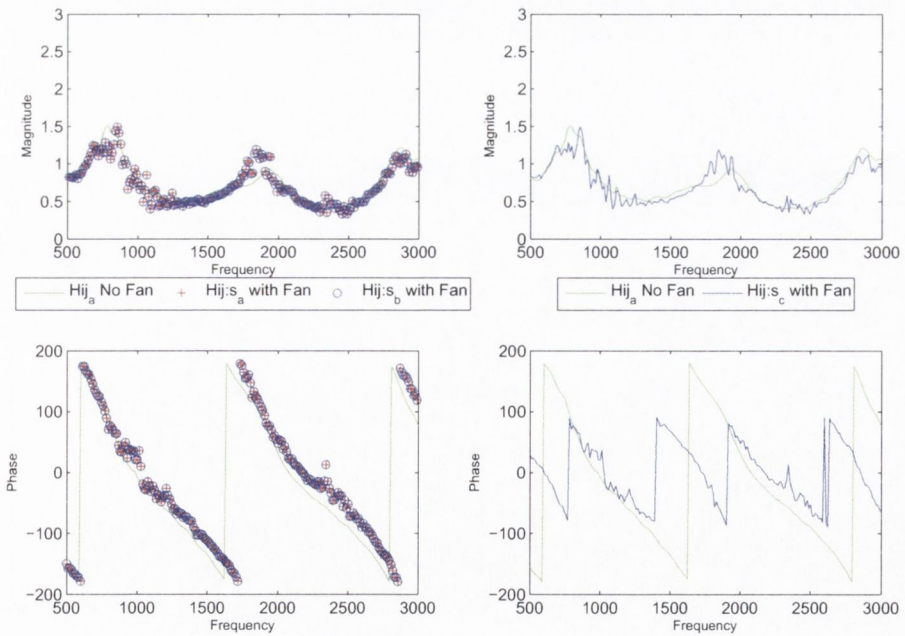


FIGURE 5.28: The frequency response functions between microphones 1 and 5 of the part correlated with the source. The fan rotating Vs the no fan case.

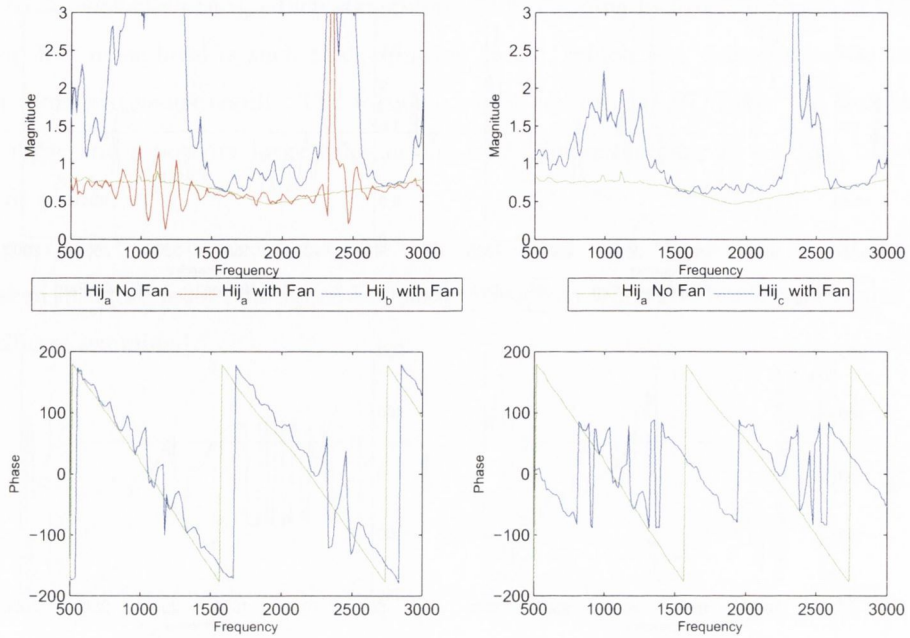


FIGURE 5.29: Basic frequency response functions between **ui** and **di**. The fan rotating Vs the no fan case.

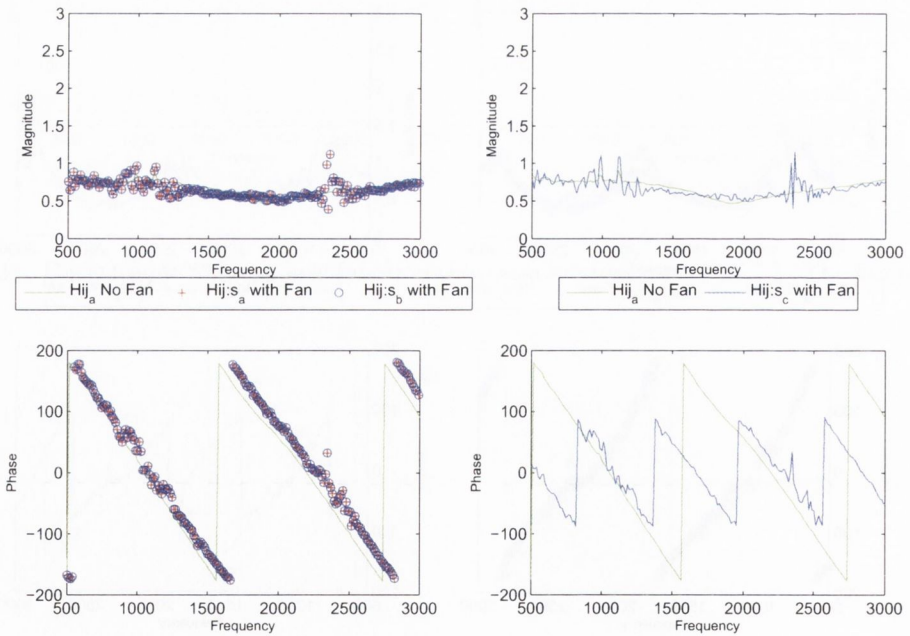


FIGURE 5.30: The frequency response functions between **ui** and **di** of the part correlated with the source. The fan rotating Vs the no fan case.

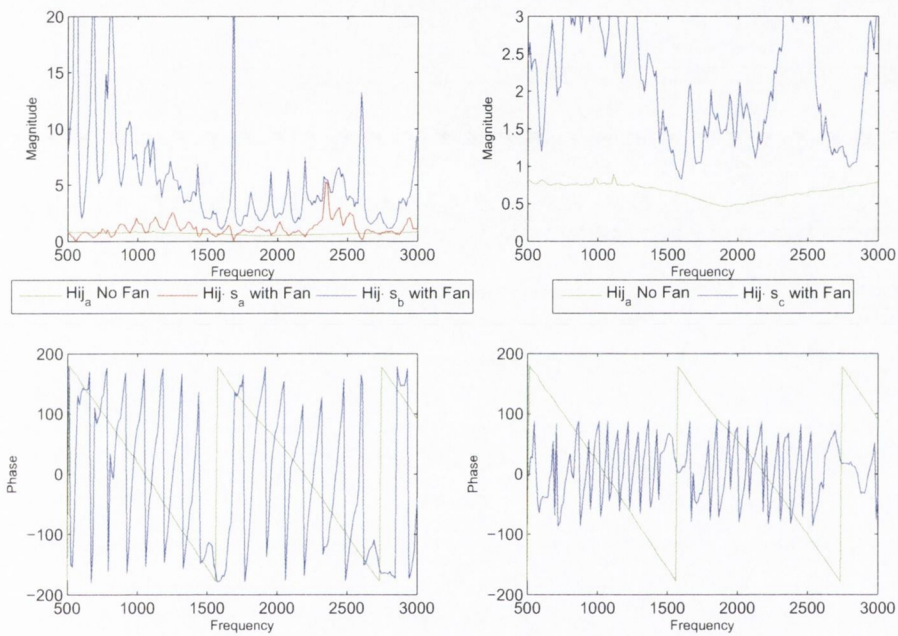


FIGURE 5.31: The frequency response functions between \mathbf{u}_i and \mathbf{d}_i of the part un-correlated with the source. The fan rotating Vs the no fan case.

Chapter 6

Non-Linear Analysis

6.1 Introduction

The model presented in figure 5.23, and all the work presented so far has assumed a linear system for the potential identification of the combustion source noise. A drop in coherence between combustion noise measurements made at the combustor can with pressure transducers, and microphone array measurements focused on the exit plane of an aero-engine, when the rpm of the engine was increased, was reported by Siller *et al* [58]. Figure 6.2 shows some typical results for two engine power settings and three different viewing angles and they concluded that, when the jet noise is low for low engine power settings, the core noise is a significant contributor to noise in the far field. However, as the jet noise becomes more significant, the coherence drops due to the relatively low contribution of the combustion noise. This rationale, assumes a linear frequency response function between the combustion can and the exit plane of the engine. It is also possible that the reduction in coherence is due to some non-linear interactions as the unsteady pressure from the combustor passes through the rotor\stator stages.

The work of Rice and Fitzpatrick [52] demonstrate how a non-linearity can be modeled as an additional term in a multiple-input\single-output model. By working with incident waves, figure 6.1 presents a block diagram, highlighting how the non-linear term, or input, is created at the fan and is measured in the incident signal downstream of it. The non-linear analysis of this thesis investigates, with reference to figure 6.3, how to accommodate, in addition to convected combustion noise and turbine noise being measured at the exit plane of an aero-engine, p_2 , the possibility of an interaction between the upstream combustion noise and the turbine, as outlined in figure 6.4. What is being suggested is that the additional inputs into the system due to non-linearities could be an alternative cause for a drop in coherence and not simply the relative decrease in importance of the combustion noise compared to the other linear terms. As will be seen, quite the opposite could be true. In a non-linear system, a drop in coherence could occur when there is no relative change in power of the

linear noise sources. This may lead to the incorrect conclusion that core noise is less significant and may, as a result, be ignored in the development of acoustical treatment.

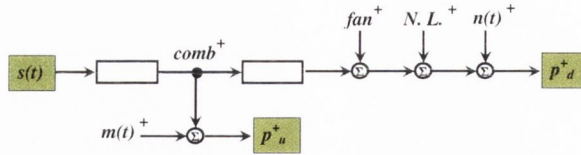


FIGURE 6.1: Block diagram for system where a non-linear term has been included as an input in the incident signal downstream.

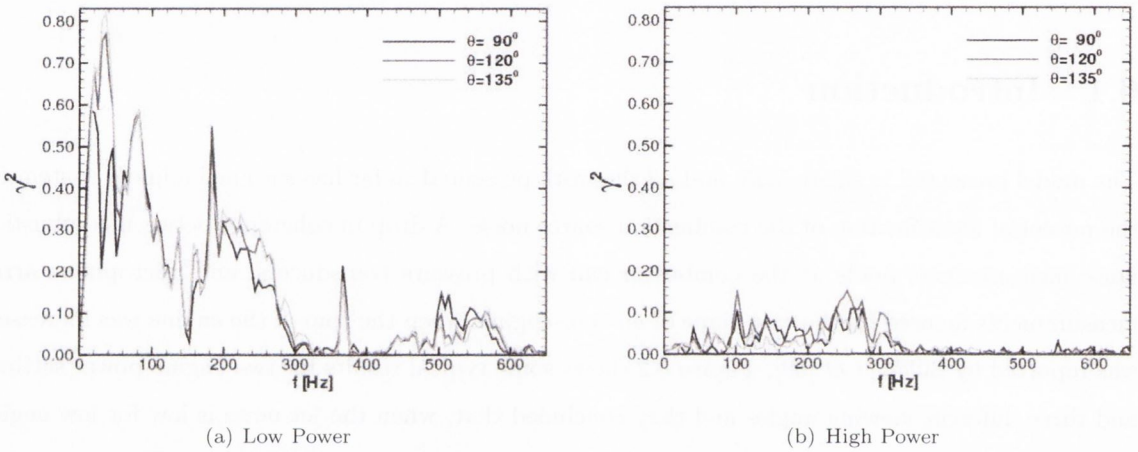


FIGURE 6.2: Results from the Resound campaign, Siller *et al* [58]. For two different engine power settings, coherence between pressure measured at the combustor cans and pressure data measured using a microphone array focused at the exit plane of an aero-engine is shown for different viewing angles.

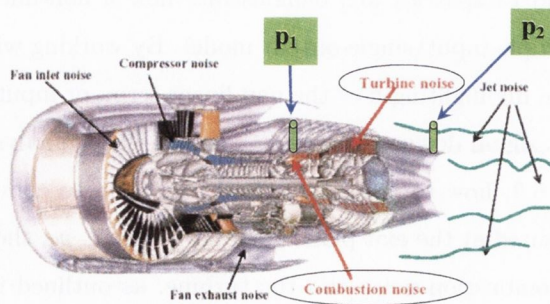


FIGURE 6.3: Schematic of an aero-engine where pressure measurements are taken at the combustion can and at the exit plane.

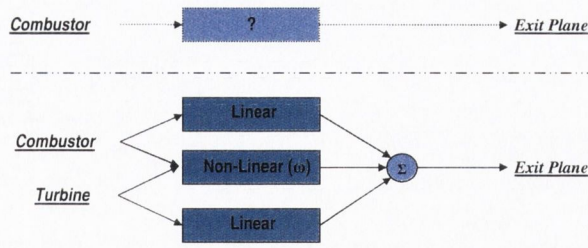


FIGURE 6.4: Frequency response function between the combustion noise and the pressure measured at the exit plane when some rpm dependent non-linearity is included in the model.

6.2 Non-Linear Simulations

In order to investigate this, a series of simulations were performed using synthetic data. When a signal is operated upon by a non-linear system, its frequency components are modified. Common interactions are quadratic in nature resulting in sum and difference frequencies as well a doubling in frequency. This can be demonstrated by observing the following two trigonometric identities.

$$[A \cos(\omega t)]^2 = \frac{1}{2} A^2 [1 + \cos(2\omega t)] \tag{6.1}$$

$$[A \cos(\omega_1 t) + B \cos(\omega_2 t)]^2 = \frac{1}{2} A^2 [1 + \cos(2\omega_1 t)] + \frac{1}{2} B^2 [1 + \cos(2\omega_2 t)] + AB \cos(\omega_1 + \omega_2)t + AB \cos(\omega_1 - \omega_2)t \tag{6.2}$$

The doubling of frequency arises from self interaction, whereas the sum and difference frequencies come about from combination interactions.

Consider a quadratic non-linearity

$$y(t) = x(t) + x^2(t) \tag{6.3}$$

where $x(t)$ is given by

$$x(t) = \cos(\omega_1 t + \phi_1) + \cos(\omega_2 t + \phi_2) \tag{6.4}$$

The resulting signal will contain the the terms $(\omega_1 + \phi_1)$, $(\omega_2 + \phi_2)$, $(2\omega_1 + 2\phi_1)$, $(2\omega_2 + 2\phi_2)$, $(\omega_1 + \omega_2, \phi_1 + \phi_2)$ and $(\omega_1 - \omega_2, \phi_1 - \phi_2)$ Such a phenomenon, where all or some of the phase relationships between components are the same as the frequency relationships, is called Quadratic Phase Coupling (QPC). The detection of QPC would suggest that the signal has arisen from a non-linear process. The Bispectrum can be used as an identification tool for this, as reported by Spaargaren and English [59] or Kim and Powers [39]. However, Fitzpatrick and Rice [21] and Fitzpatrick [20] showed that it is difficult to obtain quantitative information from bispectral analysis and they proposed an alternative technique to investigate non-linear interactions. In the aero-engine situation, figure 6.5 shows the input models for upstream and downstream of the fan.

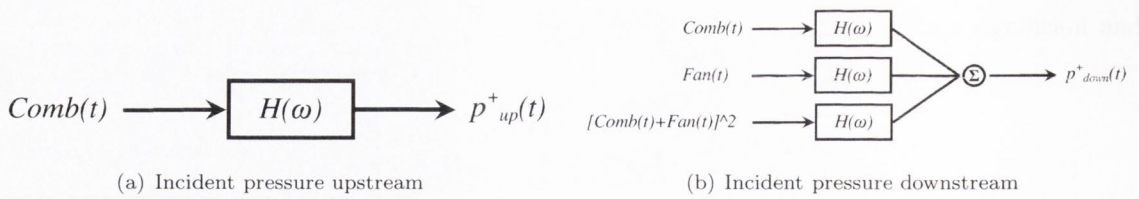


FIGURE 6.5: Incident pressure models accommodating a quadratic non-linear term.

The synthetic data was generated in Matlab using filtered statistically independent random data signals, where the filter used was a Butterworth IIR filter. Figure 6.6(A) shows the basic simulation. In addition to the input terms of figure 6.5, the exit plane measurement of an aero-engine is simulated to contain broad band jet noise in green. Tonal fan noise in is shown in red and low frequency band limited combustion noise in blue. Plots (B), (E) and (H) in figure 6.6 are identical to (A), (D) and (G) in this figure. Figure 6.6(C) shows the non-linear quadratic input $(G_{comb} + G_{fan})^2$ in addition to the others. A point to be noticed here, is how due to the frequency interactions, significant energy is created at frequencies where the linear terms' energy is quite low. Row 2 of this figure shows the sum of the components, in magenta, representing an exit plane measurement, and the combustion noise only in blue, representing an upstream measurement. Row 3 plots the coherence between these latter two, i.e. the combustion noise and the total noise. It is shown how for this *low* power case, the coherence is quite high.

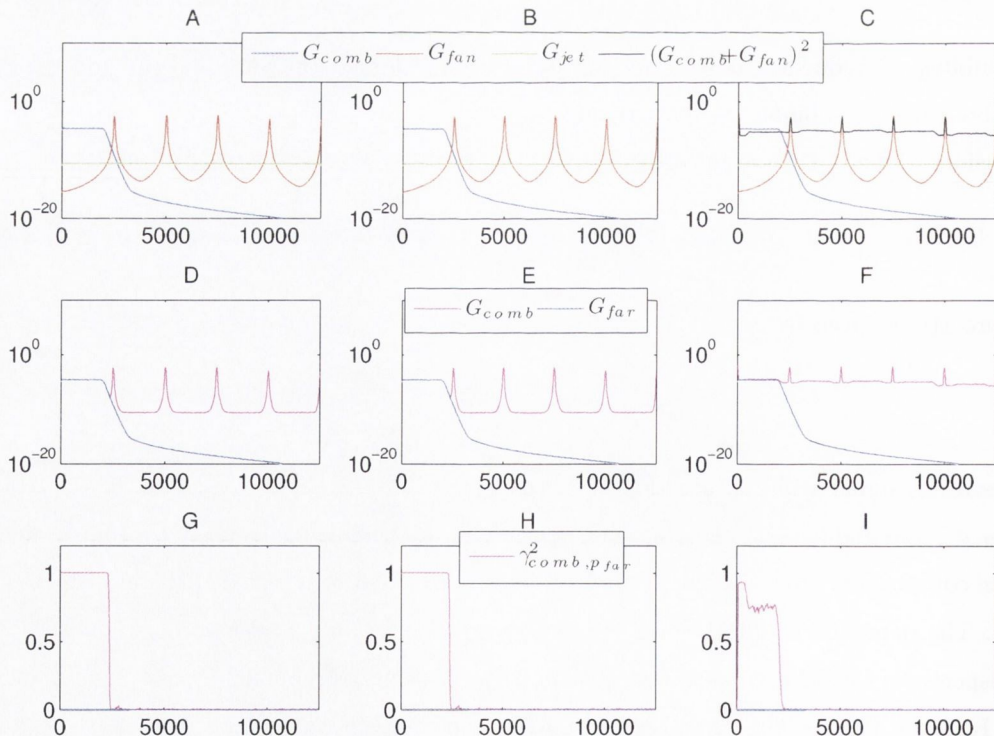


FIGURE 6.6: Combustion Noise, Fan Noise and Jet Noise simulation at a *low* power setting. Column 1 and column 2 are linear and are identical here. Column 3 contains a non-linear quadratic interaction term.

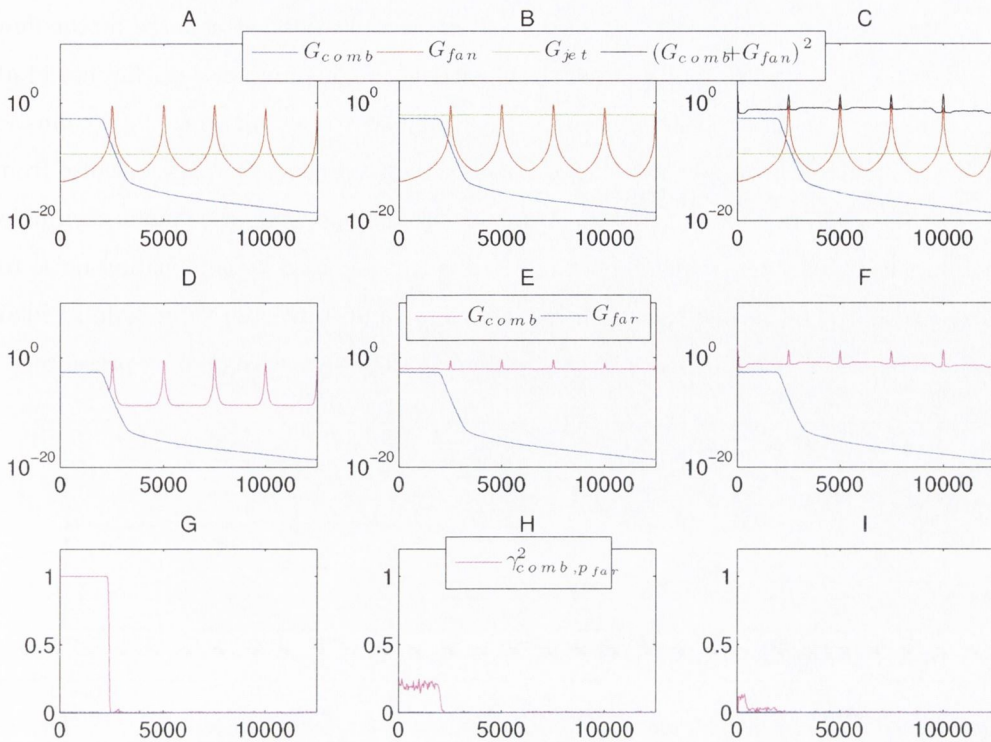


FIGURE 6.7: Combustion Noise, Fan Noise and Jet Noise simulation at a *high* power setting. In column 1, all three components have been increased by the same amount. In column 2, combustion and fan noise have been increased the same amount as column 1 but jet noise by relatively more. In column 3, the linear inputs are increased the same amount as in column 1.

Figure 6.7, plots the same information for the *high* power case. In column one all three inputs increase by the same amount resulting in no change to the coherence. In column 2, the fan noise and combustion noise increase by the same amount as in column 1, but the jet noise increases by relatively more. The coherence is seen to drop here, due to the relative decrease in contribution of the combustion noise to the total noise. This is what was assumed to be the case by Siller *et al* [58]. Column three shows the same increase in power of the three linear terms as in column 1 but in this case, due to the non-linear nature of the quadratic term, it increases relatively more, causing it to dominate, which results in the drop in coherence. It is therefore the presence of the non-linearity that causes the drop in coherence and not a decrease in the combustion noise relative to the other linear terms.

Given these two latter scenarios, *viz.* 1.) three linear terms only, where the jet noise is relatively higher than the combustion noise in that frequency range, and 2.) three linear terms, with the combustion noise being highest apart from the non-linear term in that frequency range, figure 6.8 may now be addressed. From observation of the second row, the total pressure measured is similar for the two cases, *i.e.*, tonal harmonics with a broad band noise floor. To insert a core liner aft of the fan in the first scenario will have little effect for this high power case as the fan noise is dominant and is created beyond the exit plane. In the second case however, there is a benefit to be gained, as the

low frequency noise is generated upstream of the exit plane and can be attenuated by the liner. Even greater noise attenuation may be attained by reducing the combustion noise (or fan noise) at source in the presence of a non-linear system which couples the two. By eliminating the combustion noise at source, its contribution will not only disappear from its low frequency range but also from higher interaction frequencies. In column 1 we see no benefit from eliminating the combustion noise where jet noise dominates. This figure highlights the benefits to be gained by combustion noise reduction in the presence of a non-linear interaction, but also how important it is to be able to identify the non-linear process as incorrect deductions can be made without knowledge of its presence.

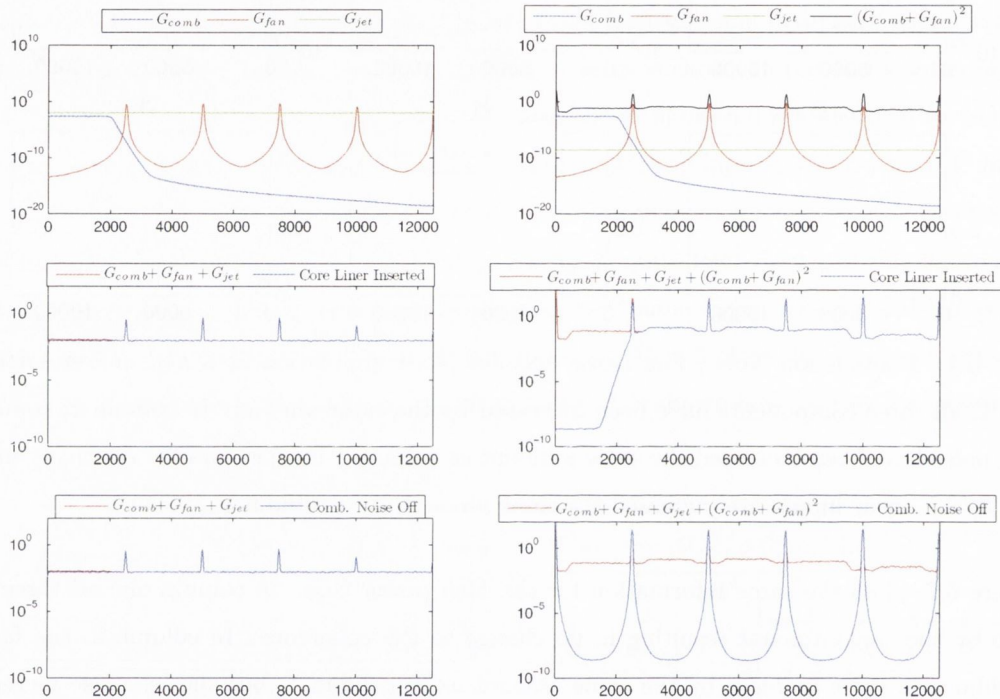


FIGURE 6.8: Comparison of the two scenarios. The total exit plane pressure is similar in both cases. However, in the first case Jet Noise dominates whilst in the second case it is the non-linear term which is greatest.

Figure 6.9 shows how a controlled experiment can test for non-linearity. By increasing the combustion noise only, the output can be observed to increase not only in the frequency range of the combustion noise but also at interaction frequencies. This technique is used on the experimental rig to detect a non-linear process across the fan.

A second set of simulations were performed with narrow band noise, for the combustor instead of the low frequency band limited noise used in the previous simulations. Jet noise is omitted from these simulations to simplify the analysis. It can be seen readily in figure 6.10(B) how the non-linear term is made up of double frequencies as well as sum and difference tones. The ability to identify the presence of the non-linear process is shown in figure 6.11 when a measure of the linear terms only is possible. By calculating the coherence between the linear sum of terms, $G_{comb} + G_{fan}$, and the

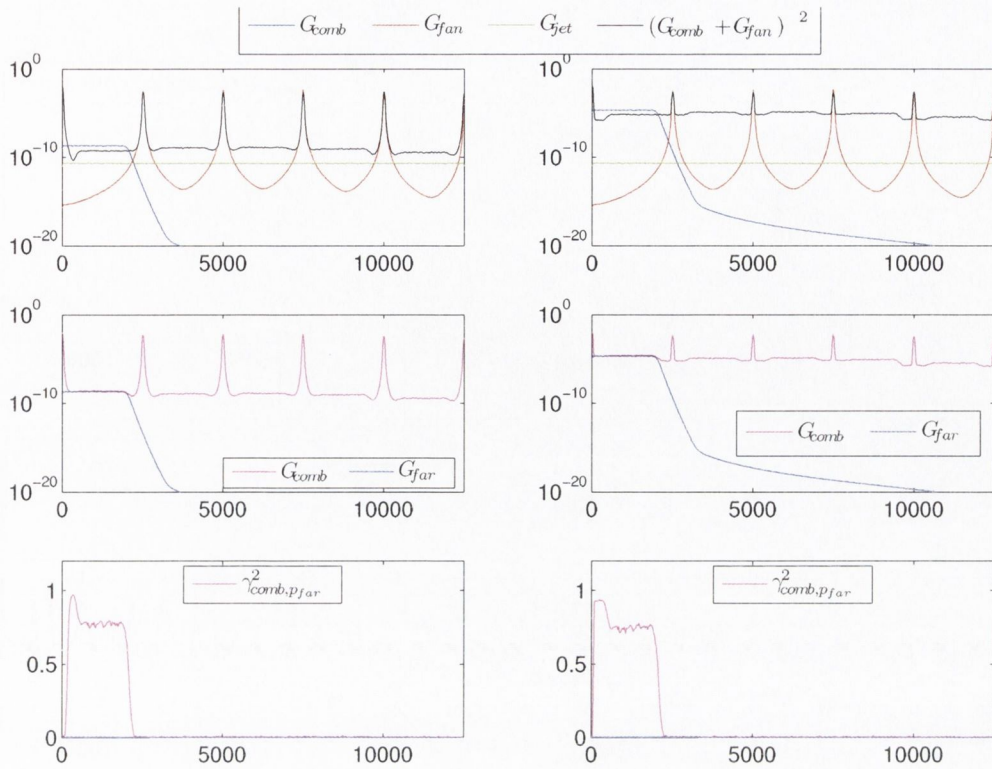


FIGURE 6.9: Technique to determine the presence of a non-linear process.

total, $G_{comb} + G_{fan} + (G_{comb} + G_{fan})^2$, subfigure (B), drops in coherence can be seen to occur at interaction frequencies. This coherence can be used in the coherent output power technique of section 5.2.1 to identify the non-linear contribution to the total measurement, see subfigure (C). The same data could be obtained by simply subtracting one from the other but can lead to negative quantities as shown in subfigure (D).

Thus, it can be seen that using this data, if the COP technique was used between the combustion noise only and the total noise, then the only contribution to the total noise made by the combustor would be identified as being low frequency narrow band noise. For a non-linear process this would be an incorrect deduction, however, as the combustor also contributes to the total noise at all the higher interaction frequencies too.

Without close inspection and measurement, the higher interaction frequencies could be misinterpreted as rotor-stator interaction noise, particularly for aero-engines with many blades and vanes over many stages.

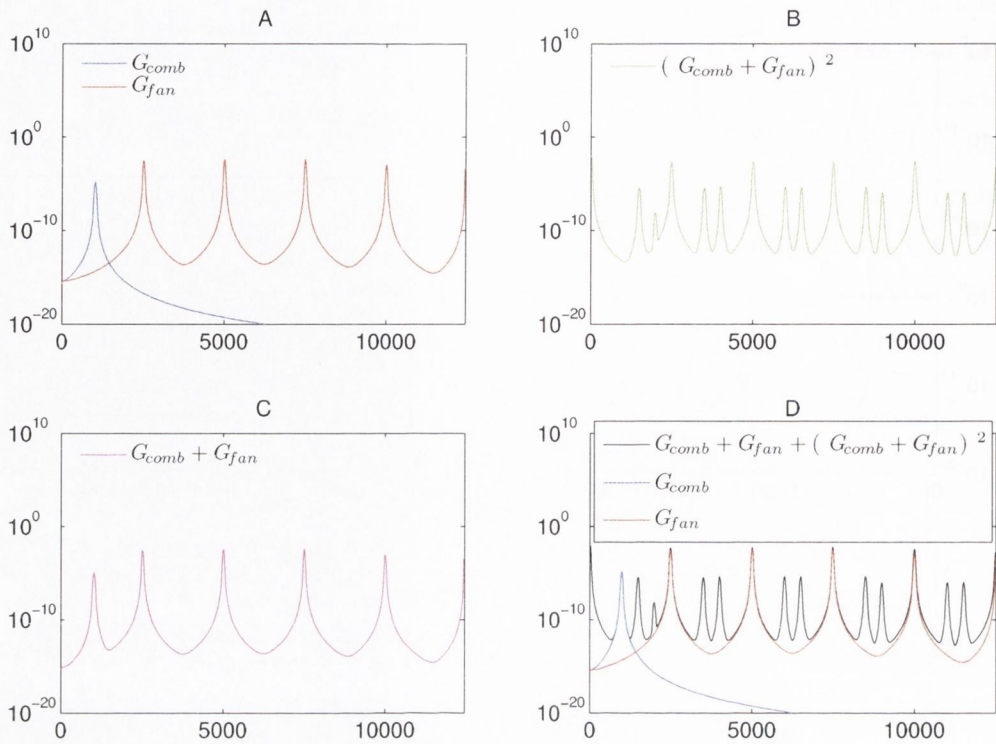


FIGURE 6.10: The non-linear interaction frequencies are more obvious when narrow band combustion and fan noise are combined. The fan noise has been omitted here to simplify the simulation.

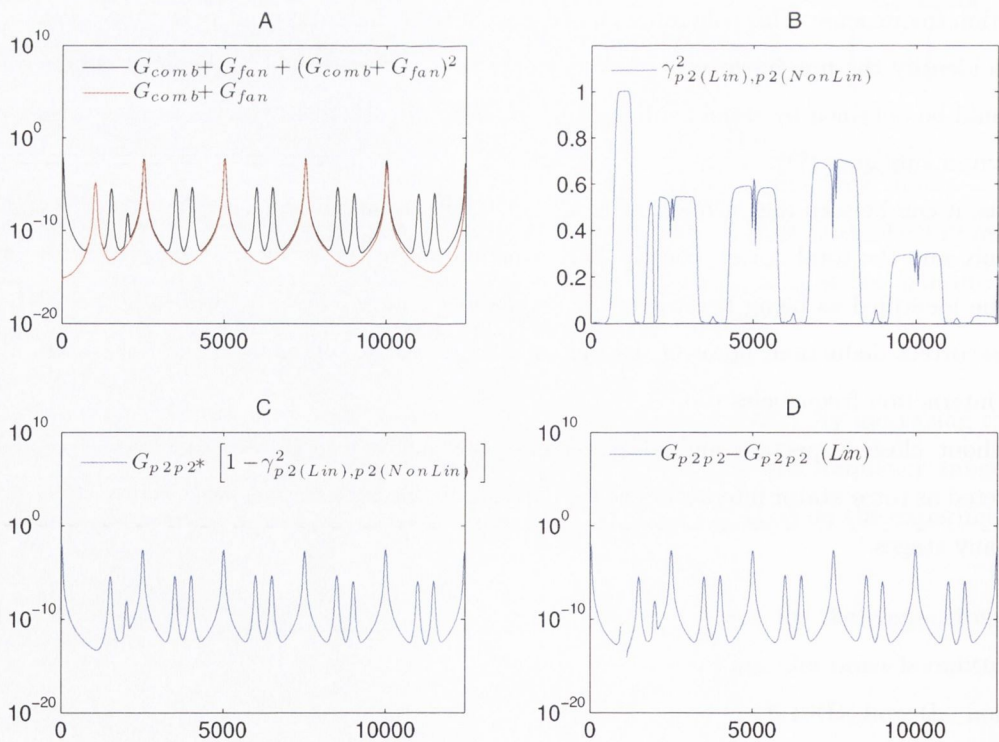


FIGURE 6.11: Using the coherent output power technique the non-linear term can be identified when a measure of the linear terms only is obtainable.

6.3 Time Domain Averaging

The previous section notes that the non-linear term could be identified if a measure of the combustion noise and fan noise separate from the total was attainable. These measurements can prove quite difficult to obtain, however, as the non-linear interaction occurs at the plane of the fan. However, a time domain averaging technique exists which is used to separate fan noise from the total noise. The basic principle is that the pressure patterns produced by the fan are repeated with every revolution of the fan. This concurs with section 2.5.2, as the spinning modes excited by rotor-stator interaction occur at nBPF. The technique consists of triggering an acquisition every time some point on the fan passes some fixed point on the duct. Successive acquired waveforms are averaged with each other in the time domain to obtain a waveform which is phase-locked to the rotor.

To investigate this a simulation of the technique was performed and is illustrated in the following figures. Figure 6.12(C) shows a simulated pressure measurement in the hot jet pipe of an aero-engine which consists of fan noise at nBPF and some other non-fan related noise which here is narrow band and titled combustion noise but could just as easily be broad band flow noise, jet noise, or the result of some non-linear interaction. Figure 6.13 shows a single decomposed block in the time domain of each of the four frequencies contributing to the signal. Each time block is a shaft revolution in length. Figure 6.14 shows a different time block for the components. Because the period for an oscillation of the combustion noise is unlikely to divide evenly into the time for a shaft resolution, this signal will be averaged out over time, whereas the fan related noise will be reinforced, as it in turn is repeated with each revolution. Figure 6.15 shows the result from the averaging, in green, after a fourier transform has been performed on the averaged time signal. Because frequency resolution is dependent on the time for a sample, see equation (B.15), the resolution deteriorates with increasing rpm. This technique has been used successfully by Yardley [65], Moore [45] and Enghardt *et al* [17] for example.

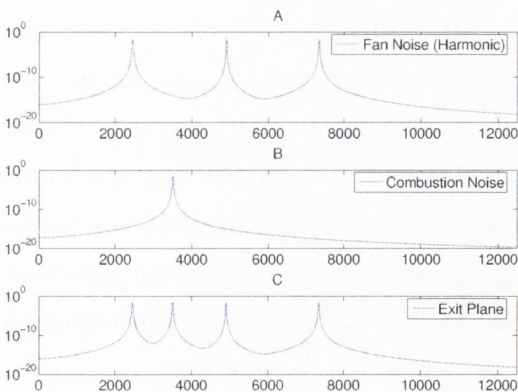


FIGURE 6.12: A simulation of an exit plane measurement comprising of three harmonics and a non-fan related input.

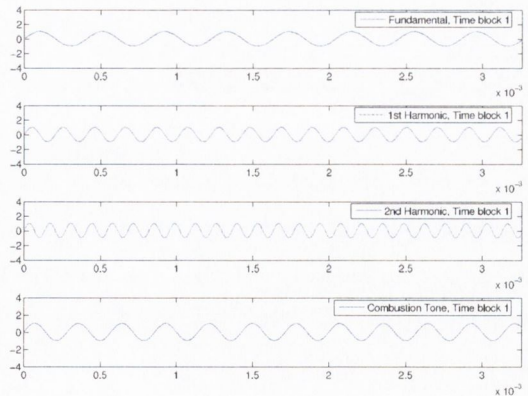


FIGURE 6.13: The four inputs in the time domain. The time block is a shaft rotation in duration.

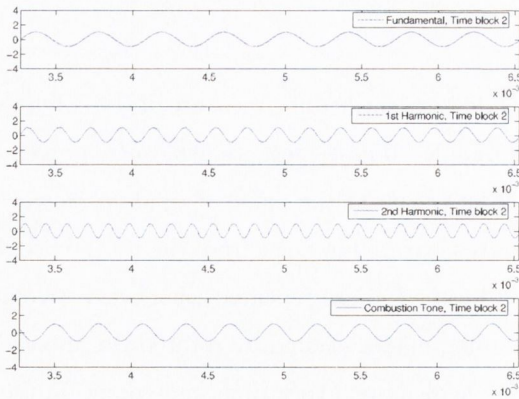


FIGURE 6.14: The same information as 6.13 but for a different time block. Only the non-fan related signal varies with time block.

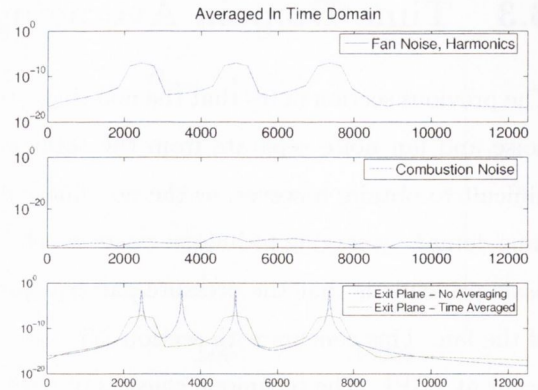


FIGURE 6.15: Result of the time domain averaging. The non-fan related term is averaged out of the measurements.

6.4 Investigation above plane wave region

An analysis was performed on the experimental rig to detect the presence of non-linearities. By varying the amplitude and frequency content of the speaker signal, the PSD of a microphone located downstream of the fan was examined. Figure 6.16 shows the PSD of the microphone when only the fan was turned on. A strong BPF is seen at $\approx 2450\text{Hz}$ and 4 other harmonics of it up to the Nyquist frequency of the acquisition. Superimposed on the plot are multiples of the rotational speed in Hz . This illustrates that some other peaks in the plot are related to imbalance in the fan. As is normal for a microphone mounted in a duct, pressure is seen to jump at cut-on frequencies of higher order modes, $\approx 4\text{kHz}$ for example. These values are given in table 6.1 for this diameter duct. Figure 6.17 shows this same data superimposed upon a measurement from the microphone when a tone from the speaker at 9.3kHz was radiated from the speaker with the fan turned off. For a linear system, this is what would be expected if both speaker and fan were turned on at the same time. However, figure 6.18 shows the actual recorded spectrum. A sum tone of the BPF plus the 9.3kHz is shown clearly at $\approx 11.7\text{kHz}$ and it is, in this case, seen to be larger in magnitude than the speaker tone. Returning to our non-linear term $[Comb(t) + Fan(t)]^2$, a simple simulation was carried out using these frequencies, i.e., $BPF = 2450$ with four harmonics, and $Comb = 9.3\text{kHz}$. Figure 6.19 shows the non-linear term in green. Superimposed upon this plot are blue dotted lines to indicate the difference frequencies (the first one being $(4 * BPF) - 9.3\text{kHz} = 500\text{Hz}$) and a red dotted line for the first sum frequency, $2450\text{Hz} + 9.3\text{kHz} = 11.75\text{kHz}$. Comparison with figure 6.18 reveals that only the sum term is present due to the interaction.

A further set of tests was carried out where the speaker tone was incremented in steps of 500Hz or 250Hz , from 500Hz to 12kHz . A waterfall plot of these results is shown in figure 6.20. The first averaged PSD in this plot is for the fan-only turned on. With each successive test, the frequency from the speaker is increased. This plot is revealing, as there is no indication of non-linear interaction until

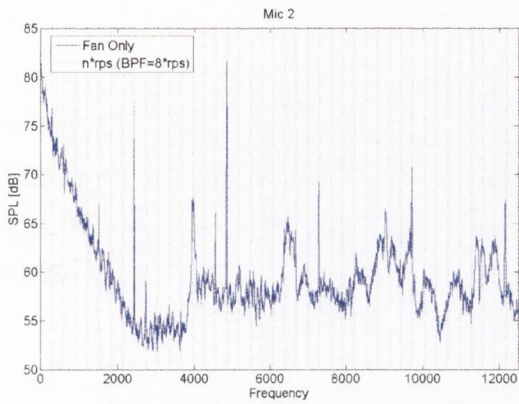


FIGURE 6.16: Spectrum from a microphone downstream of the fan rotating.

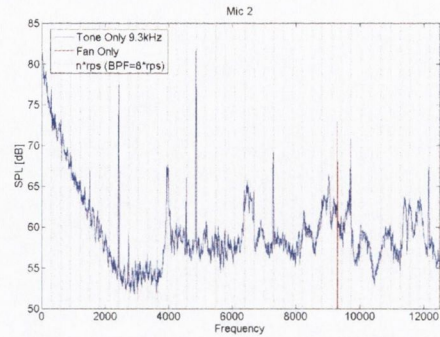


FIGURE 6.17: The same spectrum of 6.16 superimposed onto a spectrum where a tone at 9.3kHz is emitted from the speaker with the fan not rotating.

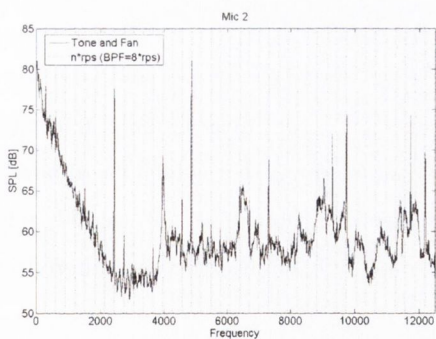


FIGURE 6.18: Spectrum downstream when both the fan is rotating *and* the tone is emitted. A sum tone at 11.7kHz is visible.

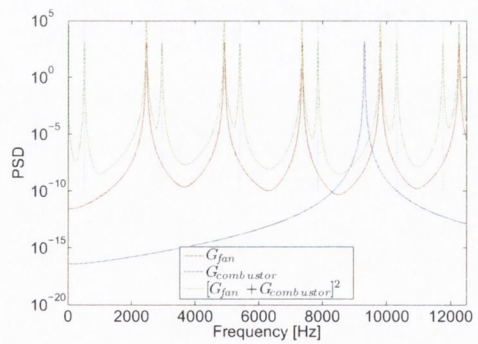


FIGURE 6.19: Simulated data representing a quadratic interaction between the fan and combustor using the BPF and harmonics of figure 6.16 and a combustor frequency of 9.3kHz .

the speaker frequency reaches 8.75Hz , above which only a sum tone is detectable. To understand the reason for this, it was necessary to carry out an analysis of the higher modes in the duct .

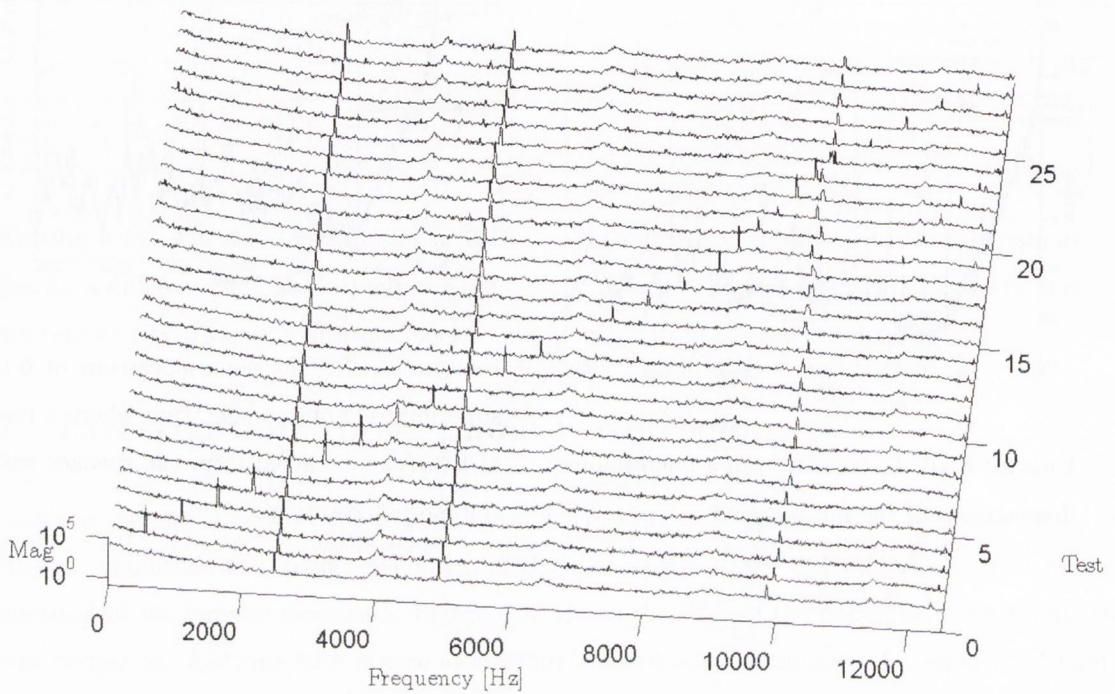


FIGURE 6.20: Waterfall plot of tests. The speaker frequency is increased in steps of either 250Hz or 500Hz. A sum frequency interaction begins to appear above $\approx 11200\text{Hz}$

6.4.1 Tyler and Sofrin Analysis

Tyler and Sofrin, [63], analysed the BPF and its harmonics in a compressor model consisting of a stator and rotor in a duct. They reported two significant results, the first in which the modes excited are not stationary but are spinning and may spin in either direction, and the second, where the number of rotor blades along with the number of stator vanes determines the circumferential order of the modes excited in the duct, in accordance with equation (2.61).

From the theory of chapter 2 and table 2.1, the cut-on frequencies for a duct of radius= 0.0256m are given in table 6.1. If, in addition to this information, the modes excited by the vane-axial fan, with blade number, $B = 8$ and vane number, $V = 5$ are calculated using the theory of section 2.5.2, then the modes present and propagating in the duct can be determined.

Figure 6.21, shows the waterfall plot with the cut-on frequencies of table 6.1 superimposed. It can be seen clearly how the interaction tone appears only above $\approx 11200\text{Hz}$, which is either the $(\pm 4, 0)$ cut-on frequency or the $(\pm 1, 1)$ cut-on frequency. It seems likely therefore, that the non-linear

m, n	0	1	2	3	4	5
0	0	8102	14835	21512	28174	34827
± 1	3893	11273	18050	24753	31430	38104
± 2	6458	14180	21081	27849	34568	41255
± 3	8884	16959	23991	30842	37615	44342
± 4	11244	19628	26816	33757	40591	47366
± 5	13566	22245	29577	36609	43508	50326

TABLE 6.1: Cut-on frequencies, $f_{m,n}^{cut-on}$, [Hz], for 0.05115m diameter cylindrical duct, $c=340\text{m/s}$ and $M=0.035$.

term $[Comb(t) + Fan(t)]^2$ plotted in figure 6.19, needs to be used in conjunction with duct modal theory. That is to say, if energy at two frequencies interact to create energy at a third, then this energy will only propagate down the duct if the mode which carries it is above its cut-on frequency. Based on this idea, it is concluded that the interaction tone has a modal structure of either $(+4, 0)$, $(-4, 0)$, $(+1, 1)$ or $(-1, 1)$, or possibly some combination of these. In addition, this modal structure comes about as a result of the interaction of the modal structure of the BPF frequency with that of the speaker frequency. Using equation (2.61), a table of some of the excited modes can be formed and are shown in table 6.2. Given the number of blades and vanes, these are the only modes which are excited by the vane-axial fan and are done so at their respective blade-pass frequency harmonic. Using table 6.1, the modes which propagate at these frequencies, i.e. once excited, are above their cut-on frequency, are given in table 6.3. These results are now plotted in figure 6.22 to indicate the theoretical modal structure of the BPF and harmonics. It should be noted that although a mode may be cut-on, its magnitude depends, among other things, on the distribution of loading on the blades and stators. This implies that some modes will contribute more to the pressure field than others. Tests by Heidelberg [26] have shown a drop of as much as 13dB by changing the sweep angle of the vanes for the same aerodynamic performance and solidity. This is one of the common motivations to experimentally measure the modal content of these tones, so that liners may be designed to address specific significant modes. It is interesting to see for example, the low energy content of the 3BPF tone. This is a counter-rotating mode and as the rotor is downstream of the stator, and if it is assumed that the mode is created between the two, i.e. by the rotor cutting through the stator wakes, then the low energy can be explained by the difficulty of the counter-rotating mode to propagate through the swirl zone and the rotor blades. Heidelberg [26] and Sutcliff [61] made similar comments. It was verified that the magnitude of the 3BPF tone was greater upstream of the assembly. More difficult to explain is the significant peak at the BPF. According to the Tyler-Sofrin analysis, no mode excited at the BPF is cut-on for that frequency, as can be seen from table 6.3. There is evidence of vibration being measured by the microphones, whether directly or as radiated sound from vibration, as in figure

6.16 for example. With harmonics of the rotational speed of the fan superimposed on the plot, strong peaks are seen at 1rps, 5rps, 9rps and 15rps for example, which must be related to imbalance in the rotor. However, the peak at the BPF cannot be direct vibrational energy, as it is also measured by a microphone outside and disconnected to the rig, see the exit region microphone 7 of figure 4.23. It must therefore be acoustic, most probably the result of manufacturing imperfections in the assembly resulting in the vanes and blades being un-equispaced and at slightly different axial locations. If one vane were to be closer to the rotor than the others for example, then the Tyler-Sofrin analysis would result in the (0,0) mode being excited which would be cut-on at this frequency.

It has been shown that acoustic energy in a duct at a certain frequency may interact with fan noise at a different frequency to scatter energy to a third frequency. This would appear to support the model suggested in figure 6.4, but as discussed above, the proposal that the process is a non-linear quadratic interaction, figure 6.19, is only partially verified. In order to understand why the sum interaction only seems to occur above the cut-on frequency of certain higher-order modes, it would be useful to perform a modal decomposition of the pressure field upstream and downstream of the fan in order to determine the modal content of the incident tone and the sum tone. In addition to this, as it would be informative to study the relationship between the upstream and downstream incident waves, with a view to determining the incident wave frequency response function or coherence across the fan, a modal decomposition is necessary to separate the incident signals. As the sum tone occurs above the plane wave cut-off frequency, the plane wave decomposition technique of section 2.4.1 is insufficient and a more advanced decomposition must be performed to separate out the different azimuthal and radial modes from each other. In order to study the relationship between upstream and downstream, a decomposition must be carried out fore and aft of the fan simultaneously.

$BPF(n=1)$		$2BPF(n=2)$		$3BPF(n=3)$		$4BPF(n=4)$		$5BPF(n=5)$	
q	$m = 8 + 5q$	q	$m = 16 + 5q$	q	$m = 24 + 5q$	q	$m = 32 + 5q$	q	$m = 32 + 5q$
-3	-7	-5	-9	-7	-11	-8	-8	-10	-10
-2	-2	-4	-4	-6	-6	-7	-3	-9	-5
-1	+3	-3	+1	-5	-1	-6	+2	-8	0
0	+8	-2	+6	-4	+4	-5	+7	-7	+5
+1	+13	-1	+11	-3	+9	-4	+12	-6	+10

TABLE 6.2: The circumferential order of some acoustic modes excited by the rotor-stator interaction

Speed	BPF (2400 Hz)	2BPF (4800 Hz)	3BPF (7200 Hz)	4BPF (9600 Hz)	5BPF (12000 Hz)
18000 rpm (Mach=0.035)	None	(+1,0)	(-1,0)	(-3,0) (+2,0)	(0,0) (0,1)

TABLE 6.3: The propagating modes excited by the vane-axial fan at the first five BPF's

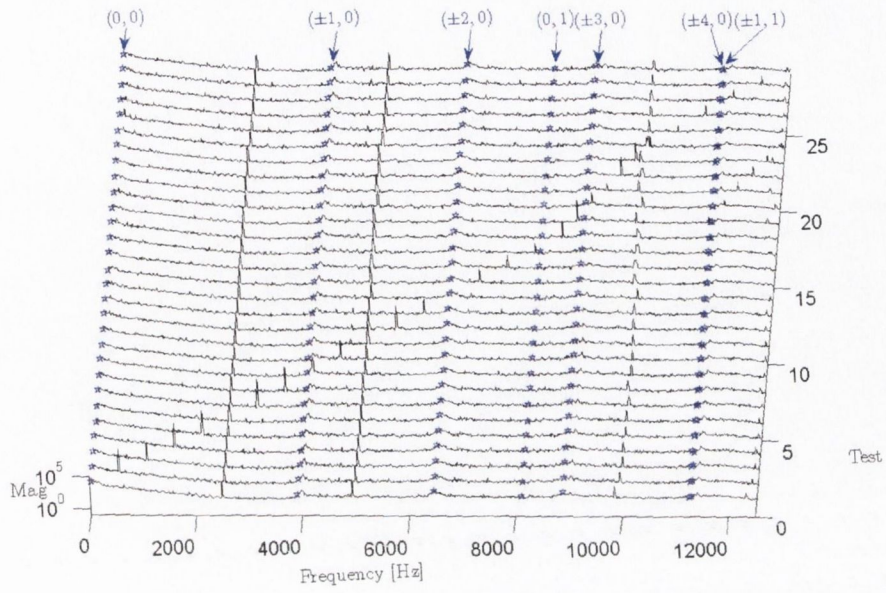


FIGURE 6.21: Waterfall results with cut-on frequencies superimposed.

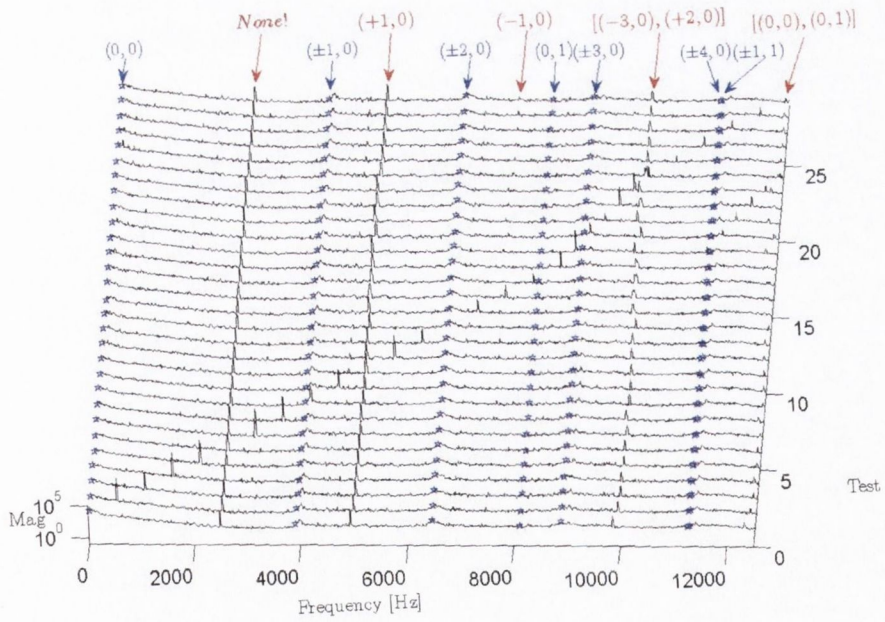


FIGURE 6.22: Waterfall results with cut-on frequencies and modes excited at BPF harmonics indicated.

Chapter 7

Acoustic Modal Decomposition In a Duct

7.1 Introduction

The sound fields in the inlet and outlet ducts of axial fans, compressors and aircraft engines propagate as higher order spinning acoustical modes in a wide frequency range. An in-duct modal decomposition technique is a measurement procedure from which one can determine the amplitudes of the acoustic modes propagating in a duct. A limited number of techniques have been reported which employ different methods to measure these modes. A combination of these techniques, in particular those of Yardley [65], Åbom [5] and Enghardt *et al* [18], is designed here with a view to decomposing the pressure field in such a way as to have the following characteristics:

1. incident and reflected modes can be identified;
2. a mean flow can be accommodated;
3. a frequency response function technique is employed;
4. radial, as well as azimuthal, modes can be identified;
5. duct-wall flush-mounted microphones only are used for the decomposition;
6. the decomposition is performed for all frequencies not only at the BPF and harmonics;
7. data is acquired at all measurement locations simultaneously.

These characteristics will each be addressed in turn:

1 A large number of the methods suggested in the literature have been formulated with the assumption that propagating modes exist only in one direction. If modes due to direct sound radiation, as well as to reflections from duct discontinuities or obstructions, are to be resolved, then the field must be decomposed into incident and reflected waves. In addition, as mentioned above, if the sound source created at the fan is to be isolated, the incident wave needs to be acquired. Incident waves acquired *simultaneously* fore and aft of the fan allow for frequency response functions and coherence across the fan to be studied.

2 Although we are interested in the fan as a source of acoustic energy, it is, by definition, an air-mover, and as a result, a mean flow is induced in the duct. As Åbom [6] reports, acoustic power measurements in a flow duct with a highly reactive field, such as from reflections, can result in large errors, even for small Mach numbers, when flow effects are ignored, Jacobsen [30]. These flow effects can be accounted for in the axial wavenumber, equations (2.21) and (2.22).

3 An extension of the transfer function technique of Åbom [6] is developed here which allows for calibration of spectra as well as for flow noise reduction by averaging in the frequency domain, as discussed in section 5.6.2.

4 With reference to figure 6.21, the sum frequency occurs at a sufficiently high frequency for five azimuthal and two radial modes to have cut-on. In order to identify the modal content at this frequency, the azimuthal modes expressed in equation (2.17), must be further decomposed into their constituent radial modes as in equation (2.18).

5 An established experimental method for assessing the sound field in ducts is to acquire a 2-D spatial sound pressure distribution in the duct at a minimum of one fixed axial location. Instead of performing a 2-D Fourier transform with the data however, it is possible to perform two 1-D Fourier transforms, as the pressure functions in the circumferential and radial directions are orthogonal over the finite range of either the radius or the complete angular revolution of 2π . When this is possible, a mixed approach of performing a 1-D Fourier transform in the circumferential direction can be used in conjunction with a set of linear equations in the radial directions to solve for the radial coefficients. However, on the inlet side of a turbo-machine, microphone probes immersed in the flow cannot be employed because the wake from microphones and their supports would disturb the inlet flow conditions of the machine and alter its acoustic characteristics. In addition, reflections would result when located either upstream or downstream. The methods of Yardley [65], Åbom [5] and Tapken *et al* [62] each employ a technique where a 1-D Fourier transform in the circumferential direction is employed, but the set of linear equations are built up by locating multiple flush-mounted rings of microphones along the axis instead of at different radial positions. A method based on this approach is presented here.

6 By examining the full frequency range up to the nyquist frequency of the acquisition, an attempt can be made to identify non-linear effects. These should be observable at interaction frequencies, more noticeable at frequencies other than multiples of the BPF.

7 By far the most common form of presenting results in the literature is as *mode power* for the circumferential mode and sometimes decomposed into the radial order mode power content also. For the case above, where the 2-D sound field is acquired at specific axial locations, the flow field disturbance brought about by the physical presence of the microphones is reduced by employing a radial rake of microphones which is rotated circumferentially at a speed accurately related to the shaft speed. An acquisition trigger is also linked to the shaft speed. As mentioned in section 6.3, using the fact that modal patterns repeat themselves with shaft rotation, this method produces a mode power which is phase-locked to the rotor, even though all measurements in the plane are not taken simultaneously. Holste and Neise [27], Enghardt *et al* [17] and Heidelberg [26] for example, all use this technique. Enghardt *et al* [18], whilst using flush-mounted microphones located linearly in the axial direction only, employs a similar triggering technique, rotating a single axial array of microphones with each acquisition. Here a set-up more similar to Yardley [65], Åbom [6] and Tapken *et al* [62] is implemented, where all duct-wall, flush-mounted measurements are acquired simultaneously. This is necessary for frequency response function and coherence measurements between modes.

7.2 Mathematical Formulation

The technique developed here uses as its basis the expression for pressure in a duct given by equation (2.19). Due to the developments of section 6.4.1, the azimuthal index m may be positive or negative due to the possibility of these modes spinning in either direction. Similar to the presentation of Åbom [5],¹ equation (2.19) may be re-written as

$$\hat{p} = \sum_{m=1-M}^{M-1} \sum_{n=0}^{N-1} \left[\hat{a}_{m,n}^+ e^{-jk_{x,m,n}^+ x} + \hat{a}_{m,n}^- e^{+jk_{x,m,n}^- x} \right] C_{m,n} J_m(k_{r,m,n} a) e^{(jm\Theta)} \quad (7.1)$$

where M is the number of azimuthal modes cut-on, and N is the number of radial modes. To decompose the sum tone of figure 6.21, $M = 5$ and $N = 2$. The fact that the measurement locations are flush-mounted to the duct wall is indicated by a value of $r = a$ in the equation.

The normalised mode shape

$$\Psi_{m,n}^n(r, \theta) = C_{m,n} J_m(k_{r,m,n} a) e^{(jm\Theta)} \quad (7.2)$$

is normalised by a constant $C_{m,n}$ in order to accommodate duct sections of differing cross-sectional shapes, using the condition

¹This development is present in the section *Extension of the measurement range* of the 1987 report by Åbom [5] but is omitted from his 1989 journal publication, [6].

$$\frac{1}{S} \int_S |\Psi^n|^2 ds = 1 \quad (7.3)$$

where S is the cross sectional area. This is the form used by Joseph *et al* [33]. This results in the normalisation constant being defined as

$$C_{m,n} = \sqrt{\frac{1}{\frac{1}{S} \int_S |\Psi^n|^2 ds}} \quad (7.4)$$

A table of normalisation constants is given in table 7.1

m, n	$k_{r,m,n}a$	$J_m(k_{r,m,n}a)$	$C_{m,n}$	$\Psi_{m,n}^n(a, 0)$
0,0	0	1	1	1
$\pm 1,0$	1.84	0.5819	2.9027	1.6891
$\pm 2,0$	3.05	0.4865	3.8578	1.8768
$\pm 3,0$	4.20	0.4344	4.6654	2.0266
$\pm 4,0$	5.32	0.3997	5.3890	2.1540
0,1	3.83	-0.4028	2.4952	-1.0051
$\pm 1,1$	5.33	-0.3461	4.1736	-1.4445

TABLE 7.1: The eigenvalue $k_{r,m,n}$, the value of the bessel function at the duct wall (from figure 2.3), the normalisation constant and the normalised mode shape at $r = a$ and $\theta = 0$ for the first 5 azimuthal modes and first 2 radial modes.

An illustration of the normalisation process is given in figure 7.1. Subfigure (B) shows the normalised (1, 1) mode, where the volume under the surface of the square of the modulus of mode (1, 1), in subfigure (A), divided by its cross-sectional area, should be equal to unity, according to equation (7.3).

The decomposition technique used here is carried out in two stages. Firstly, an azimuthal decomposition is carried out using microphones located circumferentially around the duct. This stage employs a form of equation (2.17) which is

$$\frac{\hat{p}_{l,k}}{\hat{p}_{ref}} = \sum_{m=1-M}^{M-1} h_{m,k} e^{[jm\Theta_l]} \quad \text{where} \quad \left\{ \begin{array}{l} k = 0, 1, \dots, (2N-1); \\ l = 0, 1, \dots, (2M-2); \\ \Theta_l = \frac{2\pi l}{2M-1} \end{array} \right. \quad (7.5)$$

This decomposition is repeated at different axial locations in order to decompose these modes into both the radial modes *and* their incident and reflected components. This second stage uses a form of equation (2.18) given here by

$$\hat{p}_{ref} h_{mk} = \sum_{n=0}^{N-1} \left[\hat{a}_{m,n}^+ e^{-jk_{x,m,n}^+ x_k} + \hat{a}_{m,n}^- e^{+jk_{x,m,n}^- x_k} \right] C_{m,n} J_m(k_{r,m,n}a) \quad (7.6)$$

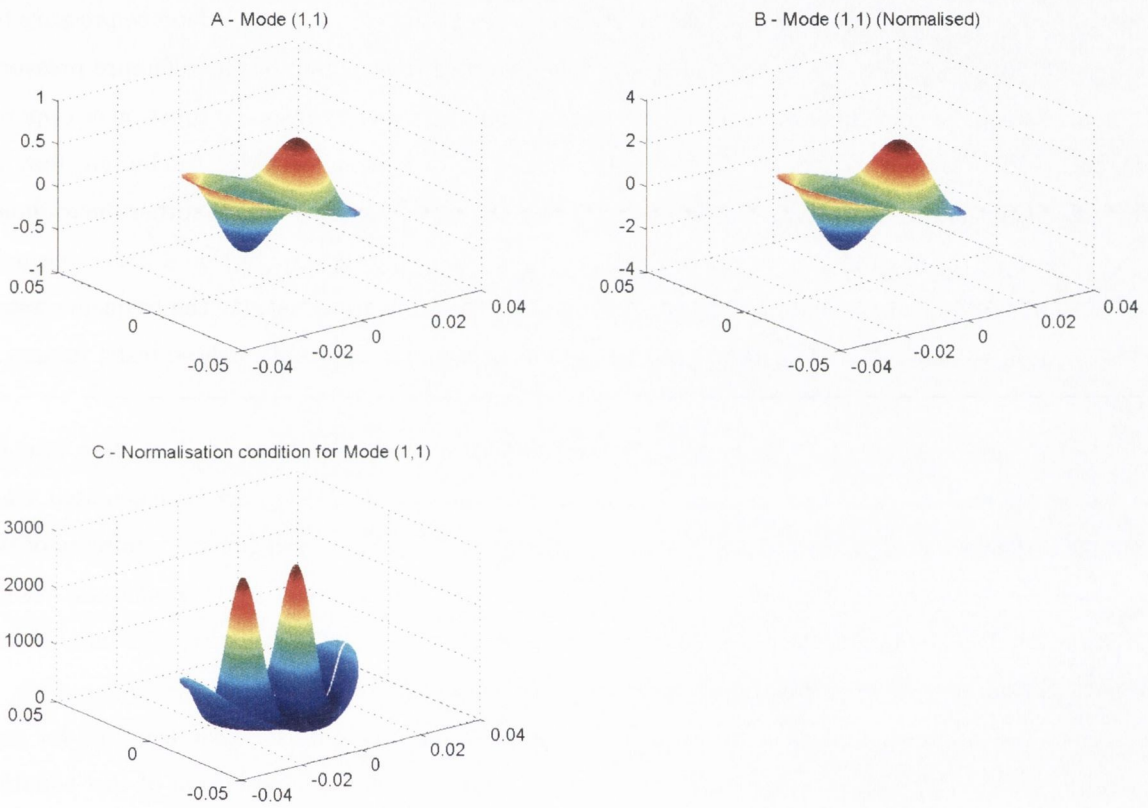


FIGURE 7.1: The (1,1) mode shape from equation (2.14), the normalised (1,1) mode shape from equation (7.2), and the normalisation condition from equation (7.3).

From this equation the unknown amplitudes $\hat{a}_{m,n}^+$ and $\hat{a}_{m,n}^-$ can be determined.

Beginning with the first stage and equation (7.5); a circumferential mode can be determined uniquely if at least two measurements per its azimuthal wavelength $\frac{2\pi}{m}$ are taken. This means 9 microphones should be sufficient for modes $m = -4$ to $+4$, where the direction is detected by the phase of the angle θ , see Holste and Neise [27] and Åbom [5] for similar reasoning. It should be noted, however, that additional microphones are required when additional modes are present, even though not cut-on, as would be the case near an obstruction. Also, aliasing is possible when insufficient microphones per modes cut-on are employed as discussed in Holste and Neise [27]. For a particular pressure measurement, $\hat{p}_{l,k}$, where l is the circumferential coordinate and k the axial coordinate, as shown in figure 7.2, a frequency response function can be calculated using any reference pressure (or the signal to the speaker), and used to calculate the modified (normalised by the reference pressure) azimuthal mode, as per equation (7.5). The benefit of using a frequency response function as opposed to the complex pressure is two-fold: firstly, flow noise, which is significant due to the fan, may be reduced, as discussed in section 5.6.2; secondly, if the reference pressure is from another microphone, as opposed to the speaker for example, then the calibration procedure of section 4.2 may be used to account for frequency response differences between different microphones. As the frequency range is so high, a second calibration rig to the one used in section 4.2 was used in these tests, images of which can be seen in appendix C.

To expand out equation (7.5) for the purposes of clarity, equations (7.7) and (7.8) show how for a particular axial location, k , the modified azimuthal modes (-4 to $+4$) may be calculated via a matrix inversion. This procedure needs to be repeated for different axial locations; a minimum of two to determine incident and reflected amplitudes. Furthermore, for the mode (-1) , for example, as the second radial mode amplitude is an additional unknown, *viz.* $(-1,0)$ and $(-1,1)$, a minimum of four axial locations are required, for the incident and reflected amplitudes.

Once the modified azimuthal modes in the circumferential direction have been acquired for each axial location, the second stage is carried out, using equation (7.6). An expansion of this equation is shown in equation (7.9) and (7.10) and consists for a second time of setting up a system of linear equations for which the unknowns may be solved by matrix inversion.

For an azimuthal mode such as $(+2)$, for example, in contrast to (-1) , only the first radial mode has been cut-on at the sum frequency, and so, only two axial rings of microphones are required to decompose the mode into the incident and reflected wave amplitudes. However, all four rings should be used if possible, to minimise disturbances from various measurement errors and to avoid the influence from the singularities discussed in section 2.4.2. This will result in an over-determined problem which can be solved using a least squares procedure such as a pseudo-inverse. Such procedures are available in *Matlab*. An example of this system of equations is given in equations (7.11) and (7.12). This decomposition formulation is applied to the experimental rig in the following section.

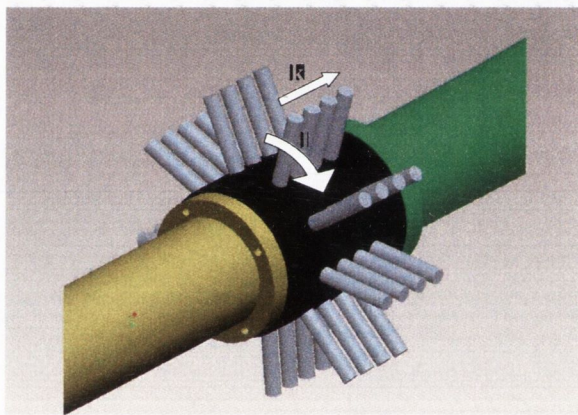


FIGURE 7.2: k and l coordinate scheme for equation (7.5)

$$\hat{p}_{ref} \begin{Bmatrix} h_{2,x_0} \\ h_{2,x_1} \\ h_{2,x_2} \\ h_{2,x_3} \end{Bmatrix} = \begin{bmatrix} e^{-jk_{x,2,0}^+ x_0} C_{2,0} J_2(k_{r,2,0} a) & e^{+jk_{x,2,0}^- x_0} C_{2,0} J_2(k_{r,2,0} a) \\ e^{-jk_{x,2,0}^+ x_1} C_{2,0} J_2(k_{r,2,0} a) & e^{+jk_{x,2,0}^- x_1} C_{2,0} J_2(k_{r,2,0} a) \\ e^{-jk_{x,2,0}^+ x_2} C_{2,0} J_2(k_{r,2,0} a) & e^{+jk_{x,2,0}^- x_2} C_{2,0} J_2(k_{r,2,0} a) \\ e^{-jk_{x,2,0}^+ x_3} C_{2,0} J_2(k_{r,2,0} a) & e^{+jk_{x,2,0}^- x_3} C_{2,0} J_2(k_{r,2,0} a) \end{bmatrix} \begin{Bmatrix} \hat{a}_{2,0}^+ \\ \hat{a}_{2,0}^- \end{Bmatrix} \quad (7.11)$$

$$\begin{Bmatrix} \hat{a}_{2,0}^+ \\ \hat{a}_{2,0}^- \end{Bmatrix} = \hat{p}_{ref} \begin{bmatrix} e^{-jk_{x,2,0}^+ x_0} C_{2,0} J_2(k_{r,2,0} a) & e^{+jk_{x,2,0}^- x_0} C_{2,0} J_2(k_{r,2,0} a) \\ e^{-jk_{x,2,0}^+ x_1} C_{2,0} J_2(k_{r,2,0} a) & e^{+jk_{x,2,0}^- x_1} C_{2,0} J_2(k_{r,2,0} a) \\ e^{-jk_{x,2,0}^+ x_2} C_{2,0} J_2(k_{r,2,0} a) & e^{+jk_{x,2,0}^- x_2} C_{2,0} J_2(k_{r,2,0} a) \\ e^{-jk_{x,2,0}^+ x_3} C_{2,0} J_2(k_{r,2,0} a) & e^{+jk_{x,2,0}^- x_3} C_{2,0} J_2(k_{r,2,0} a) \end{bmatrix}^{-1} \begin{Bmatrix} h_{2,x_0} \\ h_{2,x_1} \\ h_{2,x_2} \\ h_{2,x_3} \end{Bmatrix} \quad (7.12)$$

7.3 Experimental Results

7.3.1 Test Set-ups

In order to determine the modal content of the incident tone and the sum tone, as well as to verify the Tyler-Sofrin analysis of the nBPF frequencies shown in table 6.3, a limited modal decomposition was carried out upstream and downstream of the fan. Section 7.2 develops the need for 9 microphones circumferentially spaced per axial ring, where the axial spacing should satisfy equation (2.47) to avoid frequency drop-outs due to singularities in the formulation. For a frequency range up to the nyquist frequency of $12.5kHz$, an axial spacing of $13mm$ was chosen as being sufficient. An error analysis performed by Åbom and Bodén [4], results in a more comprehensive spacing requirement

$$0.1\pi(1 - M^2) < \frac{2\pi fs}{c} < 0.8\pi(1 - M^2) \quad (7.13)$$

This takes additional errors into account, such as those in the input data due to the frequency response function, microphone positions and Mach number, in addition to the sensitivity of the calculation formulas to errors in the input data. Equation (7.13) calculates a frequency range of $1306Hz - 10448Hz$, for a spacing of $13mm$, in which the error is of the same order of magnitude as the minimum error to be found at $ks = \pi(1 - M^2)/2$. As the lower frequency limit increases with decreasing spacing, $13mm$ was chosen as a good compromise between upper and lower error bands. Ideally, two sets of tests would be performed with different spacings, or, as already mentioned, a greater number of axial locations than the minimum required would be used, producing an overdetermined system of equations which would serve to minimise the errors, as discussed and employed by Åbom [5] and Tapken *et al* [62]. Seung-Ho Jang and Jeong-Guon Ih [31] show clearly how the error band for a fixed microphone spacing can be increased with additional axial microphones for the plane wave decomposition.

Figure 7.3 shows the ideal experimental set-up. In order to resolve up to the cut-on frequency of the $(\pm 5, 0)$ mode, i.e., to decompose the modes listed in the caption of figure 7.3, 9 circumferential

microphones are needed for the 9 spinning modes, 2 axial rings of 9 to be able to solve for the second radial mode of each of these circumferential modes and twice that amount is needed to be able to decompose into the incident and reflected amplitudes. Two banks of these 36 microphones, giving a total of 72, are needed to decompose upstream and downstream simultaneously. Due to microphone and acquisition channel limitations, this was not feasible.

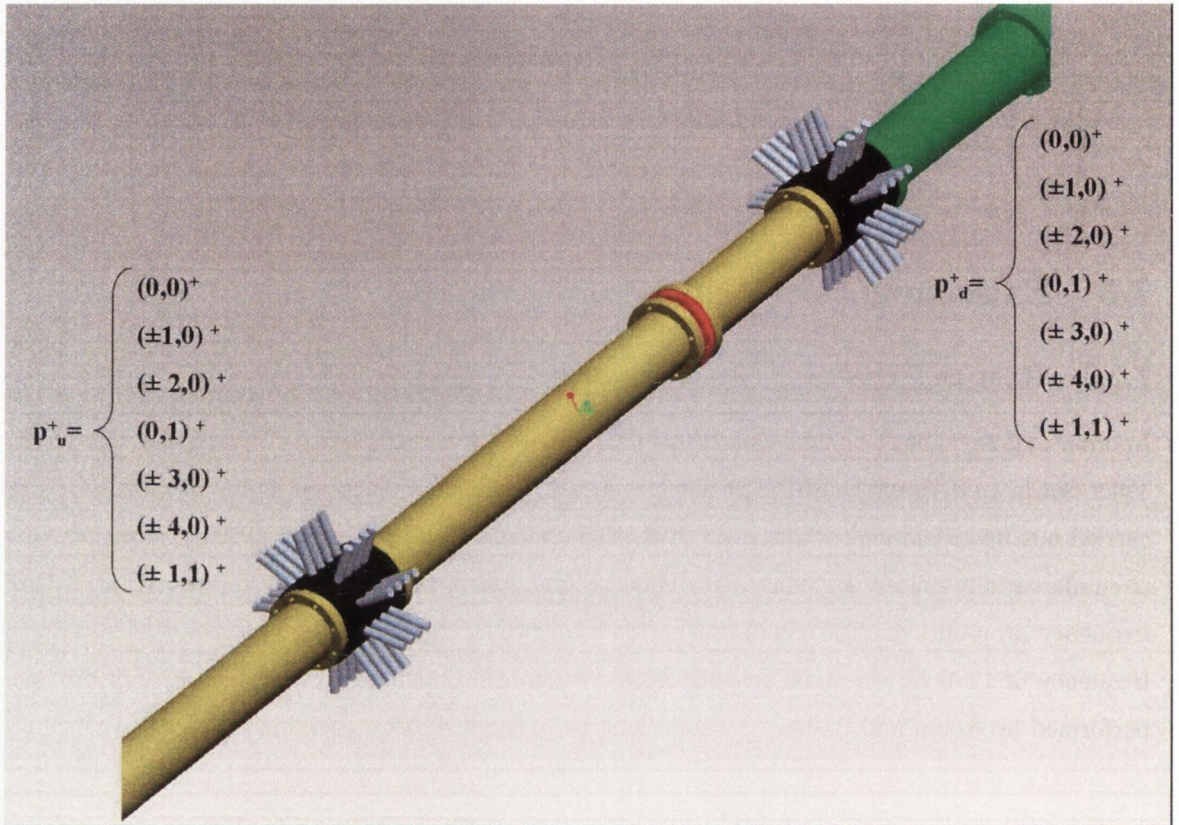


FIGURE 7.3: Close-up of figure 3.7, showing ideal experimental set-up for simultaneous upstream and downstream decomposition of incident and reflected modes; $(0,0)^{+,-}$, $(\pm 1,0)^{+,-}$, $(\pm 2,0)^{+,-}$, $(\pm 3,0)^{+,-}$, $(\pm 4,0)^{+,-}$, $(0,1)^{+,-}$, $(\pm 1,1)^{+,-}$. $2 \times 9 \times 4 = 72$ microphones required. Fan location indicated at red ring plane.

Instead, the incident and reflected amplitudes of the azimuthal modes only were decomposed, upstream and downstream separately. In addition, data was acquired to allow the radial modes which are cut-on of the first two azimuthal modes to be identified, i.e. $(0,0)^{+,-}$, $(0,1)^{+,-}$, $(\pm 1,0)^{+,-}$, and $(\pm 1,1)^{+,-}$. This latter analysis is flawed, but is assumed to be approximately correct at frequencies where it can be demonstrated that the magnitudes of any other modes which are cut-on are low enough to be assumed insignificant. The two set-ups of the 24 required microphones, downstream and upstream, are shown in figures 7.4 and 7.5. The 18 microphones required for the azimuthal decomposition are illustrated in red in figure 7.6, whereas the 12 microphones required for the radial decomposition are illustrated in red in figure 7.7. To have an indication of the behaviour across the

fan, a further decomposition, using 12 microphones upstream and downstream simultaneously, was performed; see figure 7.8. To accommodate the microphone positions, the experimental rig was fitted with two machined and reamed acetal (*Delrin*) tube sections which allowed the microphones to be flush mounted with the inside of the tube, refer to figures 7.9 and 7.10.

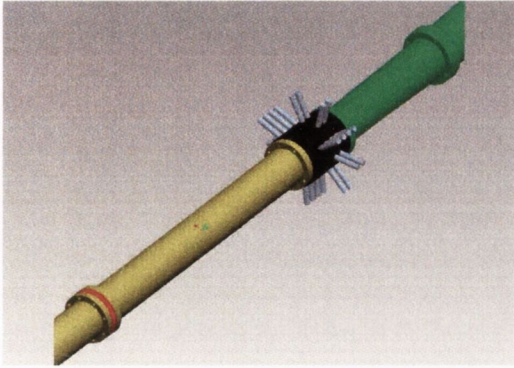


FIGURE 7.4: Set-up with 24 duct-wall flush-mounted microphones located downstream of the fan in red.

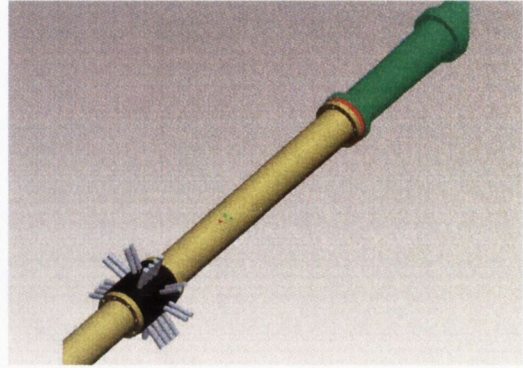


FIGURE 7.5: Set-up with 24 duct-wall flush-mounted microphones located upstream of the fan in red.

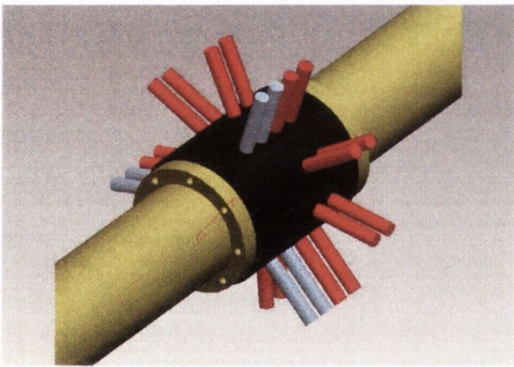


FIGURE 7.6: The 18 microphones in red are used to decompose the pressure field into incident and reflected azimuthal modes.

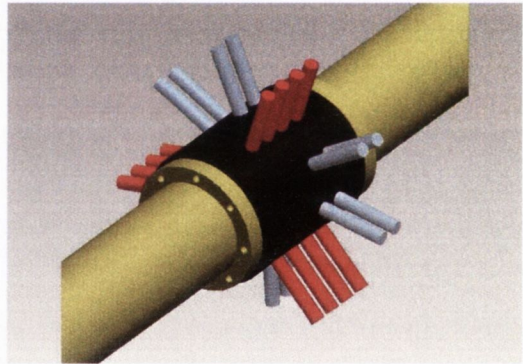


FIGURE 7.7: The 12 microphones in red are used to decompose the first two azimuthal modes into incident and reflected radial modes.

7.3.2 Decomposition Results

Downstream analysis

In accordance with the test set-up of figure 7.4, figure 7.11 shows the decomposition results of the first nine azimuthal spinning modes downstream of the fan under the same conditions of figure 6.18, i.e., the fan rotating at maximum speed and a tone from the speaker at 9.3kHz . The incident amplitudes are shown in blue and the reflected in red. The cut-on frequencies of the first radial

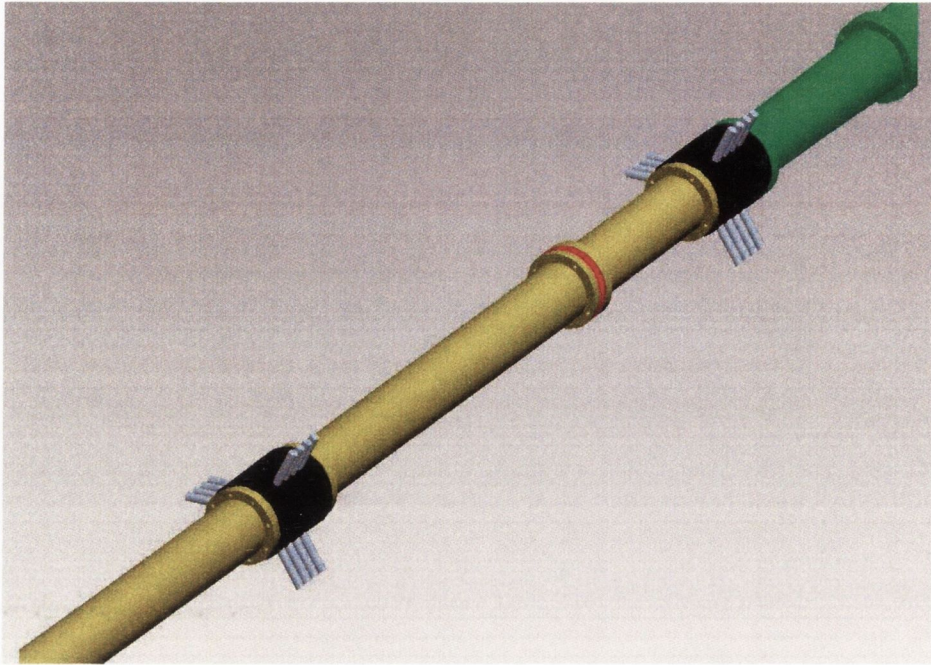


FIGURE 7.8: The test set-up of 7.7 carried out upstream and downstream simultaneously to examine the coherence and the frequency response function across the fan.

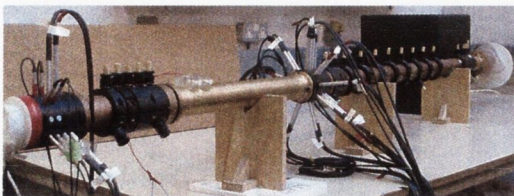


FIGURE 7.9: The experimental rig set up for modal decomposition.

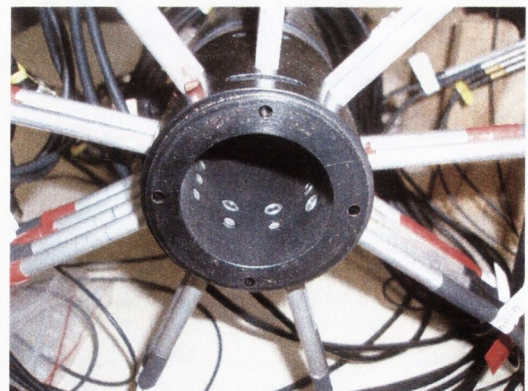


FIGURE 7.10: A close-up of one of the tube sections used for modal decomposition. The microphones can be seen to be flush mounted with the inside surface.

modes which exist in this frequency range of interest are indicated by black dotted lines in the top three subplots. These frequencies are, as per table 6.1, $8102Hz$ for the $(0, 1)$ radial mode and $11273Hz$ for the $(\pm 1, 1)$ spinning radial modes. Above these frequencies, the (0) and (± 1) azimuthal modes shown in figure 7.11, could be further decomposed to determine their radial content, (this is attempted in a later test), but in this figure, the azimuthal modal amplitudes can be considered to be the sum, or the total, of all radial contributions. It is interesting to note how the incident and reflected amplitudes converge above these frequencies in these three subplots, indicative perhaps of the necessity to further decompose. Some evidence of this behaviour of equal incident and reflected amplitudes is also seen for high frequencies for some of the other azimuthal modes, which would be unexpected in the presence of an anechoic termination, but it is thought that this is more a result of errors to be found at high frequencies due to equation (7.13) rather than due to radial cut-on. In addition, errors at very high frequency are to be expected due to possible calibration error. Appendix C shows that as the maximum diameter of the microphones used was $8mm$, a minimum calibration tube size of $16.7mm$ would in result in a maximum calibration frequency of $11925Hz$ according to equation (2.31). Frequency response functions similar to those shown in figure 4.5 verified this. Also of interest, is that the incident (flow direction) broad band noise produced, is greater in magnitude for the modes co-rotating with the rotor. This is not the case upstream of the vane-axial fan where the vanes upstream of the rotor serve their purpose well in straightening the flow. The sum of the incident and reflected broad band noise is seen to be less than that of the PSD of a reference microphone which is plotted in black for comparison. This is due to employing the averaged frequency response function in the technique which serves to reduce noise uncorrelated between microphones.

The principal aim of the decomposition performed, was to determine the relative modal content at the frequencies of interest. Figure 7.12 shows a summary of the incident magnitudes in figure 7.11 for the nBPFs, the combustor (speaker) signal and for the sum tone. In the first subplot for example, the only mode cut-on for the BPF is the $(0,0)$ mode which has a magnitude of $\approx 100dB$. In the second subplot, the $(+1)$ mode is significantly the greatest of the three modes cut-on, and is indicated in green, as this is the mode predicted by the Tyler-Sofrin analysis of table 6.3. The other three nBPF plots, show the relative modal magnitudes with, again, green indicating the modes predicted as a result of rotor-stator interaction. For the 4XBPF plot, the $(+2)$ mode is correctly identified, whereas the (-3) modes falls below the magnitude of the modes predicted not to be excited. This, for a similar reason as the (-1) mode in the 3XBPF not being well predicted, is thought to be due to the fact that the mode has difficulty propagating through the counter-rotating rotor and swirl zone. In addition, as mentioned before, although the Tyler-Sofrin analysis predicts modes excited due to rotor-stator interaction, it does not predict the magnitude, which depends on blade loading among other things. Thus it may well be the case that these modes are of naturally low magnitude.

The 5XBPF frequency is well predicted, again referring to table 6.3, as having a (0) dominant azimuthal mode content. As this mode is at least $6dB$ greater than all others, a radial mode de-

composition was carried out using three circumferentially spaced microphones at four axial locations, see figure 7.7. The results of this decomposition are shown for downstream of the vane-axial fan in figure 7.13. This analysis is correct up to the cut-on frequency of the second azimuthal mode (2), indicated by the dotted black line at $6458Hz$, and is assumed to be approximately correct for frequencies where higher modes are proven to be relatively low. This is approximately the case for the 5XBPF. A summary of figure 7.13 for the 5XBPF peak is shown in figure 7.14. This decomposition agrees successfully with the modes predicted in table 6.3 for this frequency as having a modal content of $(0, 0)$ and $(0, 1)$. An explanation of the existence of a large peak at the BPF when no mode is predicted is given at the end of section 6.4.1.

Figure 7.12 clearly identifies the sum tone as having $(+4, 0)$ as its modal content in agreement with the proposal in section 6.4.1, where it was guessed that the sum tone must have a modal content of one of the modes which cut-on at ≈ 11200 . As $(\pm 4, 0)$ and $(\pm 1, 1)$ all cut-on at around this same frequency, it was difficult to determine the modal content from figure 6.21. However, the modal decomposition technique successfully verifies this.

Upstream analysis

A second experiment, according to the test set-up of figure 7.5, was carried out. By performing an azimuthal decomposition upstream, the results of which are given in figure 7.15, a breakdown of the modal content could be calculated and these are summarised in figure 7.16. Observation of the combustor tone content, plotted in isolation in figure 7.18 for clarity, shows the tone to be composed almost entirely of the $m = (0)$ mode. This being the case, a radial mode decomposition could be carried out, see figure 7.17, which allowed the $m = (0)$ mode at this frequency to be broken down further, and as figure 7.19 testifies, is mostly of the form $(0, 1)$. From figure 2.5, one might speculate that this mode is excited by the coaxial form of the vane-axial fan assembly, which can be seen in appendix A. Figures 7.20 and 7.21 show results when the same decomposition is carried out upstream but with the fan not rotating and with only the speaker tone at $9.3kHz$. This demonstrates that this mode shape is not a result of rotation, but as the total energy of the combustor tone downstream in figure 7.12 is considerably less than that upstream in figure 7.18, it can be concluded that the rotation causes the scattering of this energy at this frequency into other modes at different frequencies.

Analysis across the fan

To have an indication of the behaviour across the fan, a further decomposition, using 12 microphones upstream and downstream simultaneously, was performed, as illustrated in figure 7.8. The incident and reflected modal amplitudes are presented in figures 7.22 and 7.23 for upstream and downstream cases respectively. Both of these decompositions were performed with data acquired simultaneously. As discussed, this decomposition is valid up to the cut-on frequency of second azimuthal mode $m = (2)$ at $6458Hz$, indicated in the figures with a dotted black line. Above this frequency, as

additional microphones would be needed to resolve for higher order modes, which if present in the absence of these microphones would result in aliasing, the data can only be assumed to be accurate if higher order modes can be assumed to be negligible, both upstream and downstream. By comparison of figure 7.16 with figure 7.12 this could be considered to be the case for the 5BPF only. It can be observed from figure 7.16 that the incident amplitudes upstream contain significant energy at the BPF and harmonics. This demonstrates that the upstream termination is not anechoic and that energy at these frequencies is being reflected back down the duct. This appears to be less the case for the interaction sum term and a coherence measured between upstream and downstream for this frequency, especially for the $m = (+4)$ mode, would be expected to be low. This coherence could not be calculated however, due to instrumentation limitations.

Figure 7.24 does plot however, the coherence between the upstream and downstream $m = (-1, 0)$ mode simply to illustrate the analysis that may be possible upon a full modal decomposition. For the 2BPF tone, the magnitude is seen to increase across the fan, as would be expected, as the energy is created between the two measurement planes, and the coherence is seen to be high. This is reflected in the frequency response function plotted in figure 7.25, with a strong amplification indicated. For the 5BPF, no indication is evident in the upstream signal of the presence of this mode, whereas a peak in the downstream amplitude, indicates that the energy was created by the fan. As would be expected, the coherence is low. It is this latter scenario which would be expected for all frequencies where energy at the fan is created, including non-linear interactions, in the presence of an anechoic termination upstream.

7.4 Discussion

Section 7.3.2 has presented results for an acoustic modal decomposition carried out in a duct where a single tone has been convected through a vane-axial fan, which in turn contributes to the sound field with energy at the BPF and harmonics. A full azimuthal decomposition was performed, both upstream and downstream of the fan, and the sound field was separated into its constituent modal components in both the incident and reflected directions. The decomposition verifies, for modes spinning in the direction of the rotor, and for the $m = (0)$ mode, the Tyler-Sofrin analysis of section 6.4.1.

A non-linear interaction tone is identified, and upon decomposition, its modal content is found to be dominated by the $m = (+4)$ mode. This is in agreement with a theory suggested from the findings of section 6.4.1 and illustrated in figure 6.21. From the modal decomposition and the waterfall plot it seems that the modal energy at the BPF and the convected tone combine to produce a sum tone, which due to its modal composition will only propagate if above its cut-on frequency.

Section 7.3.1 sets out the full experimental conditions required to perform simultaneous azimuthal and radial modal analysis. This would require 36 microphones to decompose the pressure field, for the

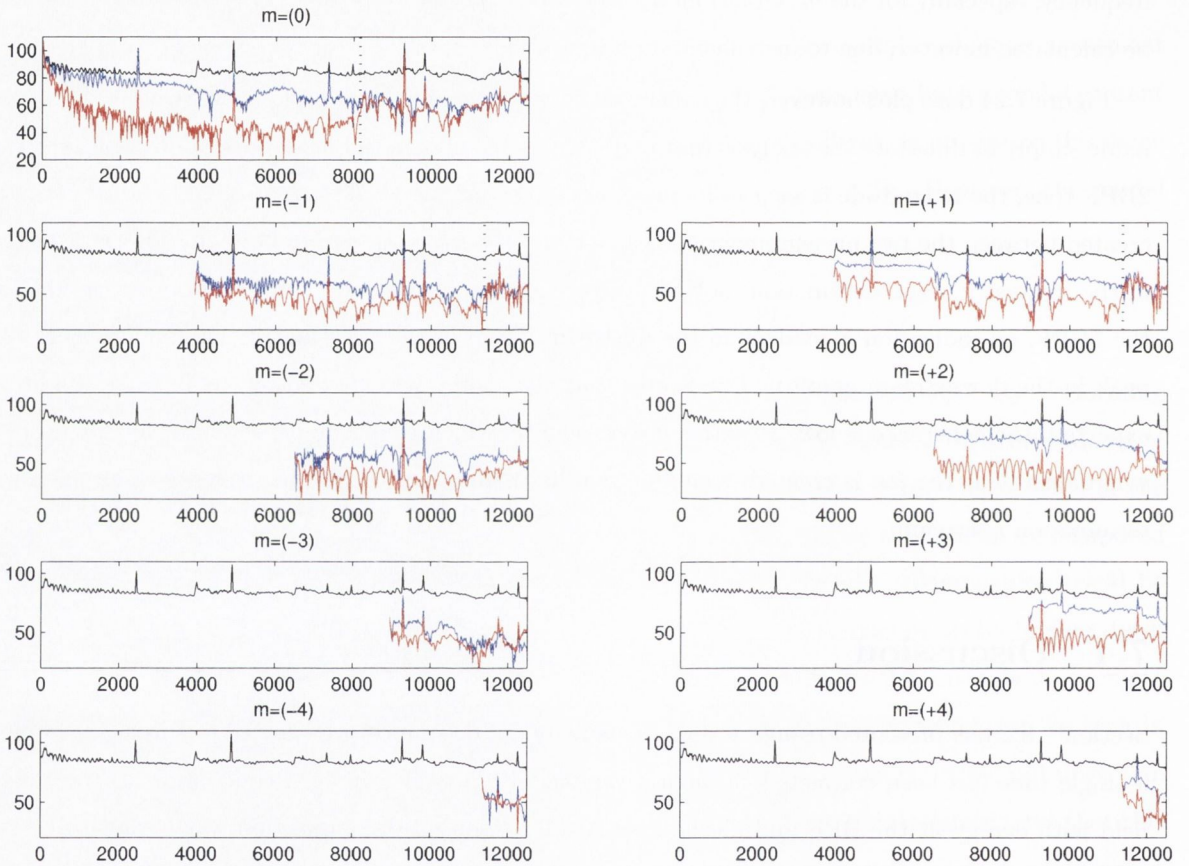


FIGURE 7.11: Azimuthal decomposition downstream of the fan. Incident amplitudes are in blue with reflected amplitudes in red. A PSD of a reference microphone is plotted in black.

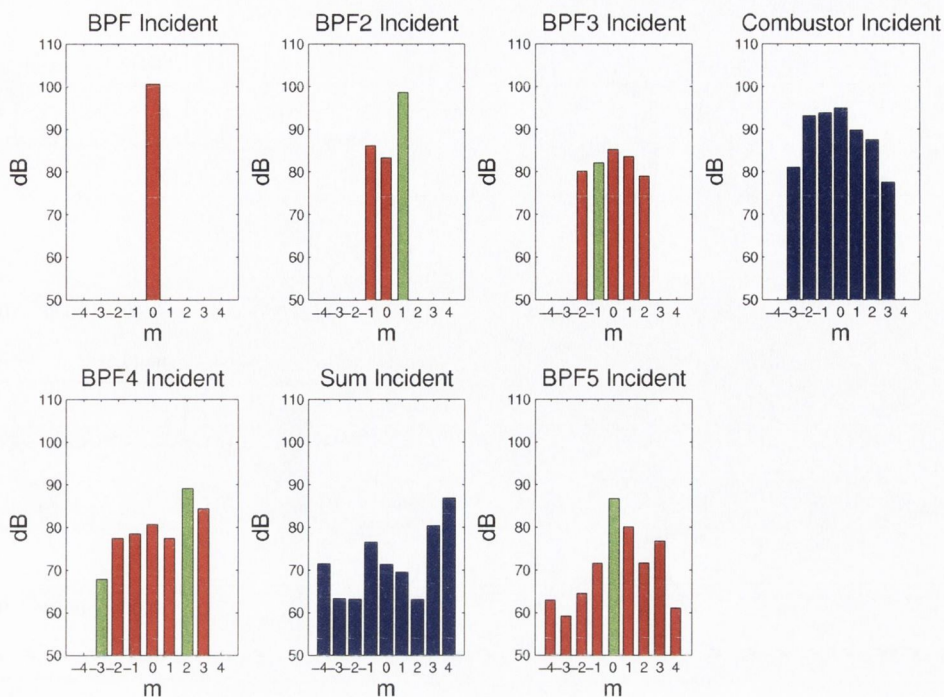


FIGURE 7.12: Incident azimuthal modal amplitudes downstream of the fan at the nBPF, combustor and sum frequencies. Modes in green are those predicted by the Tyler-Sofrin analysis given in table 6.3.

frequency range of interest, in either the upstream or downstream test section. Due to a limitation in instrumentation, a method was suggested where an azimuthal decomposition can be performed followed by a limited azimuthal\radial decomposition analysis where certain conditions would allow some radial modes such as the 5BPF tone downstream and the combustor tone upstream to be analysed.

This limited decomposition, performed upstream of the fan, determines the combustor tone to have a dominant $(m, n) = (0, 1)$ modal content. As this was measured with the fan both rotating and not, it is deduced to be not a function of rotation but more likely to be as a result of the coaxial form of the vane-axial fan. This mode shape combines with the planar mode at the BPF, through rotation, to form the $m = (+4)$ mode. This requires further analysis to determine the process but is thought to be analogous with the theories reported in section 2.5.4, i.e., the combustor mode can be viewed as a inflow-distortion interacting with the rotor.

Across the fan, the coherence and the frequency response function are useful tools for the identification of noise sources. By acquiring data from both upstream and downstream of the fan simultaneously, an evaluation of the effect of the fan on the incident sound pressure is possible on a mode by mode basis. Some preliminary processing here, with the limited decomposition technique, indicates its usefulness as a procedure in both linear and non-linear source identification.

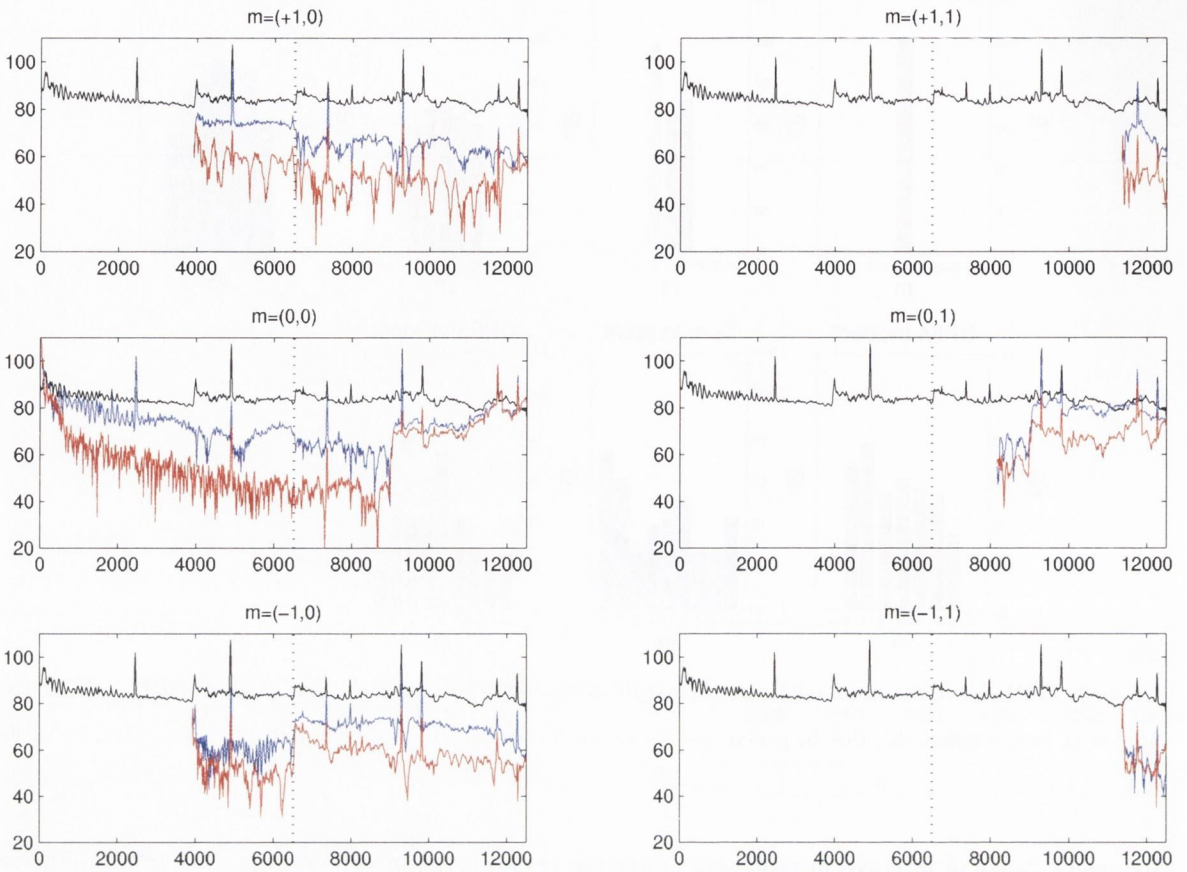


FIGURE 7.13: Radial decomposition downstream of the fan of the first two azimuthal modes. Incident amplitudes are in blue with reflected amplitudes in red. A PSD of a reference microphone is plotted in black.

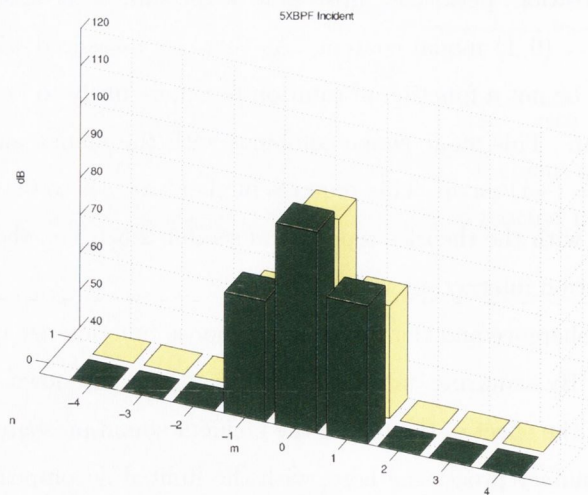


FIGURE 7.14: Incident radial modal amplitudes downstream of the fan at the 5BPF frequency. $n=0$ indicated in green, $n=1$ in yellow.

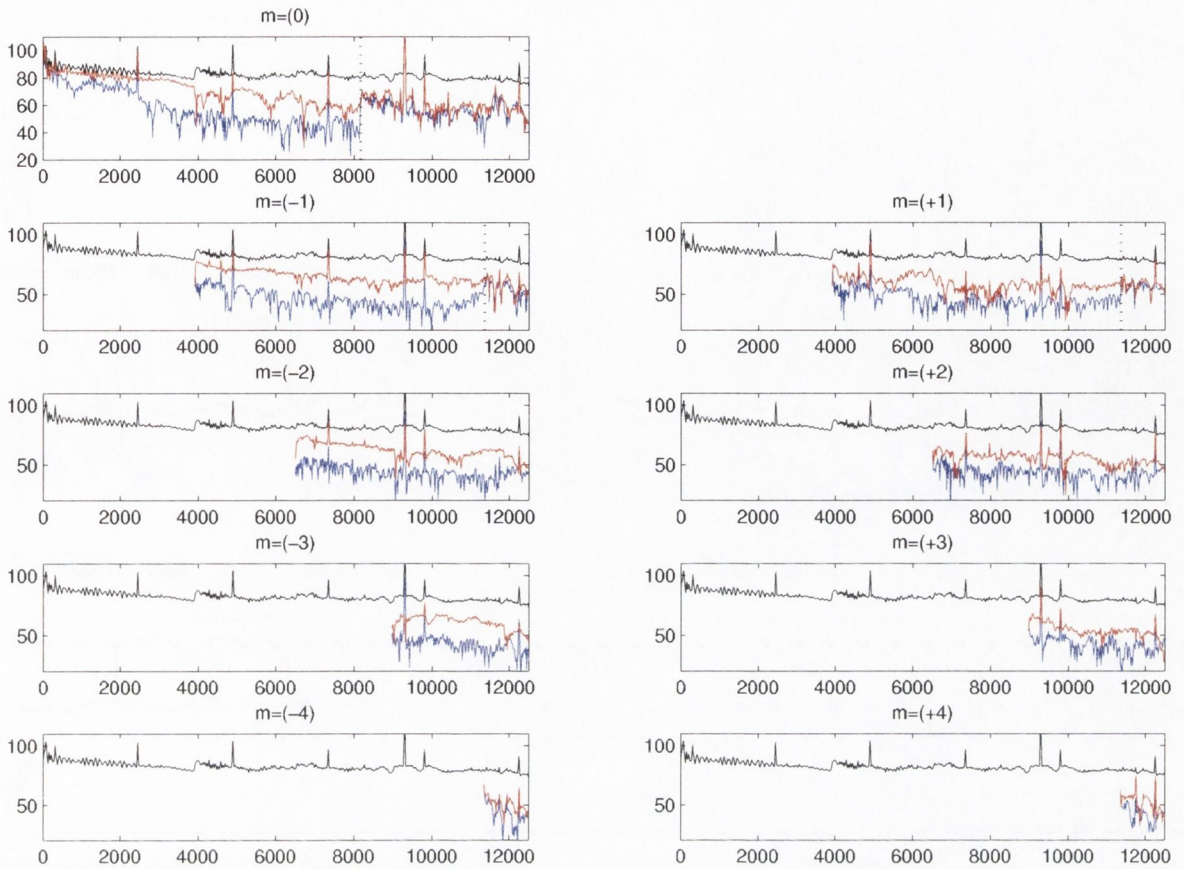


FIGURE 7.15: Azimuthal decomposition upstream of the fan. Incident amplitudes are in blue with reflected amplitudes in red. A PSD of a reference microphone is plotted in black.

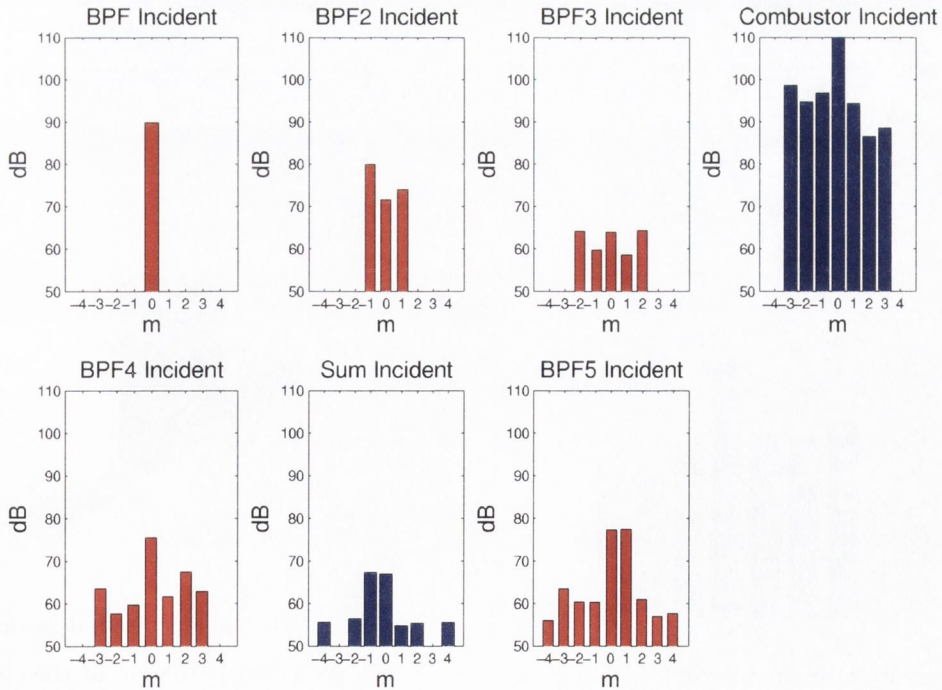


FIGURE 7.16: Incident azimuthal modal amplitudes *upstream* of the fan at the nBPF, combustor and sum frequencies. Significant energy at only the combustor frequency is expected.

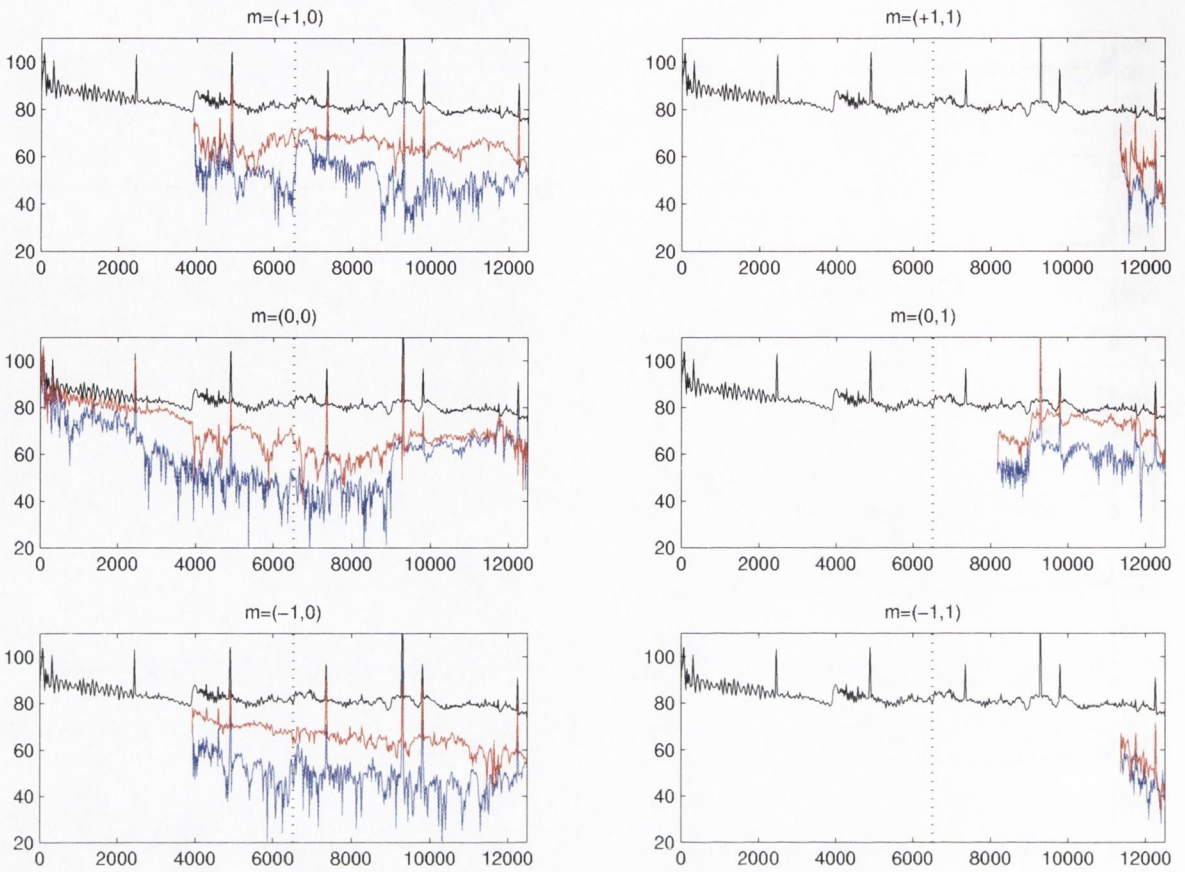


FIGURE 7.17: Radial decomposition upstream of the fan of the first two azimuthal modes. Incident amplitudes are in blue with reflected amplitudes in red. A PSD of a reference microphone is plotted in black.

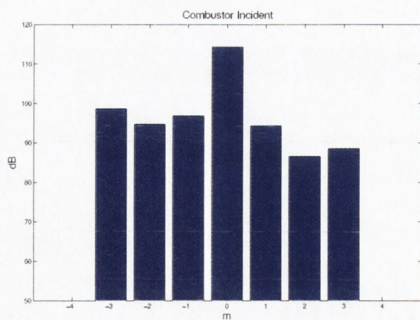


FIGURE 7.18: Incident azimuthal modal amplitudes upstream of the fan at the combustor frequency. The fan is rotating.

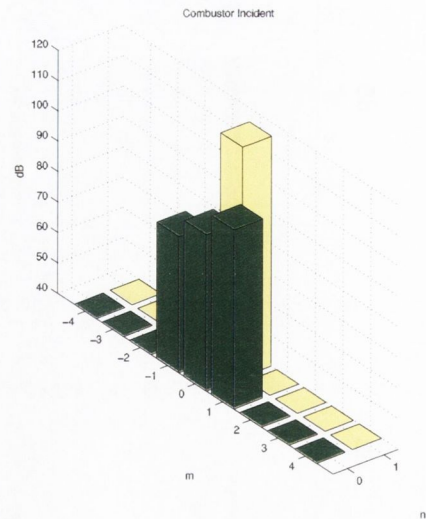


FIGURE 7.19: Incident radial modal amplitudes upstream of the fan at the combustor frequency. The fan is rotating. $n=0$ indicated in green, $n=1$ in yellow.

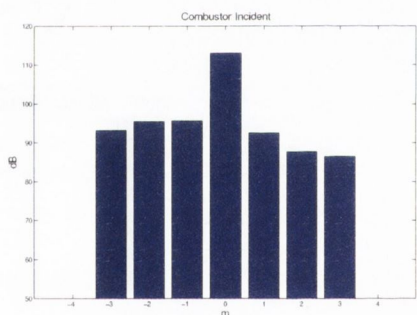


FIGURE 7.20: Incident azimuthal modal amplitudes upstream of the fan at the combustor frequency. The fan is *not* rotating.

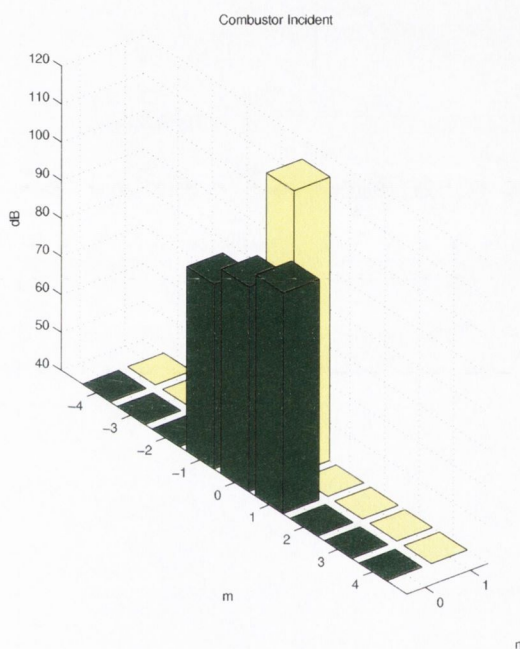


FIGURE 7.21: Incident radial modal amplitudes upstream of the fan at the combustor frequency. The fan is *not* rotating. $n=0$ indicated in green, $n=1$ in yellow.

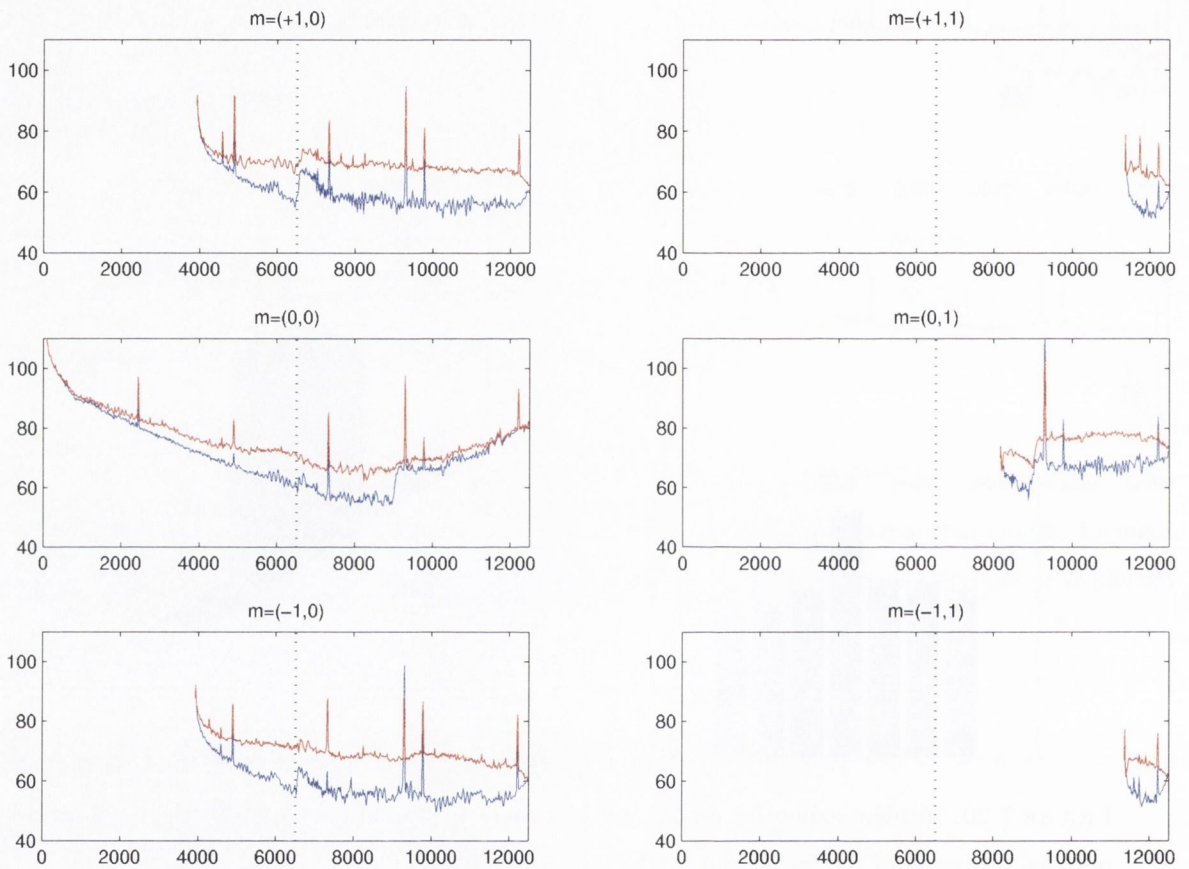


FIGURE 7.22: Radial decomposition upstream of the fan of the first two azimuthal modes for the test set-up across the fan of figure 7.8. Incident amplitudes are in blue with reflected amplitudes in red.

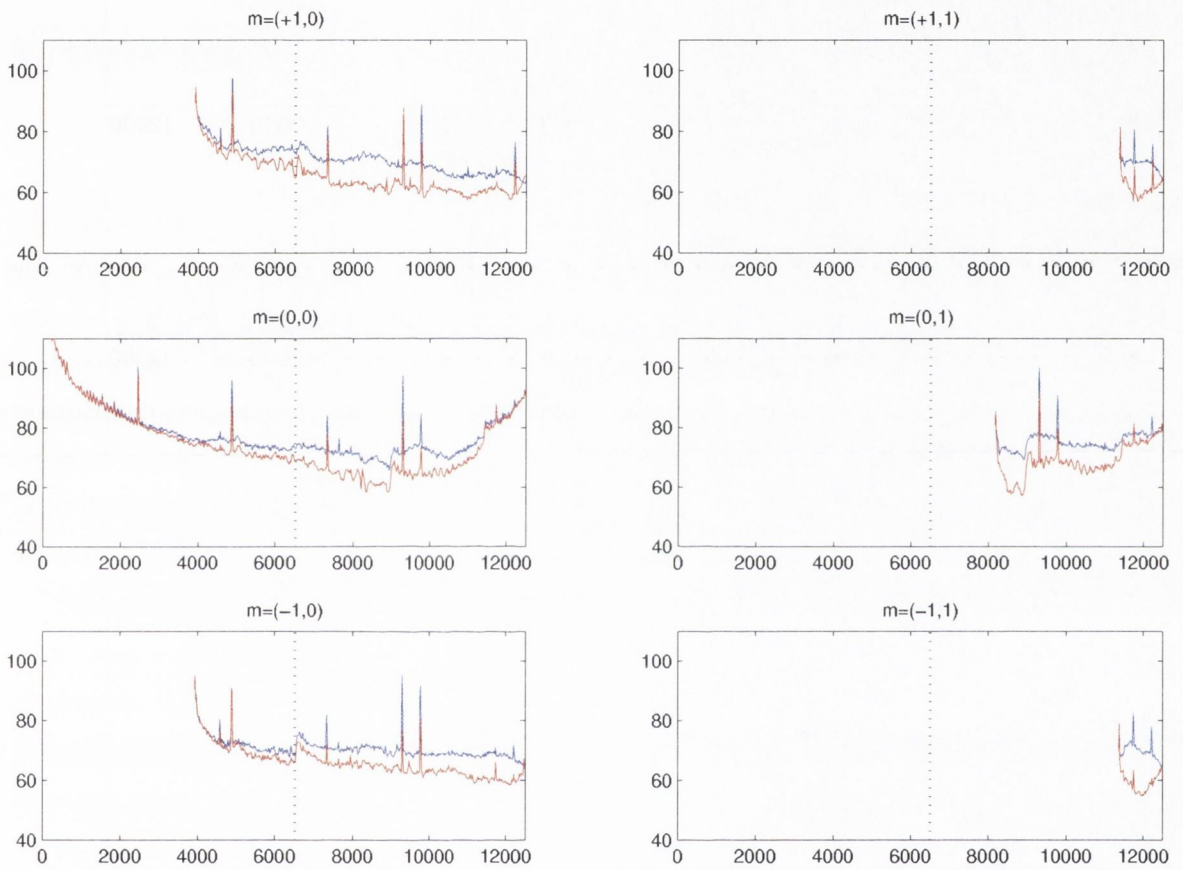


FIGURE 7.23: Radial decomposition *downstream* of the fan of the first two azimuthal modes for the test set-up across the fan of figure 7.8. Incident amplitudes are in blue with reflected amplitudes in red.

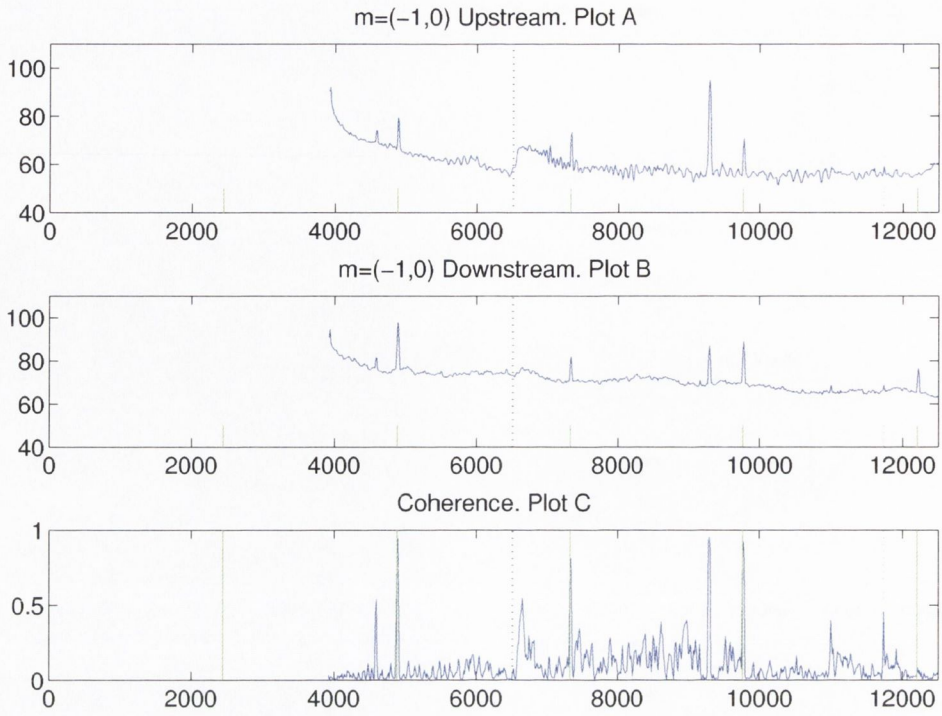


FIGURE 7.24: For the mode $(m,n)=(-1,0)$, the decomposed amplitudes upstream and downstream of the fan are plotted with the coherence between them.

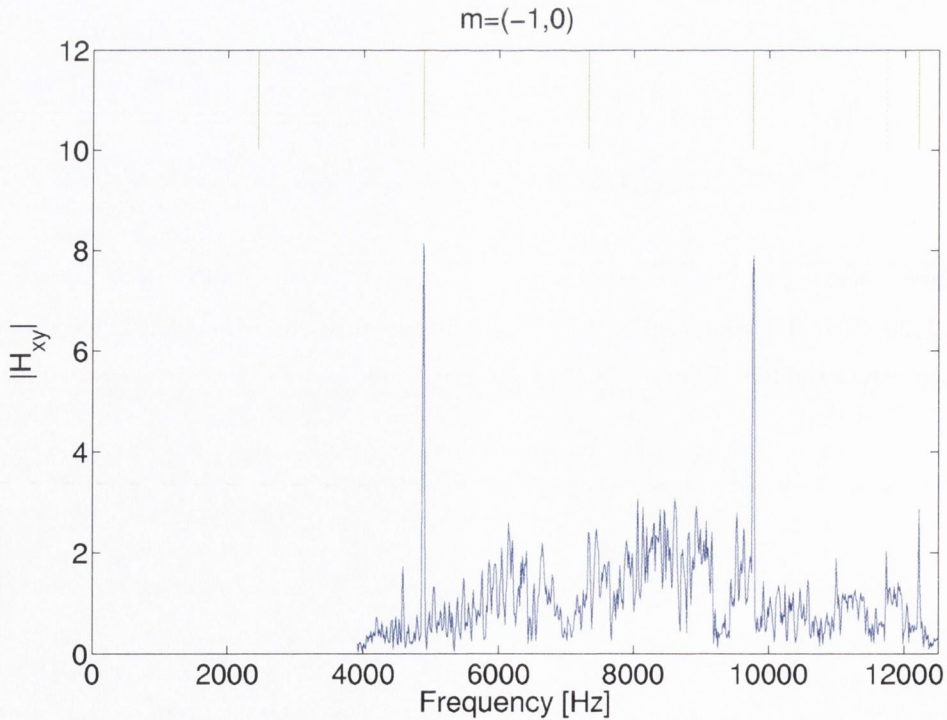


FIGURE 7.25: The frequency response function across the fan for the mode $(m,n)=(-1,0)$.

Chapter 8

Conclusions

Coherence-based noise source identification techniques have been developed which can be used to identify the contribution of combustion noise to near and far-field acoustic measurements of aero-engines. A number of existing techniques from the literature, as well as some new techniques, were implemented and evaluated under controlled experimental conditions. A series of tests were conducted to examine the efficacy of each of the procedures for specific applications. An experimental rig was designed and built to gain a fundamental physical understanding of the convection of combustion noise through the turbine of an aero-engine. The identification techniques were applied to this rig, with the objective of separating the pressure field into its constituent parts.

The underlying assumption with these identification techniques is that the propagation\convection path, from combustion can to measurement point, is a linear one. For the situation where the combustion noise is acted upon in a non-linear fashion the identified contribution will be inaccurate. The experimental rig, consisting of a vane-axial fan mounted in a duct, allowed in a simplified manner, potential interaction mechanisms between a convected sound source and the fan to be investigated.

Simple non-linear simulations were performed where synthetic data representing the combustion and turbine noise were passed through a non-linear system, quadratic in form. Tests carried out on the experimental rig allowed a non-linear interaction tone, between the rotor BPF and a convected tone, to be generated. While bearing similarities with the quadratic interaction process of the simulations, dissimilarities required a modal decomposition of the acoustic field in the duct to be performed.

An experimental technique required for a full acoustic modal decomposition was developed. Alternative formulations necessary due to an insufficiency of instrumentation were suggested and implemented with their assumptions and limitations discussed. From the modal decomposition it is suggested that the modal energy at the BPF and the convected tone combine to produce a sum tone, which due to its modal composition will only propagate once above its cut-on frequency. Further analysis to understand the exact process is required but is suggested to be analogous with rotor-rotor interaction theories, i.e., the combustor mode can be viewed as a inflow-distortion interacting with

the rotor.

A modal decomposition performed upstream and downstream of the fan simultaneously allowed the coherence and frequency response function across the fan to be examined on a mode by mode basis. For situations where noise is generated between two such measurement planes an analysis of incident signals proves to be a powerful method in noise source identification, both for linear and non-linear systems.

8.1 Future Work

This work has addressed a number of aspects of acoustic noise source identification for both linear and non-linear systems. There is scope for further development which is now briefly outlined.

- With regard to the acoustic modal decomposition, additional microphones will be acquired and a full azimuthal and radial decomposition performed. Thirty six microphones should allow the modal content of each frequency of interest to be determined.
- Seventy two microphones employed upstream and downstream simultaneously will allow the coherence and frequency response function of all modes across the fan to be investigated. A second, statistically independent noise source, will be convected down the duct at the interaction frequency. This noise source, being measured both upstream and downstream of the fan, will result in a high coherence across the fan being calculated at this frequency. By sweeping the magnitude and frequency of the first tone, a drop in coherence can be used as a procedure to detect non-linear interaction.
- Higher order spectral analysis techniques, such as bi-coherence, will be used to analyse the data with a view to detecting non-linear interaction.
- Further tests will be carried out where the number of rotor-blades and stator-vanes are varied, as well as the diameter of the duct.
- All future tests will be performed in an anechoic chamber where an upstream anechoic termination is installed.

Bibliography

- [1] *Gas turbine jet exhaust noise prediction.*, number SAE ARP876/2/. Society of Automotive Engineers, 1980. Revision D.
- [2] *Acoustics - Determination of sound absorption coefficient and impedance in impedance tubes - Part 2: Transfer-Function Method*, number BS EN ISO 10534-2:2001. British Standards, 2001.
- [3] *Acoustics - Determination of sound power radiated into a duct by fans and other air-moving devices - In-duct method*, number BS EN ISO 5136:2003. British Standards, 2003.
- [4] M. Åbom and H. Bodén. Error analysis of two-microphone measurements in ducts with flow. *J. Acoust. Soc. Am.*, 83(6):2429–2438, 1988.
- [5] Mats Åbom. Modal decomposition in ducts based on transfer function measurements between microphone pairs. Technical Report Report TRITA-TAK-8702, Department of Technical Acoustics, Royal Institute of Technology, Stockholm, Sweden, 1987.
- [6] Mats Åbom. Modal decomposition in ducts based on transfer function measurements between microphone pairs. *Journal of Sound and Vibration*, 135(1):95–114, 1989.
- [7] Julius S. Bendat and Allan G. Piersol. *Random Data: Analysis and Measurement Procedures*. John Wiley & Sons, 1986.
- [8] G. J. Bennett and J. A. Fitzpatrick. A comparison of coherence based acoustic source identification techniques. In *12th International congress on sound and vibration*, number 950, Lisbon, Portugal, 11-14 July 2005.
- [9] U. Bolleter, R. Cohen, and J. Wang. Design considerations for an in-duct soundpower measuring system. *Journal of Sound and Vibration*, 28(4):669–685, 1973.
- [10] W. T. Chu. Impedance tube measurements – a comparative study of current practises. *Noise Control Engineering Journal*, 37(1):37–41, 1991.
- [11] J. Y. Chung. Rejection of flow noise using a coherence function method. *J. Acoust. Soc. Am.*, 62(2):388–395, 1977.

- [12] J. Y. Chung and D. A. Blaser. Transfer function method of measuring in-duct acoustic properties. i. theory. *J. Acoust. Soc. Am.*, 68(3):907–913, 1980.
- [13] J. Y. Chung and D. A. Blaser. Transfer function method of measuring in-duct acoustic properties. ii. experiment. *J. Acoust. Soc. Am.*, 68(3):914–921, 1980.
- [14] N. A. Cumpsty. Sum and difference tones from turbomachines. *Journal of Sound and Vibration*, 32(3):383–386, 1974.
- [15] P. O. A. L. Davies, J. L. Bento Coelho, and M. Bhattacharya. Reflection coefficients for an unflanged pipe with flow. *Journal of Sound and Vibration*, 72(4):543–546, 1980.
- [16] T. Elnady and H. Bodén. An inverse analytical method for extracting liner impedance from pressure measurements. In *10th AIAA/CEAS Aeroacoustics Conference*, number AIAA 2004-2836, 2004.
- [17] L. Enghardt, U. Tapken, W. Neise, F. Kennepohl, and K. Heinig. Turbine blade/vane interaction noise: acoustic mode analysis using in-duct sensor rakes. In *7th AIAA/CEAS Conference on Aeroacoustics.*, number AIAA-2001-2153, Maastricht, The Netherlands., May 2001.
- [18] Lars Enghardt, Yanchang Zhang, and Wolfgang Neise. Experimental verification of a radial mode analysis technique using wall-flush mounted sensors. In *137th Meeting of the Acoustical Society of America*, Berlin, March 1999.
- [19] L. J. Eriksson. Higher-order mode effects in circular ducts and expansion chambers. *J. Acoust. Soc. Am.*, 68(2):545–550, 1980.
- [20] J. A. Fitzpatrick. Flow\acoustic interactions of two cylinders cross flow. *Journal of Fluids and Structures*, 17:97–113, 2003.
- [21] J. A. Fitzpatrick and H. J. Rice. Equivalent time domain procedures for bispectral analysis. *Journal of Sound and Vibration*, 137:131–134, 1990.
- [22] T. Fujimori, S. Sato, and H. Miura. An automated measurement system of complex sound pressure reflection coefficients. In *Inter-Noise*, Honolulu, USA, December 3-5 1984.
- [23] Y. Gervais, A. Douerin, and J.-P. Priou. Détermination d'une terminaison anéchoïque pour la mesure des caractéristiques de matériaux acoustiques en écoulement. Technical Report Commande no. TRA.B.AMP/92646, Laboratoire d'études aérodynamiques, Poitiers, France, March 1993.
- [24] Donald E. Hall. *Basic Acoustics*. Harper and Row, 1987.
- [25] W. G. Halvorsen and J. S. Bendat. Noise source identification using coherent output power spectra. *Sound and Vibration*, 9(8):15, 18–24, 1975.

- [26] L. J. Heidelberg. Fan noise source diagnostic test – tone modal structure results. In *8th AIAA/CEAS Aeroacoustics Conference and Exhibit*, number AIAA-2002-2428, Breckenridge, Colorado, June 17-19 2002. NASA/TM-2002-211594.
- [27] F. Holste and W. Neise. Noise source identification in a propfan model by means of acoustical near field measurements. *Journal of Sound and Vibration*, 203(4):641–665, 1997.
- [28] G. F. Homicz and J. A. Lordi. A note on the radiative directivity patterns of duct acoustic modes. *Journal of Sound and Vibration*, 41:283–290, 1975.
- [29] J. S. Hsu and K. K. Ahuja. A coherence-based technique to separate ejector internal mixing noise from farfield measurements. In *AIAA/CEAS 4th Aeroacoustics Conference*, number AIAA-98-2296, June 2-4 1998.
- [30] F. Jacobsen. Measurement of sound intensity in the presence of air flow. In *2nd International Congress on Acoustic Intensity*, pages 193–200, Senlis, France, 1985.
- [31] Seung-Ho Jang and Jeong-Guon Ih. On the multiple microphone method for measuring in-duct acoustic properties in the presence of mean flow. *J. Acoust. Soc. Am.*, 103(3):1520–1526, 1998.
- [32] J. Johnston and W. Schmidt. Measurement of acoustic reflection from an obstruction in a pipe with flow. *J. Acoust. Soc. Am.*, 63(5):1455–1460, 1978.
- [33] P. Joseph, E. Fruteau, and P. Nelson. Design rules and sensing strategies for the active control of turbofan engine noise. In *7th AIAA/CEAS Conference on Aeroacoustics.*, number AIAA-2001-2222, Maastricht, Netherlands, 28-30 May 2001.
- [34] Phillip Joseph and Anthony Parry. Rotor/wall boundary-layer interaction broadband noise in turbofan engines. In *AIAA/CEAS 7th Aeroacoustics Conference*, number AIAA-2001-2244, Maastricht, May 28-30 2001.
- [35] A. M. Karchmer. Core noise measurements from a small general aviation turbofan engine. Technical Report TM81610, NASA, 1980.
- [36] A. M. Karchmer. Conditioned pressure spectra and coherence measurements in the core of a turbofan engine. Technical Report TM82688, NASA, 1981. AIAA Paper 81-2052.
- [37] A. M. Karchmer and M. Reshotko. Core noise source diagnostics on a turbofan engine using correlation and coherence techniques. Technical Report TM X-73535, NASA, 1976.
- [38] A. M. Karchmer, M. Reshotko, and F. J. Montegani. Measurement of far field combustion noise from a turbofan engine using coherence function. In *AIAA 4th Aeroacoustics Conference*, number AIAA-77-1277, Atlanta, Georgia, October 3-5 1977.

- [39] Y. C. Kim and E. J. Powers. Digital bispectral analysis of self excited fluctuation spectra. *Physics of Fluids*, 21:1452–1453, 1978.
- [40] L. V. King. *Phil. Mag.*, 21:128, 1936.
- [41] L. E. Kinsler, A. R. Frey, A. B. Coppens, and J. V. Sanders. *Fundamentals of Acoustics*. John Wiley and Sons, fourth edition, 2000.
- [42] D. L. Lansing. Exact solution for radiation of sound from a semi-infinite circular duct with application to fan and compressor noise. *Analytical Methods in Aircraft Aerodynamics*, pages 323–334, 1970. nasa sp-228.
- [43] H. Levine and J. Schwinger. On the radiation of sound from an unflanged circular pipe. *Phys. Rev.*, 73(4):383–406, 1948.
- [44] Tomoyuki Minami and K. K. Ahuja. Five-microphone method for separating two different correlated noise sources from farfield measurements contaminated by extraneous noise. In *AIAA/CEAS 9th Aeroacoustics Conference*, number AIAA-03-3261, South Carolina, May 12-14 2003.
- [45] C. J. Moore. In-duct investigation of subsonic fan “rotor-alone” noise. *J. Acoust. Soc. Am.*, 51:1471–1482, 1972.
- [46] C. L. Morfey. Sound transmission and generation in ducts with flow. *Journal of Sound and Vibration*, 14(1):37–55, 1971.
- [47] P. M. Morse. *Vibration and Sound*. McGraw-Hill Book Company, 1948.
- [48] M. L. Munjal. *Acoustics of Ducts and Mufflers*. John Wiley and Sons, 1987.
- [49] M. Nallasamy, R. Hixon, S. Sawyer, R. Dyson, and L. Koch. A time domain analysis of gust-cascade interaction noise. In *9th AIAA/CEAS Aeroacoustics Conference and Exhibit*, number AIAA-2003-3134, Hilton Head, South Carolina, May 12-14 2003.
- [50] J. W. S. Rayleigh. *The theory of sound*, volume 2. Macmillan, 1894.
- [51] E. J. Rice, M. F. Heidmann, and T. G. Sofrin. Modal propagation angles in a cylindrical duct with flow and their relation to sound radiation. In *17th Aerospace Sciences Meeting*, number AIAA-79-0183, New Orleans, January 15-17 1979.
- [52] H. J. Rice and J. A. Fitzpatrick. A generalised technique for spectral analysis of non-linear systems. *Mechanical Systems and Signal Processing*, 2(2):195–207, 1988.
- [53] G. Ruiz and H. J. Rice. An implementation of a wave based finite difference scheme for a 3-d acoustic problem. *Journal of Sound and Vibration*, 256(2):373–381, 2002.

- [54] C. Schemel, F. Thiele, F. Bake, B. Lehmann, and U. Michel. Sound generation in the outlet section of gas turbine combustion chambers. In *10th AIAA/CEAS Aeroacoustics Conference*, number AIAA 2004-2929, 2004.
- [55] A. F. Seybert and D. F. Ross. Experimental determination of acoustical properties using a two-microphone random excitation technique. *J. Acoust. Soc. Am.*, 61(5):1362–1370, 1977.
- [56] B. N. Shivashankara. High bypass ratio engine noise component separation by coherence technique. In *AIAA 7th Aeroacoustics Conference*, number AIAA-81-2054, Palo Alto, October 5-6 1981.
- [57] B. N. Shivashankara. High bypass ratio engine noise component separation by coherence technique. *Journal of Aircraft*, 23(10):763–767, 1986.
- [58] H. A. Siller, F. Arnold, and U. Michel. Investigation of aero-engine core-noise using a phased microphone array. In *7th AIAA/CEAS Aeroacoustics Conference*, number AIAA-2001-2269, Maastricht, The Netherlands, 28-30 May 2001.
- [59] A Spaargaren and M J English. Late potential detection using the phase of the bispectrum. *Computers in Cardiology*, 25:393–396, 1998.
- [60] R. W. Stoker, K. K. Ahuja, and J. S. Hsu. Separation of wind-tunnel background noise and wind noise from interior measurements. In *AIAA/CEAS 2nd Aeroacoustics Conference*, number AIAA-96-1763, Palo Alto, May 6-8 1996.
- [61] D. L. Sutcliff, K. E. Konno, and L. J. Heidelberg. Duct mode measurements on the tfe731-60 full scale engine. Technical Report NASA/TM 2002-211573, Glenn Research Centre, NASA, Cleveland, Ohio, 2002.
- [62] U. Tapken, L. Enghardt, W. Neise, and P. Schimming. Active control of noise from turbomachines-results of radial mode analysis. In *Inter-Noise 2001. The 2001 International Congress and Exhibition on Noise Control Engineering*, The Hague, The Netherlands, August 2001.
- [63] J. M. Tyler and T. G. Sofrin. Axial flow compressor noise studies. *Society of Automotice Engineers Transactions*, 70:309–332, 1961.
- [64] P. R. Wagstaff and J. C. Henrio. The measurement of acoustic intensity by selective two microphone techniques with a dual channel analyser. *Journal of Sound and Vibration*, 94:156–159, 1984.
- [65] P. D. Yardley. *Measurement of Noise and Turbulence Generated by Rotating Machinery*. PhD thesis, University of Southampton, 1974.

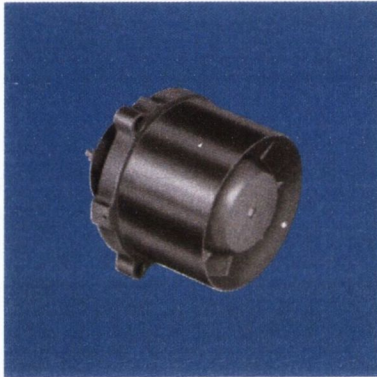
Appendix A

Fan Specifications

VAX-2-DC BLOWERS

DC Vaneaxial Blowers

C-5160



general design specification: Motor to MIL-M-8609

airflow: 35 cfm @ 1.5" H₂O, 27 cfm @ .5" H₂O

voltage: 26 VDC

impeller: Dynamically balanced, precision cast aluminum

housing: Precision die-cast aluminum

bearings: Double shielded, life-lubricated for -55°C to +85°C operation. Special lubricants available for temperature extremes

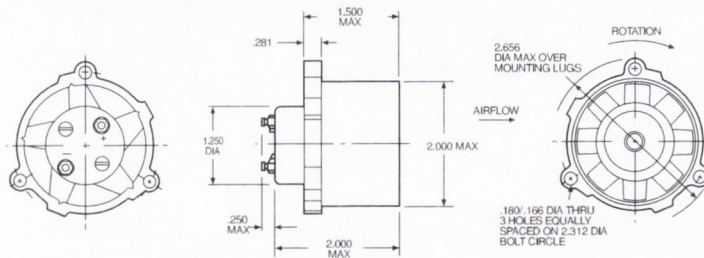
electrical connections: Two solder terminals are provided. Leads, shielded cable and RFI filters also available on special units

mounting: Standard mounting is by means of three bolts through flange, or by clamping around diameter

marking: Per MIL-STD-130

life: 500 hours minimum constant duty at 16,500 rpm and 85°C

Dimensions



ROTATION FOR SPECIFIED AIRFLOW
POSITIVE VOLTAGE TO (+), NEGATIVE VOLTAGE TO (-)

NOTE: Consult factory prior to preparing spec control prints. Dimensions are for reference only

76

© 1/01 Globe Motors

FIGURE A.1: Page 1 of Fan Specifications

C-5160



Standard Part Numbers and Data

VOLTAGE (VDC)	SPEED min @ free air (rpm)	AIRFLOW typ @ free air (cfm)	POWER INPUT max (watts)	CURRENT max @ free air (amps)	WEIGHT max (oz.)	STANDARD PART NUMBER*
26	16,500	53	29.0	1.15	5.0	19A1771
26	11,000	35	11.2	.43	5.0	19A2525

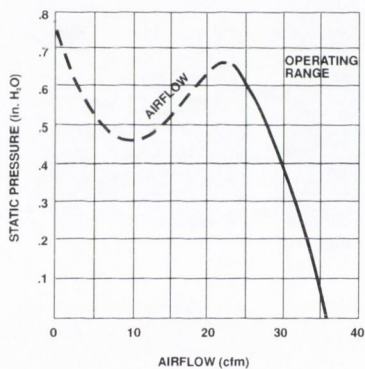
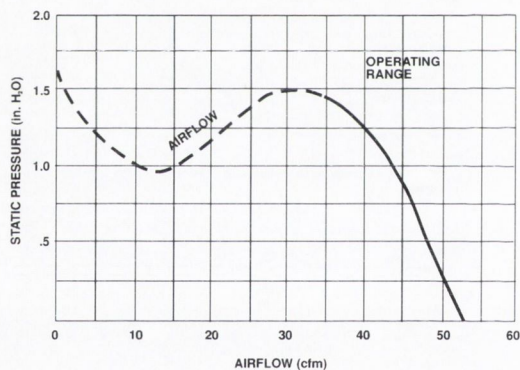
* When You Order

Units shown above are standard and may be ordered by part number. Motor windings, voltage, speed, current and airflow can usually be modified to fit your needs

Typical Performance:

Part No.: 19A1771
 Voltage: 26 VDC
 Operating Point: 37 cfm @ 1.5" H₂O

Part No.: 19A2525
 Voltage: 26 VDC
 Operating Point: 27 cfm @ .6" H₂O



Appendix B

Signal Processing

B.1 Ergodic Random Data

For situations where the random process is stationary, it may also be possible to describe its properties by computing time averages over specific sample functions in an ensemble. For example, for the k th sample function of the random process $\{x(t)\}$, the mean value $\mu(k)$ is given by

$$\mu_x(k) = \lim_{T \rightarrow \infty} \frac{1}{T} \int_0^T x_k(t) dt \quad (\text{B.1})$$

If the random process $\{x(t)\}$ is stationary, and $\mu_x(k)$ and $R_{xx}(\tau, k)$ do not differ when computed over different sample functions, the random process is said to be ergodic. For ergodic random processes, the time-averaged mean value, as well as all other time-averaged properties, is equal to the corresponding ensemble averaged value. It is important to note that only stationary random processes can be ergodic.

The concept of stationarity above relates to the ensemble averaged properties of a random process. However, data in the form of individual time history records of a random phenomenon are frequently referred to as being stationary or non-stationary. When a single time history record is referred to as being stationary, it is generally meant that the properties computed over short time intervals do not vary significantly from one interval to the next. Note that a single time record from an ergodic random process will be stationary in this sense.

Ergodic random processes are important as all their properties can be determined by performing time averages over a single sample function. Only this Ergodic class of Random Functions will be dealt with here.

B.2 Mean Value

The mean value (also called the average value) is a measure of the central tendency of the data and for a single record is given by

$$\mu_x = \overline{x(t)} = \langle x(t) \rangle = \lim_{T \rightarrow \infty} \frac{1}{T} \int_0^T x(t) dt \quad (\text{B.2})$$

where some varying notation is shown.

The *expected value* is the average or the mean of a quantity. In the case where the quantity is the function $x(t)$ itself, then the expected value of $x(t)$ is equal to the mean.

$$E[x(t)] = \mu_x = \lim_{T \rightarrow \infty} \frac{1}{T} \int_0^T x(t) dt \quad (\text{B.3})$$

In the case of the discrete variable x_i , the mean and expected value are expressed by

$$\mu_x = E[x] = \lim_{n \rightarrow \infty} \frac{1}{n} \sum_{i=1}^n x_i \quad (\text{B.4})$$

B.3 Variance

The variance is a useful measure of the dispersion or fluctuation of the data from the mean value. Its definition is the mean square value about the mean and is expressed as

$$\sigma_x^2 = E[(x - \mu_x)^2] = \lim_{n \rightarrow \infty} \frac{1}{n} \sum_{i=1}^n (x_i - \mu_x)^2 \quad (\text{B.5})$$

By definition σ_x , the *standard deviation*, is defined as the positive square root of the variance and has the same units as the mean value.

B.4 Mean Square Value

The mean square value, ψ_x^2 , which equals the variance plus the square of the mean, constitutes a measure of the combined central tendency and dispersion.

$$\psi_x^2 = E[(x)^2] = \lim_{n \rightarrow \infty} \frac{1}{n} \sum_{i=1}^n (x_i)^2 \quad (\text{B.6})$$

The relationship between the three properties is given by

$$\psi_x^2 = \sigma_x^2 + \mu_x^2 \quad (\text{B.7})$$

The root mean square, ψ_x , is defined as the positive square root of the mean square and is a measure of the power of the total signal, *i.e.* taking the mean and fluctuating part into account. It can be thought of as the D.C. equivalent signal containing the same power as the total original signal.

When the mean is equal to zero, equation (B.7) shows that the rms is equal to the standard deviation, *i.e.*

$$\psi_x = \sigma_x \quad (\text{B.8})$$

and so the standard deviation can be thought of as a measure of the power of the fluctuating part of the signal only.

B.5 Fourier Transform

The discrete frequency spectrum of periodic functions becomes a continuous one when the period τ is extended to infinity. Random functions are generally not periodic and the determination of its continuous frequency spectrum requires the use of the Fourier integral, which can be regarded as a limiting case of the Fourier series as the period approaches infinity.

$$x(t) = \int_{-\infty}^{\infty} X(f) e^{j2\pi ft} df \quad (\text{B.9})$$

In contrast to the summation of the discrete spectrum of sinusoids in the Fourier series, the Fourier integral can be regarded as a summation of the continuous spectrum of sinusoids. The quantity $X(f)$ in the previous equation is called the *Fourier Transform* of $x(t)$, which can be evaluated from the equation

$$X(f) = \int_{-\infty}^{\infty} x(t) e^{-j2\pi ft} dt \quad (\text{B.10})$$

The Fourier transform has become the underlying operation for the modern time series analysis. Like the Fourier coefficient c_n , $X(f)$ is a complex quantity which is a continuous function of f from $-\infty$ to ∞ . Equation (B.10) resolves the function $x(t)$ into harmonic components $X(f)$, whereas Equation (B.9) synthesizes these harmonic components to the original time function $x(t)$. The two previous equations above are referred to as the *Fourier transform pair*.

Theoretically, this transform $X(f)$ will not exist for an $x(t)$ that is a representative member of a stationary random process when the infinite limits are used. However, by restricting the limits to a finite time interval of $x(t)$, say in the range $(0, T)$, then the *finite-range Fourier transform* will exist, as defined by

$$X(f, T) = \int_0^T x(t) e^{-j2\pi ft} dt \quad (\text{B.11})$$

For a discretised record, where $x(t)$ is sampled into N equally spaced points a time Δt apart, a discrete form of the Fourier Transform is needed. The sampling times are $t_n = n\Delta t$, but as it is usual to start at time $t = 0$, the time axis is defined as

$$t_n = n\Delta t \quad n = 0, 1, 2, \dots, N - 1 \quad (\text{B.12})$$

with sampling rate

$$f_{\text{samp}} = \frac{1}{\Delta t} \quad (\text{B.13})$$

The usual selection of discrete frequency values for the computation of $X(f, T)$ is

$$f_k = \frac{k}{T} = \frac{k}{N\Delta t} \quad k = 0, 1, 2, \dots, N - 1 \quad (\text{B.14})$$

It can be seen from this that the frequency resolution is

$$\Delta f = \frac{1}{T} = \frac{1}{N\Delta t} \quad (\text{B.15})$$

At these frequencies, the *Discrete Fourier Transform*, (the DFT), of $x_n = x(n\Delta t)$ is defined by

$$X(f_k) = \underbrace{\sum_{n=0}^{N-1} x_n e^{[-j \frac{2\pi kn}{N}]} \Delta t}_{\text{Matlab FFT}} \quad k = 0, 1, 2, \dots, N - 1 \quad (\text{B.16})$$

It is important to note that Fast Fourier Transform (*FFT*) methods are designed to compute the quantity, $X(k)$, which is the quantity $X(f_k)$ normalised with the Δt , viz.,

$$X(k) = \frac{X(f_k)}{\Delta t} \quad (\text{B.17})$$

B.6 Power Spectrum and Power Spectral Density

The frequency composition of a random function $x(t)$ can be described in terms of the spectral density of the mean square value, ψ_x^2 .

It can be demonstrated that the mean square value of a periodic time function is the sum of the mean square value of the individual harmonic components present,

$$\psi_x^2 = \sum_{n=-\infty}^{\infty} E[(c_n)^2] \quad (\text{B.18})$$

Thus, ψ_x^2 is made up of discrete contributions in each frequency interval Δf .

We first define the contribution to the mean square in the frequency interval Δf as the *Power Spectrum* $P_{xx}(f_k)$ by

$$P_{xx}(f_k) = E[(c_n)^2] \quad (\text{B.19})$$

The mean square value is then

$$\psi_x^2 = \sum_{n=-\infty}^{\infty} P_{xx}(f_k) \quad (\text{B.20})$$

We now define the discrete *Power Spectral Density* $S_{xx}(f_k)$ (PSD) as the power spectrum divided by the frequency interval Δf ;

$$S_{xx}(f_k) = \frac{P_{xx}(f_k)}{\Delta f} \quad (\text{B.21})$$

giving the PSD units of $\frac{\text{units}^2}{\text{Hz}}$.

The mean square value may be written in terms of the power spectral density as

$$\psi_x^2 = \sum_{n=-\infty}^{\infty} S_{xx}(f_k) \Delta f \quad (\text{B.22})$$

One again, the discrete form above for a periodic time function may be extended to random functions, which are generally not periodic, by allowing the period to approach infinity, resulting in the continuous frequency spectrum with $\Delta f \rightarrow 0$;

$$\psi_x^2 = \int_{-\infty}^{\infty} S_{xx}(f) \, df \quad (\text{B.23})$$

As power has units of energy per unit time, the Energy Spectral Density function is related to the PSD by

$$\mathcal{S}_{xx}(f) = T S_{xx}(f) \quad (\text{B.24})$$

The energy spectral density function is usually used for the analysis of transient random data where T is the length of the transient records.

B.7 The PSD from Digital Data Analysis

In practical applications, data records have finite length and are discrete in nature. In addition, in order to reduce the random error associated with spectral estimates, the spectra are averaged in the frequency domain.

Consider a data record $x(t)$ of total length T_r that is stationary with zero mean ($\mu_x = 0$). Let the record be divided into n_d contiguous segments, each of length T . Each segment of $x(t)$ is termed $x_i(t)$, where $i = 1, 2, \dots, n_d$. In digital terms, each record segment $x_i(t)$, is represented by N data values $\{x_{in}\}$, with $n = 0, 1, 2, \dots, N - 1$

The discrete, finite, two sided, autospectral density function estimate can now be written as

$$\hat{S}_{xx}(f_k) = \frac{1}{n_d N \Delta t} \sum_{i=1}^{n_d} |X_i(f_k)|^2 \quad k = 0, 1, \dots, N-1 \quad (\text{B.25})$$

For FFT procedures, the Nyquist frequency f_c occurs where $k = N/2$. Hence the first $(N/2) + 1$ spectral values at $k = 0, 1, \dots, N/2$ define the autospectral density estimate in the frequency range from $0 \leq f_k \leq f_c$, while the last $(N/2) - 1$ spectral values at $k = (N/2) + 1, (N/2) + 2, \dots, N - 1$, can be interpreted as the autospectral density estimate in the frequency range from $-f_c < f < 0$. The one-sided autospectral density function is estimated directly from equation (B.25)

$$\hat{G}_{xx}(f_k) = \frac{2}{n_d N \Delta t} \sum_{i=1}^{n_d} |X_i(f_k)|^2 \quad k = 0, 1, \dots, \frac{N}{2} \quad (\text{B.26})$$

B.8 Matlab and the PSD

As shown in equation (B.16), the FFT can be calculated to have a scale factor of unity before the summation, *i.e.* normalised by Δt ;

$$\hat{G}_{xx}(f_k) = \frac{2}{n_d N \Delta t} \sum_{i=1}^{n_d} \left| \underbrace{\sum_{n=0}^{N-1} x_{in} e^{-j \frac{2\pi k n}{N}}}_{\text{Matlab FFT}} \Delta t \right|^2 \quad k = 0, 1, \dots, \frac{N}{2} \quad (\text{B.27})$$

Thus, the correct implementation of the Matlab FFT, $fft(x_{in}, N)$, to calculate the one sided PSD is

$$\hat{G}_{xx}(f_k) = \frac{2}{n_d N \Delta t} \sum_{i=1}^{n_d} |fft(x_{in}, N) \Delta t|^2 \quad k = 0, 1, \dots, \frac{N}{2} \quad (\text{B.28})$$

Where the inclusion of N as an argument allows the N point FFT to be calculated in Matlab.

For a signal of zero mean, the mean square value is equal to the variance, eqt. (B.7), and can be calculated directly from the PSD as the area under the curve,

$$\psi_x^2 = \sigma_x^2 = \sum_{k=0}^{N/2} \hat{G}_{xx}(f_k) \Delta f \quad (\text{B.29})$$

Similarly, with zero mean, the root mean square value (RMS) is equal to the standard deviation, eqt. (B.8), and can be calculated from $\hat{G}_{xx}(f_k)$ as the square root of the area under the curve,

$$\psi_x = \sigma_x = \sqrt{\sum_{k=0}^{N/2} \hat{G}_{xx}(f_k) \Delta f} \quad (\text{B.30})$$

B.9 The dB Spectrum

Once again, as the units of the PSD are $\frac{\text{units}^2}{\text{Hz}}$, by dividing the PSD by the frequency resolution F_{res} , and calculating the square root, the $unit_{rms}$ as a function of frequency can be found. This is used to calculate the dB spectrum as shown below.

$$unit_{rms}(f_k) = \sqrt{\hat{G}_{xx}(f_k)\Delta f} \quad (\text{B.31})$$

$$dB_{rms} = 20\log_{10} \frac{unit_{rms}(f_k)}{2 \times 10^{-5}} \quad (\text{B.32})$$

B.10 Matlab Code to Calculate the PSD

```

%Variables-----
Npts=122880           %No. of discretised points in a signal (for example)
block_len=4096        %No. of points in block for averaging (for example)
N_overlap=block_len/2 %No. of points for overlapping (for example)
fsamp=8000            %Sampling Frequency. (for example)

Fres=fsamp/block_len  %Frequency Resolution
win_shape=hanning(block_len); %Windowing. Can try others
window_corr=sqrt(8/3); %Window correction factor for Hanning window

%Characterstics of the processing-----
Nav=Npts/block_len    %No. of averages
fres=fsamp/block_len  %Frequency resolution
t_delta=1/fsamp       %Delta t

%Create Time Axis-----
bin=1:Npts;
taxis=t_delta*(bin-1);

%Calculate the PSD from the traditional fft method.-----
%PSD has units squared per Hertz, e.g. (Volts^2/Hz)
spec=zeros(1,block_len);
for ptr=1:Nav
    ini=((ptr-1)*block_len)+1;
    fini=ptr*block_len;
    x_block=x1(ini:fini)-mean(x1(ini:fini)); %Form blocks and subtract mean
                                           %at each step
    x_win=x_block.*win_shape'; %Filter with Window

```

```

X1=t_delta*window_corr*fft(x_win,block_len); %Multiply fft by delta t and
                                                %the window correction factor
spec=spec+(conj(X1).*X1);                    %Calculate spectrum
end
PSD_fft=2*(spec(1:(block_len/2)+1))/(Nav*block_len*t_delta); %Calculate PSD

%Calculate the root mean square from the PSD-----
rms_PSD_fft=sqrt(sum(PSD_fft*Fres));

%Calclate dB spectrum from PSD-----
unit_fft=sqrt(PSD_fft*Fres);                %First calculate signal rms as function of
                                                %frequency from PSD (e.g. Volts_rms(f))

spec_refdB_fft=20.*log10(unit_fft./2E-5); %Then calculate dB(f) with reference
                                                %to threshold of hearing for each case.

```

B.11 The Cross Spectral Density Function

Similar to equation (B.26), the cross spectral density function can be calculated as follows.

$$\hat{G}_{xy}(f_k) = \frac{2}{n_d N \Delta t} \sum_{i=1}^{n_d} X_i^*(f_k) Y_i(f_k) \quad k = 0, 1, \dots, \frac{N}{2} \quad (\text{B.33})$$

Using the averaged PSD and CPSD functions, a number of useful frequency domain functions can be defined.

B.12 The Frequency Response Function

In real situations extraneous noise may be measured at the input and/or output of a system. Figure B.1 shows the general model where $u(t)$ passes through the system to produce the true output $v(t)$. $m(t)$ and $n(t)$ represent the extraneous noise measured within $x(t)$ and $y(t)$ which is due to non-linear operations or contributions from other unaccounted for input/outputs. It will be assumed that $m(t)$ and $n(t)$ are not correlated with each other, the input or the output.

Considering figure B.1, where it is assumed that records are from stationary random processes with zero mean values and that systems are constant-parameter linear systems, the frequency response function, represented by $H(f)$, can be defined as follows;

$$H(f) = \frac{\hat{G}_{xy}(f)}{\hat{G}_{xx}(f)} \quad (\text{B.34})$$

where the frequency dependent notation has been dropped for clarity. Further development of the frequency response function can be found in section 5.6.2.

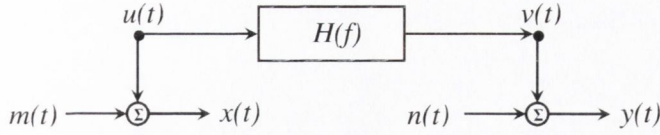


FIGURE B.1: Single-Input/Single-Output System with extraneous noise specified

B.13 The Ordinary Coherence Function

The *coherence function*¹ (sometimes called the coherency squared function) is defined as

$$\gamma_{xy}^2 = \frac{|\hat{G}_{xy}|^2}{\hat{G}_{xx}\hat{G}_{yy}} \leq 1 \tag{B.35}$$

Due to the *cross spectrum inequality* it is seen that the coherence function is bounded between zero and one. For the ideal case of a constant-parameter linear system with a single clearly defined input and output with no noise, the coherence function will be unity. If $x(t)$ and $y(t)$ are completely unrelated, the coherence function will be zero. If the coherence function is greater than zero but less than unity, one or more of the three possible physical situations exist.

1. Extraneous Noise is present in the measurements
2. The system relating $x(t)$ and $y(t)$ is not linear
3. $y(t)$ is an output due to an input $x(t)$ as well as to other inputs

For linear systems, the coherence function γ_{xy}^2 can be interpreted as the fractional portion of the mean square value at the output $y(t)$ that is contributed by the input $x(t)$ at frequency f . Conversely, the quantity $[1 - \gamma_{xy}^2]$ is a measure of the mean square value of $y(t)$ not accounted for by $x(t)$ at frequency f .

A *complex coherence function* may be defined by

$$\gamma_{xy} = |\gamma_{xy}|e^{-j\phi_{xy}} \tag{B.36}$$

where

$$|\gamma_{xy}| = +\sqrt{\gamma_{xy}^2} \tag{B.37}$$

and ϕ_{xy} is the phase angle of \hat{G}_{xy} .

¹The frequency dependent notation will be omitted for simplicity of representation.

B.14 Phase Angle and Convection Speed

The physical meaning of the phase angle ϕ_{xy} of \hat{G}_{xy} , measured in radians, between $x(t)$ and $y(t)$, is seen when expressed in the form

$$\phi(f) = 2\pi f\tau(f) \quad (\text{B.38})$$

Here, $\tau(f)$ represents the time delay between position $x(t)$ and $y(t)$ at frequency f , measured in seconds. For a convection speed of V and sound speed at atmospheric conditions calculated according to

$$c = \sqrt{\gamma RT} \quad (\text{B.39})$$

where γ is the ratio of specific heat at constant pressure to that at constant volume for air and is taken to be 1.4, $R = 287.1 \text{ J/kgK}$ is the specific gas constant for air and T is the temperature in Kelvin, the time $\tau(f)$ can represent the time taken for a pressure source to travel a distance d between two measurement locations at x and y

$$\tau(f) = \frac{d}{c + V} \quad (\text{B.40})$$

With this knowledge, the convection speed can be calculated using the phase angle by

$$V = \frac{2\pi f d}{\phi} - c \quad (\text{B.41})$$

In degrees, and using the slope of the unwrapped phase ($\text{slope} = \frac{\text{degrees}}{f}$) the above expression can be re-written as

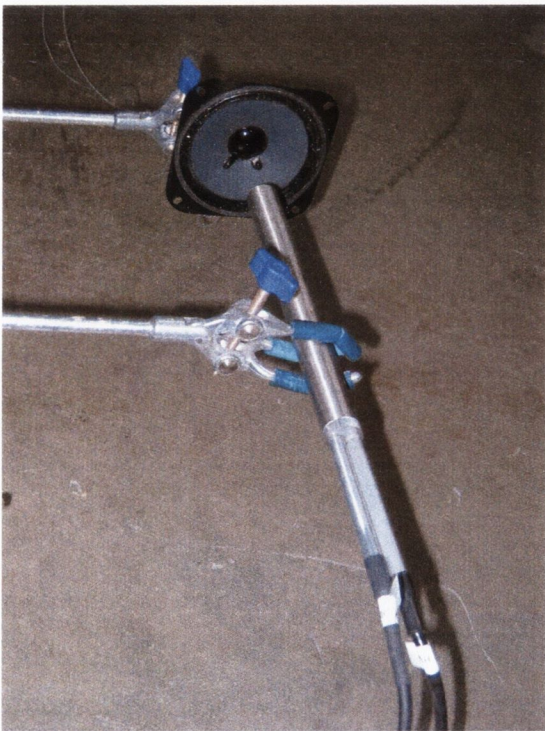
$$V = \frac{360 d}{\text{slope}} - c \quad (\text{B.42})$$

Also, when $V = 0$ the distance can be calculated from

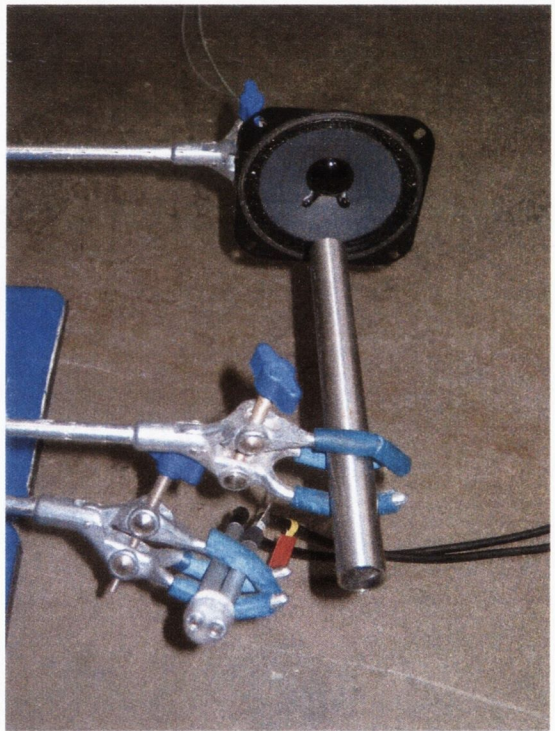
$$d = \frac{\text{slope } c}{360} \quad (\text{B.43})$$

Appendix C

Microphone Calibration



(a) Internal diameter of pipe equal to 16.7mm.



(b) Microphone mounting plug detail shown.

FIGURE C.1: Set-up for high frequency calibration. As 16.7mm was the minimum diameter tube size which could be used with two microphone diameters of 8mm, 11925Hz was the maximum calibration frequency possible in accordance with equation 2.31

Appendix A

Microphone Calibration

Microphone

Microphone Calibration



Microphone Calibration

Appendix D

FEA Analysis of Duct

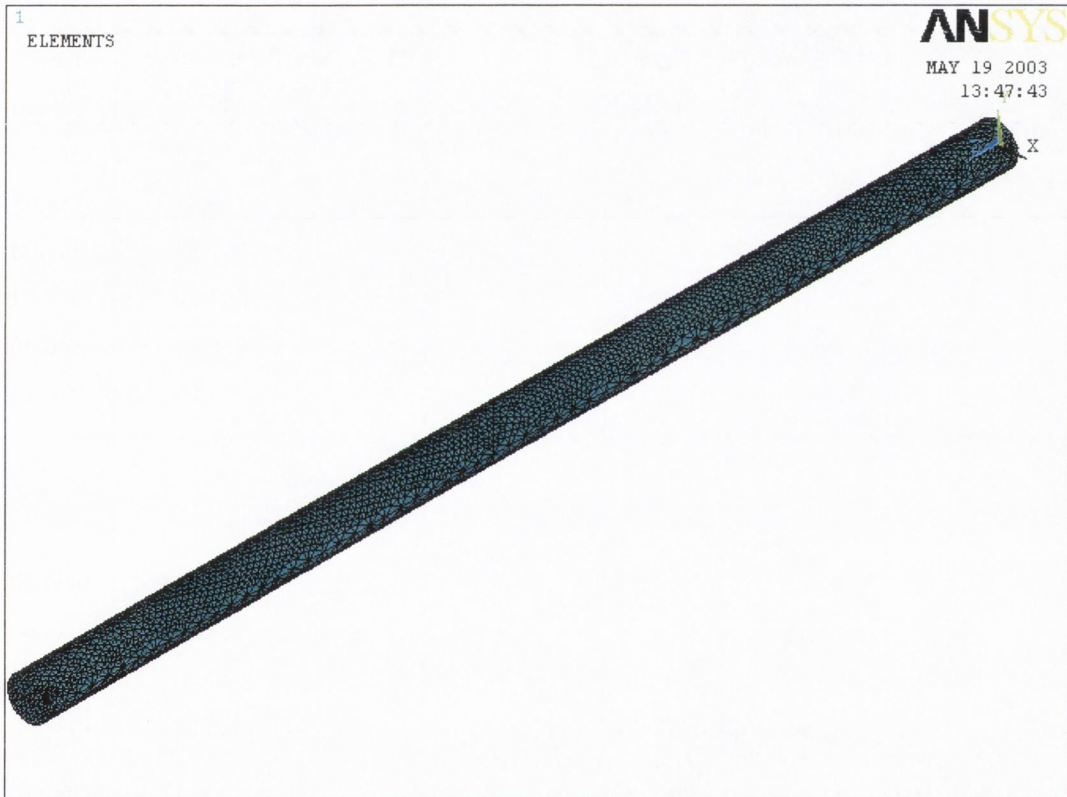


FIGURE D.1: Finite Element Mesh of Duct

FEA analysis on a duct was performed with Ansys for a two simplified cases;

- to validate the resonant frequencies of the duct as calculated from equations (4.3) and (4.13).
- to visualise some of the mode shapes

- to contrast the pressure distribution above the cut-off frequency, equation (2.31), with the plane wave behaviour below.

A simple duct was modelled in Ansys with a mesh of about 75,000 elements using the 3-D acoustic *Fluid30* element, ref. figure D.1. The duct was 1.2m long and 0.05115m in diameter. Some experimental pressure readings from microphones mounted flush with the inside surface of a duct of equal dimensions were taken for comparison.

FEA - Closed Duct

For the closed duct, a boundary condition of 1Pa was given to the source end.

With reference to table D.1, we see a comparison of the resonant frequencies of the closed duct as determined from equation (4.3) with those calculated from the Ansys programme. Over 30 modes were calculated with an error of less than about 1% up to the cut-off frequency.

Mode No.	Theoretical	FEA
1	69.73	69.69
2	209.19	209.16
3	348.65	348.55
4	488.11	487.99
5	627.56	627.50
6	767.02	766.99
7	906.48	906.60
.	.	.
.	.	.
.	.	.
27	3695.65	3729.60
28	3835.11	3873.50
29	3974.57	3993.00
30	4114.03	4040.00

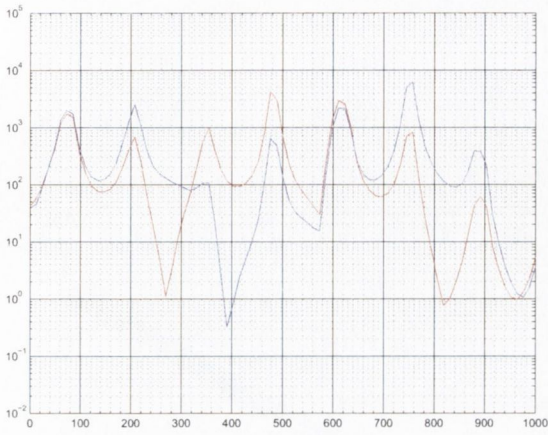
Mode No.	Theoretical	FEA
1	139.46	139.40
2	278.92	278.70
3	418.38	418.08
4	557.83	557.53
5	697.29	697.14
6	836.75	836.45
7	976.21	976.15
.	.	.
.	.	.
.	.	.
27	3765.38	3800.30
28	3904.84	3949.60
29	4044.30	4017.80
30	4183.76	4087.30

TABLE D.1: Resonant Frequencies for closed duct.

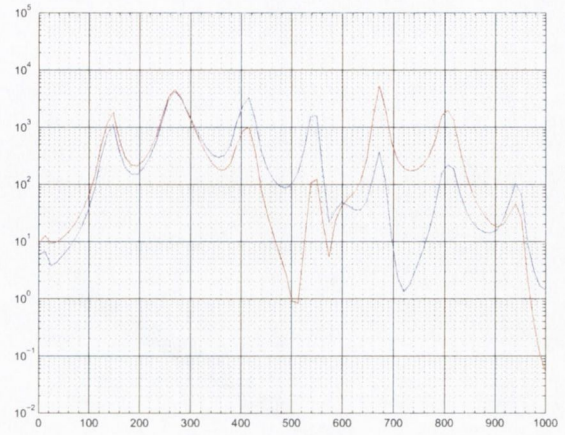
TABLE D.2: Resonant Frequencies for open duct.

Figure D.2(a) shows some experimental results for the closed duct when excited with the chirp algorithm using the HP Signal Analyser as discussed in section 3.4. The spectra from both microphones are shown, the differences between them being explained by their different locations along the pipe. Good agreement exists for these results when compared with table D.1.

Figures D.3(a) and D.3(b) show the pressure distribution in the pipe for the first two modes. It can be seen clearly how there is a node at the source end and an anti-node at the closed end for

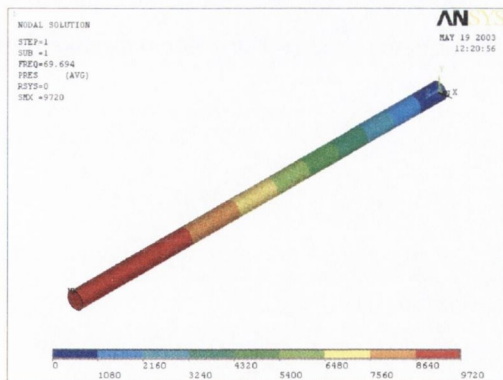


(a) Closed duct.

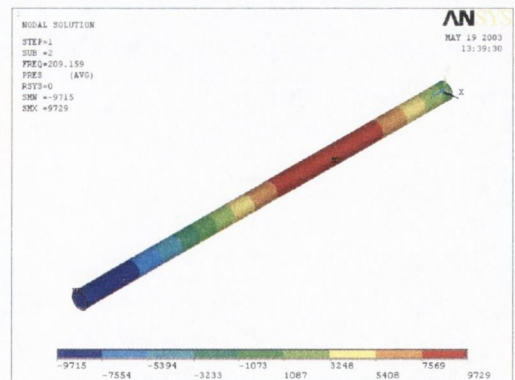


(b) Open duct.

FIGURE D.2: Pressure autospectra, microphones 1 & 2.



(a) 1st Mode Solution. Resonant Frequency = 69Hz



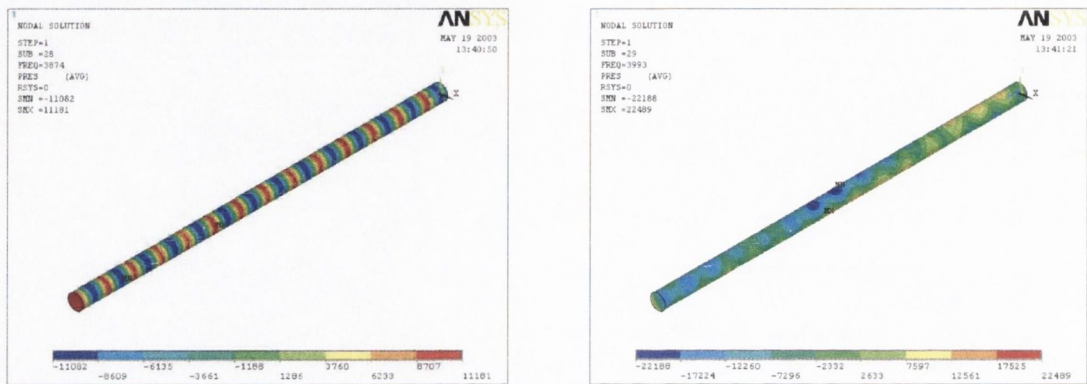
(b) 2nd Mode Solution. Resonant Frequency = 209Hz

FIGURE D.3: The first two modal Ansys solutions for the closed duct.

both of these modes. The first mode corresponds to a $\frac{1}{4}$ wave length, whereas the second corresponds to a $\frac{3}{4}$ wave length. The frequencies satisfy the physics of the situation, i.e. for the first mode the frequency has to be such that a quarter wave length fits in that length pipe when the speed of sound is $c = 340m/s$. In other words, the equation

$$c = f\lambda \quad (D.1)$$

is satisfied.



(a) 28th Mode Solution. Resonant Frequency = 3893Hz (b) 29th Mode Solution. Resonant Frequency = 3993Hz

FIGURE D.4: Two higher modal Ansys solutions for the closed duct showing the transition above the plane wave cut-off frequency.

As per equation (4.1), the plane wave cut-off frequency is $3894Hz$. That is to say plane wave behaviour should exist up to this frequency, above which higher modes are excited. Figure D.4(a) shows the last planar mode shape below the cut-off frequency before the system breaks down as shown in figure D.4(b)

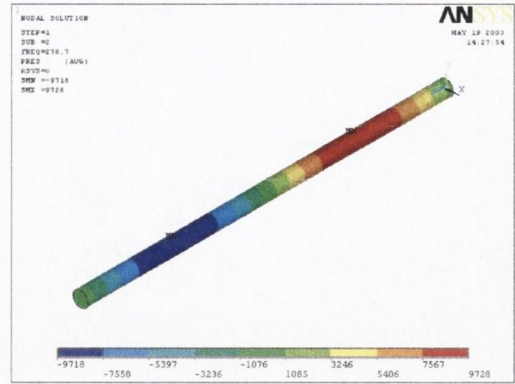
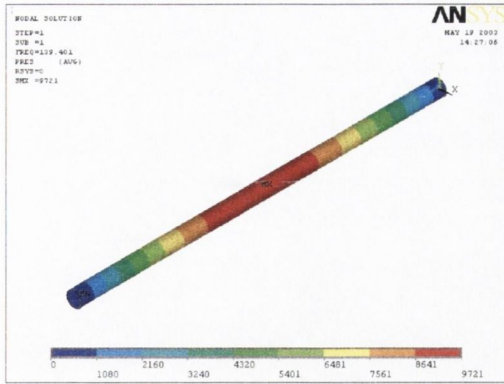
FEA - Open Duct

The boundary conditions for the open duct are $1Pa$ at the source end and $0Pa$ at the open end. This is the same case as for the simple open ended duct of section 4.4.

Again we see in table D.2 the comparison between the theoretical resonant frequencies of an open duct as calculated by equation (4.13) with those produced by Ansys. Once again they compare very well with less than a 1% error up to the cut-off frequency.

This time however, when we compare these figures with the experimental spectra of figure D.2(b) we see they over-estimate the higher frequencies. This is to be expected as in reality the duct behaves as if it is longer than that used in the theory if the condition that $p = 0$ at Δ is taken into account. This, as discussed, is due to the added inertance of the atmosphere.

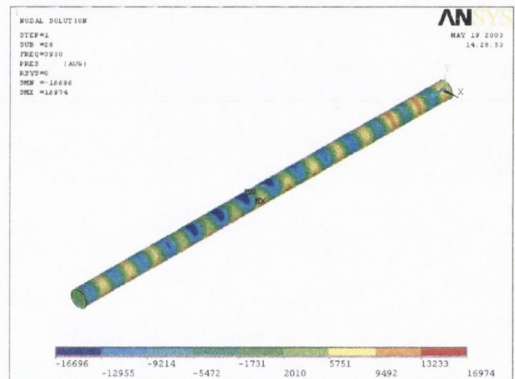
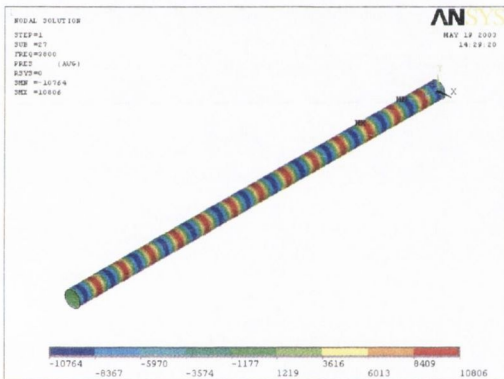
The first two pressure modes for the open duct are shown in figures D.5(a) and D.5(b). Here,



(a) 1st Mode Solution. Resonant Frequency = 139Hz (b) 2nd Mode Solution. Resonant Frequency = 278Hz

FIGURE D.5: The first two modal Ansys solutions for the open duct.

with nodes obligatory at both ends, the first mode is a $\frac{1}{2}$ wave length with the second 1 wavelength long.



(a) 27th Mode Solution. Resonant Frequency = 3800Hz (b) 28th Mode Solution. Resonant Frequency = 3950Hz

FIGURE D.6: Two higher modal Ansys solutions for the open duct showing the transition above the plane wave cut-off frequency.

Once again we see the plane wave formation breaking down above the cut-off frequency of 3894Hz, which is a frequency between those to be found in figures D.6(a) and D.6(b).

